EPFL

Thèse n° 8806

Multiaxial fatigue behavior and strengthening of riveted double-angle connections in steel bridges using prestressed CFRP rods

Présentée le 17 septembre 2021

Faculté de l'environnement naturel, architectural et construit
Laboratoire des structures métalliques résilientes
Programme doctoral en génie civil et environnement

pour l'obtention du grade de Docteur ès Sciences

par

Hossein HEYDARINOURI

Acceptée sur proposition du jury

Prof. C. J. D. Fivet, président du jury
Prof. A. Nussbaumer, Dr E. Ghafoori, directeurs de thèse
Prof. X. L. Zhao, rapporteur
Dr S. Chataigner, rapporteur
Prof. A. Taras , rapporteur

École polytechnique fédérale de Lausanne

2021

Dedicated with the deepest love to my father, who taught me the commitment, my mother for her endless compassionate love, and my wonderful sister.

Acknowledgements

The present PhD study was conducted at the Structural Engineering Research Laboratory of Empa, Swiss Federal Laboratories for Materials Science and Technology in conjunction with the Resilient Steel Structures Laboratory (RESSLab) at the École Polytechnique Fédérale de Lausanne (EPFL), which are highly acknowledged. The acknowledgement goes also to the Swiss Innovation Agency–Innosuisse (Grant ID: 19240.1 PFIWIW) for the financial support of the PhD study.

The sincere gratitude goes to the followings:

- Prof. Alain Nussbaumer (RESSLab, EPFL), my supervisor. His deep expertise in fatigue, critical thinking, and dedication to research as well as his innovative ideas were always inspiring during my 4-year PhD study.
- Dr. Elyas Ghafoori, my co-supervisor at Empa, from whom I learned on a daily basis. His great contribution in the development of the ideas and sharing his experiences facilitated the path to overcome the challenges.
- Prof. Masoud Motavalli, the head of Structural Engineering Research Laboratory at Empa, who gave me the opportunity to work at Empa and to make personal and technical progress.
- The industrial partners of the PhD project:
  (i) Mr. Martin Hüppi at S&P Clever Reinforcement Company AG, Switzerland, for providing financial, technical, and material supports.
  (ii) Mr. Herbert Friedl, Mr. Lukas Bodenmann, and Mr. André von Aarburg at Swiss Federal Railways (SBB) AG, Bern, for their interest to this research project and providing the infrastructure for strengthening the connections of a railway bridge in Lachen, Switzerland.
  (iii) Dr. Ann Schumacher at dsp Ingenieure + Planer AG Engineering Office, Uster, Switzerland, for her useful consultations.
- The examination jury consisting of Prof. Andreas Taras (ETH, Zurich), Prof. Xiao-Ling Zhao (UNSW, Australia), Prof. Sylvain Chataigner (Université Gustave Eiffel, France), Prof. Jacob-Wittrup Schmidt (Aalborg University, Denmark), and Prof. Corentin Fivet (EPFL, Switzerland) for their thoughtful comments on my PhD thesis.
- Robert Widmann, Slavko Tudor, Dimitri Ott, Giovanni Saragoni, and Werner Studer, as the testing hall (Bauhalle) team of Empa. The considerable number of experiments would not be successfully performed without the technical supports of this great team.

- Dr. Ardalan Hosseini, for his useful scientific and technical supports, which were of significant help during the project.
- Dr. Christoph Czaderski, Dr. Glauco Feltrin Dr. Moslem Shahverdi, Dr. Bernhard Schranz, Dr. René Steiger, and Dr. Pedro Palma for the instructive technical discussions during my time at Empa.
- Veronika Huber (Empa) and Emma Sorrentino (EPFL) for their administrative support.
- My friends: Dr. Saeed Abbasion, Dr. Abdola Sadeghi, Dr. Niluofar Moshiri, Dr. Mohammadreza Izadi, Dr. Maryam Mohri, and Mr. Ali Jafarabadi for their supports during the last four years.

My deepest gratitude goes to my dear father, Reza, my beloved mother, Zohreh, and my amazing sister, Haleh for their inspiring supports throughout the last four years.

Hossein Heydarinouri

Dübendorf, July 27th, 2021

Abstract

A large number of aging road and railway riveted metallic bridges suffer from fatigue problems. Stringer-to-floor-beam double-angle bridge connections are among the most fatigue-prone details due to the many cyclic distortion-induced stresses from axle loads. Increasing service loads and corrosion put these components at a higher risk of fatigue cracking. As the replacement of existing structures is costly, lengthy, and thus in some cases almost impossible, the development of retrofitting techniques is of great importance. However, fatigue strengthening of angle connections in bridges is a challenging task. The geometric complexities of these details hinder the development of applicable retrofitting techniques, and the multiaxial stress state in connections complicates fatigue analysis.

The first objective of this work is to develop an applicable retrofitting system for strengthening the stringer-to-floor-beam double-angle connections in bridges, considering the fact that the traditional retrofitting techniques such as stop holes, welding additional elements or the softening of connections are not capable of effectively tackling the problem. In recent decades, the application of carbon fiber-reinforced polymer (CFRP) composites has attracted much interest for the fatigue strengthening of metallic structures owing to their superior properties such as high strength, light weight, high corrosion and fatigue resistance. The strengthening system developed in this study consists of a new adhesive-free mechanical wedge–barrel anchor for prestressed CFRP rods and a friction-based clamping system. Extensive finite element simulations are performed to optimize the design of the strengthening system. In addition, the static and fatigue performance of the developed system is experimentally investigated in laboratory tests. The ultimate tensile strength of the strengthening system is found to be greater than the nominal strength of the CFRP rods, which ensures achieving the full capacity of the CFRP rod strength. In addition, the fatigue tests show neither failure of the CFRP rods nor prestressing loss due to slippage in the anchorage components.

The second objective is to determine the high-cycle fatigue thresholds for the prediction of crack initiation in angle connections subjected to multiaxial stresses. The critical plane approach is employed as an advanced approach for multiaxial high-cycle fatigue analysis. In addition, the effect of prestressed strengthening is incorporated into multiaxial fatigue models. Using identified proper critical plane-based multiaxial fatigue thresholds, a design approach is proposed for the fatigue strengthening of angle connections subjected to distortion-induced multiaxial stresses.

Finally, the third objective is to apply the developed retrofitting system to strengthen the connections of a 92-year-old riveted railway bridge in Switzerland as a demonstration of a field application. The results of the short-term measurements demonstrate the effectiveness of the retrofitting system in improving the high-cycle fatigue behavior of the bridge connections through the reduction of the mean values of the stress components. The post-installation long-term measurements show no prestressing loss in the CFRP rods, indicating that no slippage occurs in the strengthening system components.

Keywords: bridge connections, distortion-induced loading, multiaxial high-cycle fatigue, critical plane approach, crack initiation, retrofitting, prestressed CFRP, wedge–barrel anchor.

Résumé

Un grand nombre de ponts métalliques rivetés routiers et ferroviaires vieillissants souffrent de problèmes de fatigue. Les assemblages entre longerons et entretoises réalisés avec des double cornières sont parmi les détails les plus sujets à la fatigue en raison de l'application de nombreux cycles de contraintes induites par distorsion sous les charges d'essieux. L'augmentation des charges de service et la corrosion exposent ces éléments à un risque plus élevé de fissuration par fatigue. Comme le remplacement des structures existantes est coûteux, long et donc dans certains cas presque impossible, le développement de techniques de réparation est d'une grande importance. Cependant, le renforcement à la fatigue des assemblages par double cornières dans les ponts est un véritable défi. Les complexités géométriques de ces détails entravent le développement de techniques de réparation/renforcement utilisables, et l'état de contrainte multiaxial dans ces assemblages complique l'analyse à la fatigue.

Le premier objectif de cette étude est de développer un système de réparation utilisable pour renforcer les assemblages par double cornières entre longerons et entretoises dans les ponts, compte tenu du fait que les techniques de réparation traditionnelles telles que les trous en pointe de fissure, le soudage d'éléments supplémentaires ou l'assouplissement dans les assemblages ne sont pas capables de résoudre efficacement ce problème. Au cours des dernières décennies, l'application de composites polymères renforcés de fibres de carbone (CFRP) a suscité un grand intérêt pour le renforcement à la fatigue des structures métalliques en raison de leurs propriétés supérieures telles que résistance élevée, légèreté, excellente résistance à la corrosion et à la fatigue. Le système de renforcement développé dans cette étude se compose d'un nouvel ancrage mécanique à clavettes sans adhésif, système de serrage basé sur le frottement, pour maintenir les tiges CFRP précontraintes. Des simulations détaillées aux éléments finis sont effectuées pour optimiser la conception du système de renforcement. De plus, les performances statiques et en fatigue du système développé sont étudiées expérimentalement lors d'essais en laboratoire. Les résultats ont montré que la résistance ultime à la traction du système de renforcement est supérieure à la résistance nominale des tiges CFRP, ce qui permet d'atteindre la pleine capacité de résistance de ces tiges. De plus, les essais de fatigue n'ont montré ni rupture des tiges CFRP ni perte de précontrainte due au glissement dans les éléments d'ancrage.

Le deuxième objectif est la détermination des valeurs de la limite de fatigue (seuils à grand nombre de cycles) pour la prévision de l'amorçage des fissures dans les assemblages par double cornières soumis à des contraintes multiaxiales. L'approche dite « du plan critique » est utilisée comme méthode avancée pour l'analyse à la fatigue multiaxiale à grand nombre de cycles. De

plus, l'effet du renforcement précontraint est incorporé dans les modèles de fatigue multiaxiale. En utilisant les seuils obtenus en fatigue multiaxiale basés sur le plan critique, une méthode de dimensionnement est proposée pour le renforcement à la fatigue des assemblages par double cornières soumis à des contraintes multiaxiales induites par distorsion.

Enfin, le troisième objectif est d'appliquer le système de renforcement développé à des assemblages d'un pont-rail riveté en Suisse et vieux de 92 ans comme démonstrateur d'une utilisation réelle sur site. Les résultats des mesures à court terme ont montré l'efficacité du système de renforcement dans l'amélioration du comportement à la fatigue à grand nombre de cycles pour les assemblages grâce à la réduction des contraintes moyennes du tenseur des contraintes. Les mesures post-installation et à long terme ne montrent aucune perte de précontrainte dans les tiges CFRP, indiquant qu'aucun glissement ne se produit dans les composants du système de renforcement.

Mots-clés: assemblages de ponts, chargement induit par distorsion, fatigue multiaxiale à grand nombre de cycles, approche par plan critique, initiation de fissure, renforcement, tiges CFRP précontraintes, ancrage à clavette.

Table of Contents

Acknowledgements v

Abstract vii

Résumé vii

1. Introduction 1

1.1. Background and motivation 1

1.2. Scope, objectives, and research methodology 3

1.2.1. Scope 3

1.2.2. Objectives 4

1.2.3. Research methodology 4

1.3. Outline of the thesis 5

1.3.1. Chapter 2 6

1.3.2. Chapter 3 7

1.3.3. Chapter 4 7

1.3.4. Chapter 5 7

References 7

2. Development of a mechanical retrofitting system for bridge connections 9

2.1. FE analysis and experimental validation of mechanical wedge–barrel anchors for CFRP rods 11

2.1.1. Introduction 12

2.1.1.1. Innovations of this study 15

2.1.1.2. Outline of study 16

2.1.2. FE simulations 17

2.1.2.1. Parts of FE model 17

2.1.2.2. Material properties 18

2.1.2.3. Boundary conditions and analysis steps 19

2.1.2.4. Contact behavior 19

2.1.3. Validation of FE model 20

2.1.3.1. Measurement of draw-ins in experiment 21

2.1.3.2. Calibration of FE model 22

2.1.3.3. Verification of FE model 23

2.1.4. Various configurations for anchors 23

2.1.5. Results of FE analyses 25

2.1.5.1. Contact pressures on CFRP rods for anchor types 1 and 2 25

2.1.5.2. Contact pressures on CFRP rods for modified anchors 26
2.1.6. Selection of optimal anchor 27
2.1.6.1. Stress state on CFRP rod 27
2.1.6.2. Selection criterion 27
2.1.6.3. Fs values for different anchor configurations 28
2.1.6.4. Slippage between wedge and CFRP rod 30
2.1.7. Discussions 30
2.1.7.1. Effect of constant differential angle 30
2.1.7.2. Effect of geometric modifications 31
2.1.7.3. Effect of curved profile 32
2.1.8. Summary and conclusions 33
Appendix A. Mesh sensitivity analysis 34
Appendix B. Slippage between wedge and CFRP rod 35
References 35
2.2. Development of a mechanical wedge–barrel anchor for CFRP rods: static and fatigue behaviours 39
2.2.1. Introduction 40
2.2.1.1. CFRP plate anchorages 40
2.2.1.2. CFRP rod anchorages 41
2.2.1.3. Fatigue tests on mechanical wedge-barrel anchors 42
2.2.1.4. Primary objectives and outline of the study 43
2.2.2. Proposed anchorage system 43
2.2.2.1. Different anchor configurations 44
2.2.2.2. Material properties of the anchorage components 45
2.2.3. Preliminary static tests 45
2.2.3.1. Test results 46
2.2.3.2. Modification on the split-wedge anchors 48
2.2.4. Experimental study on the modified split-wedge anchors 48
2.2.4.1. Standard static and fatigue testing procedures 48
2.2.4.2. Static tests on the modified split-wedge anchors 49
2.2.4.3. Fatigue tests on the modified split-wedge anchors 52
2.2.4.4. Effect of the loading frequency 56
2.2.4.5. Residual strength tests 57
2.2.5. Field application of the proposed anchorage 59
2.2.6. Summary and conclusions 60
Appendix I. FE model development 60
Appendix II. Modifications on the split-wedge anchor 62

Appendix III. Resulting presetting force by the new presetting system 62
References 63
2.3. Development of mechanical strengthening system for bridge connections using prestressed CFRP rods 67
2.3.1. Introduction 67
2.3.1.1. Research significance 69
2.3.1.2. Outline of the study 70
2.3.2. Introduction to the strengthening system 71
2.3.2.1. Description of the clamping system 71
2.3.2.2. Installation procedure 72
2.3.2.3. Dismantling procedure 74
2.3.2.4. Advantages of the proposed retrofit system 74
2.3.3. Static and fatigue tests on wedge-barrel anchors 75
2.3.4. Static pull-off tests 76
2.3.4.1. Test set-up and instrumentation 77
2.3.4.2. Results of the static pull-off tests 78
2.3.5. Finite Element (FE) model 81
2.3.5.1. Description of the model 81
2.3.5.2. Correlation between the FE model and experimental results 84
2.3.5.3. Tensile stress in the top flange of the beam 85
2.3.6. Performance of the clamping system under fatigue loading 86
2.3.6.1. Test set-up 86
2.3.6.2. Stress in the CFRP rods 88
2.3.7. Effect of the strengthening system on the stresses in the connections 89
2.3.7.1. Description of the FE model developed for the connection tests 89
2.3.7.2. Experimental results 91
2.3.8. Field application of the proposed strengthening system 94
2.3.9. Summary and conclusions 94
2.3.10. Recommendations for future studies 96
Appendix I. Detailed dimensions of the clamping system and different setups 96
Appendix II. FE modeling of the imperfections in the connection tests 99
References 102

3. Multiaxial fatigue criteria for steel connections 105
3.1. Multiaxial fatigue criteria for prestressed strengthening of steel connections 107
3.1.1. Introduction 108
3.1.1.1. High-cycle fatigue behavior of the connections 108
3.1.1.2. Gaps to be filled in this study 110

3.1.1.3. Outline of this study 111
3.1.2. Critical plane approach 112
3.1.3. Calculation procedure for multiaxial fatigue analysis 112
3.1.4. Stress-based critical plane models 115
3.1.4.1. Modified Wohler curve method (MWCM) 115
3.1.4.2. Fatemi-Socie's (FS) model 116
3.1.4.3. Estimation of the fully reversed fatigue limits 117
3.1.4.4. Comparison with experimental data 118
3.1.5. Description of the test setup 119
3.1.5.1. Different parts of the setup 119
3.1.5.2. Instrumentation 121
3.1.6. Initial stress state 122
3.1.6.1. Residual stresses 123
3.1.6.2. Effect of the prestressing force 125
3.1.7. Fatigue test results 126
3.1.7.1. Effective stresses in the fatigue tests 126
3.1.7.2. Comparison of the test results with the MWCM and FS thresholds 128
3.1.7.3. Effect of $[\sigma_{res,\,m}]$ on the threshold 129
3.1.7.4. Initiation and propagation of the fatigue cracks 130
3.1.8. Strengthening effect 131
3.1.8.1. Additional flexural stiffness 131
3.1.8.2. Prestressing effect 131
3.1.8.3. Example of the strengthening effect 133
3.1.9. Conclusions 135
Appendix A. Equations for the calculation of stresses from the measured strains 136
Appendix B. Measurement results for $\sigma_{res,\,m\text{-}x}$ and $\sigma_{res,\,m\text{-}y}$ as a function of the cut depth 136
References 137

4. Multiaxial fatigue strengthening of connections of an old railway bridge 141
4.1. Strengthening of Steel Connections in a 92-Year Old Railway Bridge using Prestressed CFRP Rods: a Multiaxial Fatigue Design Criterion 143
4.1.1. Introduction 143
4.1.2. Outline of the study 147
4.1.3. Development of the strengthening system 147
4.1.3.1. Laboratory tests on the retrofitting system 148
4.1.3.2. Effect of removing the bolts 149
4.1.3.3. Advantages of the proposed strengthening system 150
4.1.4. Geometrical details of Aabach Bridge 151

4.1.5. Installation of the strengthening system on the Aabach Bridge 152
4.1.5.1. Presetting procedure 153
4.1.5.2. Procedure of CFRP prestressing 154
4.1.6. Short-term measurements 156
4.1.6.1. Left angle 157
4.1.6.2. Right angle 163
4.1.6.3. Stresses in the web 163
4.1.7. Long-term measurements over a 7-month period 164
4.1.8. Protection of the strengthening system 166
4.1.9. Multiaxial fatigue criterion 166
4.1.9.1. Critical plane approach 167
4.1.9.2. Multiaxial calculations for the measured cycles 169
4.1.9.3. Determination of the prestressing level in the strengthening system 171
4.1.10. Summary and conclusions 171
Appendix I. Stress history in the web for Trains (6) and (14) 172
Appendix II. Multiaxial fatigue tests 173
References 175

5. Conclusions and recommendations for future studies 179
5.1. Conclusions 179
5.1.1. FE analysis and experimental validation of mechanical wedge–barrel anchors for CFRP rods 179
5.1.2. Development of a mechanical wedge–barrel anchor for CFRP rods: static and fatigue behaviours 179
5.1.3. Development of mechanical strengthening system for bridge connections using prestressed CFRP rods 180
5.1.4. Multiaxial fatigue criteria for prestressed strengthening of steel connections 181
5.1.5. Strengthening of Steel Connections in a 92-Year Old Railway Bridge using Prestressed CFRP Rods: a Multiaxial Fatigue Design Criterion 182
5.2. Recommendations for future studies 183
5.2.1. Development of wedge-type anchors for CFRP tendons 183
5.2.2. Prediction of crack initiation and propagation in angle connections 184

Supplement A: Supplementary materials for Paper III 187
A.1. Stress distribution in top flange of the beam in the clamped area 187
A.2. Strain in angle connections during fatigue test 187

Supplement B: Supplementary materials for Paper IV 189

B.1. MATLAB script for multiaxial fatigue analysis based on the critical plane approach 189
B.2. Stresses in prestressed CFRP rods during fatigue tests 191
B.3. Strain measurements in cut-compliance method 192
B.4. Probabilistic analysis of the fatigue test data 192
B4.1. Calculation procedure based on the lower tolerance bound method 192
B4.2. Calculation procedure based on annex D of Eurocode 194
B4.3. Results of the probabilistic analysis 196
B4.3.1. Uniaxial test results 196
B4.3.1.1. Lower tolerance bound method 196
B4.3.1.2. annex D of Eurocode 197
B4.3.2. Multiaxial test results 198
References 200

Supplement C: Supplementary materials for Paper V 201
C.1. Effect of bolt removal 201
C.2. Removal of rivets 201
C.3. MATLAB script for strain and stress calculations from measurements on the Aabach Bridge 202
C.3.1. Before strengthening the connections 202
C.3.2. During prestressing 203
C.3.3. After strengthening the connections 203
C.4. Stresses in web of stringer before and after strengthening 205

Curriculum Vitae 207

1. Introduction

1.1. Background and motivation

The load-carrying capacity of old steel bridges owing to corrosion, lack of proper maintenance, and fatigue-sensitive details is a worldwide concern [1]. In Europe, almost 22% of railway bridges are metallic, nearly 70% of all metallic bridges are more than 50 years old, and nearly 30% are over 100 years old [2]. According to a report by the Federal Highway Administration (FHWA) in the US, until December 2013, nearly 56% of 181 000 steel bridges were over 50 years old, and 5% were more than 100 years old [3]. In 2016, the FHWA reported that steel bridges accounted for 52% of the 56 000 structurally deficient bridges in the US [3]. In China, the number of highway bridges reached 689 400 by the end of 2011 [4], which is close to 605,103 bridges in the US at this year. Although the age of Chinese bridges on average is much lower than that in the US, the proportion of structurally deficient bridges has already surpassed that of the US [5].

Governments across the globe allocate a huge annual budget for the maintenance, upgrading, and replacement of existing bridges. According to the report on the assessment of highway structures in Europe in 2015 [6], the annual cost for the maintenance, repairs, and renewals of highway bridges was estimated at €4–6 billion, which was 1–1.5% of the replacement cost on average. In Switzerland, an annual cost of €78.8 million was estimated, which was evaluated as 0.98% of the replacement cost [6]. In Australia, the government provided a budget of $640 million from 2015 to 2023 to "enhance access for local communities and facilitate higher productivity vehicle access" [7]. In 2016, the FHWA estimated a total cost of more than $47 billion to replace all structurally deficient highway bridges [3].

In most cases, the replacement of structurally deficient bridges is more costly than the rehabilitation and repair cost, which usually takes less time and reduces service interruption. According to an FHWA report, the cost for the rehabilitation of structurally deficient bridges is estimated to be 68% of the cost for their complete replacement [3]. This means that the rehabilitation of the existing structurally deficient bridges in the US would nearly result in a $15 billion savings.

In addition, the replacement of the metallic bridges is not a sustainable solution considering that the iron and steel sector is a highly energy- and CO_2- intensive industry [8]. According to a recent survey in 2020, steel and iron are responsible for about 8% of global final energy demand

and 7% of energy sector CO_2 emissions (including process emissions), and, buildings and infrastructure account for around half of the total steel demand [8]. Considering the EU strategy to become climate-neutral by 2050, that is, an economy with net-zero greenhouse gas emissions (GHEs) [9], the demand for the production of new or recycled steel (note that steel recycling is also an energy-intensive process) must be reduced. To achieve this goal, the International Energy Agency [8] provides a series of strategies such as the development of lightweight and modular designs, reducing material waste (e.g., through additive manufacturing that forms complex shapes with minimal material losses), and retrofit/repair and reuse to extend lifetimes. The largest contributor to reducing the steel demand by 2050 has been identified to be extending the lifetime of structures.

The structural engineering sector can make a significant contribution to reducing the steel demand through the development of effective and economic retrofitting solutions to extend the lifetimes of metallic structures and diminish the need for entire bridge replacements. This is the driving force for the continuous research on the development of strengthening solutions.

Fatigue is a major problem in the aging metallic bridges. Distortion-induced fatigue cracks account for nearly 90% of the fatigue damage in steel bridges [10, 11]. Angle connections, which are subjected to distortion-induced loadings, are considered to be one of the most fatigue-prone details in bridges [11]. A typical stringer-to-floor-beam double-angle connection and possible fatigue failures are shown in Fig. 1. Although modern specifications provide some prescriptive rules to prevent fatigue failure in new bridges, a large number of bridges are susceptible to cracking [10]. Therefore, the development of a retrofitting system for bridge connections is a significant task.

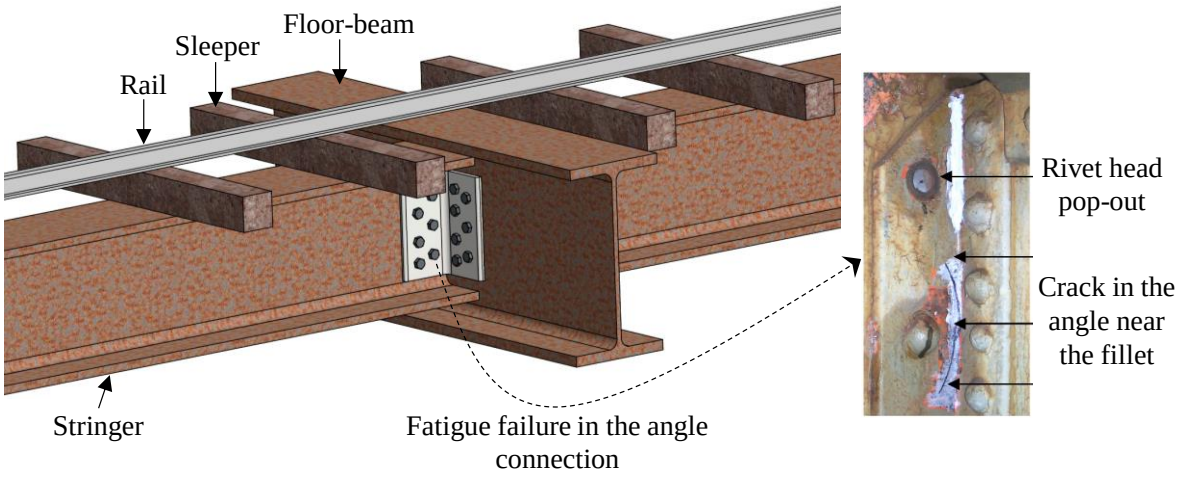

Fig. 1. Typical stringer-to-floor-beam double-angle connection in a railway bridge and fatigue failure in the angle.

Various repairing techniques have been proposed in previous studies to address fatigue problems in existing bridges. The use of stop holes, the welding of additional elements [12-14], the use of high-strength pre-tensioned bolts [15-17], and the softening of connections by removing rivets [18] are among the proposed techniques. However, these strengthening solutions have not been able to completely tackle the problem because they were either a source of stress concentration (e.g., stop holes or welds) or only altered the loading path. Consequently, using these solutions, fatigue cracks often re-initiated from either the same location or elsewhere [19].

In recent years, the application of prestressed carbon-fiber reinforced polymer (CFRP) materials for the strengthening of metallic structures has attracted attention [20, 21], taking advantage of the high strength-to-weight ratio and superior fatigue and corrosion resistance of CFRPs compared to steel. However, these retrofitting techniques are applicable only for strengthening bridge girders and not for connections.

One of the main challenges in the development of applicable strengthening solutions for bridge connections is the geometric complexity due to the presence of various components connected with fasteners, floor-beams, sleepers, and rails as shown in Fig. 1. The other challenge is the lack of failure criteria for the prediction of fatigue failure, which requires an understanding of the complex multiaxial stresses applied to connections.

In the present thesis, a new retrofitting solution for bridge angle connections is developed using prestressed CFRP rods, which is applicable to the complex geometries found in practice. For the prediction of crack initiation in the angle connections subjected to distortion-induced loadings, proper multiaxial fatigue thresholds, which can consider the effect of multiaxiality as well as different sources of stresses, are determined, and a design approach is proposed for the fatigue strengthening of connections using the developed retrofitting system.

1.2. Scope, objectives, and research methodology

1.2.1. Scope

The present thesis provides an understanding of multiaxial fatigue crack initiation and the corresponding threshold in steel angle connections subjected to distortion-induced loadings. In addition, a design approach for the prestressed strengthening of connections is proposed.

The following aspects are not within the scope of this research and are not addressed in the present thesis:

1. The effect of the application of non-proportional and/or variable amplitude loadings on

2. the connections.
3. Crack initiation in connections considering the effect of cyclic plastic strain.
4. Analysis of the propagation of a fatigue crack once initiated.
5. Effect of different steel grades on the fatigue behavior of connections.

1.2.2. Objectives

The main objectives of the present thesis are as follows:

(i) Development of a practical fatigue retrofitting solution for bridge connections:
The goal is development of a practical retrofitting system applicable to the complex geometric details in real applications using prestressed CFRP materials to improve the multiaxial fatigue behavior of angle connections. Numerical investigations are conducted to optimize the design of the retrofitting system using finite element (FE) simulations. In addition, the reliable performance of the system and its effectiveness in improving the fatigue behavior of connections are experimentally evaluated in laboratory tests under static and fatigue loadings.

(ii) Development of multiaxial fatigue crack initiation criteria for bridge connections:
It is aimed to determine the appropriate stress-based multiaxial fatigue thresholds for the prediction of crack initiation in angle connections subjected to distortion-induced loadings. The critical plane approach is employed, and the effect of prestressed strengthening is incorporated into the multiaxial fatigue analyses. Finally, a design approach for fatigue strengthening of connections made of steel grade S235 is presented.

1.2.3. Research methodology

The overall path to tackle the thesis objectives are: (i) understanding the origins of fatigue failure in angle connections subjected to distortion-induced stresses, (ii) identification of the challenges to solve the fatigue issue, (iii) proposition of a conceptual design for an applicable strengthening solution for the connections, and (iv) framing the required experimental and numerical studies. Various experimental studies and FE simulations conducted to achieve the objectives are summarized in the following subsections.

1.2.3.1. Experimental program

(i) Uniaxial static tensile tests on mechanical wedge–barrel anchors to obtain the ultimate

tensile strength of the post-tensioned (PT) system and the required presetting force to prevent slippage of the CFRP rods inside the wedges.

(ii) Uniaxial fatigue tests on the mechanical wedge–barrel anchors according to the standard testing procedures, such as ETAG 013 to evaluate the fatigue performance of the PT system, including premature rupture of the CFRP rods, slippage of the anchorage components, and the sensitivity of the PT system to loading frequency.

(iii) Static pull-off tests on the whole clamping system to evaluate the slippage resistance and ultimate tensile capacity of the strengthening system. Static and fatigue tests on the strengthened connections in a real-scale experiment to investigate the effectiveness of the developed system to reduce the stresses in the connections, the slippage of the retrofitting system components, and the prestressing loss in the CFRP rods.

(iv) Fatigue tests on the steel angle connections strengthened with the developed system to determine the appropriate critical plane-based multiaxial fatigue thresholds for the prediction of crack initiation at different angles.

(v) Strengthening the connections of a riveted railway bridge in Switzerland, named Aabach Bridge (built in 1928), and implementation of the onsite measurements to evaluate the effectiveness of the developed retrofitting system as well as its short- and long-term behaviors under the passage of different trains over the bridge.

1.2.3.2. FE simulation

(i) Development of FE models for various configurations of wedge–barrel anchors to achieve an optimal design configuration.

(ii) FE simulations of the mechanical clamping system to optimize the dimensions of the parts and to achieve a proper stress distribution in the components of the clamping system and the clamped area of the beam.

(iii) Development of FE models of the strengthened angle connections to investigate the multiaxial stresses in the connections due to the application of the CFRP prestressing force and superimposed loads on the stringers in laboratory tests.

1.3. Outline of the thesis

The current thesis consists of five journal papers, which are incorporated into five chapters. Fig. 2 illustrates the outline and structure of thesis. In the first chapter, an introduction is given to the thesis, and the contents of the next chapters are briefly described below.

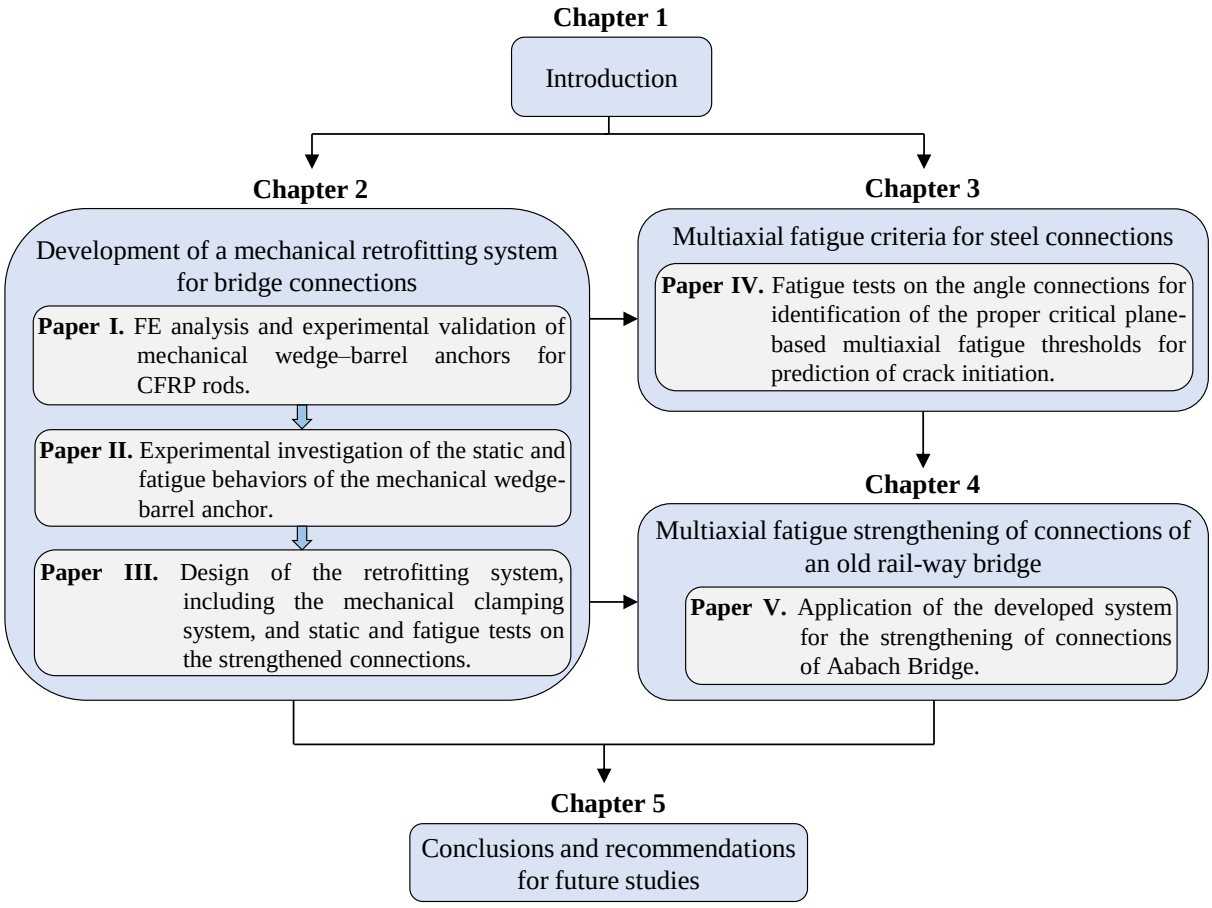

Fig. 2. Outline of the thesis.

1.3.1. Chapter 2

This chapter is devoted to the development of a new strengthening system for bridge connections using prestressed CFRP rods conducted in the framework of an Innosuisse Swiss Innovation Agency project (Grant ID: 12993.1 PFIW-IW). This chapter consists of three journal papers: Papers I, II, and III.

Papers I and II are dedicated to the development of a new friction-based wedge–barrel anchor. In Paper I, a comparative study is conducted on different configurations of mechanical wedge–barrel anchors using FE simulations to identify the optimal anchor configuration having the lowest stress concentration. Based on the obtained results, the static and fatigue performances of the selected anchor are experimentally investigated in laboratory tests presented in Paper II. Paper III is dedicated to the numerical and experimental investigations of the entire strengthening system, consisting of the developed wedge–barrel anchor and a mechanical clamping system. Both the static and fatigue performance of the developed strengthening system are experimentally studied. In addition, the effectiveness of the strengthening system in reducing the multiaxial distortion-induced stresses in the strengthened connections is evaluated.

1.3.2. Chapter 3

This chapter is dedicated to the determination of proper multiaxial fatigue thresholds for the prediction of crack initiation in angle connections. Paper IV in this chapter presents the results of the fatigue tests on the angle connections, where different critical plane-based multiaxial fatigue models are compared, and the most suitable models are selected. In addition to the effect of the prestressed strengthening system, the effects of residual stresses in the connections due to the manufacturing process and the stresses due to the fastening of fasteners (bolts) during the installation are considered in the models. Finally, a design approach for the prestressed fatigue strengthening of angle connections is presented. The retrofitting system developed in Chapter 2 is used for strengthening the connections in the fatigue tests in this chapter.

1.3.3. Chapter 4

In this chapter, using the outcomes of chapters 2 and 3, the developed retrofitting system is used to strengthen the angle connections of the Aabach Bridge, addressed in Paper V. In this study, the applicability of the developed retrofitting system in real applications with complex geometric details is demonstrated. In addition, the improvement in the multiaxial fatigue behavior of the strengthened connections is evaluated using the results of short-term on-site measurements. Furthermore, long-term monitoring of the strengthening system using a wireless sensor network (WSN) system is presented.

1.3.4. Chapter 5

In this chapter, the main conclusions of the thesis are summarized, and a list of recommendations for future studies is provided.

References

1. Tavakkolizadeh M, Saadatmanesh H. Strengthening of steel-concrete composite girders using carbon fiber reinforced polymers sheets. Journal of Structural Engineering 2003;129(1)30-40. http://www.scopus.com/inward/record.url?eid=2-s2.0-0141963450&partnerID=40&md5=e4e4484c0a3fe1eb4c75ce866f4e61b0.
2. Bien J, Elfgren L, Olofsson J. Sustainable bridges, assessment for future traffic demands and longer lives. Wroclaw: Dolnoslaskie Wydawnictwo Edukacyjne 2007. urn:nbn:se:ltu:diva-21622
3. FHWA. FHWA, Federal Highway Administration. U.S. Dempartment of Transportation 2016. https://www.fhwa.dot.gov/bridge/.
4. Casas JR. The bridges of the future or the future of bridges? Frontiers in Built Environment 2015;13.
5. Zhang X, Liu G, Ma J, Wu H, Wu W. Design concept and approach on sustainable development of bridge engineering. Proceedings of IABMAS-2014, Shangai 2014.

6. Brady K, O'Reilly M, Bevc L, Žnidarič A, O'Brien E, Jordan R. COST 345–Procedures Required for the Assessment of Highway Structures–Final Report. European Commission, Directorate General Transport and Energy: Bruxelles, Belgium 2015.
7. http://investment.infrastructure.gov.au/. [accessed on 25 Apr. 2021].
8. International Energy Agency, Iron and Steel Technology Roadmap: Towards more sustainable steelmaking, www.iea.org. 2020.
9. European Union climate strategies & targets, 2050 Long-Term Strategy: https://ec.europa.eu/clima/policies/strategies/2050_en [Accessed 24 July 2021].
10. Connor RJ, Fisher JW. Identifying effective and ineffective retrofits for distortion fatigue cracking in steel bridges using field instrumentation. Journal of Bridge Engineering 2006;11(6)745-752. https://doi.org/10.1061/(ASCE)1084-0702(2006)11:6(745)
11. Haghani R, Al-Emrani M, Heshmati M. Fatigue-prone details in steel bridges. Buildings 2012;2(4)456-476. https://doi.org/10.3390/buildings2040456
12. Connor RJ, Lloyd JB Maintenance Actions to Address Fatigue Cracking in Steel Bridge Structures. 2017, NCHRP Project.
13. Dexter RJ, Ocel JM Manual for repair and retrofit of fatigue cracks in steel bridges. 2013, United States. Federal Highway Administration.
14. Kuehn B, et al. Assessment of existing steel structures: recommendations for estimation of remaining fatigue life. 2008. http://publications.jrc.ec.europa.eu/repository/handle/JRC43401.
15. Al-Emrani M Fatigue in Riveted Railway Bridges. 2002, PhD Thesis, Chalmers University of Technology, Gothenburg, Sweden.
16. Baker K, Kulak G. Fatigue of riveted connections. Canadian Journal of Civil Engineering 1985;12(1)184-191. https://doi.org/10.1139/l85-017
17. Reemsnyder HS. Fatigue life extension of riveted connections. Journal of the Structural Division 1975;101(ASCE# 11795 Procceding).
18. Bowman MD. Fatigue evaluation of steel bridges. Vol. 721. 2012: Transportation Research Board.
19. Roeder CW, MacRae G, Leland A, Rospo A. Extending the fatigue life of riveted coped stringer connections. Journal of Bridge Engineering 2005;10(1)69-76. https://doi.org/10.1061/(ASCE)1084-0702(2005)10:1(69)
20. Ghafoori E, Motavalli M. Innovative CFRP-Prestressing System for Strengthening Metallic Structures. Journal of Composites for Construction 2015;19(6)04015006. https://doi.org/10.1061/(ASCE)CC.1943-5614.0000559. http://www.scopus.com/inward/record.url?eid=2-s2.0-84939204537&partnerID=40&md5=3422ce7a81b87ad1b00e68ab9a965d3e.
21. Hosseini A, Ghafoori E, Motavalli M, Nussbaumer A, Zhao XL, Al-Mahaidi R. Flat Prestressed Unbonded Retrofit System for Strengthening of Existing Metallic I-Girders. Composites Part B 2018;155156-172. https://doi.org/10.1016/j.compositesb.2018.08.026

2. Development of a mechanical retrofitting system for bridge connections

Motivation

The goal for this chapter is the development of a mechanical strengthening system for stringer-to-floor-beam double-angle connections to reduce distortion-induced multiaxial stresses and to enable an easy field application using prestressed CFRP materials.

Summary

In section 2.1, a comparative study of various configurations of friction-based wedge–barrel anchors using FE simulations is presented. The anchor configurations consist of a steel barrel and split aluminum wedges with either a curved or a constant differential angle conical profile. In addition, geometrical modifications are introduced to the anchors using a cut or fillet. The FE models are validated using the experimental results, and the contact pressure distributions on the CFRP rods are obtained. The optimal wedge–barrel configuration is chosen as having the smallest stress concentration on the CFRP rod at the loading end. The developed wedge–barrel anchor is versatile and has a general applicability.

Section 2.2 is dedicated to the evaluation of the static and fatigue behaviors of mechanical wedge–barrel anchors based on the outcome of the FE simulations presented in section 2.1. The test procedures are implemented according to European guidelines for testing post-tensioning kits, e.g., ETAG 013, and the reliable performance of the anchors in both static and fatigue tests is presented. In addition, the significance of the wedge seating distance in the fatigue performance of the anchors is highlighted, and subsequently, a new displacement-controlled presetting system is developed to ensure an adequate wedge seating distance. Finally, the sensitivity of the anchorage system to high loading frequencies is experimentally investigated.

After ensuring the reliable performance of the wedge–barrel anchors, a new retrofitting system for double-angle connections using prestressed CFRP rods is introduced in section 2.3. In addition to the wedge–barrel anchors that hold the prestressed CFRP rods, the strengthening system consists of a friction-based clamping system attached to the stringer flange to transmit the prestressing force to the structure. A series of FE models are developed to optimize the design of the clamping system. The static performance of the strengthening system is evaluated in the static pull-off tests in the laboratory. Finally, using a full-scale test setup representing the bridge

connections in real applications, the fatigue performance of the strengthening system, including the rupture or prestressing loss in the CFRP rods, is experimentally investigated. In addition, the capability of the developed strengthening system in reducing the multiaxial distortion-induced stresses in the angle connections is demonstrated.

Supplementary materials to this chapter is provided in Supplement A at the end of the thesis. This supplement gives: (i) stress distribution in top flange of the beam in the clamped area, and (ii) strain in angle connections during fatigue test.

Bibliographic details

Section 2.1 presents the paper with the following full bibliographic details:

- Hossein Heydarinouri, Aleksandar Vidovic, Alain Nussbaumer, Elyas Ghafoori. FE analysis and experimental validation of mechanical wedge–barrel anchors for CFRP rods. Submitted to Composite Structures and accepted on 1st of August 2021.

Section 2.2 presents the post-print version of the paper with the following full bibliographic details:

- Hossein Heydarinouri, Masoud Motavalli, Alain Nussbaumer, Elyas Ghafoori. Development of a Mechanical Wedge-Barrel Anchor for CFRP Rods: Static and Fatigue Behaviors. Journal of Composites for Construction 2021, 25(3)04021015. https://ascelibrary.org/doi/abs/10.1061/%28ASCE%29CC.1943-5614.0001124

Section 2.3 presents the post-print version of the paper with the following full bibliographic details:

- Hossein Heydarinouri, Masoud Motavalli, Alain Nussbaumer, Elyas Ghafoori. Development of Mechanical Strengthening System for Bridge Connections Using Prestressed CFRP Rods. Journal of Structural Engineering 2021; 147(3)04020351. https://doi.org/10.1061/(ASCE)ST.1943-541X.0002923

Author's contribution

Hossein Heydarinouri, as the first author of the above-mentioned papers, developed the FE models, designed the experiments, analyzed the results of the FE simulations and experiments, wrote the manuscripts, and revised the final version of the papers. The co-authors provided support, supervision, and revision of the contents of this chapter.

2.1. FE analysis and experimental validation of mechanical wedge–barrel anchors for CFRP rods*

Abstract

This paper presents a comparative study of the geometrical optimization of mechanical wedge–barrel anchors for prestressed carbon fiber-reinforced polymer (CFRP) rods. Various anchor configurations were simulated using three-dimensional finite-element (FE) models. The FE models were validated using the draw-ins of the wedges, which were measured in static tensile tests. The configurations consisted of a steel barrel and aluminum wedges, taking advantage of the previous anchors. The conical profile of the wedge and barrel in different configurations had either a curve or a constant differential angle. In addition, a series of geometric modifications were introduced to the wedge at the loading using a fillet or cut. The stress concentration on the CFRP rod was evaluated using failure index *F*s in the Tsai–Wu failure criterion for composite materials. The results of the FE simulations showed that a greater differential angle resulted in a smaller stress concentration at the loading end of the anchor and the modifications led to a reduction in the stress concentration. In addition, the anchor with a curved profile was selected as the optimal design because it had the smallest stress concentration owing to the smooth transition of the differential angle distribution along the wedge profile.

Keywords: Wedge–barrel anchor, CFRP rods, Finite element (FE), Prestressed tendons

* Hossein Heydarinouri, Aleksandar Vidovic, Alain Nussbaumer, Elyas Ghafoori. Submitted to composite structures, Accepted on 1st of August 2021.

Nomenclature

E_1	Longitudinal elasticity modulus	$\Delta w_{presett}$	Draw-in of the wedge after presetting
$E_{2,3}$	Transverse elasticity modulus	θ	Differential angle
Fs	Tsai–Wu failure index	ν_{12}	Major Poisson's ratio
F_i, F_{ij}	Coefficients of Tsai–Wu failure criterion	ν_{21}, ν_{31}	Minor Poisson's ratio
f_{ut}	Ultimate tensile strength of the CFRP rod	σ_1	Tensile stress of the CFRP rod
G	Shear modulus	σ_2	Contact pressure on the CFRP rod
P	Presetting force	σ_3	Hoop stress in the CFRP rod
T	Tensile force of the CFRP rod	σ^*_{1t}	Tensile strength of the CFRP rod along the fiber direction
U	Displacement	σ^*_{1c}	Compressive strength of the CFRP rod along the fiber direction
α	Angle of the wedge cone with the vertical axis	σ^*_{2t}	Tensile strength of the CFRP rod transverse to the fiber direction
β	Angle of the barrel cone with the vertical axis	σ^*_{2c}	Compressive strength of the CFRP rod transverse to the fiber direction
Δr	Draw-in of the CFRP rod	τ^*_{12}	Shear strength of the CFRP rod along the fiber direction
Δw	Draw-in of the wedge	τ^*_{23}	Shear strength of the CFRP rod transverse to the fiber direction

2.1.1. Introduction

Prestressing steel strands have been used in civil structures for a long time. As an alternative to prestressing steel, carbon fiber-reinforced polymer (CFRP) materials have been introduced and applied in prestressed structures because of their superior properties, including a higher strength-to-weight ratio, corrosion resistance, and fatigue resistance [1]. Substituting CFRP materials for steel in new structures or for strengthening existing structures has great potential in the prestressing industry considering the wide range of applications to different types of civil structures, e.g., concrete [2-6] and metallic [7-12] members and hangers for cable-stayed and suspension bridges [13, 14]. However, one of the main challenges for the widespread use of CFRPs in prestressed structures is the development of safe anchors.

Mechanical wedge–barrel anchorage systems for prestressing steel strands have traditionally been used in various applications. However, the anisotropy, brittleness, and weak mechanical properties of prestressed CFRP materials in the transverse direction make the development of anchorage systems more difficult [15]. Different anchorage systems for prestressed CFRP plates [16-19] and rods [2, 6, 20-28] have been proposed by different researchers, and the static and fatigue performances of the anchors have been investigated experimentally.

Wedge-type anchorage systems have been introduced and developed for CFRP rods. In wedge-type anchors, the contact pressure on the CFRP rod and tensile force are simultaneously high at the loading end. This can lead to a stress concentration in this area and, thus, premature

rupture. Consequently, the high tensile capacity of the CFRP rods cannot be achieved. Therefore, the main challenge for the development of wedge-type anchors for prestressed CFRP rods is minimizing the stress concentration on the CFRP rod at the loading end to prevent premature rupture.

Wedge-type anchors have been developed in two forms: (i) bonded anchors, which use adhesive around the rod, and (ii) mechanical anchors, which hold the rods purely through friction. Various types of mechanical systems have been introduced. A review of the existing bonded and unbonded anchorage systems was presented in [15]. This study focused on anchors based on gradient systems, as explained below.

A gradient system was introduced for bonded wedge-type anchors to prevent the premature rupture of the rod [23, 24]. In this anchor, a wedge was fabricated using epoxy. Particles were added to the epoxy to gradually increase the stiffness of the wedge at the loading end toward the free end of the anchor. Therefore, a gradient stiffness distribution along the wedge was achieved. In this manner, the contact pressure on the CFRP rod was minimized at the loading end, and a tensile capacity of 92% of the nominal strength of the CFRP rod was achieved. However, the on-site application of bonded anchors is complicated because they must be carefully prepared in the shop, which can make the installation procedure more difficult.

Mechanical wedge–barrel anchors have been proposed to address the above-mentioned limitations of bonded anchors. These anchors hold the CFRP rods through friction. The mechanism of these mechanical wedge–barrel anchors, including different stages of loading, is illustrated in Fig. 1. In the initial state, the CFRP rod and wedges are placed in the barrel. The next stage is presetting, in which the wedges are pushed into the barrel as a result of the compressive force of P on the surface of the wedges. The presetting is performed before pulling the rod. Thus, the contact pressure around the CFRP rod increases, which prevents the slippage of the rod when the rod is pulled. As a result of the presetting, the wedges are inserted into the barrel at a distance of $\Delta w_{\text{presett}}$. The last stage is pulling, in which a tensile force of T is applied to the CFRP rod.

The insertion of the wedge and rod into the barrel, shown by Δw and Δr in Fig. 1, respectively, is called the "draw-in." The draw-ins measured with respect to the initial state. The ideal behavior of the anchor is that the draw-ins for the wedges and rod to be the same, i.e., $\Delta w=\Delta r$, which means that no slippage occurs between the wedges and rod. However, in practice, slippage between the wedges and rod may occur, i.e., $\Delta w\neq\Delta r$. In addition, in anchors with split wedges, different wedges might not have identical draw-ins.

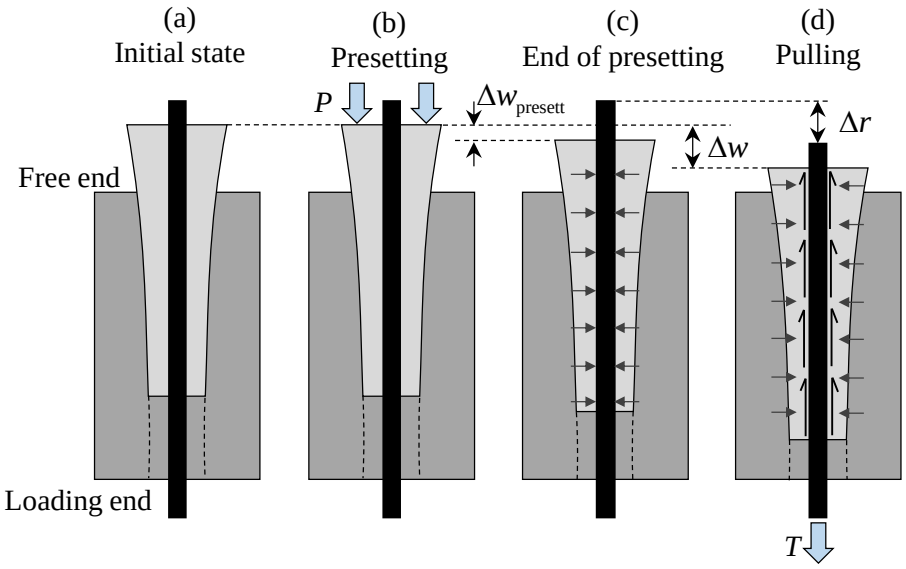

Fig. 1. Loading stages for mechanical wedge–barrel anchors.

Designing mechanical wedge–barrel anchors, which work purely through friction, is difficult because, on the one hand, the draw-in of the wedges must be large enough to prevent the slippage of the rod, while on the other hand, large draw-ins could result in a high contact pressure on the rod, which would lead to a stress concentration at the loading end and, consequently, a premature rupture in the rod.

Two methods have been introduced to prevent a stress concentration in mechanical wedge–barrel anchors. In the first method, a constant differential angle of θ is adopted between the wedge and barrel along the conical profile, as shown in Fig. 2(a). In this figure, $\alpha>\beta$. In the second method, shown in Fig. 2(b), the wedge and barrel have a conical curved profile. The curved profile creates a distributed differential angle along the cone, which increases toward the free end of the anchor. In both systems, the goal is to achieve a proper contact pressure distribution on the CFRP rod, i.e., the contact pressure is minimized at the loading end and increases toward the free end of the anchor. Both methods lead to a gradient distribution of the contact pressure on the CFRP rod.

For anchors with a constant differential angle, different values of θ have been introduced, ranging from 0.1° to 0.4°. To avoid damage to the rod in these anchors, either a soft sleeve (made of aluminum or copper) was used between the wedge and barrel [25, 26] or the wedge itself was made of a soft material such as aluminum [27, 28] or glass fibers (PPS-GF40) [6], without any sleeve. Anchors with curved profiles have been developed to further reduce the stress concentration at the loading end. Fig. 2(b) shows the dimensions used for the wedge–barrel anchor in a previous study [2] except for the length of the wedge, which was 80 mm rather than 70 mm. In this anchor, the conical profile of the wedge and barrel is a part of circle

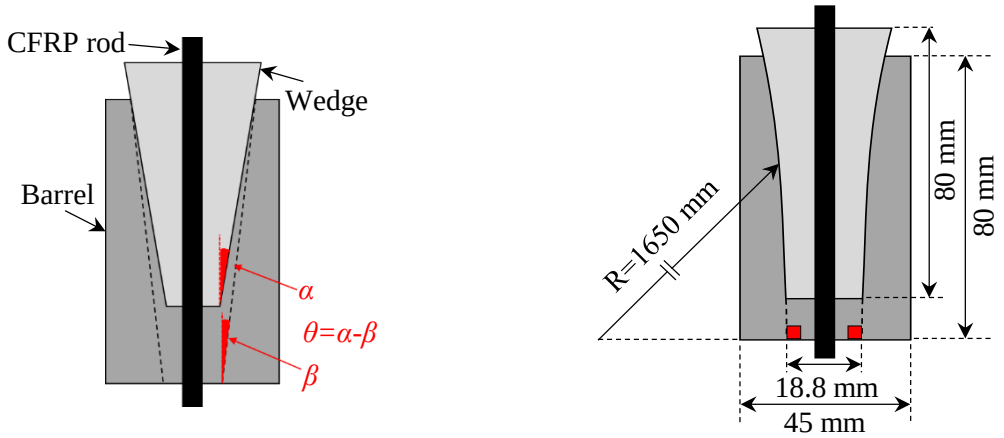

(a) Constant differential angle (b) Curved profile

Fig. 2. Two possible designs for wedge–barrel anchors.

with a radius of R=1650 mm.

Numerical simulations using the finite-element (FE) method have been performed for mechanical wedge–barrel anchors using two-dimensional (2D) [20, 26, 29, 30] and three-dimensional (3D) [6, 28, 31, 32] models. The contact pressure distributions on the CFRP rods were obtained using these FE models. One of the challenges in the numerical simulations of wedge–barrel anchors is the validation of the models with experimental results. In one study [28], the FE model was validated by comparing the FE results with the optically measured strains at the surface of the barrel using ARAMIS 3D [28] or by comparing the load–displacement or drawins of the components [6].

However, none of these studies performed a comparative investigation of anchors with different configurations, i.e., curved or constant differential angle profiles, to highlight the effect of the geometry on the stress concentration at the anchor loading end. In addition, none of these studies used a criterion to evaluate the stress concentration.

2.1.1.1. Innovations of this study

A comparative study was performed on various configurations of mechanical wedge–barrel anchors with curved and constant differential angles to identify the optimal configuration with the smallest stress concentration at the loading end. In addition, geometrical modifications to the anchors were introduced, and the effects of these modifications on the stress concentrations were investigated.

The anchor configurations considered in this study take the advantages of the anchors previously proposed anchors in [2, 27]. In the anchor proposed in [2], the wedge and barrel had a

curved profile, as shown in Fig. 2(b). However, in this anchor, a soft sleeve was required between the wedge and barrel to prevent damage to the CFRP rod. The anchor proposed in another report [15] had a constant differential angle and eliminated the need for a sleeve because the wedges were made of aluminum. However, to prevent slippage of the rod inside the anchor, the anchor was longer than that in Fig. 2(b). In the configurations considered for the anchors in this study, aluminum wedges were used, without any sleeve around the rod, using the dimensions shown in Fig. 2(b). The use of aluminum also reduced the required presetting force because it has a relatively low elastic modulus. In addition, it improved the contact pressure distribution on the CFRP rod through plasticization inside the barrel [33].

For the numerical analyses, 3D FE simulations were performed using the ABAQUS software. In the FE models, the plastic deformations of the aluminum wedges and the orthotropic properties of the unidirectional CFRP rods were considered. The FE models were validated using the experimental results from the draw-ins of the wedges after presetting and during the pulling of the rod.

To identify the anchor configuration with the smallest stress concentration, a criterion is required. Various failure criteria have been proposed for composite materials. The maximum tensile stress criterion predicts failure once each of the three principal stresses exceeds the material strength. However, this criterion overestimates the composite strength under multiaxial stresses [34]. The Tsai–Hill failure criterion is used for anisotropic materials and is an extension of the von Mises criterion, which is used for predicting the yielding of isotropic materials under multiaxial stresses. The limitation of the former criterion is that it is only applicable to composite materials with equal tensile and compressive strengths [35]. The Tsai–Wu failure criterion considers the influence of different tensile and compressive strengths [36]. This criterion is widely used in the design and failure analysis of composite materials because of its simplicity and high prediction accuracy under a multiaxial stress state [34]. In this study, the CFRP rods had different tensile and compressive strengths and were subjected to multiaxial loading inside the anchors. Therefore, the Tsai–Wu failure criterion was employed to determine the optimal anchor configuration.

2.1.1.2. Outline of study

The current paper is outlined as follows. First, the developed FE model is explained, including the details of the parts, material properties, boundary conditions, and contact behavior. Second, the validation of the FE model using the experimental results from the draw-ins of the wedges

is discussed. Third, different configurations of anchors for the CFRP rods are introduced. Fourth, the contact pressure distributions on the CFRP rod for different anchor configurations are analyzed and interpreted using the FE models. Finally, the anchor with the optimal design is selected using the Tsai–Wu failure criterion.

2.1.2. FE simulations

2.1.2.1. Parts of FE model

The FE model developed for the wedge–barrel anchors using the ABAQUS software (version R2019x) is illustrated in Fig. 3(a). The parts in the model are the wedge, barrel, and CFRP rod. Because of its geometric symmetry, only one third of the anchor was modeled—that is, a 120° revolution was applied, as shown in Fig. 3(a).

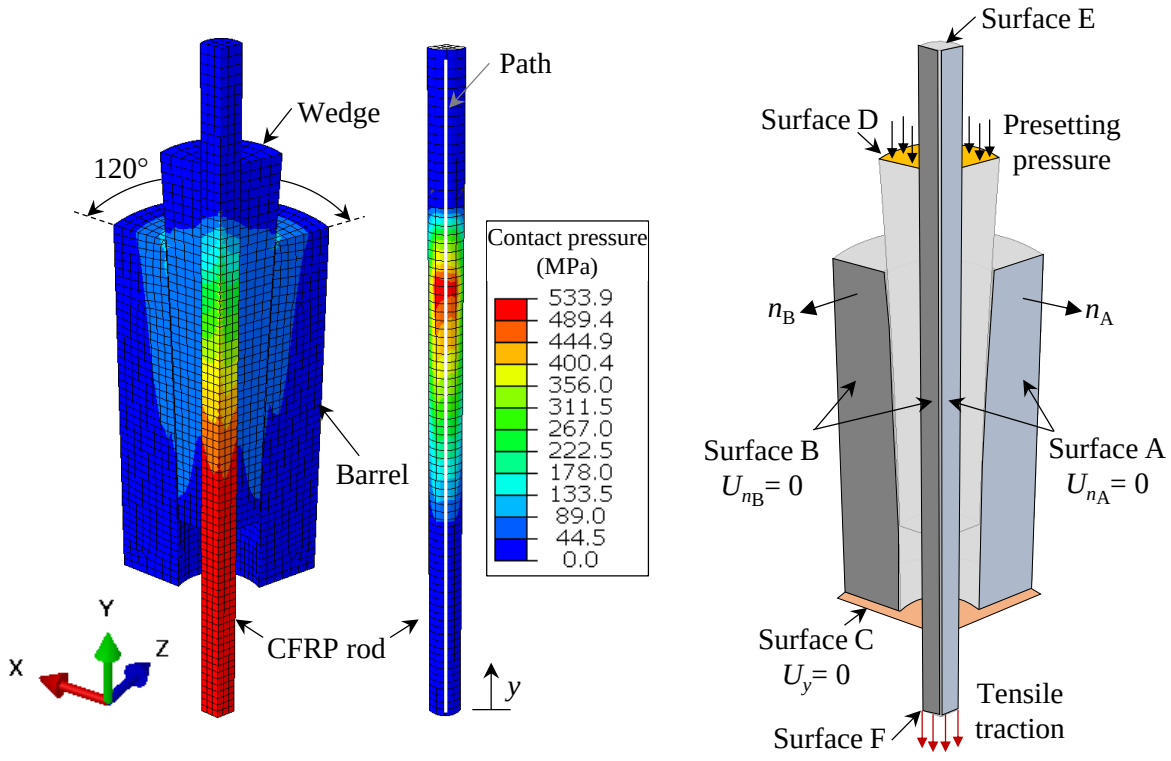

(a) Stress distribution (b) Boundary conditions

Fig. 3. FE model of wedge–barrel anchors.

Information about the element type and mesh for each part is presented in Table 1. The wedge and barrel were modeled as isotropic materials, and the CFRP rod was modeled as orthotropic. An investigation of the element type showed that the use of linear elements resulted in an inaccurate stress distribution in the parts, especially in the areas where bending deformations were dominant, e.g., at the loading end of the anchor, where local bending occurred. Therefore, the parts were discretized into quadratic reduced-integration elements, which have a larger number

of integration points compared with linear elements and are appropriate for bending-dominated areas. A structured mesh was used for all the parts. A uniform mesh was obtained for the barrel using the sweeping technique. The mesh size for all the parts was 1.8 mm.

Table 1. Element types and meshes of parts in FE model.

Part	Parameter			
	Isotropy	Element type	Mesh type	Mesh size (mm)
Rod	Orthotropic	3D quadratic reduced-integration	Structured	1.8
Wedge	Isotropic	3D quadratic reduced-integration	Structured	1.8
Barrel	Isotropic	3D quadratic reduced-integration	Sweep	1.8

2.1.2.2. Material properties

The material properties for the different parts of the FE model are listed in Table 2. The material properties were either obtained from tests or provided by the manufacturer. Otherwise, values proposed in the literature were used.

Table 2. Material properties.

Part	Rod	Barrel	Wedge
Material	CFRP	Steel HSX 130	Aluminum EN AW-6026
Ultimate tensile strength f_{ut} (MPa)	2370[a]	1250–1400[b]	442[a]
Longitudinal elasticity modulus E_1 (GPa)	160[a, b]	200[b]	71.7[a]
Transverse elasticity modulus E_2, E_3 (GPa)	7.4[c]	200[b]	71.7[a]
Shear modulus G_{12}, G_{13} (GPa)	7[c]	-	-
Major Poisson ratio ν_{12}	0.26[c]	0.3[b]	0.35
Minor Poisson ratio ν_{21}, ν_{31}	0.02[c]	0.3[b]	0.35

[a]Based on the tensile coupon tests
[b]Provided by the manufacturer (S&P Clever Reinforcement Company AG, Switzerland)
[c]Proposed in [32]

The CFRP rods used in the simulations, and later in the experiments, had a nominal diameter of 8 mm and were manufactured by the S&P Clever Reinforcement Company AG, Switzerland. To avoid large plasticization, a high-strength steel, HSX 130, was used for the barrel, and the barrel was modeled as a linear elastic material. For the wedge, aluminum EN AW-6026 was used, with the true stress–strain curve shown in Fig. 4, which was obtained in static coupon tests based on DIN EN ISO 6892-1:2017 [37] using a 250-kN testing machine at Empa, Switzerland. In the FE model, the plasticity of the aluminum wedge was considered using a bilinear true stress–strain curve that was calibrated to the test results, as shown in the figure.

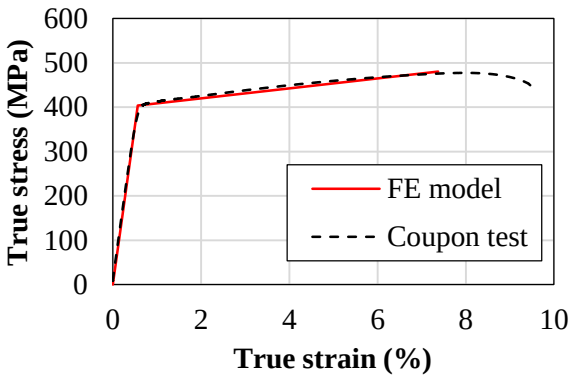

Fig. 4. Bilinear true stress–strain curve for aluminum EN AW-6026 used for wedges.

2.1.2.3. Boundary conditions and analysis steps

The boundary conditions of the FE model are shown in Fig. 3(b). Surfaces A and B, with the normal directions of n_A and n_B, respectively, are shown in the figure. The displacements in normal directions n_A and n_B were zero, i.e., $Un_A=0$ and $Un_B=0$. To define these constraints in ABAQUS, cylindrical coordinate systems were defined for surfaces A and B. In these cylindrical coordinate systems, the theta direction was parallel to the normal vectors of the surfaces, and the displacement in the theta direction was zero. In addition, the vertical displacement of the bottom surface of the barrel, shown by surface C, was fixed at zero, i.e., $U_y=0$.

The FE analysis was performed in three steps—installation, presetting, and loading—as presented in Table 3. In the installation step, setting up an initial contact was necessary to avoid the convergence problem in the subsequent steps. In addition, an ultimate tensile load of 120 kN was considered in the FE analyses.

Table 3. Steps of FE analysis in ABAQUS.

Step	Description
(I) Installation	The rod and wedge were translated by a specific distance into the barrel until the first contact was set up between the wedge and barrel. The translation was made by applying a specific displacement to surfaces D and E in Fig. 3(b).
(II) Presetting	Once all the parts were in contact, a presetting force was applied to the wedge to insert it into the barrel. The force was applied as a pressure on surface D in Fig. 3(b).
(III) Loading	A tensile load was applied on the CFRP rod, which displaced the rod and wedge. A tensile load was applied on surface F in Fig. 3(b) using a surface traction.

2.1.2.4. Contact behavior

To model the contact between the wedge and barrel, as well as between the rod and wedge, a

surface-to-surface master/slave discretization using finite sliding formulation was applied. Using the finite sliding formulation, the contacting surfaces could exhibit arbitrary finite sliding and rotation. The sliding properties in different directions were assumed to be identical. Therefore, isotropic directionality was selected in ABAQUS.

For the contact behavior in the normal direction, a "hard contact" was applied to prevent the parts from penetrating the adjacent surface. For the "tangential contact," a penalty function formulation was used, making possible a small relative movement between the surfaces (in the order of a small fraction of the element size) before the shear stress on the surface reached a critical value [38].

In previous studies, values of 0.15 [33] and 0.24 [32] were used for the friction coefficients at the rod–wedge and rod–sleeve interfaces, respectively. In the anchors in this study, the inner surface of the wedges was sandblasted, resulting in a greater friction coefficient at the rod–wedge interface. In the FE models, a friction coefficient of μ_{rw}=0.3 was considered. The friction coefficient at the wedge–barrel interface, μ_{wb}, was obtained by calibrating the FE model with the experimental results, as described in the next section.

2.1.3. Validation of FE model

A mechanical wedge–barrel anchor was developed at Empa, Switzerland [39], as shown in Fig. 5. The anchorage consisted of a steel barrel in contact with three split aluminum wedges holding the CFRP rod. The anchorage has a curved conical profile, with the dimensions shown in Fig. 2(b).

The experimental setup used for the uniaxial static tests is shown in Fig. 5. In the static tests, wedge–barrel anchors were subjected to different presetting forces of P=30, 50, and 70 kN, and were loaded up to failure. The draw-ins of the wedges, Δw, after presetting and under the application of different tensile forces to the CFRP rod were measured. The results of these measurements were used to validate the FE model.

To validate the FE model developed based on the dimensions shown in Fig. 2(b), first, the model was calibrated. For this purpose, under a presetting force of P=50 kN, the friction coefficient at the wedge–barrel interface, μ_{wb}, in the FE model was changed to fit the measurements of Δw in the static tests. Second, the calibrated model was verified by comparing the values of Δw obtained in the FE models and experiments under different presetting forces of P=30 and 70 kN.

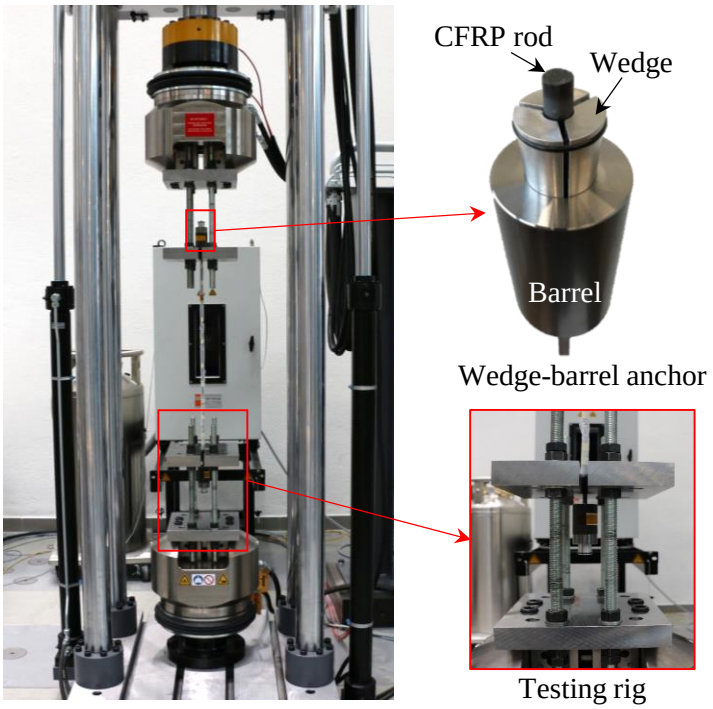

Fig. 5. Setup for static tests on wedge–barrel anchors.

2.1.3.1. Measurement of draw-ins in experiment

The draw-ins of the wedges, Δw, were measured using a Mitutoyo digital dial gauge with a reading precision of 0.001 mm and a ring located on the top surface of the barrel, as shown in Fig. 6. The initial state in the figure corresponds to the state when the wedges were placed in the barrel and the wedge surface was 22.2 mm from the barrel surface.

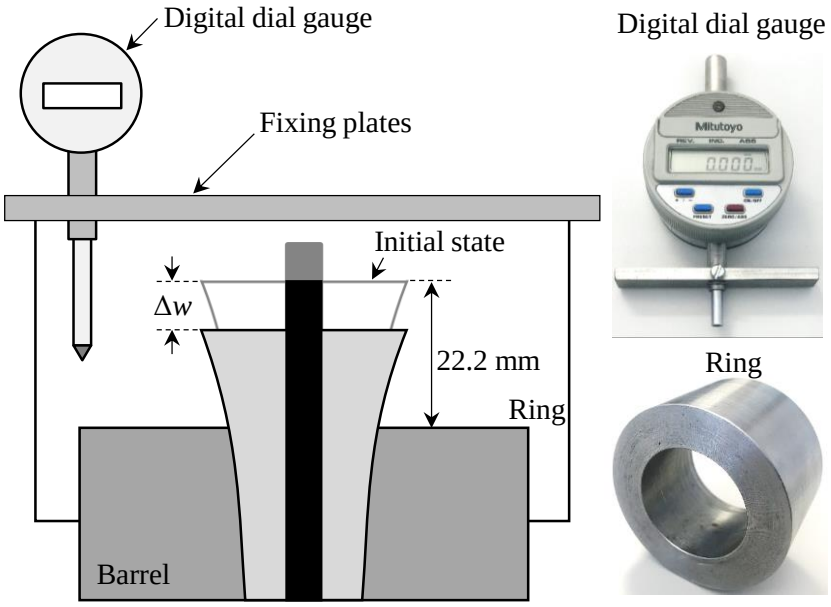

Fig. 6. Measurement of draw-ins.

The loading protocol of the static tests (according to [40]) is shown in Fig. 7, in which the load increased gradually. At tensile load levels of 20.6, 41.2, 61.7, and 72 kN, the draw-ins of the wedges and CFRP rod were measured after 5 min. These load levels corresponded to 0.2, 0.4, and 0.6 of the CFRP rod nominal tensile strength (T_{nom}=102.9 kN). In addition, at a load level of 72 kN, the stabilization of the draw-ins was checked after 30 min. To verify the FE model, only the draw-ins after 5 min were used because the increase in the draw-ins after 30 min at a load of 72 kN was attributed to creep deformations, which were not considered in the simulations.

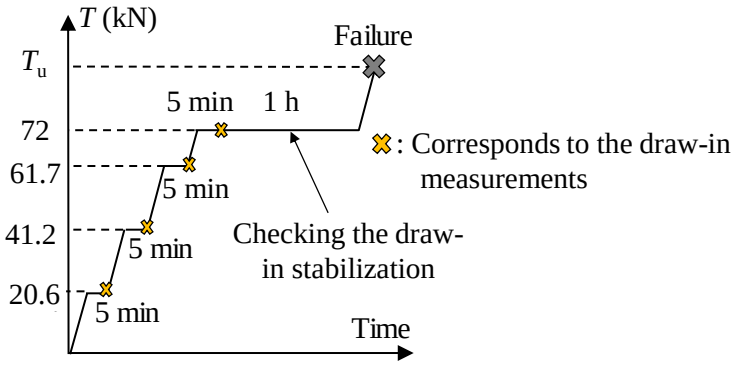

Fig. 7. Loading protocol for static tests.

2.1.3.2. Calibration of FE model

In the FE model, the mesh size and friction coefficients at the wedge–barrel interface, μ_{wb}, were adjusted to fit the experimental results obtained from a presetting force of P=50 kN. In the first step, an initial value of 0.3 was considered for μ_{wb}, and the mesh size was changed to obtain the optimal mesh size for each part. As given in Table 1, a mesh size of 1.8 mm for all parts was selected in the FE model because mesh sizes finer than 1.8 mm did not change the stress values in the model.

Once the appropriate mesh size was determined, the mesh size was kept constant in the model, and μ_{wb} was changed until the Δw values approached the experimental results. Finally, a value of μ_{wb}=0.19 was chosen for the friction coefficients at the wedge–barrel interface. In a previous study [28], the optimal friction coefficient at the wedge–barrel interface was found to be 0.15, which was relatively close to the value considered in this study. The draw-ins of the wedge, Δw, with respect to the tensile force in the CFRP rod, T, are shown in Fig. 8. In this figure, the Δw value at T=0 corresponds to the draw-in after the presetting force, i.e., $\Delta w_{presett}$.

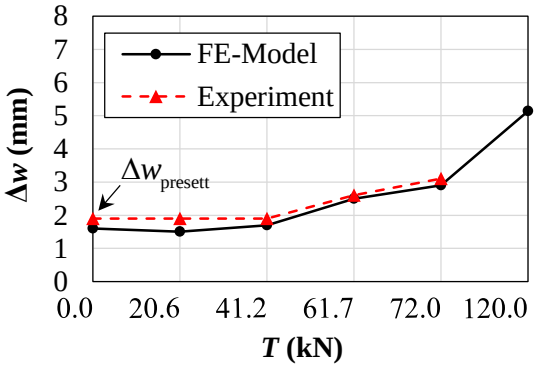

Fig. 8. Calibration of FE model using measured draw-ins of wedges under P=50 kN.

In the experiments, the specimens were subjected to a tensile load up to failure. However, the draw-ins were not measured for tensile loads greater than 72 kN. Therefore, only the draw-ins up to a tensile load of 72 kN are compared in Fig. 8.

2.1.3.3. Verification of FE model

The FE model was verified using the Δw values measured in the static tensile tests under pre-setting forces of P=30 and 70 kN, as shown in Fig. 9. The figure shows that the draw-ins obtained in the FE model and experiments were similar. Therefore, the FE model was validated.

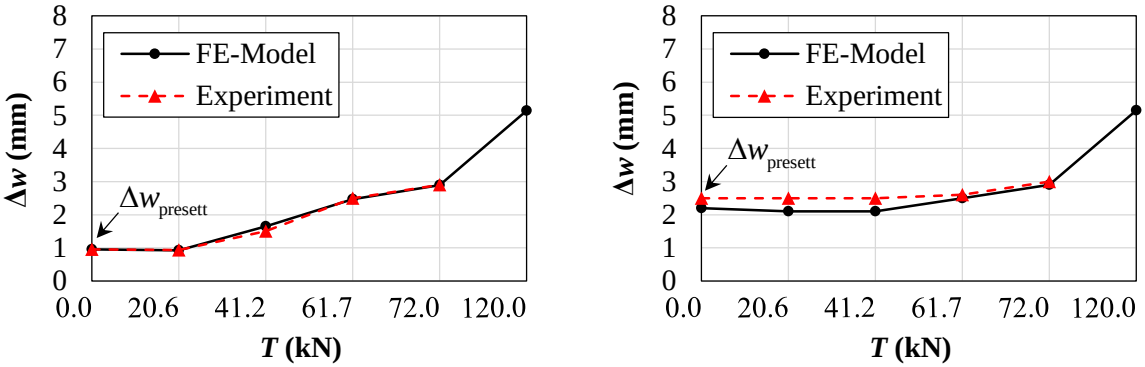

(a) Presetting P=30 kN (b) Presetting P=70 kN

Fig. 9. Verification of FE model using measured draw-ins of wedges under different presetting forces.

2.1.4. Various configurations for anchors

After validating the FE model, a comparative study was performed on various configurations for the wedge–barrel anchors, with either curved or constant differential angle conical profiles. The dimensions used for the wedge and barrel were similar to those used by anchor A in a previous study [2], as shown in Fig. 2(b). The different anchor configurations are presented in Table 4. In this table, A, cd, and fr represent the anchor, constant differential angle, and friction

radius, respectively, e.g., A-cd-0.23° is an anchor with a constant differential angle of 0.23°.

Table 4. Different types of anchors used in parametric study.

Anchor type	Anchor name	Description of the anchor
(1) Curved profile	A-curved	A curved profile for the wedge
(2) Constant differential angle	A-cd-0.1°	A constant differential angle of 0.1°
	A-cd-0.16°	A constant differential angle of 0.16°
	A-cd-0.23°	A constant differential angle of 0.23°
(3) Anchors modified using fillet	A-fr-0.5	A fillet with a 0.5-mm radius on the wedge at the loading end
	A-fr-2	A fillet with a 2-mm radius on the wedge at the loading end
	A-fr-4	A fillet with a 4-mm radius on the wedge at the loading end
(4) Anchors modified using cut	A-cut-3°	A cut with a 3° angle on the wedge at the loading end
	A-cut-40°	A cut with a 40° angle on the wedge at the loading end

As shown in the table, the configurations were divided into four types. The first type, A-curved, is an anchor with a curved conical profile for the wedge and barrel, as shown in Fig. 2(b). For anchor type 2, A-cd, three different differential angles were considered: 0.1°, 0.16°, and 0.23° (see Fig. 2(a)). The differential angles considered were in the range of those introduced in previous studies [6, 26, 30].

In addition, two modified configurations were considered as anchor types 3 and 4. In these anchors, the wedges and barrels had a constant differential angle of θ=0.1°. The intention of these modifications was to remove a volume of material from the wedge at the loading end to reduce the stress concentration in this area, which is explained in section 5.

The type 3 anchors are shown in Fig. 10. Different radii of 0.5, 2.0, and 4.0 mm were applied to the fillet at the loading end to investigate the effect of the fillet radius on the contact pressure distribution on the CFRP rod. These anchors are A-fr-0.5, A-fr-2, and A-fr-4 in Table 4.

In the other type of modified anchor, i.e., type 4, the geometry of the wedge at the loading end was changed by cutting a volume of material, as shown in Fig. 11. For anchors A-cut-3° and A-cut-40°, as listed in Table 4, the lengths of the inclined cut line were 20 and 6 mm and the angles of the inclined cut lines were 3° and 40°, respectively.

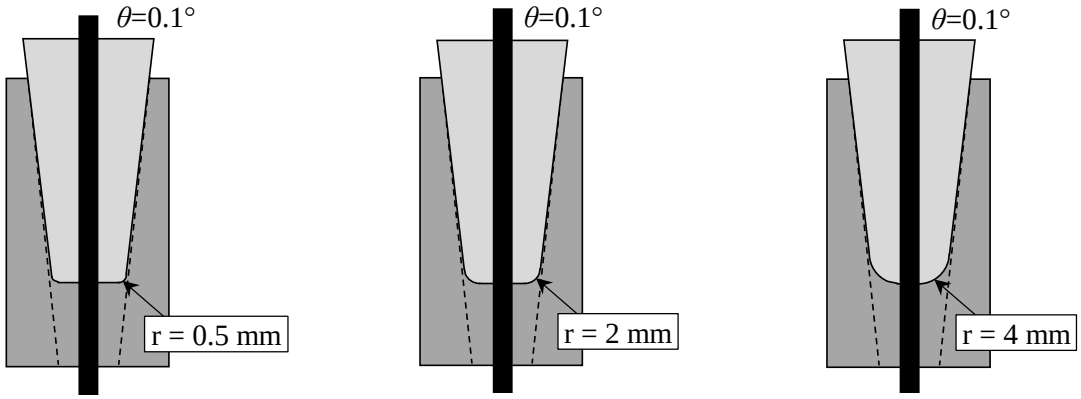

(a) A-fr-0.5 (b) A-fr-2 (c) A-fr-4

Fig. 10. Type 3 anchors, with fillets on wedge at loading end.

(a) A-cut-3°. (b) A-cut-40°.

Fig. 11. Type 4 anchors, with cut on wedge at loading end.

2.1.5. Results of FE analyses

2.1.5.1. Contact pressures on CFRP rods for anchor types 1 and 2

The contact pressure on the CFRP rod for the anchor with a curved profile (type 1) was compared with that of the anchors with different constant differential angles (type 2). For these anchors, the contact pressure on the CFRP rod on the path shown in Fig. 3(a) was obtained using the FE models. Fig. 12 shows the results under a presetting force of P=50 kN. As shown in Fig. 12(a), at a tensile load of T=72 kN, the contact pressure gradually increased from the loading end and reached a maximum at the free end.

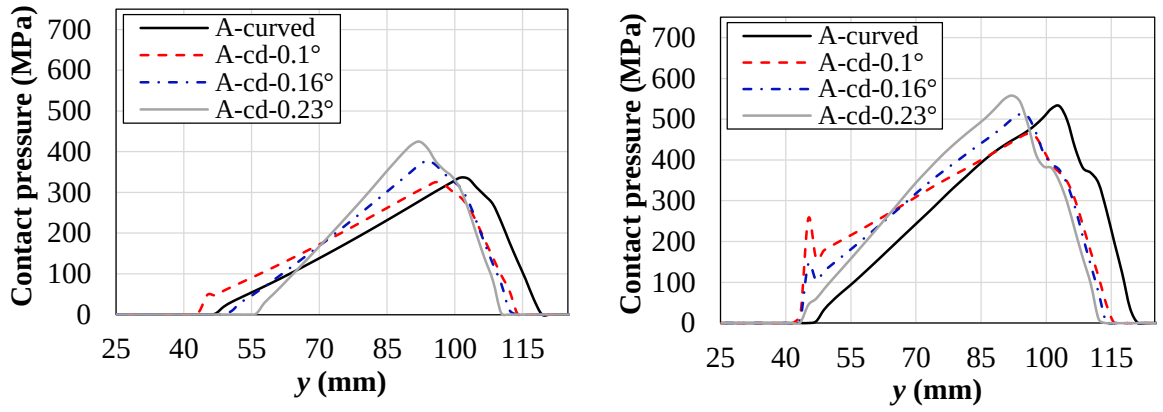

(a) T=72 kN (b) T=120 kN

Fig. 12. Contact pressure on CFRP rod for the type 1 and 2 anchors under a presetting force of P=50 kN.

As a result of the greater tensile force of T=120 kN on the CFRP rod, as shown in Fig. 12(b), the contact pressure on the rod increased because of the larger draw-ins of the wedges. However, at the loading end, a peak appeared in the contact pressure for anchors A-cd-0.1° and A-cd-0.16°, while for anchors A-cd-0.23° and A-curved, no stress peak was observed.

The effect of the mesh size on the peak value of the contact pressure on the CFRP rod for anchor A-cd-0.1° is presented in Appendix A. The peak values were sensitive to the mesh size, i.e., the smaller the mesh size, the greater the peak.

2.1.5.2. Contact pressures on CFRP rods for modified anchors

The simulations discussed in section 4.1 showed that anchor A-cd-0.1° had the highest peak for the contact pressure at the loading end. To minimize the peak value, geometric modifications were introduced to the anchor. The change in the geometry was performed in two ways: (i) adding a fillet at the loading end of the wedge and (ii) cutting a volume of material from the wedge at the loading end area. In both these modifications, a volume of wedge material was removed at the loading end area to reduce the contact pressure between the wedge and barrel and, consequently, the contact pressure on the CFRP rod.

The contact pressure distributions on the CFRP rod for anchor A-cd-0.1° and the modified anchors are compared in Fig. 13 under a presetting force of P=50 kN and a tensile force of T=120 kN. The anchors with smaller fillet radii, i.e., A-fr-0.5 and A-fr-2, had peaks in the contact pressure, although the peak stress was smaller than that of anchor A-cd-0.1°. A larger fillet radius of 4 mm in anchor A-fr-4 eliminated the peak stress.

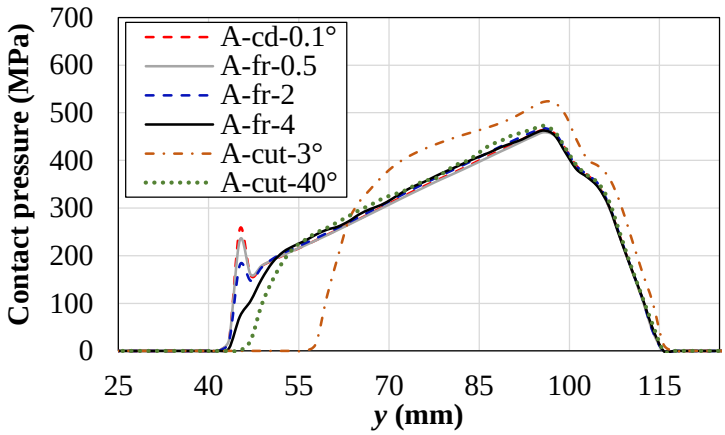

Fig. 13. Contact pressures on CFRP rods for modified anchors under P=50 kN and T=120 kN.

2.1.6. Selection of optimal anchor

2.1.6.1. Stress state on CFRP rod

Stresses in different directions were applied to the surface of the CFRP rod, as shown in Fig. 14. The stress components σ_1, σ_2, σ_3, and τ_{12} were the stresses applied to an element of the CFRP rod on Path A. In the coordinate system shown in the figure, direction 1 is the fiber direction, and directions 1 and 2 are perpendicular to the fibers. According to the FE model, the applied stresses on the element are defined as follows: σ_1 is the tensile stress caused by the application of the tensile load on the CPRP rod, σ_2 is the contact pressure, σ_3 is the compressive circumferential stress, and τ_{12} is the shear stress applied on the element resulting from friction between the rod and wedge. The other components of the shear stress were negligible. To obtain these stress components in ABAQUS, the stresses of the nodes on Path A were picked up using a cylindrical coordinate system.

2.1.6.2. Selection criterion

The Tsai–Wu failure criterion [36] was used to select the optimal anchor. This criterion has been widely used for the failure of composite (anisotropic) materials because of its simplicity and applicability under multiaxial stress states [34] such as the stress state shown in Fig. 14. The Tsai–Wu formulation for a unidirectional CFRP rod composite is as follows [36]:

$$Fs = F_{11}\sigma_1^2 + F_{22}(\sigma_2^2 + \sigma_3^2) + (2F_{22} - F_{44})\sigma_2\sigma_3 + 2F_{12}\sigma_1(\sigma_2 + \sigma_3) + F_1(\sigma_2 + \sigma_3) + F_2\sigma_3 + F_{66}\tau_{12}^2, \quad (1)$$

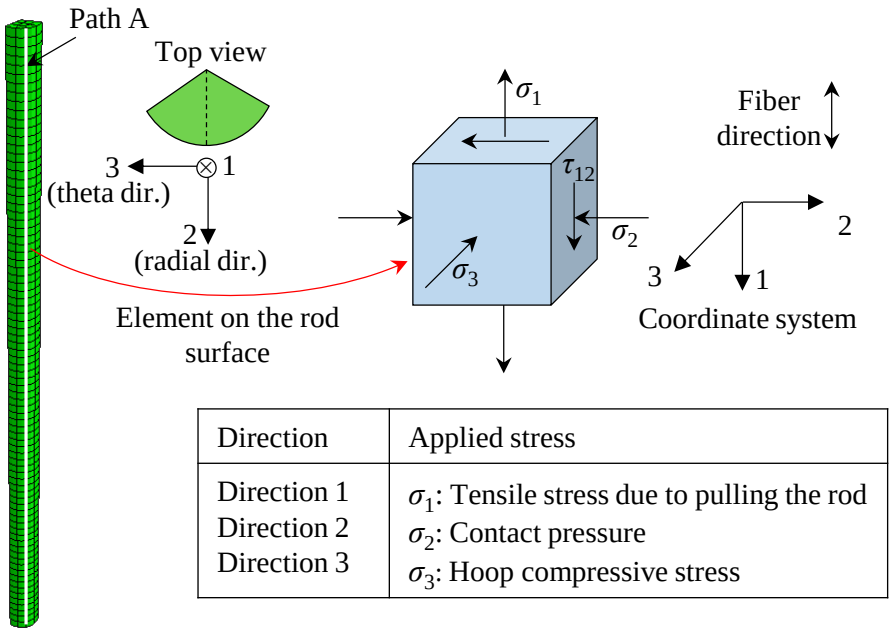

Direction	Applied stress
Direction 1 Direction 2 Direction 3	σ_1: Tensile stress due to pulling the rod σ_2: Contact pressure σ_3: Hoop compressive stress

Fig. 14. Applied stresses on element of CFRP rod on Path A.

where *F*s is the Tsai–Wu failure index, and F_{11}, F_{22}, F_{44}, F_{66}, F_1, F_2, and F_{12} are coefficients that are calculated using material strength values, as given in Eq. (2):

$$F_{11} = -\frac{1}{\sigma^*_{1t}\sigma^*_{1c}} \quad F_{22} = -\frac{1}{\sigma^*_{2t}\sigma^*_{2c}} \quad F_{44} = \frac{1}{(\tau^*_{23})^2} \quad F_{66} = \frac{1}{(\tau^*_{12})^2}$$
$$F_1 = \frac{1}{\sigma^*_{1t}} + \frac{1}{\sigma^*_{1c}} \quad F_2 = \frac{1}{\sigma^*_{2t}} + \frac{1}{\sigma^*_{2c}} \quad F_{12} = -\frac{1}{2}\sqrt{F_{11}F_{22}} \quad , \qquad (2)$$

where σ^*_{1t} and σ^*_{1c} are the tensile and compressive strengths of the material along the fiber direction, respectively; and σ^*_{2t} and σ^*_{2c} are those in the direction transverse to the fibers, respectively. Moreover, τ^*_{12} and τ^*_{23} are the shear strengths along and transverse to the fibers, respectively. The stress limits and corresponding coefficients for the Tsai–Wu criterion are listed in Table 5.

Based on the Tsai–Wu failure criterion, a failure occurs in a composite material when failure index *F*s reaches unity (i.e., *F*s=1) [36, 43]. In this study, failure index *F*s was used to select the optimal design configuration considering the fact that a greater *F*s value corresponded to a more critical stress condition.

2.1.6.3. Fs values for different anchor configurations

The *F*s values for all the nodes on Path A were calculated for different anchor configurations, and the anchor with the smallest value of *F*s (at the loading end) was considered to be the optimal design. The results are presented in Fig. 15. For all the anchors, a peak occurred at the

Table 5. Tsai–Wu limits and coefficients for CFRP rods.

Stress limits	Coefficients
σ^*_{1T}=2370[a] MPa	$F_{11}=2.93\times10^{-7}$ (1/MPa)^2
σ^*_{1c}=−1440[b] MPa	F_{22}=0.000019 (1/MPa)^2
σ^*_{2T}=88[c] MPa	F_1=−0.0003 (1/MPa)
σ^*_{2c}=−600[d] MPa	F_2=−0.0097 (1/MPa)
τ^*_{12}=100[e] MPa	F_{44}=0.0001 (1/MPa)^2
τ^*_{23}=100[e] MPa	F_{66}=0.0001 (1/MPa)^2
	$F_{12}=-1.18\times10^{-6}$ (1/MPa)^2

[a]Based on the tests [39]
[b]ACI-440.4R-04 [41]
[c]Provided by the manufacturer
[d]Proposed in [42]
[e]Proposed in [43]

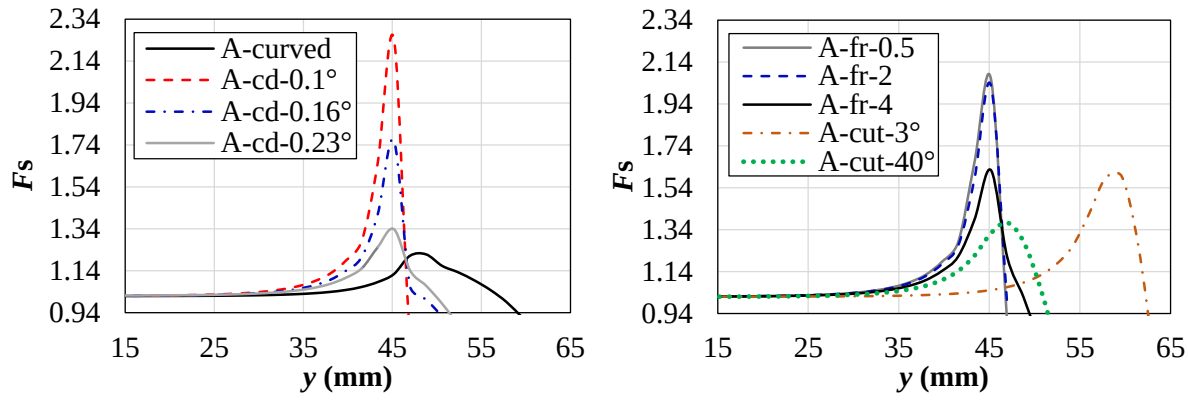

(a) Anchors with curved and constant differential angle profiles

(b) Modified anchors

Fig. 15. Tsai–Wu parameter for different configurations of anchors under P=50 kN and T=120 kN.

loading end. The greatest Fs value was for anchor A-cd-0.1°, with Fs=2.25. With the modifications on this anchor, the Fs values were reduced to 1.62 and 1.37 in anchors A-fr-4 and A-cut-40°, respectively. The lowest Fs value was obtained for the A-curved anchor with Fs=1.22. Therefore, this anchor was selected as the optimal design.

For all the anchors, the failure index exceeded unity at the loading end (i.e., Fs>1), as shown in Fig. 15, as under T=120 kN, the failure was predicted in the CFRP rod. In this study, however, for the sake of comparison and choosing the optimal anchor, only the relative Fs indices for various anchor configurations were of interest, rather than the absolute values of Fs.

2.1.6.4. Slippage between wedge and CFRP rod

The slippage between the wedge and CFRP rod was not considered when selecting the optimal anchor because no large slippage was observed in any of the anchors, even at an ultimate load of T=120 kN. Appendix B presents the slippage values of the rod inside the wedge for different anchors under various presetting and tensile forces, showing that the slippage was always smaller than 0.08 mm.

2.1.7. Discussion

In this section, the effects of the constant differential angles, geometric modifications, and curved conical profile on the contact pressure distribution on the CFRP rods (see Figs. 12 and 13) and, consequently, on the resulting stress concentration at the anchor loading end are discussed.

2.1.7.1. Effect of constant differential angle

To understand the reason for the peaks in the contact pressures on the CFRP rods, the contact pressure distributions on the inner and outer surfaces of the wedges for anchors A-cd-0.1° and A-cd-0.23° are depicted in Fig. 16. For anchor A-cd-0.1°, shown in Fig. 16(a), the contact pressure on the inner surface of the wedge at the loading had a peak. For anchor A-cd-0.23°, however, the contact pressure was zero, as shown in Fig. 16(b). This was attributed to the fact that for the anchor A-cd-0.23°, the wedge at the loading end tended to separate from the inner surface of the barrel due to its greater constant differential angle (see the illustration in Fig. 2(a)). Thus, at the loading end, the contact pressure on the outer surface of the wedge was smaller for an anchor with a greater differential angle (i.e., anchor A-cd-0.23°), as shown in Fig. 16, which, consequently, resulted in a smaller contact pressure on the CFRP rod. Therefore, it is concluded that a greater differential angle would lead to the reduction or elimination of the peak in the contact pressure on the CFRP rod.

It is noted that although the increase in the constant differential angle results in a reduction of the peaks of contact pressure at the anchor loading end, it leads to the reduction of contact area between the wedge and barrel. This can be observed in Fig. 12(a), in which the contact pressure is distributed in a shorter length for the anchor with the greatest constant differential angle, i.e., A-cd-0.23°. This effect is more pronounced under smaller tensile forces, under which the wedges are not well inserted into the barrel (compare the contact pressure distribution of anchor A-cd-0.23° under T=72 and 120 kN in Fig. 12). This can lead to the slippage of the rod inside

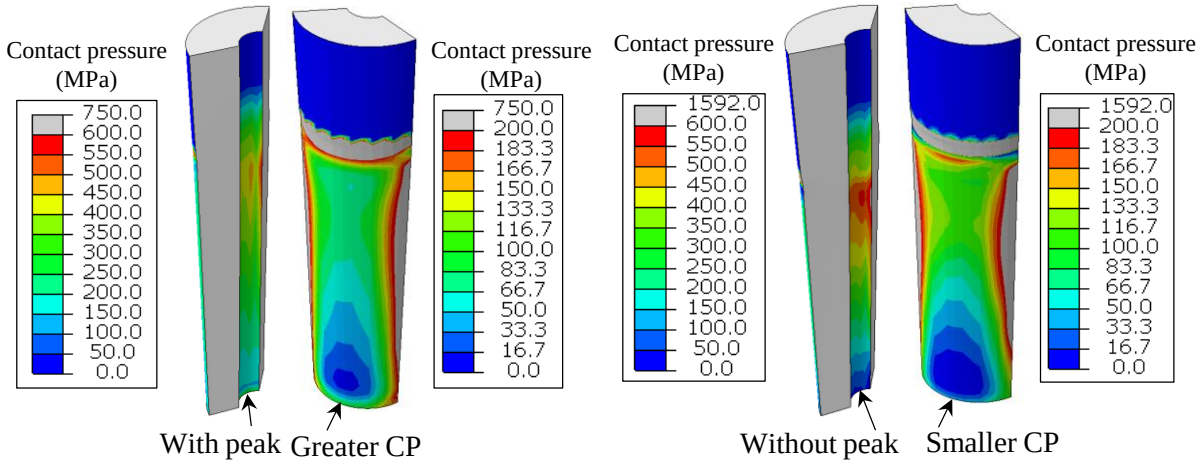

(a) A-cd-0.1° (b) A-cd-0.23°

Fig. 16. Contact pressure on wedge under P=50 kN and T=120 kN.

the wedges due to an insufficient frictional resistance under service (smaller) tensile loads, which is not the case for the anchors considered in this study.

2.1.7.2. Effect of geometric modifications

For the anchors with a cut, i.e., anchors A-cut-3° and A-cut-40°, no peaks in the contact pressure at the loading end area were observed, as shown in Fig. 13. Fig. 17 shows the contact pressures on the wedges of the modified anchors with cuts. The introduction of the cuts resulted in the elimination of the stress peaks on the inner surfaces of the wedges due to the removal of a volume of material at the loading end. The contact pressure gradually increased within the cut area.

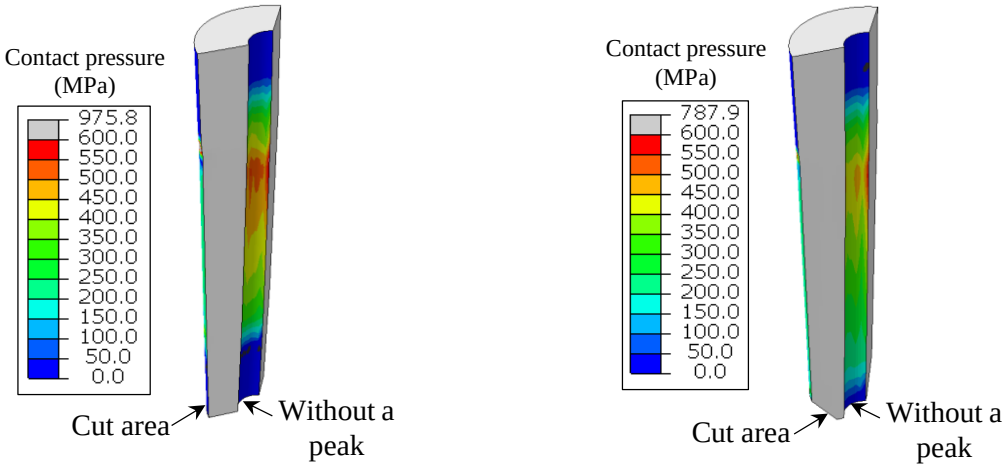

(a) A-cut-3° (b) A-cut-40°

Fig. 17. Contact pressure on modified wedges with cuts under presetting forces of P=50 kN and T=120 kN.

For the anchors, which were geometrically modified using fillet, the increase in the fillet radius resulted in a reduction in the contact pressure on the CFRP rod, as shown in Fig. 13. The reason is that by a greater fillet radius, a bigger volume of the material was removed from the loading end area of the wedge, which resulted in smaller contact pressure on the outer surface of the wedges and, consequently, on the CFRP rod.

As shown in Fig. 13, for both types of modified anchors, i.e., using cut or fillet, a rapid increase occurred in the contact pressure in a small length at the loading end, leading to a higher stress concentration at this area.

2.1.7.3. Effect of curved profile

For the anchor with a curved profile, i.e., A-curved, the differential angle varied along the anchor, resulting in a distribution of differential angle. The effect of the curved profile on the distribution of the differential angle at the loading end is schematically illustrated in Fig. 18(a). In the initial state, the differential angle is zero because the curvatures of the profiles for the wedge and barrel are the same, as shown in Fig. 2(b). When the wedge moves into the barrel, the wedge tends to separate from the barrel at the loading end, which reduces the contact pressure on the CFRP rod. The differential angle between the wedge and barrel continuously increases toward the free end of the anchor. Fig. 18(b) depicts the contact pressure on the wedge under P=50 kN and T=120 kN, revealing a small contact pressure at the loading end and a gradual increase toward the free end (see also Fig. 12(b)).

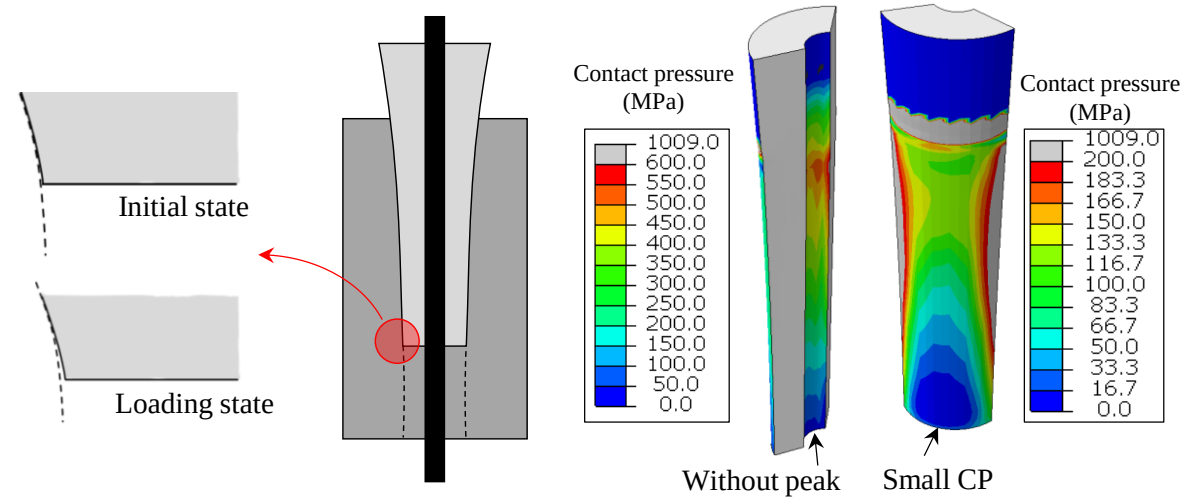

(a) Effect of curved profile on distribution of differential angle

(b) Contact pressure on wedge under P=50 kN and T=120 kN

Fig. 18. Effect of curved profile on distribution of differential angle and contact pressure for A-curved anchor.

The smallest *F*s value obtained for the A-curved anchor was attributed to the smooth transition of the differential angle owing to the existence of the curved profile, that is, the combination of the contact pressure with the tensile, hoop, and shear stresses (see Fig. 14) on the CFRP rod resulted in the smallest *F*s value for this anchor.

2.1.8. Summary and conclusions

In this study, 3D FE simulations were performed for various configurations of mechanical wedge–barrel anchors to achieve an optimal design with the smallest stress concentration at the loading end. The FE models were validated by comparing the draw-ins of the wedges with experimental results. The configurations considered were anchors with curved and constant differential angle profiles. In addition, geometrical modifications were applied to the anchors with a constant differential angle. The CFRP rod had a diameter of 8 mm, but the same approach could be implemented for different rod diameters. The main findings of this study are summarized as follows.

- The FE model was calibrated using the measured draw-ins of the wedges, Δw, from static tests. For this purpose, under a presetting force of P=50 kN, the friction coefficient at the wedge–barrel interface was changed to fit the measured values for Δw. Then, the draw-ins corresponding to P=30 and 70 kN were used to verify the FE model.
- For the anchors with a constant differential angle, the increase in the value of the differential angle from 0.1° to 0.23° reduced the peak in the contact pressure on the wedge and, consequently, on the rod at the loading end.
- To reduce the peak in the contact pressure on the wedge in the anchor with a constant differential angle of 0.1°, i.e., A-cd-0.1°, geometric modifications were introduced by removing a volume of material from the wedges at the loading end using a cut or fillet.
- The geometric modifications resulted in a reduction in the peaks for the contact pressure on the rod at the loading end, especially for anchors with a fillet radius of 4 mm, i.e., A-fr-4, and a cut angle of 40°, i.e., A-cut-40°.
- The Tsai–Wu failure criterion was used to identify the anchor with the smallest stress concentration on the CFRP rod. Therefore, the anchor with the smallest *F*s values for the nodes on the CFRP rod surface at the loading end was selected as the optimal design. The greatest *F*s value was obtained for anchor A-cd-0.1°, with *F*s=2.25. Modifications could reduce the *F*s values to 1.62 and 1.37 for anchors A-fr-4 and A-cut-40°, respectively.

- The smallest *F*s value was achieved for the A-curved anchor with *F*s=1.22. Therefore, this anchor was chosen as the optimal design. This was attributed to the smooth transition and gradual increase in the differential angle from the loading end toward the free end.

Declaration of Competing Interest

The authors declare that they have no known competing financial interests or personal relationships that could have appeared to influence the work reported in this paper.

Acknowledgment

The authors acknowledge the Innosuisse Swiss Innovation Agency (Grant ID: 19240.1 PFIW-IW) for funding this research project and the project partners, namely the S&P Clever Reinforcement Company AG, Switzerland, the Swiss Federal Railways (SBB) AG, Bern, and dsp Ingenieure + Planer AG Engineering Office, Uster, Switzerland. We also thank the laboratory technicians of the Structural Engineering Research Laboratory of Empa for their support in conducting the experiments.

Appendix A. Mesh sensitivity analysis

To investigate the effect of the mesh size on the peak value of the contact pressure on the CFRP rod, the mesh size of the wedge and rod for anchor A-cd-0.1° was changed locally at the loading end, as shown in Fig. A1. Mesh sizes of 0.1, 0.07, and 0.06 mm were considered. As shown, the peak value of the contact pressure increased with smaller mesh sizes, indicating the sensitivity of the results to the mesh size.

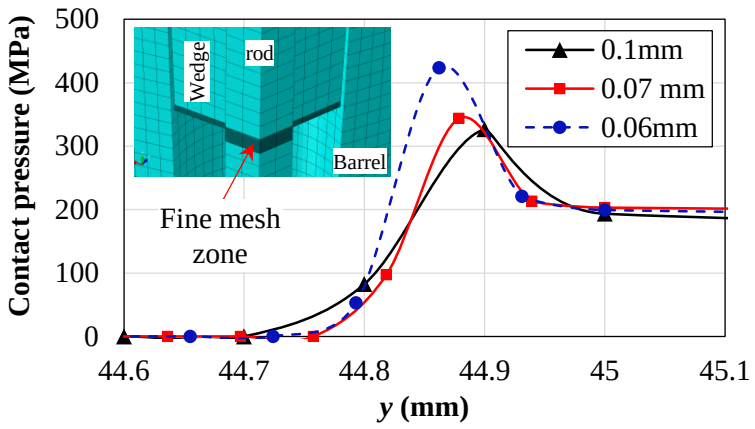

Fig. A1. Effect of mesh size on contact pressure on CFRP rod at loading end for anchor A-cd-0.1° under *P*=50kN and *T*=120kN.

Appendix B. Slippage between wedge and CFRP rod

The values of the slippage between the wedge and CFRP rod under different presetting forces are shown in Fig. B.1. In the FE model, the slippage was determined by deducting the displacement of a node on the surface of the rod at the free end from that of a node on the wedge surface. As shown in the figure, the slippage generally decreased when the presetting force increased. This was attributed to the higher contact pressure around the rod when the presetting force was greater. In addition, the slippage values for the A-curved and A-cd-0.23° anchors was greater than those for the other anchors. However, for all the anchors, the slippage was negligible, i.e., in the order of hundredths of millimeters.

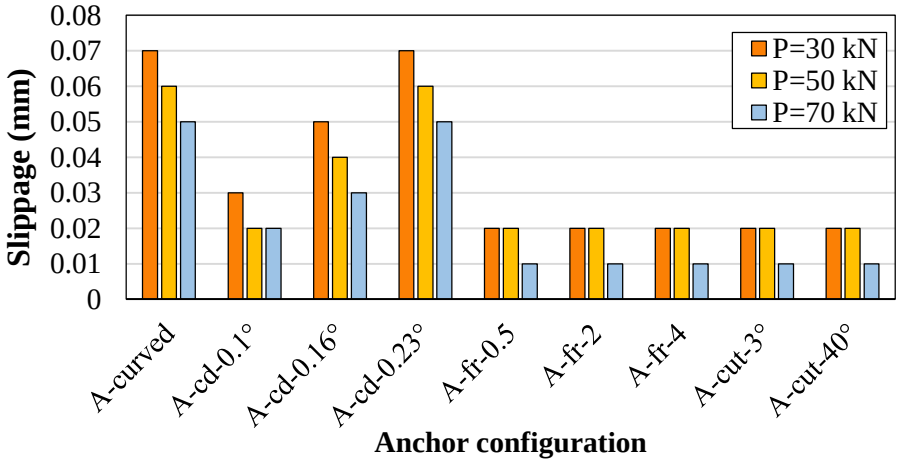

Fig. B1. Slippage between wedge and rod for different anchors under T=120 kN.

Data availability

Some or all data and FE models that support the findings of this study are available from the corresponding author upon reasonable request.

References

1. Zhao XL. FRP-Strengthened Metallic Structures. 2013, Boca Raton, FL: Taylor and Francis.
2. Al-Mayah A, Soudki K, Plumtree A. Development and assessment of a new CFRP rod–anchor system for prestressed concrete. Applied Composite Materials 2006;13(5)321-334. https://doi.org/10.1007/s10443-006-9019-6
3. Bennitz A, Schmidt JW, Nilimaa J, Täljsten B, Goltermann P, Ravn DL. Reinforced concrete T-beams externally prestressed with unbonded carbon fiber-reinforced polymer tendons. ACI Structural Journal 2012;109(4)521.
4. Sayed-Ahmed EY, Lissel SL, Tadros G, Shrive NG. Carbon fibre reinforced polymer (CFRP) post-tensioned masonry diaphragm walls: prestressing, behaviour, and design recommendations. Canadian Journal of Civil Engineering 1999;26(3)324-344. https://doi.org/10.1139/l98-073
5. Taha MMR, Shrive NG. New concrete anchors for carbon fiber-reinforced polymer post-tensioning tendons—Part 2: Development/experimental investigation. Structural Journal 2003;100(1)96-104. 10.14359/12443
6. Terrasi GP, Affolter C, Barbezat M. Numerical optimization of a compact and reusable pretensioning anchorage system for CFRP tendons. Journal of composites for construction 2011;15(2)126-135. https://doi.org/10.1061/(ASCE)CC.1943-5614.0000080

7. Ghafoori E, Hosseini A, Al-Mahaidi R, Zhao X-L, Motavalli M. Prestressed CFRP-strengthening and long-term wireless monitoring of an old roadway metallic bridge. Engineering Structures 2018;176585-605. https://doi.org/10.1016/j.engstruct.2018.09.042
8. Ghafoori E, Motavalli M, Nussbaumer A, Herwig A, Prinz G, Fontana M. Design criterion for fatigue strengthening of riveted beams in a 120-year-old railway metallic bridge using pre-stressed CFRP plates. Composites Part B: Engineering 2015;681-13. https://doi.org/10.1016/j.compositesb.2014.08.026
9. Heydarinouri H, Motavalli M, Nussbaumer A, Ghafoori E. Development of Mechanical Strengthening System for Bridge Connections Using Prestressed CFRP Rods. Journal of Structural Engineering 2021;147(3)04020351. https://doi.org/10.1061/(ASCE)ST.1943-541X.0002923
10. Heydarinouri H, Nussbaumer A, Motavalli M, Ghafoori E. Strengthening of Steel Connections in a 92-Year-Old Railway Bridge Using Prestressed CFRP Rods: Multiaxial Fatigue Design Criterion. Journal of Bridge Engineering 2021;26(6)04021023.
11. Hosseini A, Ghafoori E, Al-Mahaidi R, Zhao X-L, Motavalli M. Strengthening of a 19th-century roadway metallic bridge using nonprestressed bonded and prestressed unbonded CFRP plates. Construction and Building Materials 2019;209240-259. https://doi.org/10.1016/j.conbuildmat.2019.03.095
12. Hosseini A, Ghafoori E, Motavalli M, Nussbaumer A, Zhao X-L, Al-Mahaidi R, Terrasi G. Development of prestressed unbonded and bonded CFRP strengthening solutions for tensile metallic members. Engineering Structures 2019;181550-561. https://doi.org/10.1016/j.engstruct.2018.12.020. http://www.sciencedirect.com/science/article/pii/S0141029618312926.
13. Baschnagel F, Härdi R, Triantafyllidis Z, Meier U, Terrasi GP. Fatigue and durability of laminated carbon fibre reinforced polymer straps for bridge suspenders. Polymers 2018;10(2)169.
14. Meier U, Brönnimann R, Anderegg P, Terrasi G 20 years of experience with structural health monitoring of objects with CFRP components, in Nondestructive Testing of Materials and Structures. 2013, Springer. p. 959-976.
15. Schmidt JW, Bennitz A, Täljsten B, Goltermann P, Pedersen H. Mechanical anchorage of FRP tendons–A literature review. Construction and Building Materials 2012;32110-121. https://doi.org/10.1016/j.conbuildmat.2011.11.049
16. Ghafoori E, Motavalli M. Innovative CFRP-Prestressing System for Strengthening Metallic Structures. Journal of Composites for Construction 2015;19(6)04015006. https://doi.org/10.1061/(ASCE)CC.1943-5614.0000559. http://www.scopus.com/inward/record.url?eid=2-s2.0-84939204537&partnerID=40&md5=3422ce7a81b87ad1b00e68ab9a965d3e.
17. Hosseini A, Ghafoori E, Motavalli M, Nussbaumer A, Zhao XL, Al-Mahaidi R. Flat Prestressed Unbonded Retrofit System for Strengthening of Existing Metallic I-Girders. Composites Part B 2018;155156-172. https://doi.org/10.1016/j.compositesb.2018.08.026
18. Mohee FM, Al-Mayah A. Development of an innovative prestressing CFRP plate anchor: numerical modelling and parametric study. Composite Structures 2017;1771-12. https://doi.org/10.1016/j.compstruct.2016.12.039
19. Mohee FM, Al-Mayah A, Plumtree A. Anchors for CFRP plates: State-of-the-art review and future potential. Composites Part B: Engineering 2016;90432-442. https://doi.org/10.1016/j.compositesb.2016.01.011
20. Al-Mayah A, Soudki K, Plumtree A. Mechanical behavior of CFRP rod anchors under tensile loading. Journal of Composites for Construction 2001;5(2)128-135.
21. Arnautov A, Terrasi G, Kulakov V, Portnov G. Fastening of a High-Strength Composite rod with a Splitted and Wedged end in a Potted Anchor 1. Experimental Investigation. Mechanics of composite materials 2014;49(6)595-604. https://doi.org/10.1007/s11029-013-9376-9
22. Li C, Guo R, Xian G, Li H. Innovative compound-type anchorage system for a large-diameter pultruded carbon/glass hybrid rod for bridge cable. Materials and Structures 2020;53(4)1-15. https://doi.org/10.1617/s11527-020-01510-y
23. Meier U. Extending the life of cables by the use of carbon fibers. in: Proc., International Association for Bridge and Structural Engineering Symp. 1995.
24. Meier U. Carbon fiber reinforced polymer cables: Why? Why not? What if? Arabian Journal for Science and Engineering 2012;37(2)399-411. https://doi.org/10.1007/s13369-012-0185-6
25. Sayed-Ahmed EY. Single-and multi-strand steel anchorage systems for CFRP tendons/stays. in: Proceedings, Annual Conference-Canadian Society for Civil Engineering. 2002.
26. Sayed-Ahmed EY, Shrive NG. A new steel anchorage system for post-tensioning applications using carbon fibre reinforced plastic tendons. Canadian Journal of Civil Engineering 1998;25(1)113-127. https://doi.org/10.1139/l97-054

27. Schmidt JW, Bennitz A, Täljsten B, Pedersen H. Development of mechanical anchor for CFRP tendons using integrated sleeve. Journal of Composites for Construction 2010;14(4)397-405. https://doi.org/10.1061/(ASCE)CC.1943-5614.0000096
28. Schmidt JW, Smith ST, Täljsten B, Bennitz A, Goltermann P, Pedersen H. Numerical simulation and experimental validation of an integrated sleeve-wedge anchorage for CFRP rods. Journal of Composites for Construction 2011;15(3)284-292. https://doi.org/10.1061/(ASCE)CC.1943-5614.0000171
29. Al-Mayah A, Soudki KA, Plumtree A. Experimental and analytical investigation of a stainless steel anchorage for CFRP prestressing tendons. PCI journal 2001;46(2)88-99.
30. Campbell T, Shrive NG, Soudki K, Al-Mayah A, Keatley J, Reda M. Design and evaluation of a wedge-type anchor for fibre reinforced polymer tendons. Canadian Journal of Civil Engineering 2000;27(5)985-992.
31. Al-Mayah A, Soudki K, Plumtree A. Variable thickness barrel anchor for CFRP prestressing rods. Special Publication 2005;231237-252.
32. Al-Mayah A, Soudki K, Plumtree A. Novel anchor system for CFRP rod: Finite-element and mathematical models. Journal of Composites for Construction 2007;11(5)469-476.
33. Al-Mayah A, Soudki K, Plumtree A. Simplified anchor system for CFRP rods. Journal of Composites for Construction 2013;17(5)584-590.
34. Chen X, et al. Rationalized improvement of Tsai–Wu failure criterion considering different failure modes of composite materials. Composite Structures 2021;256113120.
35. Gu J. Research on failure criteria for aircraft structural materials. Nanjing University of Aeronautics and Astronautics 2018;88-95.
36. Tsai SW, Wu EM. A general theory of strength for anisotropic materials. Journal of composite materials 1971;5(1)58-80.
37. DIN E 6892-1: 2017-02: Metallic materials-Tensile testing-Part 1: Method of test at room temperature (ISO 6892-1: 2016). 2017, Beuth Verlag GmbH.
38. Abaqus F. Analysis User's Manual 6.14. Dassault Systemes Simulia Corp., Providence, RI 2011.
39. Heydarinouri H, Motavalli M, Nussbaumer A, Ghafoori E. Development of a Mechanical Wedge-Barrel Anchor for CFRP Rods: Static and Fatigue Behaviors. Journal of Composites for Construction 2021;25(3)04021015. doi:10.1061/(ASCE)CC.1943-5614.0001124. https://ascelibrary.org/doi/abs/10.1061/%28ASCE%29CC.1943-5614.0001124
40. Rostásy FS. Draft guidelines for the acceptance testing of FRP posttensioning tendons. Journal of Composites for Construction 1998;2(1)2-6. https://doi.org/10.1061/(ASCE)1090-0268(1998)2:1(2)
41. ACI-440.4R-04 Prestressing concrete structures with FRP tendons. 2004.
42. Collings T. Transverse compressive behaviour of unidirectional carbon fibre reinforced plastics. Composites 1974;5(3)108-116.
43. Hyer MW, White SR. Stress analysis of fiber-reinforced composite materials. 2009: DEStech Publications, Inc.

2.2. Development of a mechanical wedge–barrel anchor for CFRP rods: static and fatigue behaviours*

Abstract

In this study, a mechanical anchorage for prestressed carbon fibre-reinforced polymer (CFRP) rods was proposed. The proposed anchorage consists of a steel barrel with a conical hole and three separate aluminium wedges that are in direct contact with the CFRP rod. The anchorage system relies only upon friction, without any adhesives required. The static and fatigue behaviours of the anchor were experimentally investigated according to the European guidelines for testing post-tensioning kits and fulfilled their requirements. The average tensile strength of the anchorage system for the 8-mm CFRP rods was 2371.4 MPa, being greater than the guaranteed value of 2047 MPa. The fatigue tests revealed that the wedge seating distance (prior to pulling the rod) significantly affected the occurrence of slippage between the anchor components. Therefore, a new displacement-controlled presetting system was developed to ensure adequate wedge seating distance. It eliminated the need for hydraulic jacks and demonstrated the capability of applying presetting forces greater than 110 kN. Furthermore, the anchors were tested under loading frequencies of 5, 17, and 23 Hz. The proposed anchorage was observed to be insensitive to the loading frequency because no slippage or temperature rise occurred under these loading frequencies.

Keywords: CFRP tendon; Fatigue; Post-tensioning; Strengthening; Wedge–barrel anchor.

Nomenclature

f	loading frequency	P	presetting force;
D_r	dial gage reading for the CFRP rod	T	tensile load of the CFRP rod
$D_{r,ref}$	dial gage reading for the CFRP rod in the reference state	T_{nom}	nominal tensile strength of the CFRP rod
D_w	dial gage reading for the wedges;	T_{res}	residual tensile strength of the CFRP rod
$D_{w,ref}$	dial gage reading for the wedges in the reference state	T_u	ultimate tensile strength of the CFRP rod
N	number of cycles	Δr	relative draw-in of the CFRP rod
S	wedge seating distance	Δw	relative draw-in of the wedges
$S_{61.9}$	wedge seating distance at the lower fatigue load		

* Hossein Heydarinouri, Masoud Motavalli, Alain Nussbaumer, Elyas Ghafoori. Journal of Composites for Construction 2021; 25(3)04021015. https://ascelibrary.org/doi/abs/10.1061/%28ASCE%29CC.1943-5614.0001124.

2.2.1. Introduction

Post-tensioned (PT) steel strands have traditionally been used in prestressed structures such as concrete girders, post-tensioned concrete slabs, cable-stayed bridges, and post-tensioned walls. Carbon fibre-reinforced polymer (CFRP) materials have been considered as effective substitutes for prestressed steel strands because steel is vulnerable to fatigue and corrosion while CFRP provides a higher strength-to-weight ratio and superior corrosion and fatigue resistance [1]. However, because CFRP materials are weak in their transverse directions [1], the conventional anchorages used for steel components cannot be applied to these materials. Therefore, the development of proper anchorages for CFRP tendons, especially for prestressed applications, has been a research topic for the last couple of decades [2]. Various bonded and unbonded (mechanical) PT anchorages have been developed for both CFRP plates and rods. In this study, a mechanical wedge–barrel anchor system for CFRP rods was is introduced.

In the majority of the existing studies, only the static performance of the anchorages has been investigated, aiming to achieve the maximum tensile capacity of the CFRP tendons. However, only a limited number of studies have investigated the fatigue performance of PT anchorages for CFRP tendons due to the lack of standard test procedures and acceptance criteria. Some of the studies employed test procedures that were not based on standards. The following sub-sections present an in-depth literature review. First, a brief review of the PT systems for CFRP plates is presented. The existing PT systems for CFRP rods are reviewed in more detail, and previous studies of the fatigue performance of mechanical wedge–barrel anchors are presented. Finally, the main objectives of this study are summarised.

2.2.1.1. CFRP plate anchorages

Various resin-based anchors have been developed and experimentally investigated. Michels et al. [3] proposed a gradient anchorage system for CFRP strips, and Li and Xian [4, 5] developed wedge-shape anchors with optimized anchor parameters. At the Swiss Federal Laboratories for Materials Science and Technology, Empa, Switzerland, trapezoidal [6] and flat [7] mechanical prestressed unbonded reinforcement (PUR) anchorage systems were developed and later used to strengthen the girders of two bridges in Switzerland [8] and Australia [9, 10], respectively. These anchorage systems clamped the prestressed laboratoryCFRP plates and relied only upon friction. A friction-based wedge-type anchorage for prestressed CFRP plates was also developed and presented in [11, 12]. In this type of anchorages, the wedges had a curved profile that provided proper contact pressure distribution on the CFRP plates, leading to a high static tensile

strength. Various types of anchorages for CFRP plates have been reviewed [13].

2.2.1.2. CFRP rod anchorages

As an alternative to CFRP plates, CFRP rods have been used in post-tensioned structures. Information regarding various types of bonded anchorages for FRP materials was collected and compared in [2]. Among the bonded anchorage systems for CFRP rods, the wedge-type anchor proposed in [14, 15] is of substantial importance, because it was the first time a gradient epoxy material was used in the wedge. In wedge-type anchors, when the tensile stress and contact pressure on the CFRP tendon are simultaneously high at the loading end, the CFRP premature rupture occurs due to the stress concentration. Meier [14, 15] developed an anchorage to avoid this stress concentration by fabricating the wedge using an epoxy, to which particles were added at different levels to achieve a stiffness gradient. In this anchorage, the elastic modulus of the mixture of the epoxy and particles continuously increased along the anchor, from the loading end to the free end, reducing the contact pressure on the CFRP tendon at the loading end and providing an anchorage efficiency of 92%. The anchorage efficiency was defined as the ratio between the actual PT tensile strength and the nominal tensile strength of the tendons. In another type of bonded wedge anchorage, the CFRP rod was split in the middle of its cross-section along a certain length, and a wedge was placed in the split [16, 17]. The rod was anchored by applying epoxy between the CFRP rod and the steel barrel.

In addition, unbonded anchorages have been used in post-tensioned structures. In mechanical wedge anchors, when the wedges insert into the conical barrel hole, the contact pressure on the tendon increases, providing friction resistance against rod slippage. Similar to the gradient adhesive concept in bonded anchorages [14, 15], two common methods to prevent premature rupture due to the stress concentration at loading end of the anchor are: (i) providing a constant differential angle between the wedge and barrel cones and (ii) using curved conical shapes for both the wedge and barrel, thus providing a distribution of the differential angles along the anchor. The mechanism of contact pressure reduction at the loading end of the anchors using a constant differential angle was presented in [18]. In this method, a volume of the material is removed from the loading end of the wedge, leading to a reduction in the contact pressure on the wedge induced by the barrel. Consequently, it leads to a reduction in the contact pressure on rod at the loading end. The same mechanism is valid for the anchors with curved conical profiles.

Different researchers have developed mechanical wedge–barrel anchors with constant differential angles. In the anchorage system introduced in [19, 20], four steel split wedges had a differential angle of 0.1°. A soft sleeve, made of aluminium or copper, was used between the wedges and CFRP rod to avoid damaging the rod. The failure mode in the static tests was the CFRP rod rupture, with an average tensile capacity of 10% greater than the guaranteed value of the CFRP rods. A split-wedge–barrel anchor for 5.4 mm CFRP rods was introduced later in [21] for prestressed concrete applications. The barrel and wedges were made of steel and polymer with glass fibres (PPS-GF40), respectively, with a constant differential angle of 0.23°. They performed static and creep tests on their anchor, which demonstrated an anchorage efficiency of only 73.4%. An easy-to-use two-piece wedge anchorage was introduced and investigated in [22, 23], in which the wedges were integrated with the sleeve and in direct contact with the CFRP rod. The integrated wedge was made of aluminium and had a differential angle of 0.4°. Static tests were performed on the 8 mm CFRP rods according to the European standards [24-26], demonstrating that the tensile capacity of the anchorage exceeded the nominal strength of the CFRP rods.

Al-Mayah et al. [27] proposed a wedge anchor with a curved conical shape for both the barrel and wedges to further reduce the stress concentration; the curves were circular. The differential angle at the loading end was small and increased towards the free end. It enabled a rapid increase in the contact pressure on the rod from the small value at the loading end. In this anchorage system, three split steel wedges were in contact with a steel barrel and a copper or aluminium sleeve. The tensile strength of the anchorage system exceeded the guaranteed strength of the CFRP rods.

2.2.1.3. Fatigue tests on mechanical wedge-barrel anchors

In most of the previously discussed studies, only the static performance of the anchors was investigated. Few studies have addressed the critically important factor of fatigue performance and the corresponding acceptance criteria. The most relevant studies on the fatigue performance of mechanical wedge–barrel anchors are briefly presented in this sub-section with highlights of the limitations of each study.

The fatigue performance of a wedge–barrel anchor for an 8 mm CFRP rod with a constant differential angle was investigated in [28]. In their study, three cyclic loads with different stress ranges and ratios were applied, and the fatigue life and slippage of the CFRP rod during the

fatigue tests were reported. However, no further information was provided regarding the selected cyclic load history and fatigue acceptance criteria. In other studies, fatigue tests were performed according to the procedure recommended by the Post-Tensioning Institute (PTI) [29], which is typically used for steel tendons [20, 30-32]. These studies concluded that the fatigue performance of the anchors could fulfil the requirements in [29]. More recently, Kar et al. [33] conducted tension–tension fatigue tests on the CFRP rods, with different stress ratios, focusing on the damage mechanisms during the fatigue loading. Li et al. [34] performed tension-tension fatigue tests on hybrid carbon/glass rods, with different maximum stress levels at a fixed stress ratio. The focus of this study was the fatigue failure mode. However, none of these studies addressed the slippage behaviour of the anchorage components during the cyclic loadings in accordance to an acceptance criteria.

2.2.1.4. Primary objectives and outline of the study

In this study, a mechanical wedge–barrel anchor for CFRP rods is introduced, taking the advantages of the existing anchorages. To the best of the authors' knowledge, all previous studies performed their fatigue tests according to the PTI [29]. For the first time, in the present study, the European codes and standards are used to evaluate both the static and fatigue performance of the developed anchor. In addition, the effect of the wedge seating distance in the barrel (prior to the rod pulling) on the slippage behaviour of the anchor during the fatigue tests is investigated. Subsequently, a new displacement-controlled presetting system is proposed to ensure an adequate wedge seating distance. Finally, the effect of frequency on the slippage and temperature change in the anchorage components during the cyclic loadings is experimentally investigated.

2.2.2. Proposed anchorage system

The wedge–barrel anchor introduced in this study is a combination of anchors developed in [27] and [22, 23]. In the anchor developed in [27], a curved (circular) profile was used for the contact surfaces between the wedges and barrel along the anchor length. The curved profile prevented stress concentration at the loading end while increasing the contact pressure rapidly towards the free end, resulting in a shorter anchor length required to achieve adequate frictional resistance. However, in this anchor, a soft sleeve (i.e., aluminium or copper) was used to prevent CFRP damage. Schmidt et al. [22] eliminated the need for a soft sleeve by developing a wedge–barrel anchor that employed an integrated sleeve; the wedges and sleeve were both made of aluminium.

In the present study, a wedge–barrel anchor with a curved profile was used, as shown in Fig. 1. The profile curvature of the wedges and barrel was similar to that of Anchor A introduced in [27]. The wedges were made of aluminium and were in direct contact with the CFRP rod, without the need for a sleeve. The use of aluminium wedges reduced the required presetting force because aluminium has a lower stiffness than steel, resulting in an easier insertion into the barrel. This trend was demonstrated in a numerical study in [35], which compared the insertion of different wedges composed of soft and hard steels. In addition, the aluminium plasticisation that occurs due to the high contact pressure inside the barrel can improve the gripping of the CFRP rod.

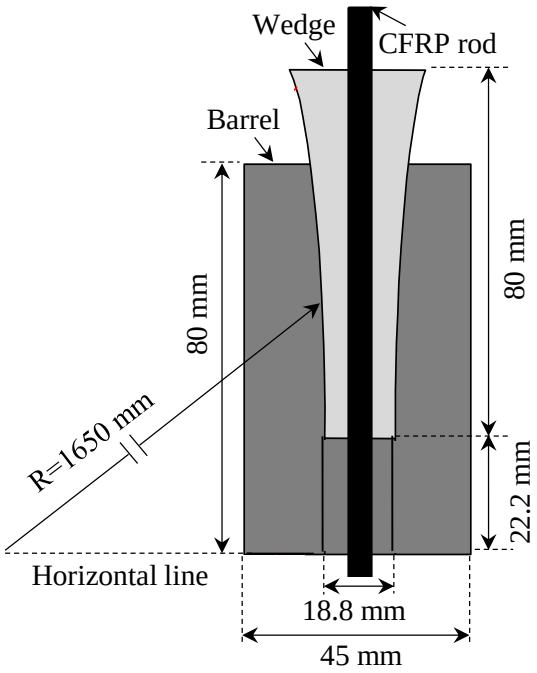

Fig. 1. Geometric details of the developed wedge–barrel anchor.

It is noted that an FE model of the wedge–barrel anchor was developed using ABAQUS software to achieve a proper contact pressure on the CFRP rod and was verified by the experimental results. The applied FE model is briefly described in the Appendix I. The FE model showed that the contact pressure on the CFRP rod for the split-wedge anchor was desirably the minimum at the loading end. Detailed descriptions of the FE model or a parametric study considering various wedge–barrel anchor configurations and geometries were beyond the scope of the present study and will be addressed in a future study.

2.2.2.1. Different anchor configurations

Two configurations of the wedge–barrel anchors, i.e., with integrated and split wedges, were

developed for the preliminary static tests, as shown in Fig. 2(a) and (b), respectively. The integrated wedge shown in Fig. 2(a) had two 1-mm slits and a 3 mm gap. When the CFRP rod was pulled, it tended to bring the wedge into the barrel. When the wedges were inserted into the barrel, the circumferential pressure from the barrel caused wedge deformation. The existence of the slits and gaps facilitated this deformation during the insertion, i.e., the slits opened, and the gap tended to close. The anchor with the other configuration, shown in Fig. 2(b), had three split wedges with a gap distance of 1.5 mm.

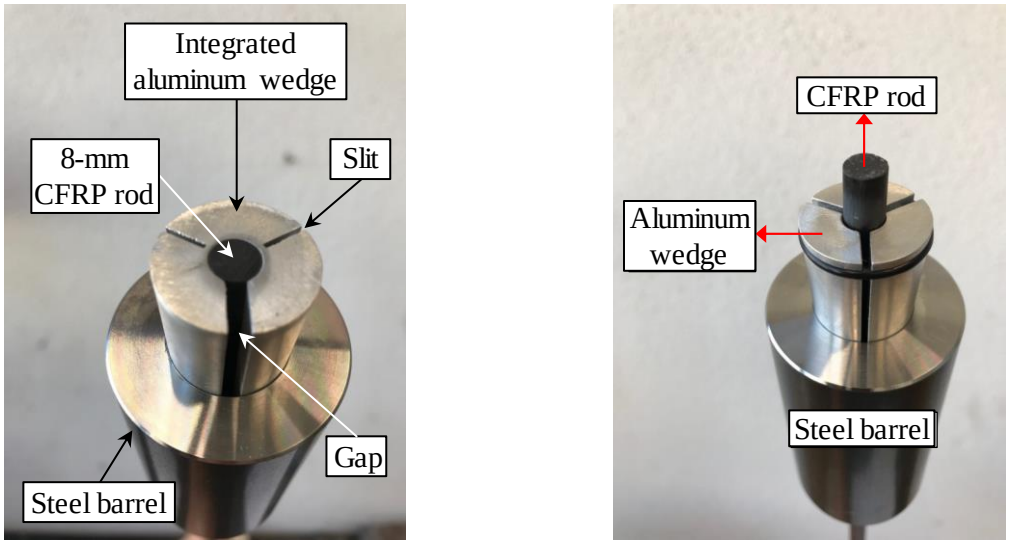

(a) (b)

Fig. 2. Anchor configurations with: (a) Integrated and (b) Split wedges.

2.2.2.2. Material properties of the anchorage components

The wedges were made of EN AW-6026 aluminium with an elastic modulus of 71.7 GPa, yield strength of 404 MPa, and ultimate tensile strength of 442 MPa, based on coupon tests according to DIN EN ISO 6892-1 [36]. The barrel was made of high strength V155 steel with a nominal elasticity modulus and tensile strength of 200 GPa and 1300 MPa, respectively. The CFRP rods had a nominal diameter of 8 mm, a guaranteed tensile strength of 102.9 kN (equivalent to 2047 MPa), a fibre volume fraction of 65%, and a longitudinal elastic modulus of 160 GPa, according to ASTM D7205/D7205M-06 [37], provided by S&P Clever Reinforcement Company AG, Switzerland.

2.2.3. Preliminary static tests

The static performance of the integrated and split-wedge anchors was investigated in the preliminary design stage. Before pulling the CFRP rods, the wedges were preset using a 200 kN

Amsler testing machine in a setup shown in Fig. 3(a). In this setup, the wedges were compressed by lifting the anchor to contact the fixed plate. A shaft was placed between the fixed plate and top surface of the wedges to transmit the compressive presetting force. The shaft had a hole in the center, with a diameter of 9 mm, so that the rod could pass through the hole. Therefore, the shaft completely rested on the top surface of the wedges. The static tensile tests on the wedge–barrel anchors were performed using the setup shown in Fig. 3(b).

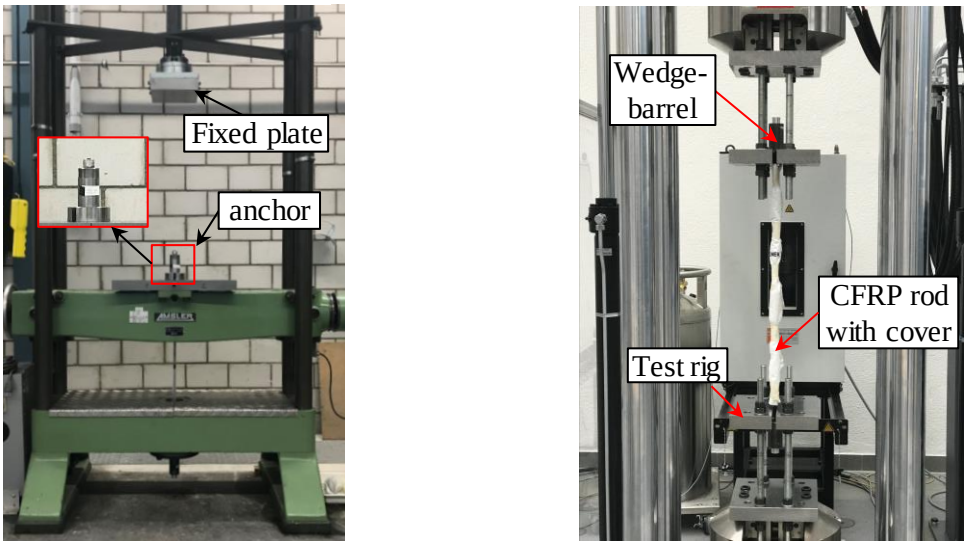

(a) (b)

Fig. 3. Test set-up used for: (a) Application of the presetting force; (b) Static and fatigue tests.

2.2.3.1. Test results

The results of the preliminary static tests are presented in Fig. 4. The tests were performed on anchors with different presetting forces, *P*, ranging from 10 to 50 kN. As shown in Fig. 4(a), for the integrated wedge anchor and up to a presetting force of *P*=30 kN, the failure mode of the PT system was CFRP rod slippage inside the integrated wedge. For the presetting forces of 40 and 50 kN, the failure mode changed to CFRP rod rupture; however, the ultimate tensile strength was approximately 80 kN, which is around 78% of the guaranteed tensile strength of the rod. Fig. 4(b) shows the CFRP rod and integrated wedge after failure. Interlaminar shear failure occurred in the gap area of the CFRP rod. In addition, cracks appeared near the slit because the slit opened during the insertion of the wedge into the barrel. The existence of a crack at the slit resulted from the constraint against the slit opening.

The results of the preliminary static tests on the split-wedge anchors are shown in Fig. 4(c) and indicated that, up to a presetting force of 20 kN, the failure mode was the rod slipping inside the wedges. No slippage of the CFRP rod occurred with a presetting force of 30 kN. This value

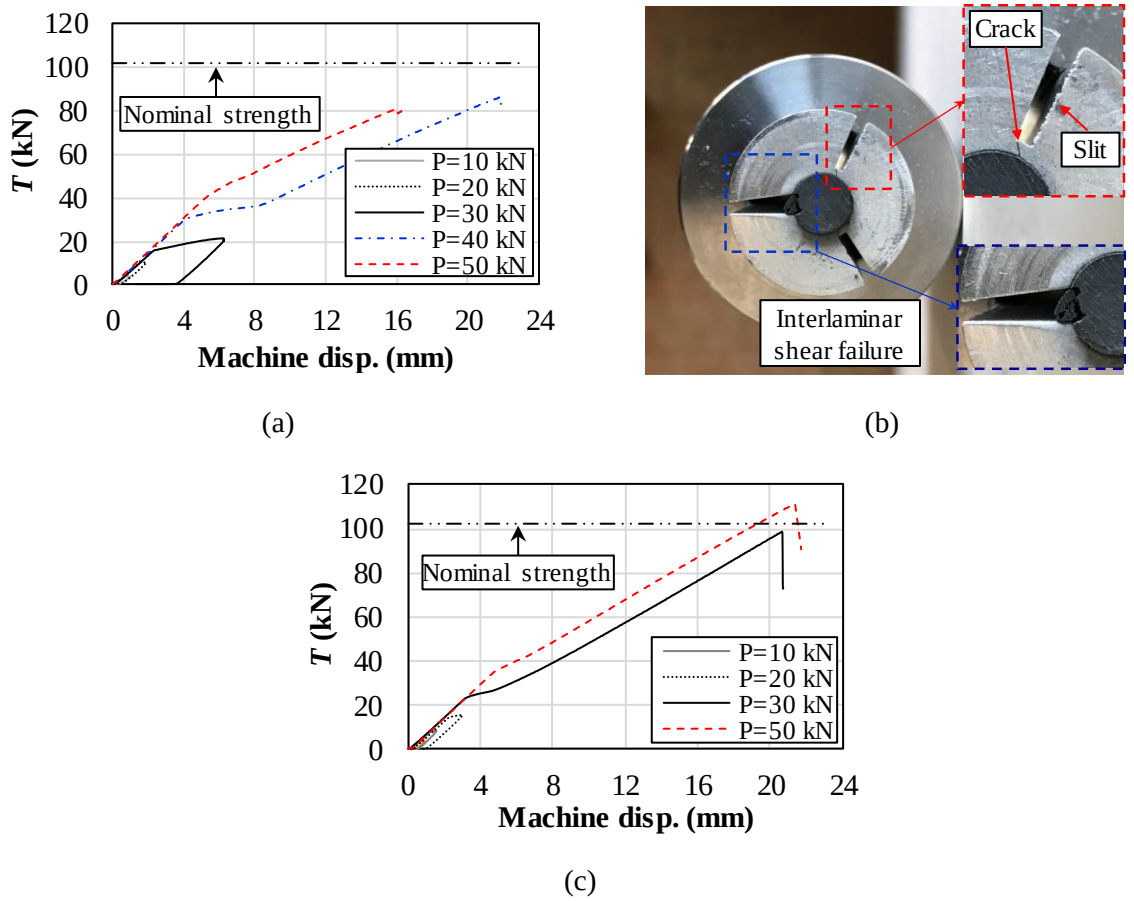

Fig. 4. Preliminary static test results: (a) Load–displacement curves for the integrated wedge anchor; (b) Failure of the integrated wedge anchor; (c) Load–displacement curves for the split-wedge anchor.

was less than the 40 kN required to prevent the slipping in the integrated wedges. Because the split wedges were not connected to each other and, thus, did not resist the circumferential deformation of the adjacent wedges. Thus, they deformed more easily under the circumferential stresses compared to the integrated wedges. Therefore, a higher presetting force was required to activate the integrated-wedge anchor system. The tensile strength was in the same order of magnitude as the CFRP rod guaranteed tensile strength. Further, interlaminar shear failure did not occur in the split-wedge anchor system. This resulted from the fact that the free surfaces of the CFRP rod in the split-wedge anchor occurred in three small areas (see Fig. 2(b)). In the integrated-wedge anchor, however, the concentration of the free surface in the gap area triggered the premature interlaminar shear failure of the CFRP rod.

Notably, although the integrated wedge system demonstrated the lower tensile strength in the present study, an integrated wedge anchor system with a longer wedge and barrel, i.e., 95 and 105 mm, respectively, was statically tested in [22] and provided a relatively higher tensile

strength. This implies that further changes in the integrated wedge anchor geometry in the current study might result in a higher tensile capacity.

2.2.3.2. Modification on the split-wedge anchors

The split-wedge anchor was selected for further experimental and numerical investigations, based on the preliminary test results. The wedge and barrel geometries were modified to increase the tensile capacity of the PT system. Fillets were added to the edges of the wedge that were in contact with the CFRP rods to prevent stress concentration at the edges, i.e., the edges near the loading end and the longitudinal edges. In addition, the gap between the adjacent wedges was reduced from the initial 1.5 mm to 1 mm to increase the contact area. A fillet was created in the barrel cone edges at the free end to enable an easier insertion of the wedges. The modifications are shown in the Appendix II.

2.2.4. Experimental study on the modified split-wedge anchors

In this section, the European standard testing procedures for PT systems as well as the static and fatigue tests on the modified split-wedge–barrel anchors are described.

2.2.4.1. Standard static and fatigue testing procedures

This section discusses the relevant static and fatigue testing procedures and the acceptance criteria recommended in: (i) the European Technical Approval Guidelines ETAG 013 [24], (ii)), the International Federation for Structural Concrete (fib) recommendations for the acceptance of PT systems [25], which is typically used for steel PT systems, and (iii) the draft guideline for the acceptance testing of FRP PT tendons [26].

2.2.4.1.1. Standard static tensile tests

The goal of static tensile testing is determining the tensile strength of the PT system, T_u, or the reduction in the tensile capacity (compared to the tendon strength) due to the anchorage effect. According to ETAG 013 [24] and the recommendations for the acceptance of PT systems [25], the acceptance criteria for static tests are as follows:

(i) The failure mode must be a tendon fracture and not the failure of the anchorage components, i.e., excessive residual deformation in the anchorage components after testing.

(ii) The maximum measured tensile load must be greater than 95% of the actual ultimate strength of the tendon, i.e., an efficiency factor of 0.95.

(iii) The relative movements of the anchorage components must stabilise within the first 30 minutes at a tensile load level representing 80% of the characteristic tensile strength of the prestressing steel.

In the acceptance criteria proposed in the draft guideline for FRP post-tensioning tendons [26], the failure mode criterion is the same as item (i). However, it does not propose a criterion for the efficiency factor. In addition, it recommends a tensile load level of 70% instead of 80% of the tensile strength of the tendon for the slippage stabilisation of the anchorage components in item (iii).

In this study, the acceptance criteria for the static tests were as follows:

- For the failure mode, item (i) was adopted.
- An efficiency factor of 95% was required.
- For the relative movement stabilisation of the anchorage components, a tensile load level of 70% of the guaranteed tensile strength of the CFRP rod was applied.

2.2.4.1.2. Standard fatigue tests

The aim of fatigue tests is determining the fatigue strength of the anchors, which is defined as the stress range under which the PT system endures 2 million cycles. All the previously discussed standards and recommendations state that no fatigue failure should occur in either the anchorage or tensile elements during the fatigue tests. ETAG 013 [24] and fib [25] state that the minimum fatigue strength of PT systems for steel tendons is 80 MPa, with a maximum fatigue load of 65% of the characteristic tensile strength of the tendon. The draft guideline for FRP PT tendons [26], however, does not provide a recommendation for the fatigue strength, only stating that the fatigue strength should be equal to the maximum in-service stress range. In this study, a stress range of 100 MPa, with a maximum load level of 65% of the CFRP nominal tensile strength applied for 2 million cycles without failure, was set as the acceptance fatigue criterion. In the following section, the procedures for and results of the static and fatigue tests on the split-wedge anchors are presented.

2.2.4.2. Static tests on the modified split-wedge anchors

2.2.4.2.1. Test procedure

The loading protocol for the static tests is shown in Fig. 5(a), in which the load increased stepwise at a loading rate of 0.08 kN/s (100 MPa/min) according to [24, 25]. At load levels of 0.2,

0.4, and 0.6 of the CFRP rod nominal tensile strength, T_{nom}, which was 102.9 kN, the displacement of the wedges and CFRP rod relative to the barrel, called relative draw-ins, were measured after five minutes, using a Mitutoyo digital dial gauge with a reading precision of 0.001 mm, as shown in Fig. 5(b). In addition, at a load of $0.7T_{nom}$, the stabilisation of the draw-ins after 30 minutes was evaluated.

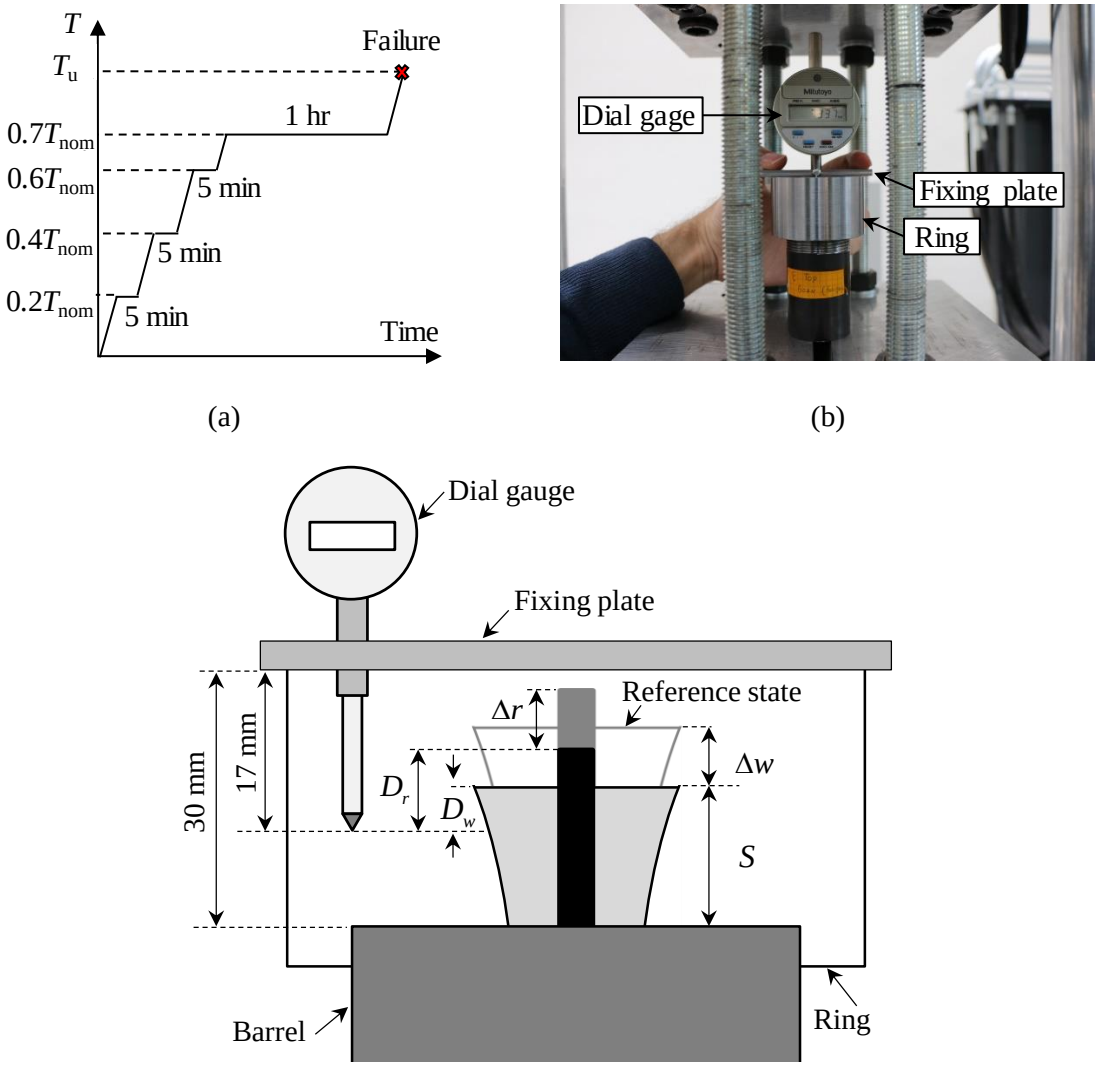

Fig. 5. Static test procedure and measurements: (a) Loading protocol; (b) Relative draw-in measurement using the digital dial gauge, (c) Relative draw-in measurement detail.

A schematic of the dimensions of the dial gauge and ring and the parameters required for the measurement of the relative draw-ins are provided in Fig. 5(c). The relative draw-ins for the wedges, Δw, and CFRP rod, Δr, were calculated relative to a reference state. In the static tests, the reference states were the beginnings of the periods corresponding to each load level of 0.2, 0.4, 0.6, and 0.7 of T_{nom}. They were calculated based on the dial gauge measurements using the

following equations:

$$\Delta w = D_{w,ref} - D_w; \tag{1-a}$$

$$\Delta r = D_{r,ref} - D_r, \tag{1-b}$$

where $D_{w,ref}$, D_w, $D_{r,ref}$, and D_r are the dial gauge readings at the reference state and after the insertion of the wedges and CFRP rod, respectively. In Fig. 5(c), the wedge seating distance, S, which is the distance between the top surfaces of the wedges and barrel, determines the placement of the wedges in the barrel. This parameter significantly affects the fatigue performance of the anchors, which is discussed in more detail later in this paper and is obtained by

$$S = 13 + D_w. \tag{2}$$

2.2.4.2.2. Test results

The results of the static tests are presented in Table 1. Three presetting forces, P, i.e., 30, 50, and 70 kN, were applied to the wedges. As shown in Table 1, in all static tests, the tensile loading capacity was at least 10% greater than the nominal strength of the CFRP rods, even at the smallest presetting force of 30 kN. The relative draw-in measurements indicated that at a load of 70% of the nominal tensile strength, the draw-ins stabilised after 30 min. The load–displacement curves for the different anchors as well as the failed specimen S1 are illustrated in Fig. 6(a) and (b), respectively.

Table 1. Results of the split-wedge anchor static tensile tests

Specimen	P (kN)	Sandblasting	T_u (kN)	Observation
S1	50	Yes	113.5	A*
S2	70	Yes	118.6	A
S3	30	Yes	118.3	A
S4	30	No	117.8	Excessive slippage

*A: Accepted.

Specimen S4 was not sandblasted so that the effect of the friction between the inner surface of the wedges and the CFRP rod could be investigated. As shown in Fig. 6, although the loading capacity for this specimen was greater than the CFRP rod nominal strength, the CFRP rod slipped considerably inside the wedges. It was concluded that Samples S1 to S3 met the static test requirements.

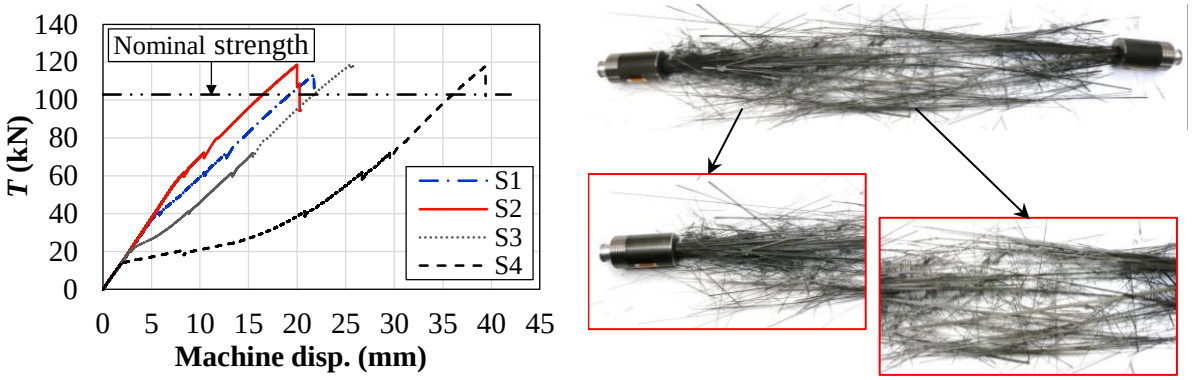

Fig. 6. Static test results for the modified split-wedge anchors: (a) Load–displacement curve; (b) Fractured CFRP rod for specimen S1.

2.2.4.3. Fatigue tests on the modified split-wedge anchors

2.2.4.3.1. Test procedure

The fatigue tests were performed under a load-controlled constant amplitude condition and a frequency of 12 Hz. The loading protocol for the fatigue tests is shown in Fig. 7. The upper load in the fatigue tests was $0.65T_{nom}$ (66.9 kN), which was equivalent to 1330.6 MPa for an 8 mm rod, with a stress range of 100 MPa. Each sample was subjected to a minimum of 2 million cycles.

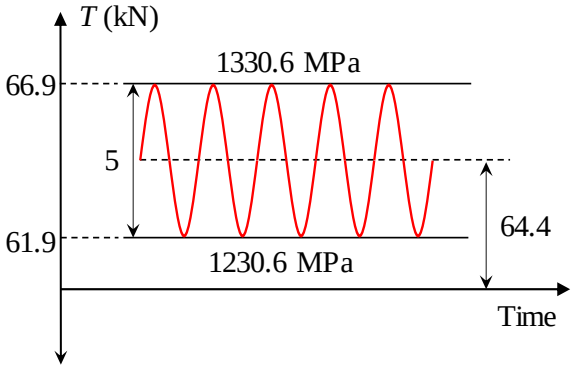

Fig. 7. Loading protocol in the fatigue tests.

Before the cyclic loading began, each specimen was statically loaded to 61.9 kN (i.e., the fatigue lower load) according to the test procedure presented in [24, 25]. This state was considered to be the reference state, and the dial gauge readings for the wedges, $D_{w,ref}$, and CFRP rod, $D_{r,ref}$, were measured. The subsequent relative draw-ins for the wedges and CFRP rod were calculated relative to the reference state using Eq. (1). Then, each specimen was statically loaded to 66.9 kN (i.e., the upper fatigue load), and then the load was reduced to 61.9 kN; the relative draw-

ins were measured at each of these load levels. The fatigue test then began and was stopped after every half-million cycles to determine the relative draw-ins of the CFRP rod and wedges for each anchor at the lower and upper loads.

In the acceptance test reports for steel strands, several single wedges and strands are selected, for which the relative draw-ins corresponding to the lower and upper loads are separately reported. In this study, measurements were performed for all the wedges and CFRP rods. The average of the relative draw-ins of all the wedges in the anchor was calculated and used to determine the relative draw-ins. In addition, after each half-million cycles, the averages of the relative draw-ins corresponding to the lower and upper loads were considered for both the wedges and CFRP rod. In this way, only the average values were reported for the wedges and CFRP rods for each anchor and after each half million cycles. This method of reporting the results helped to demonstrate the slippage of the anchor components during the fatigue tests more clearly.

The anchors were subjected to load-controlled fatigue loading, as given in Table 2. Because the top and bottom anchors were subjected to identical cyclic loading during the fatigue tests, the properties and test results for the top and bottom anchors are presented separately in Table 2.

Table. 2. Fatigue test results

Specimen	Anchor	P (kN)	Lubricant	N (millions)	Observation during the fatigue test	$S_{61.9}$ (mm)	T_{res} (kN)
F5	F5-T	50	No	2	NA*: Slippage	20.4	-
	F5-B		No		NA: Slippage	20.4	
F6	F6-T	50	No	2.5	NA: Slippage	19.6	118.2
	F6-B		Yes		A**	18.3	
F7	F7-T	50	Yes	2	A	19.0	129
	F7-B		Yes		A	18.9	
F8	F8-T	***	Yes	9	A	18.5	-
	F8-B		Yes		A	18.5	

*NA: Not accepted; **A: Accepted; ***Using developed system.

2.2.4.3.2. Test results

For all specimens, no CFRP failure occurred during the fatigue tests. In addition, there was no increase in the machine displacement, showing that the stiffness of the post-tensioning system was constant during the fatigue tests. It would indicate that no significant damage occurred in the CFRP rods inside the anchors.

Lubricant was not used between the wedges and barrels in anchors F5-T, F5-B, and F6-T to

investigate the effect of the friction between the wedges and barrel on the anchor fatigue performance. The presetting force for these anchors was 50 kN. As shown in Fig. 8, the relative draw-ins for these anchors during the fatigue tests showed that the CFRP rods started slipping after several cycles. The slippage, shown in Fig. 8, represents the difference in the relative draw-in between the CFRP rod and wedges. The fatigue performance of these anchors did not meet the requirements of the aforementioned standards and recommendations due to the continuous slippage and excessive residual deformations of the anchorage components.

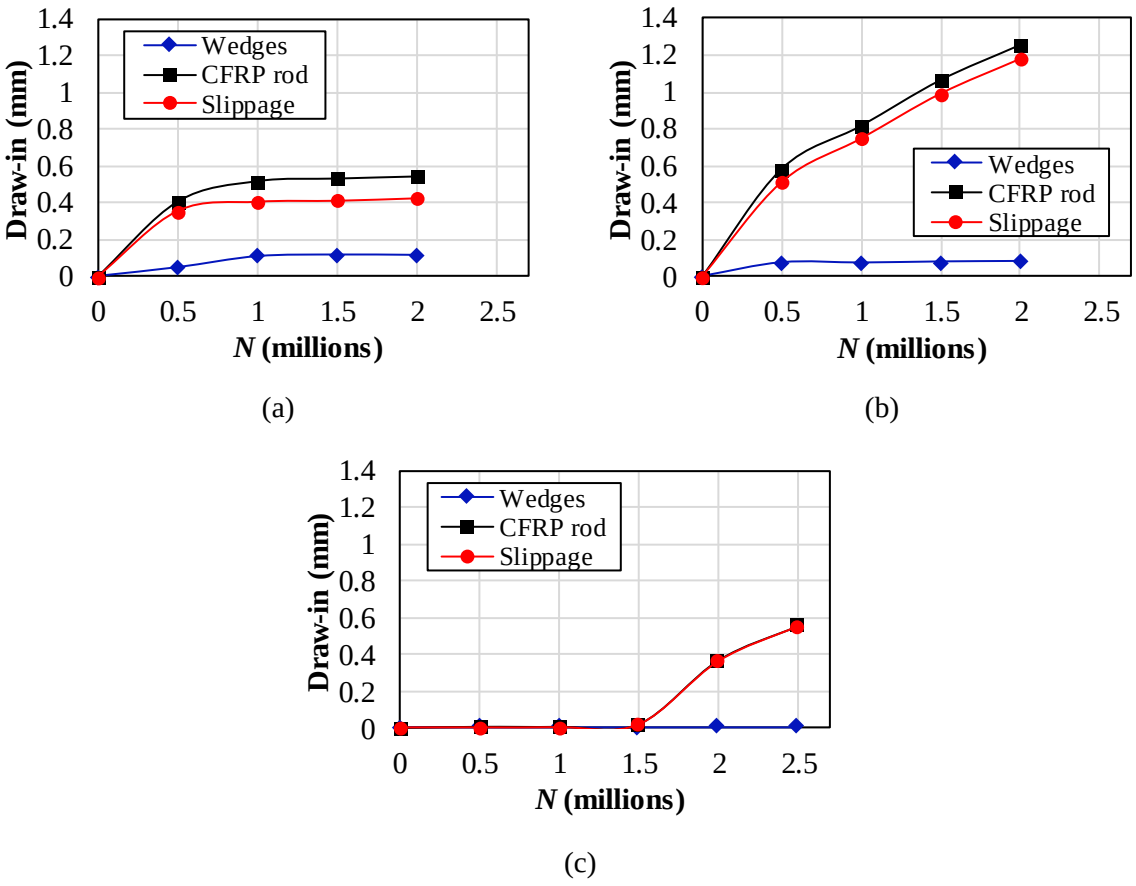

Fig. 8. Relative draw-ins for the anchors without lubricant: (a) F5-T; (b) F5-B; (c) F6-T.

The use of the lubricant in anchors F6-B, F7-T, and F7-B, which all had a presetting force of 50 kN, resulted in no slippage during the cyclic loading, as shown in Fig. 9. Comparing the seating distances of the wedges, S, for the anchors with and without lubricant revealed that, for a given presetting force, the application of the lubricant between the wedges and barrels resulted in a greater insertion (a smaller S), due to the reduction in the friction between the wedges and barrel. This greater insertion of the wedges resulted in a higher contact pressure around the CFRP rods, and, consequently, no slippage occurred during the fatigue tests for anchors F6-B, F7-T, and F7-B (see Fig. 9).

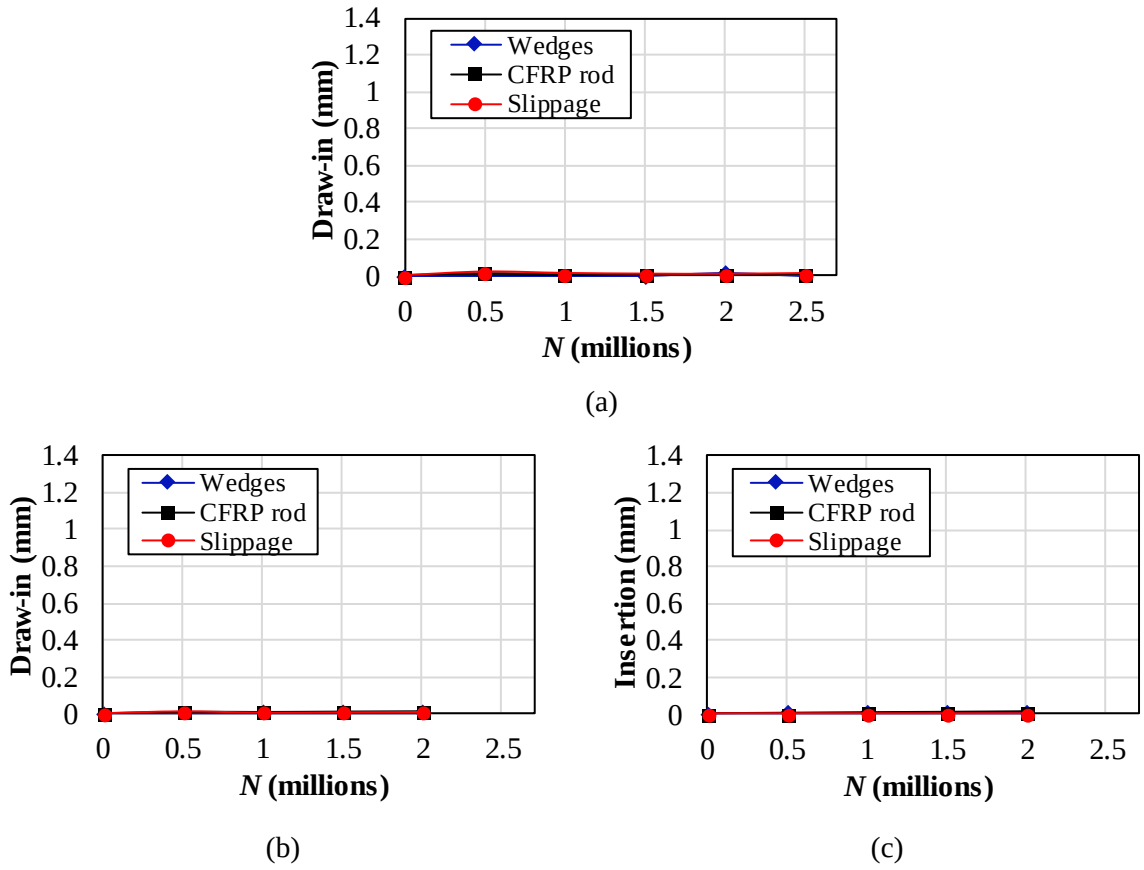

Fig. 9. Relative draw-ins for the lubricated anchors: (a) F6-B, (b) F7-T, (c) F7-B.

The wedge seating distance under the tensile load of T=61.9 kN, i.e., the minimum CFRP load in the fatigue tests, was measured for specimens F5 to F7 and the results are listed as $S_{61.9}$ in Table 2. The fatigue test results demonstrated that, when the value of $S_{61.9}$ was less than 19 mm, no slippage of the anchorage components occurred. It could be inferred that presetting the wedges (before pulling the CFRP rod) to a seating distance less than 19 mm would prevent the slippage. Therefore, the key parameter for preventing the CFRP rods from slipping inside the wedges during the fatigue tests (regardless of the lubrication condition) is the wedge insertion prior to the cyclic loadings and not necessarily the presetting force level.

2.2.4.3.3. Introduction of a new presetting system

A new presetting system was developed to ensure adequate wedge insertion, as shown in Fig. 10. In this presetting system, a ring was placed around the barrel using the threads at the free end (see Fig. 11). A hollow shaft was located around the wedges on the barrel surface. Adequate insertion of the wedges was determined to require 18.5 mm high hollow shafts. This value which was less than the 19 mm obtained based on the $S_{61.9}$ values and the corresponding fatigue test results in Table 2. Six M8 bolts were passed through the holes in the top plate and fastened

using the threaded holes in the ring. By fastening the bolts, caused the top plate to push the wedges into the barrel until the top plate touched the hollow shaft, at which point the presetting was complete.

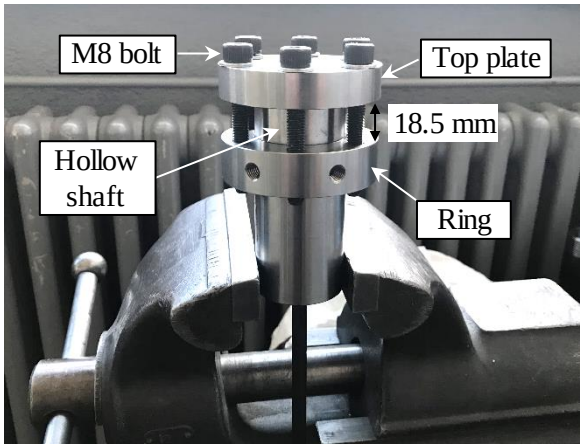

Fig. 10. Proposed presetting system.

Although the proposed presetting system presets the wedges up to a certain displacement (i.e., it is a displacement-controlled system), it could also apply a substantial presetting force, depending on the bolt strength. For example, it was observed that using six M8, 8.8 bolts, it was possible to provide an approximately 110 kN presetting force by applying the standard bolt torque. The correlation between the applied torque to the bolts and the resultant presetting force is shown in the Appendix III. Moreover, the proposed system eliminated the need for hydraulic jacks to apply the presetting force. This is significant for cases wherein the use of hydraulic jacks is not possible, for example, due to geometric complexity. The anchors in specimen F8 were preset using the proposed system, and the fatigue test results for this anchor are presented in the following section.

2.2.4.4. Effect of the loading frequency

The relative displacement between the wedges, CFRP rod, and barrel could generate heat during fatigue tests, depending on the loading frequency [38]. The draft guideline for FRP PT tendons [26] recommends that the loading frequency in the fatigue tests not be greater than 2 Hz.

The frequency effect on the slippage between the anchorage components was investigated by applying thermocouples to the barrel and one of the wedges in anchors F8-T and -B, as shown in Fig. 11(a) and (b), respectively. A thermocouple was also used to measure the room temperature. Any heating was considered to be an indication of slippage between the components.

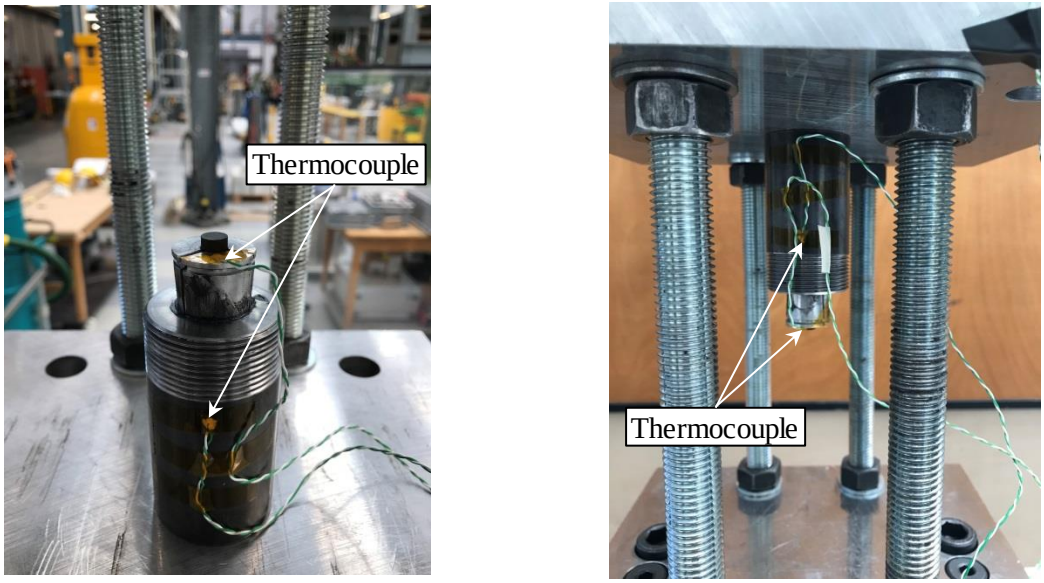

(a) (b)

Fig. 11. Thermocouples on: (a) F8-T; (b) F8-B.

The load-controlled constant amplitude fatigue tests followed the loading protocol shown in Fig. 7 and were performed at 5, 17, and 23 Hz for 0.5, 1, and 2 million cycles, respectively. The temperature changes in the anchorage components during the fatigue tests are represented in Fig. 12. The results show that, during the fatigue tests, the temperature changes in the different components were synchronised with the room temperature, without any progressive temperature rise. This indicates that no relative displacement occurred between the anchorage components.

After two million cycles at a loading frequency of 23 Hz, the thermocouples were dismantled, and the fatigue test was resumed under the same frequency up to 9 million cycles. The relative draw-ins are shown in Fig. 13. At frequencies as high as 23 Hz, no increase in the relative draw-ins was observed. Therefore, it could be concluded that the anchorage system was not sensitive to the loading frequencies. The fluctuation that can be seen in the magnified view of the relative draw-ins for anchor F8-T in Fig. 13(a) resulted from measurement error and was negligible. In addition, specimen F8 was preset with the developed presetting system, thus, the results of the fatigue tests on this anchor confirmed that the use of the proposed presetting system would provide reliable fatigue performance.

2.2.4.5. Residual strength tests

After the completion of the fatigue tests, Specimens F6 and F7 were statically loaded to failure to investigate if any significant damage developed in the system during the cyclic loadings. For

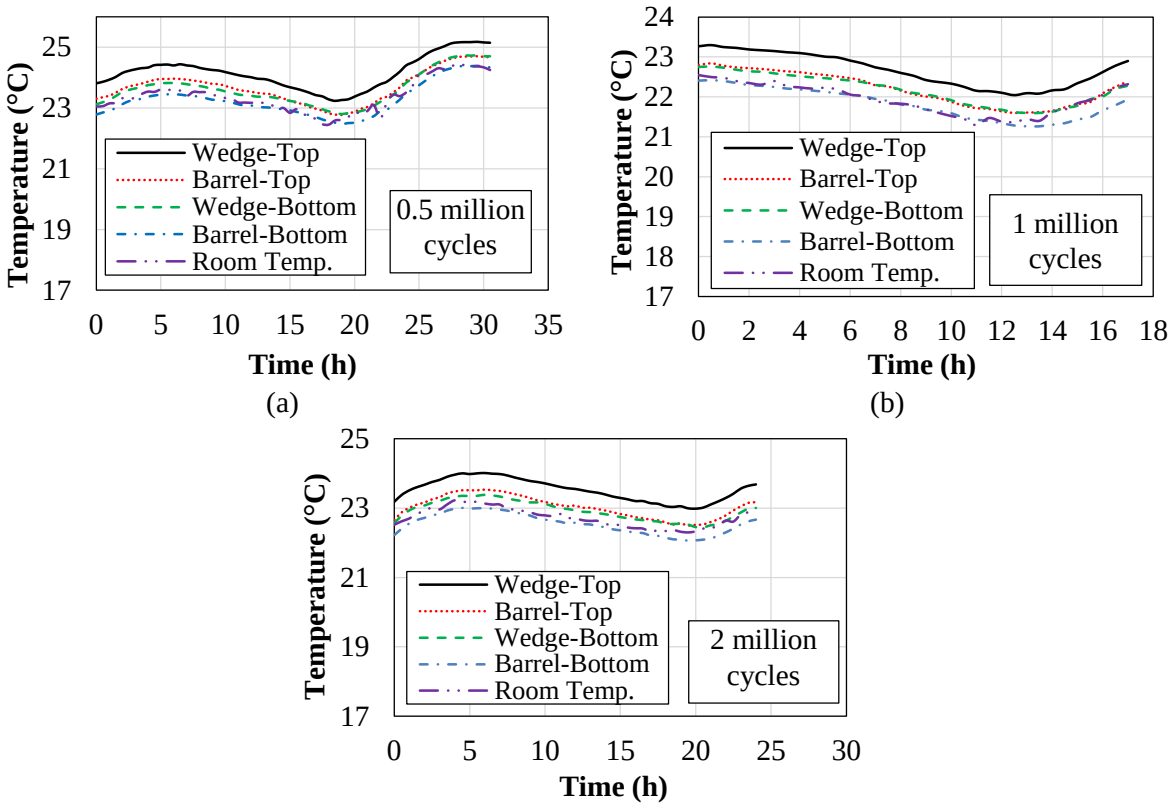

Fig. 12. Temperature changes in the anchor components under the loading frequencies of: (a) 5 Hz; (b) 17 Hz; (c) 23 Hz.

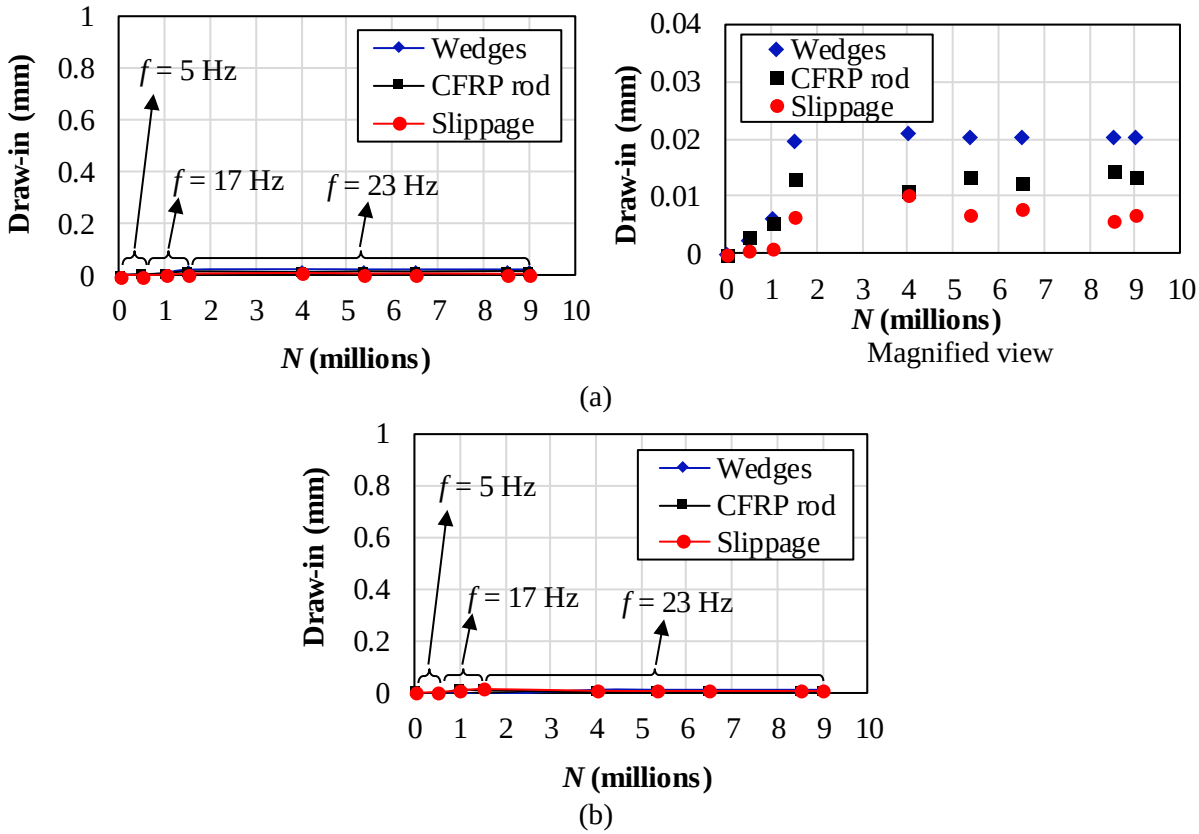

Fig. 13. Relative draw-ins under different loading frequencies for anchors: (a) F8-T; (b) F8-B.

both specimens, the tensile capacity was greater than the CFRP rod guaranteed strength, as shown in Table 2 (T_{res}) and Fig. 14. This indicates that no significant damage accumulated in the anchors during the fatigue tests. Specimen F7 had the highest tensile capacity, with a tensile strength of 129 kN (equivalent to 2566 MPa). One possibility for such a high residual tensile capacity could be the alignment of carbon fibres with the loading direction during the fatigue test, which could lead to an increase in the tensile strength.

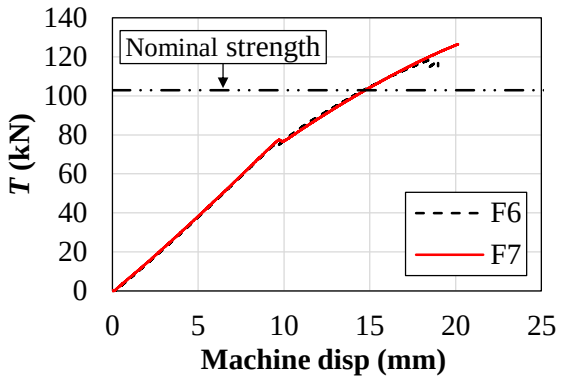

Fig. 14. Residual tensile strengths of Specimens F6 and F7.

Considering these two static tests together with the static test results presented in Table 1, the average tensile capacity of the tested anchors was 119.2 kN (equivalent to 2371.4 MPa), which was approximately 16% greater than the nominal tensile strength of the CFRP rods.

2.2.5. Field application of the proposed anchorage

The proposed mechanical wedge–barrel anchor was used for fatigue-strengthening of the connections in an old riveted railway bridge in Switzerland [39]. The reliable fatigue performance of the strengthening system attached to the beam was confirmed in laboratory tests [40]. The CFRP rods used for the strengthening were prestressed to 994.7 MPa (approximately 50% of the guaranteed tensile strength of the rod). In this application, the wedges were required to be preset onsite, because the use of hydraulic jacks would have been difficult due to the geometric complexity of the structure. Therefore, the presetting system proposed in this study was used to preset the wedges onsite. On the bridge, the anchors were completely isolated from the air to prevent galvanic corrosion. The effectiveness of the proposed anchor in reducing the stresses in the bridge angles was demonstrated through short-term onsite measurements. In addition, the long-term performance of the anchor, i.e., the loss in the CFRP rod prestressing resulting from anchorage component slippage has been monitored using a wireless sensor network system since the anchors were installed in February 2020. No reduction in the prestressing level has

yet been identified. More information about the application of prestressed CFRP rods for bridge strengthening can be found in [39].

2.2.6. Summary and conclusions

In this study, a mechanical wedge–barrel anchor consisting of a steel barrel and three split aluminium wedges was introduced. The proposed anchor took the advantages of existing mechanical wedge–barrel anchors: (i) a curved conical profile for both the wedge and barrel to achieve a proper contact pressure distribution on the CFRP rod and (ii) aluminium wedges to eliminate the need for sleeves and reduce the required presetting force. For the first time, the European standard test procedures for mechanical PT anchorages were used to examine the static and fatigue performance of the anchorage. The conclusions regarding the performance of the anchor are summarised as follows:

- The uniaxial static tensile tests showed that the failure mode was always the rupture of the CFRP, with an average tensile strength of 2371.4 MPa, which is approximately 16% greater than the guaranteed value of 2047 MPa.
- In the fatigue tests, the CFRP rods did not rupture up to the minimum of 2 million cycles. However, for some of the anchors, progressive slippage occurred between the wedges and CFRP rods, which revealed the importance of the wedge seating distance before pulling the CFRP rod.
- A new displacement-controlled presetting system was developed to ensure an adequate wedge seating distance. The wedges could be preset to a specific distance using this system, regardless of the lubrication condition between the wedges and barrel.
- The developed anchorage was not sensitive to the loading frequency. No noticeable slippage or temperature rise occurred in the anchorage components under loading frequencies between 5 and 23 Hz.
- The residual tensile capacity of the system at the end of the fatigue tests was greater than the guaranteed tensile strength of the CFRP rods, with a maximum residual strength of 2566 MPa. This indicated that no significant fatigue damage accumulated in the anchors during the cyclic loading.

Appendix I. FE model development

An FE model was developed for the wedge–barrel anchor using the ABAQUS FEM software

to optimise the contact pressure on the CFRP rod. The FE model shown in Fig. 15(a) is briefly described here. Only one-third of the anchor was modelled (i.e., one wedge) due to its symmetry, as shown in Fig. 15(a). In the FE analysis, the components were modelled as 3D eight-node quadratic solid elements. The wedge and barrel were modelled as an isotropic material, and the CFRP rod was modelled as an orthotropic material. The plastic behaviour of the aluminium wedge was considered, while the other parts (i.e., the barrel and rod) exhibited linear elastic behaviours. In the normal direction, hard contact was used to prevent the parts from penetrating each other. Tangential contact was considered using a penalty function formulation.

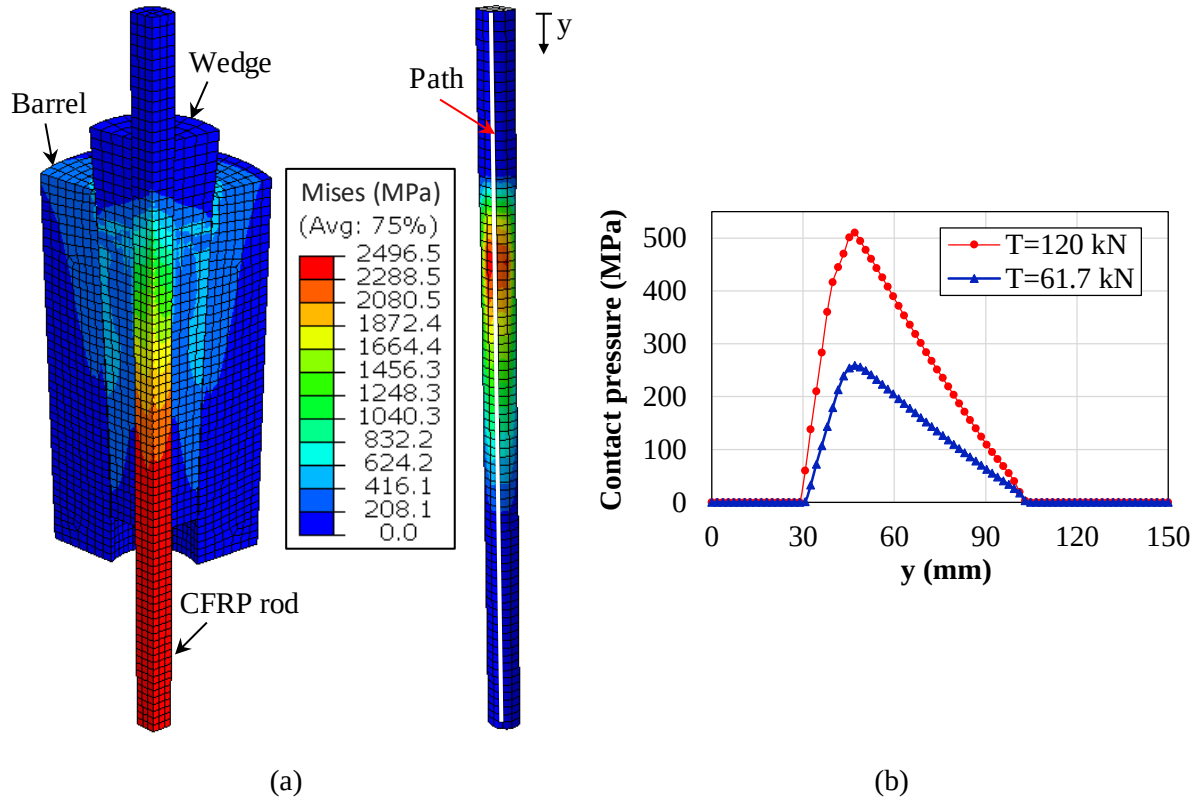

(a) (b)

Fig. 15. FE model of the split-wedge–barrel anchor: (a) von Mises stress distribution under the tensile load of T=120 kN; (b) Contact pressure on the CFRP rod.

The contact pressure on the CFRP rod on the path shown in Fig. 15(a) is shown in Fig. 15(b) for CFRP tensile loads of 61.7 and 120 kN. Fig. 15(b) shows that the contact pressure gradually increased from its minimum value at the loading end, which is the desired distribution to avoid stress concentration. Furthermore, due to the greater CFRP tensile load of T=120 kN, the wedges inserted further into the barrel, and consequently, the maximum contact pressure on the rod was nearly twice that when T=61.7 kN.

Appendix II. Modifications on the split-wedge anchor

Fig. 16(a) shows the fillets on the wedges, with the radii of 0.2 and 1 mm, to prevent the damage of the fibres. In addition, a 1-mm gap (instead of 1.5 mm gap in the initial design) was used between the wedges. For the barrel, as shown in Fig. 16(b), a fillet with a radius of 1 mm was applied at the free end to facilitate the insertion of the wedges.

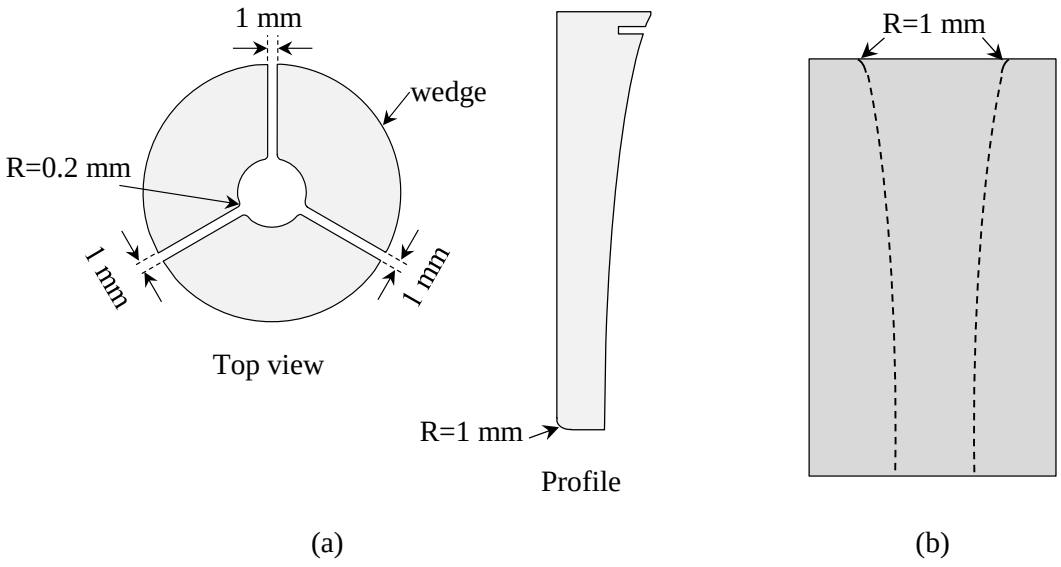

Fig. 16. Modifications on the split-wedge anchors (a) Wedges; (b) Barrel.

Appendix III. Resulting presetting force by the new presetting system

The correlation between the applied torque to each of the six M8, 8.8 bolts and the resulting presetting force applied to the wedges was obtained by measuring the presetting force using a KMR 200 kN load cell (HBM, AG, Darmstadt, Hesse, Germany), as shown in Fig. 17(a). The load cell was located on top of the wedges.

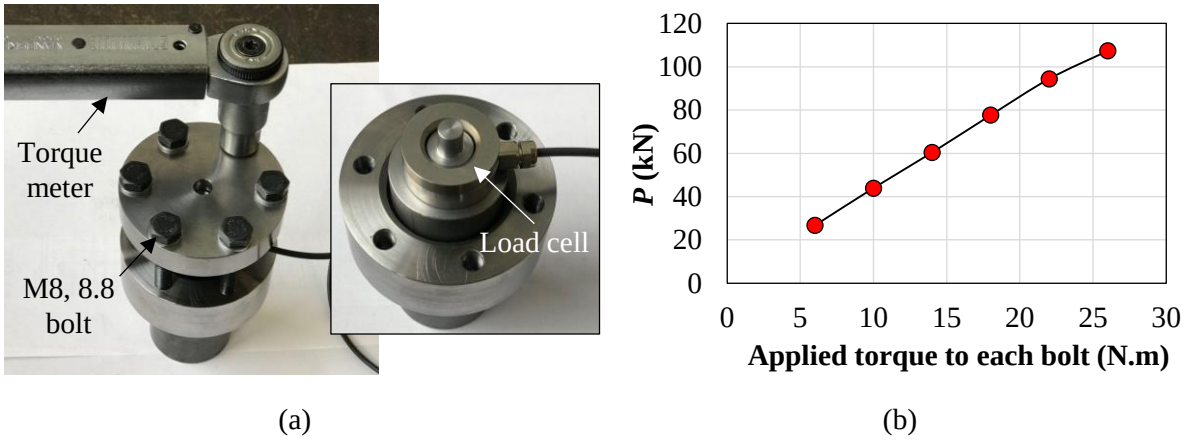

Fig. 17. (a) Measuring the presetting force using a 200 kN load-cell; (b) Measured presetting force versus the applied torque to each bolt.

The measured presetting force versus the applied torque to each bolt is plotted in Fig. 17(b). As shown in the figure, there is a nearly linear relationship between the applied torque to each bolt and the resulting presetting force. In addition, application of a standard torque of 27 N.m. to each bolt resulted in a presetting force of approximately 110 kN.

Data Availability Statement

All data and models from the experimental results and FE models that support the findings of this study are available from the corresponding author upon reasonable request.

Acknowledgement

The authors acknowledge the Innosuisse Swiss Innovation Agency (Grant ID: 19240.1 PFIW-IW) for funding this research project. The authors would also like to acknowledge the financial and technical support from the project partners, namely: S&P Clever Reinforcement Company AG, Switzerland; the Swiss Federal Railways (SBB) AG, Bern; and dsp Ingenieure + Planer AG Engineering Office, Uster, Switzerland.

References

1. Zhao XL. FRP-Strengthened Metallic Structures. 2013, Boca Raton, FL: Taylor and Francis.
2. Schmidt JW, Bennitz A, Täljsten B, Goltermann P, Pedersen H. Mechanical anchorage of FRP tendons–A literature review. Construction and Building Materials 2012;32110-121. https://doi.org/10.1016/j.conbuildmat.2011.11.049
3. Michels J, Sena-Cruz J, Czaderski C, Motavalli M. Structural strengthening with prestressed CFRP strips with gradient anchorage. Journal of Composites for Construction 2013;17(5)651-661. https://doi.org/10.1061/(ASCE)CC.1943-5614.0000372
4. Li C, Xian G. Novel wedge-shaped bond anchorage system for pultruded CFRP plates. Materials and Structures 2018;51(6)162. https://doi.org/10.1617/s11527-018-1293-x
5. Li C, Xian G. Design optimization and experimental validation of a novel wedge-shaped bond anchorage system for prestressed CFRP plates. Polymer Testing 2019;75167-174. https://doi.org/10.1016/j.polymertesting.2019.02.001
6. Ghafoori E, Motavalli M. Innovative CFRP-Prestressing System for Strengthening Metallic Structures. Journal of Composites for Construction 2015;19(6)04015006. https://doi.org/10.1061/(ASCE)CC.1943-5614.0000559. http://www.scopus.com/inward/record.url?eid=2-s2.0-84939204537&partnerID=40&md5=3422ce7a81b87ad1b00e68ab9a965d3e.
7. Hosseini A, Ghafoori E, Motavalli M, Nussbaumer A, Zhao XL, Al-Mahaidi R. Flat Prestressed Unbonded Retrofit System for Strengthening of Existing Metallic I-Girders. Composites Part B 2018;155156-172. https://doi.org/10.1016/j.compositesb.2018.08.026
8. Ghafoori E, Motavalli M, Nussbaumer A, Herwig A, Prinz G, Fontana M. Design criterion for fatigue strengthening of riveted beams in a 120-year-old railway metallic bridge using pre-stressed CFRP plates. Composites Part B: Engineering 2015;681-13. https://doi.org/10.1016/j.compositesb.2014.08.026
9. Ghafoori E, Hosseini A, Al-Mahaidi R, Zhao X-L, Motavalli M. Prestressed CFRP-strengthening and long-term wireless monitoring of an old roadway metallic bridge. Engineering Structures 2018;176585-605. https://doi.org/10.1016/j.engstruct.2018.09.042. http://www.sciencedirect.com/science/article/pii/S0141029618320224.

10. Hosseini A, Ghafoori E, Al-Mahaidi R, Zhao X-L, Motavalli M. Strengthening of a 19th-century roadway metallic bridge using nonprestressed bonded and prestressed unbonded CFRP plates. Construction and Building Materials 2019;209240-259. https://doi.org/10.1016/j.conbuildmat.2019.03.095
11. Mohee FM, Al-Mayah A. Development of an innovative prestressing CFRP plate anchor: numerical modelling and parametric study. Composite Structures 2017;1771-12. https://doi.org/10.1016/j.compstruct.2016.12.039
12. Mohee FM, Al-Mayah A. Effect of barrel, wedge material and thickness on composite plate anchor performance through analytical, finite element, experimental and 3D prototype investigations. Engineering Structures 2018;175138-154. https://doi.org/10.1016/j.engstruct.2018.08.003
13. Mohee FM, Al-Mayah A, Plumtree A. Anchors for CFRP plates: State-of-the-art review and future potential. Composites Part B: Engineering 2016;90432-442. https://doi.org/10.1016/j.compositesb.2016.01.011
14. Meier U. Extending the life of cables by the use of carbon fibers. in: Proc., International Association for Bridge and Structural Engineering Symp. 1995.
15. Meier U. Carbon fiber reinforced polymer cables: Why? Why not? What if? Arabian Journal for Science and Engineering 2012;37(2)399-411. https://doi.org/10.1007/s13369-012-0185-6
16. Arnautov A, Terrasi G, Kulakov V, Portnov G. Fastening of a High-Strength Composite rod with a Splitted and Wedged end in a Potted Anchor 1. Experimental Investigation. Mechanics of composite materials 2014;49(6)595-604. https://doi.org/10.1007/s11029-013-9376-9
17. Li C, Guo R, Xian G, Li H. Innovative compound-type anchorage system for a large-diameter pultruded carbon/glass hybrid rod for bridge cable. Materials and Structures 2020;53(4)1-15. https://doi.org/10.1617/s11527-020-01510-y
18. Kerstens J, Bennenk W, Camp J. Prestressing with carbon composite rods: a numerical method for developing reusable prestressing systems. ACI Structural Journal 1998;9543-50. 10.14359/525
19. Sayed-Ahmed EY. Single-and multi-strand steel anchorage systems for CFRP tendons/stays. in: Proceedings, Annual Conference-Canadian Society for Civil Engineering. 2002.
20. Sayed-Ahmed EY, Shrive NG. A new steel anchorage system for post-tensioning applications using carbon fibre reinforced plastic tendons. Canadian Journal of Civil Engineering 1998;25(1)113-127. https://doi.org/10.1139/l97-054
21. Terrasi GP, Affolter C, Barbezat M. Numerical optimization of a compact and reusable pretensioning anchorage system for CFRP tendons. Journal of composites for construction 2011;15(2)126-135. https://doi.org/10.1061/(ASCE)CC.1943-5614.0000080
22. Schmidt JW, Bennitz A, Täljsten B, Pedersen H. Development of mechanical anchor for CFRP tendons using integrated sleeve. Journal of Composites for Construction 2010;14(4)397-405. https://doi.org/10.1061/(ASCE)CC.1943-5614.0000096
23. Schmidt JW, Smith ST, Täljsten B, Bennitz A, Goltermann P, Pedersen H. Numerical simulation and experimental validation of an integrated sleeve-wedge anchorage for CFRP rods. Journal of Composites for Construction 2011;15(3)284-292. https://doi.org/10.1061/(ASCE)CC.1943-5614.0000171
24. EOTA ETAG 013 Guideline for European Technical Approval of Post-Tensioning Kits for Prestressing of Structures. 2002, EOTA Brussels, Belgium.
25. fib IFfSC. Recommendations for the acceptance of post-tensioning systems 1993. Lausanne, Switzerland: fib.
26. Rostásy FS. Draft guidelines for the acceptance testing of FRP posttensioning tendons. Journal of Composites for Construction 1998;2(1)2-6. https://doi.org/10.1061/(ASCE)1090-0268(1998)2:1(2)
27. Al-Mayah A, Soudki K, Plumtree A. Development and assessment of a new CFRP rod–anchor system for prestressed concrete. Applied Composite Materials 2006;13(5)321-334. https://doi.org/10.1007/s10443-006-9019-6
28. Al-Mayah A, Soudki K, Plumtree A. Mechanical behavior of CFRP rod anchors under tensile loading. Journal of Composites for Construction 2001;5(2)128-135. doi:10.1061/(ASCE)1090-0268(2001)5:2(128)
29. PTI. Post-tensioning manual. 1985: Post-Tensioning Institute.
30. Campbell T, Shrive NG, Soudki K, Al-Mayah A, Keatley J, Reda M. Design and evaluation of a wedge-type anchor for fibre reinforced polymer tendons. Canadian Journal of Civil Engineering 2000;27(5)985-992. https://doi.org/10.1139/l00-048
31. Taha MMR, Shrive NG. New concrete anchors for carbon fiber-reinforced polymer post-tensioning tendons—Part 2: Development/experimental investigation. Structural Journal 2003;100(1)96-104. 10.14359/12443
32. Elrefai A, West JS, Soudki K. Performance of CFRP tendon–anchor assembly under fatigue loading. Composite structures 2007;80(3)352-360. https://doi.org/10.1016/j.compstruct.2006.05.023

33. Kar N, Hu Y, Barjasteh E, Nutt S. Tension–tension fatigue of hybrid composite rods. Composites Part B: Engineering 2012;43(5)2115-2124. https://doi.org/10.1016/j.compositesb.2012.03.006
34. Li C, Xian G, Li H. Tension-tension fatigue performance of a large-diameter pultruded carbon/glass hybrid rod. International Journal of Fatigue 2019;120141-149. https://doi.org/10.1016/j.ijfatigue.2018.11.007
35. Al-Mayah A, Soudki K, Plumtree A. Simplified anchor system for CFRP rods. Journal of Composites for Construction 2013;17(5)584-590. https://doi.org/10.1061/(ASCE)CC.1943-5614.0000367
36. DIN E 6892-1: 2017-02-Metallische Werkstoffe-Zugversuch-Teil 1: Prüfverfahren bei Raumtemperatur (ISO 6892-1: 2016); Deutsche Fassung EN ISO 6892-1: 2016. 2017, Beuth Verlag GmbH, Berlin. .
37. ASTM D/DM. Standard Test Method for Tensile Properties of Fiber Reinforced Polymer Matrix Composite Bars. ASTM International 2016;West Conshohocken, PA.
38. Baschnagel F, Härdi R, Triantafyllidis Z, Meier U, Terrasi GP. Fatigue and durability of laminated carbon fibre reinforced polymer straps for bridge suspenders. Polymers 2018;10(2)169.
39. Heydarinouri H, Nussbaumer A, Motavalli M, Ghafoori E. Strengthening of Steel Connections in a 92-Year-Old Railway Bridge Using Prestressed CFRP Rods: Multiaxial Fatigue Design Criterion. Journal of Bridge Engineering 2021;26(6)04021023.
40. Heydarinouri H, Motavalli M, Nussbaumer A, Ghafoori E. Development of Mechanical Strengthening System for Bridge Connections Using Prestressed CFRP Rods. Journal of Structural Engineering 2021;147(3)04020351.

2.3. Development of mechanical strengthening system for bridge connections using prestressed CFRP rods*

Abstract

Stringer-to-floor beam web-to-web double-angle connections are among the most fatigue-prone elements in old riveted bridges. These connections are often designed to carry only shear loads. However, in these elements, fatigue damage occurs because of the out-of-plane deformation of the connections, which is ignored in the original design. In this study, a new retrofitting system is developed to reduce the out-of-plane deformation of the connections using prestressed carbon fiber reinforced polymer (CFRP) rods. The proposed system consists of a mechanical wedge-barrel anchor to hold the prestressed CFRP rod and a clamping system to attach to the parent structure and to transmit forces via friction. A series of finite element (FE) simulations was conducted to optimize the size and performance of the retrofit system. Laboratory static pull-off tests were conducted and different failure modes were studied and discussed. A novel test set-up (with four supports) was designed for testing the steel connections. The effect of the geometrical imperfections during the installation of the connection was carefully investigated using the FE models and was verified through the laboratory tests. Laboratory fatigue tests were conducted on steel connections with the same dimensions as those in a railway bridge. The designed retrofit system was found to be capable of reducing the stresses at the angle connections by more than 40%. The results of the fatigue tests demonstrated that the designed system could survive more than 11 million load cycles without any fatigue damage or any indication of a loss in the CFRP prestressing level.

Keywords: Bridge connections, Carbon fiber-reinforced polymer (CFRP), Finite element (FE), Post-tensioned CFRP tendons, Strengthening, Wedge-barrel anchor.

2.3.1. Introduction

Fatigue is a major problem in aging steel bridges in Europe. This problem is further exacerbated in old steel bridges, which are approaching the end of their originally designed fatigue lives [1]. Most of the old metallic bridges in Europe are riveted bridges. In these bridges, the stringer-to-floor-beam double angle web-to-web connections are one of the most common fatigue prone

* Hossein Heydarinouri, Masoud Motavalli, Alain Nussbaumer, Elyas Ghafoori. Journal of Structural Engineering 2021; 147(3)04020351. https://doi.org/10.1061/(ASCE)ST.1943-541X.0002923

details [2].

Out-of-plane deformation of the angles is the primary reason for the fatigue problem in this type of connections [3-5]. The out-of-plane deformation results from the application of the loads on the stringers, leading to secondary deformation-induced tensile stresses in the connections. In the past, this effect was not considered in the design; therefore, the engineers would design the connections to carry only shear loads. Owing to the out-of-plane deformation, the fatigue failure can occur either in the angle (near the fillet) or in the rivets (popping out of the rivet head) [6]. The out-of-plane deformation due to the superimposed loads on the stringers, as well as the potential failure locations in the connections, are schematically illustrated in Fig. 1(a).

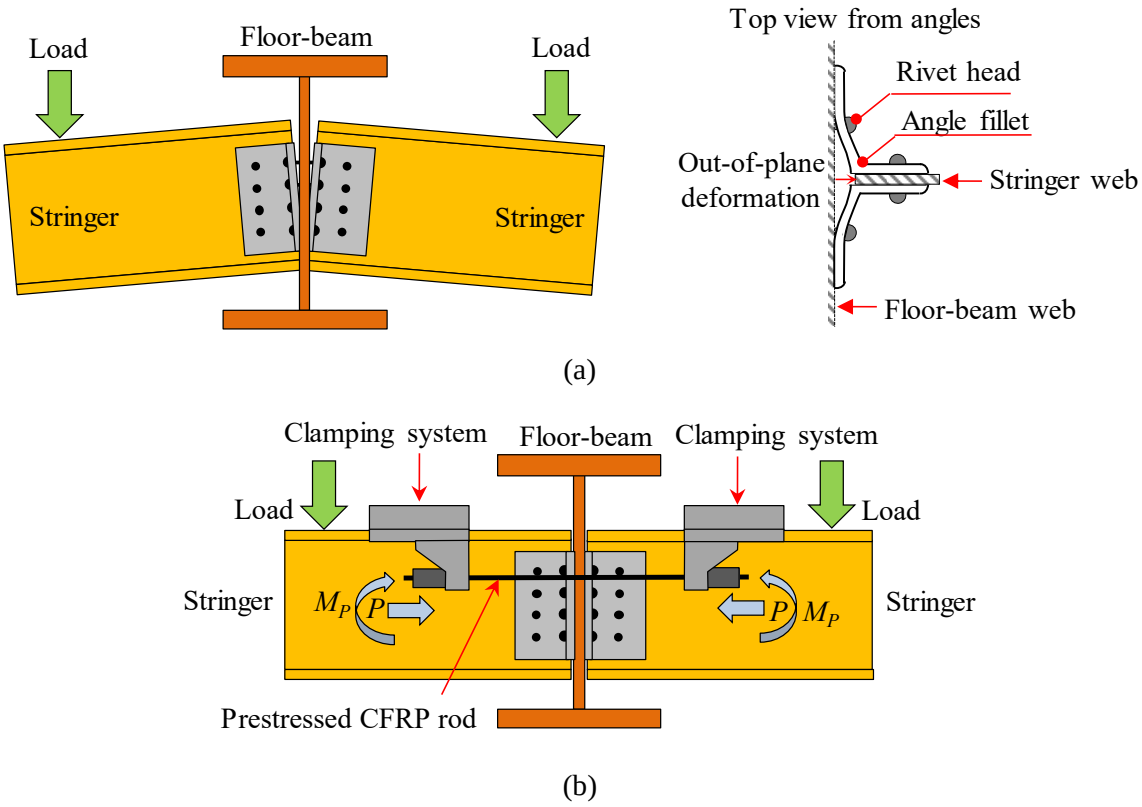

Fig. 1. Out-of-plane deformation in stringer-to-floor-beam connections: (a) out-of-plane deformation due to superimposed load on the stringers and the potential failure locations in the connections; and (b) concept of the proposed strengthening system to reduce out-of-plane deformation.

The replacement of the bridges to address the fatigue related failures of the bridges is rarely a preferred solution for the owners of the bridges. Therefore, they always look for effective and sustainable strengthening solutions. Until now, many different strengthening techniques have been proposed for the prolongation of the fatigue life of riveted structures, such as replacement of rivets with high-strength bolts [6-8], using stop holes and welding additional elements [9], and softening connections by removing some rivets [10]. The drawback of these strengthening

solutions is that they are not capable of permanently addressing the problem — when these solutions were tried, the fatigue cracks have either reinitiated after a certain number of cycles or have initiated from another location (see [11]).

New materials, such as carbon fiber reinforced polymers (CFRP) have been used for strengthening metallic structures as non-prestressed bonded retrofitting systems [12-16] owing to their superior fatigue and corrosion resistance and light weight compared to steel [17]. However, in several cases, bonded systems cannot be applied on the surface of riveted members.

Recently, prestressed unbonded reinforcement (PUR) systems have been developed for strengthening bridge structures [18, 19]. Different configurations of the PUR systems, i.e., trapezoidal PUR (TPUR), flat PUR (FPUR), contact PUR (CPUR), and triangle PUR (TrPUR) have been designed, and their performances have been examined numerically and analytically [20]. Such systems consist of mechanical clamps holding prestressed CFRP plates and working purely through friction. The PUR systems can be used for strengthening steel beams against flexural [21], buckling [22], and fatigue [23] loading. These systems were successfully used for strengthening old steel bridge girders in Switzerland [24] and Australia [25, 26]. More recently, a series of PUR systems has been developed for strengthening steel plates [27, 28]. The PUR concept has also been used with shape memory alloy (SMA) plates (instead of CFRP plates). SMAs are a new class of structural materials that can be prestressed through an activation process that includes heating and cooling [29]. The SMA-based PUR systems have been using for strengthening steel plates [30, 31], girders [32, 33] and connections [34].

2.3.1.1. Research significance

Nearly all the aforementioned retrofitting solutions are applicable only to steel girders and plates, and not to the connections. For stringer-to-floor beam double angle connections, finding an effective strengthening solution is a considerable challenge owing to a lack of space, as well as additional complexity of the geometry in these details. Hence, sufficient research has not been conducted on the strengthening of bridge connections (unlike in the case of bridge girders). In fact, in such design elements, the existence of floor-beams and other elements, such as sleepers renders the application of CFRP plates almost impossible. For similar reasons, the system proposed in [34], in which prestressed SMA plates were used for strengthening stringer-to-floor-beam double angle connections, may not be applicable in real structures, although its performance was proven through laboratory tests.

Considering the aforementioned issues, this study, for the first time, proposes the application

of prestressed CFRP rods for strengthening bridge connections. Thus far, different mechanical anchorages have been developed for post-tensioned CFRP rods [35-42]. In these studies, the proposed mechanical anchorages consisted of a barrel with a conical hole inside, and split or integrated wedges holding the CFRP rod. Such anchors have been already used for externally prestressed concrete beams [43]. These mechanical anchors hold the CFRP rod through friction, without requiring any adhesive, thus increasing their versatility for on-site applications compared to bonded systems, an example of which was proposed in [44].

In this study, a novel mechanical strengthening system using prestressed CFRP rod is proposed. The proposed strengthening system in this study is a combination of the clamping system proposed in [45, 46] and the idea of using a CFRP rod as a prestressing element. In previous PUR systems, two symmetric prestressed CFRP elements are required. However, the proposed system operates with unsymmetrical prestressed CFRP elements; this feature increases its versatility and adaptability for applications to various types of structures.

A conceptual representation of the proposed strengthening system is illustrated in Fig. 1(b). Here, the out-of-plane deformation of the angles is reduced, i.e., the prestressed CFRP rods apply a compressive load P on both sides of the stringers. In addition, the prestressing force applies a sagging moment, M_P, opposing the out-of-plane deformation of the angles, which results in a reduction in the secondary stresses in the angles.

Furthermore, the proposed system uses a novel wedge-barrel anchor component, which was developed at the Structural Engineering Research Laboratory at Empa, Switzerland. This study mainly focuses on the behavior of the entire clamping system; however, a brief description of the developed wedge-barrel anchor and the main experimental results are also presented here.

In addition, one of the main challenges in the existing wedge-barrel anchors is the requirement of a high presetting force; in other words, before pulling the CFRP rod, to increase the contact pressure around the CFRP rod, the wedges have to be pushed (preset) into the barrel. Otherwise, when pulled, the CFRP rod would slip inside the wedges. In this study, a new presetting system for on-site application of high forces is developed, which obviates the need for using hydraulic jacks.

2.3.1.2. Outline of the study

This paper outlines the introduction of a new retrofitting system concept. The results from static pull-off tests are presented and discussed. Thereafter, a finite element (FE) model, developed for designing the clamping system, is presented. Then, the fatigue performance of the proposed

strengthening system is investigated. The effectiveness of the proposed system in reducing the stresses in the connections is numerically and experimentally investigated. Finally, the application of the proposed strengthening system on an old riveted railway bridge in Switzerland is briefly described.

2.3.2. Introduction to the strengthening system

2.3.2.1. Description of the clamping system

The configuration of the proposed strengthening system is shown in Fig. 2(a). It consists of two main components, the mechanical wedge-barrel anchor and the clamping system, as shown in the figure. The wedge-barrel anchor holds the prestressed CFRP rod, and the clamping system grabs the top flange of the stringer and transmits the CFRP prestressing force to the stringer through friction.

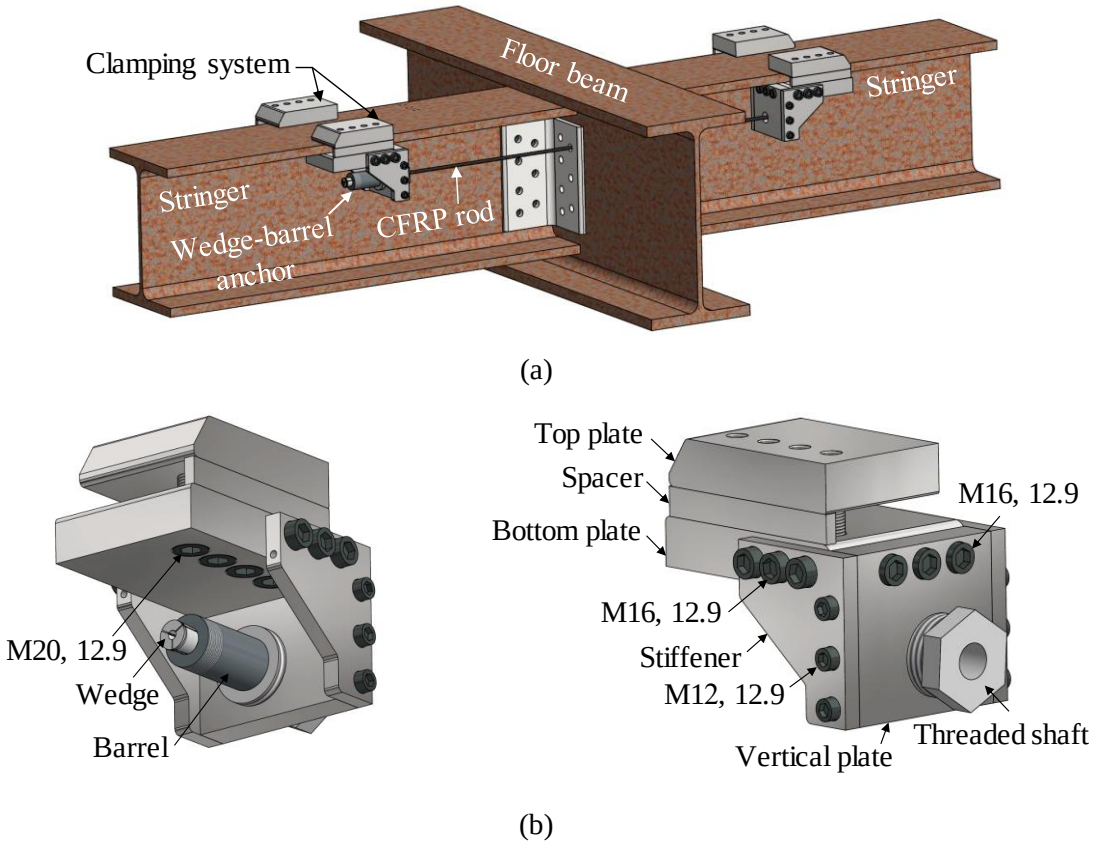

Fig. 2. Proposed strengthening system for double-angle stringer-to-floor-beam connections: (a) configuration of the proposed strengthening system; and (b) different parts of the strengthening system.

The two aforementioned components consist of different parts, as shown in Fig. 2(b). The wedge-barrel anchor consists of a barrel with a conical hole inside and three separate aluminum wedges, which are in direct contact with the CFRP rod. The clamping system is assembled from

different plates, which are bolted to each other. For assembling the clamping system, first, the bottom plate, the vertical plate, and the two stiffeners are bolted to each other. The bolts are M16, 12.9 and M12, 12.9 , with clamping forces of 135 and 72 kN, respectively. The spacer is also bolted to the bottom plate using two M4 bolts, which fix the spacer in the position. Next, the top plate is placed on top of the beam top flange, and then the top and bottom plates are connected to each other using four M20, 12.9 bolts. A total compressive force of 484 kN is applied to the top flange by these bolts to prevent the clamping system from slipping through friction. Thus, through the wedge-barrel anchor, the prestressing force of the CFRP rod is transmitted to the clamping system by a threaded hollow shaft in the vertical plate. All the plates in the clamping system are made of M200 high-strength steel with a nominal yield strength of approximately 1000 MPa. The details of the dimensions of the clamping system components are given in the Appendix I.

As mentioned before, in the PUR system proposed by [45, 46], prestressed CFRP plates were used for strengthening the girders. However, the presence of floor-beams, together with sleepers resting on the stringers rendered it impossible to use CFRP plates. Instead, in this study, a prestressed CFRP rod is used. Here, the CFRP rod passes through a rivet/bolt hole, as shown in Fig. 2(a), and requires removal of the rivets/bolt prior to strengthening. It is noted that the rivets/bolts are removed from the second row of the rivets/bolts (see Fig. 2(a)) and their absence does not affect the out-of-plane deformation of the connections [47, 48]. In addition, hollow high-strength bolts are placed and fastened, as a replacement for the removed rivets/bolts. The CFRP rods then pass through the hollow bolts. The main aim of using hollow bolts is to prevent corrosion inside the opening hole caused by the removal of the rivet/bolt.

2.3.2.2. Installation procedure

The strengthening system is installed in two stages: presetting and prestressing. These two stages are described in the following sections.

2.3.2.2.1. Presetting procedure

In the proposed strengthening system, presetting is performed as shown in Fig. 3(a) to (c). The parts required for presetting are shown in Fig. 3(a). The presetting steps are outlined as follows: Once the clamping system is fixed, the CFRP rod passes the threaded hollow shaft, and the barrel and the wedges are placed around it. Then, the presetting shaft, which has a specific length, is placed around the wedges on the barrel. At the free end of the barrel, there is a threaded region, which allows the placement of the presetting ring around the barrel, as shown in Fig.

3(a) and b. Then, the presetting plate is placed on the wedges, and six M8 presetting bolts pass through the presetting plate and the threaded holes of the presetting ring. Before the presetting bolts are fastened, a gap exists between the presetting plate and the presetting shaft, as shown in Fig. 3(b). By fastening the bolts, the presetting plate pushes the wedges into the barrel. The bolts are fastened until the prestressing plate touches the presetting shaft; at this point, the presetting is completed. With the six M8, 8.8 bolts, it is possible to apply a total force of approximately 110 kN. The length of the presetting shaft was determined based on the tests to ensure that when the shaft touches the presetting plate, adequate presetting force is applied to the wedges.

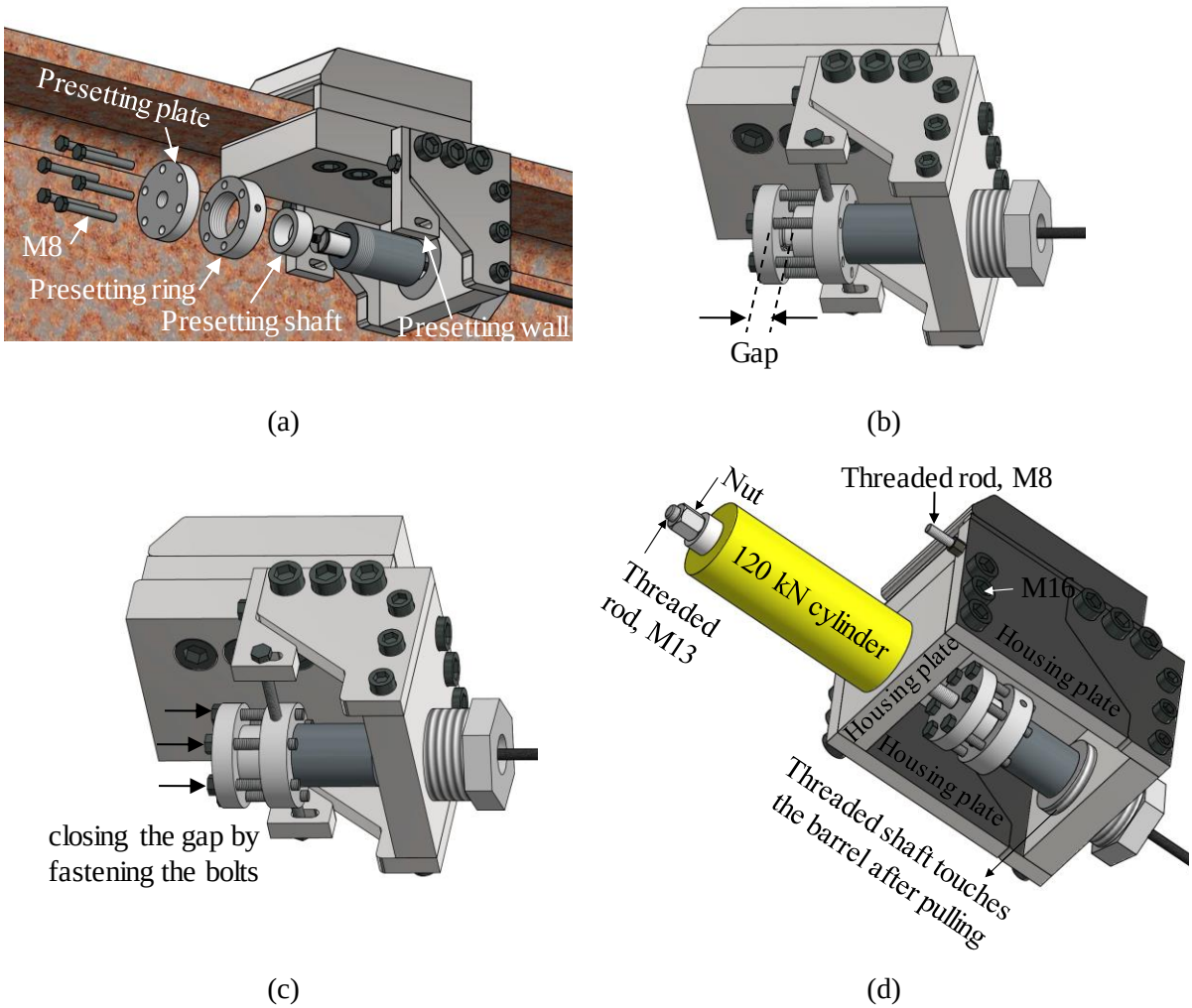

Fig. 3. Presetting and prestressing procedures: (a) required parts for presetting; (b) Before fastening the presetting bolts; (c) after fastening the presetting bolts; and (d) prestressing procedure.

It is important to note that in the proposed system, the CFRP rod has to, first, pass through a small hole (rivet or bolt hole) in the floor beam, and then, it should be clamped on the other side as shown in Fig. 2(a). Thus, it is not possible to carry out the presetting procedure for both

active and dead anchors in advance using hydraulic jacks; i.e., only one anchor can be prepared beforehand and the other one has to be preset on-site.

In addition, to prevent the rotation of the wedge-barrel anchor during the fastening of the presetting bolts, two presetting walls are connected to the stiffeners. Next, the two stiffeners are connected to the prestressing ring using two M8 bolts, as illustrated in Fig. 3(b) and c. Once the presetting is completed, the presetting walls are removed; however, the other parts used for presetting are kept in place to be used later for prestressing the rod.

2.3.2.2.2. Prestressing procedure

After the wedges are preset, the CFRP rod is ready to be pulled. To apply the prestressing force, a temporary housing is used, as shown in Fig. 3(d). The housing consists of three plates connected to each other by M16, 12.9 bolts. Further details regarding the housing components are shown in the Appendix I. The housing is fixed on the clamping system using two M8 threaded rods. Next, a high-strength M13 threaded rod is inserted into the threaded hole embedded in the presetting plate. The tensile strength of this rod is 150 kN.

In the final step, a 120-kN hydraulic cylinder provides the pulling force (see Fig. 3(d)) for the prestressing procedure. When the CFRP rod is pulled, the barrel moves away from the surface of the threaded shaft. Once the required prestressing force is reached, the threaded shaft is rotated until it touches the back of the barrel. At this stage, the system is fixed; the oil pressure in the hydraulic cylinder is released; and the housing and the plates required for presetting and prestressing are removed.

2.3.2.3. Dismantling procedure

To disassemble the system, the same procedure as shown in Fig. 3(d) can be followed. In the first step, a pulling force slightly higher than the existing prestressing force in the CFRP is provided by the hydraulic cylinder. Thus, the barrel becomes separated from the threaded shaft; therefore, it is possible to take the shaft out (away from the barrel). Finally, the oil pressure in the hydraulic cylinder is released; consequently, the CFRP prestressing force is removed. To ensure practicality, before the application of the pulling load by the cylinder, the cylinder should have an adequate displacement capacity to release all the oil pressure.

2.3.2.4. Advantages of the proposed retrofit system

Most existing solutions for strengthening bridges have been designed for bridge girders rather than for connections. Strengthening of connections is often difficult owing to issues, such as

the need for removal of the decks, lack of space, and geometric complexities. There are two main differences between the system proposed in this study and the previously developed PUR systems. Firstly, an unsymmetrical clamp was proposed, which provides increased freedom and versatility for the application in different structures with edges, while the previous PUR systems have utilized CFRP plates symmetrically placed in the clamping system. Secondly, unlike the previous PUR systems for CFRP plates, the PUR system developed in this study uses CFRP rods, as they can be easily passed through the connection by removing bolts/rivets.

One of the main advantages of the proposed strengthening concept for bridge connections is that it works only by accessing the system from the lower space of the bridge (i.e., flooring system) without requiring the removal of the bridge deck. Therefore, it minimizes the interventions, i.e., no bridge closure, no interruptions for the traffic on the bridge, and no holes to be drilled in the parent structure. Finally, the proposed system can also be considered, in some cases, for other types of connections, such as welded connections.

2.3.3. Static and fatigue tests on wedge-barrel anchors

One of the key components of the proposed strengthening system is the wedge-barrel anchor that holds the CFRP rod. A new, purely mechanical wedge-barrel anchor was developed in Empa, Switzerland for this purpose. To ensure that the anchor performs reliably under both static and fatigue loadings, a series of tests was conducted according to European Technical Approval Guidelines ETAG 013 [49], the International Federation for Structural Concrete (fib) recommendation for posttensioning systems [50]; and the draft guideline for the acceptance testing of FRP posttensioning tendons [51].

The test set-up used for the uniaxial tensile static and fatigue tests on the wedge-barrel anchors with a CFRP rod having an 8-mm diameter is shown in Fig. 4(a), with a nominal tensile strength of 102.9 kN. A cover was used around the CFRP rod to limit the dispersion of the fibers after a rupture. The mechanical wedge-barrel anchor consists of a steel barrel in contact with three split aluminum wedges holding the CFRP rod. The components of the wedge-barrel anchor are shown in Fig. 4(b).

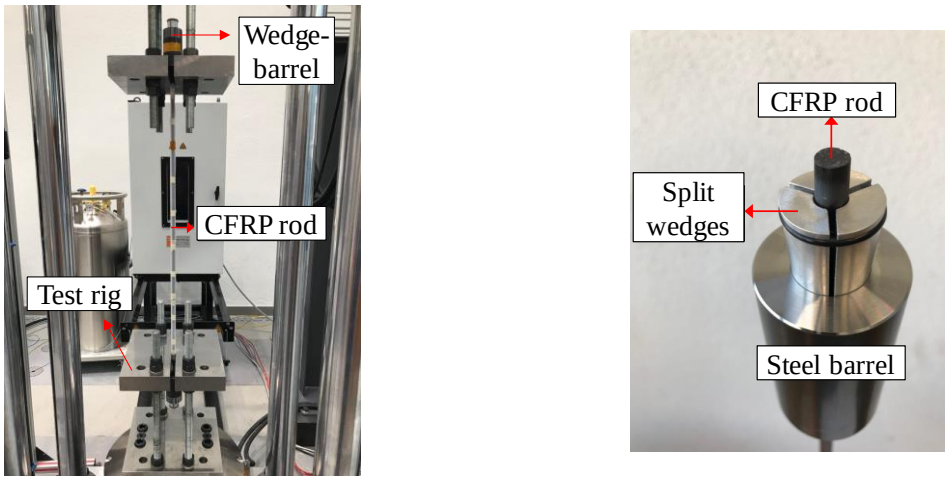

(a) (b)

Fig. 4. Wedge-barrel anchor developed at Empa: (a) the test set-up for uniaxial static and fatigue tests; and (b) components of the wedge-barrel anchor.

The experimental results indicate that the developed wedge-barrel satisfies all the requirements listed by the above-mentioned codes and recommendations. The results are summarized as follows:

The static tests indicate that the fracture of the CFRP rod was the failure mode and not the slippage of the CFRP rod inside the barrel. For each static test, the failure load of the post-tensioned system was higher than 95% of the nominal tensile strength of the CFRP rod. The average failure load was 119 kN (equivalent to approximately 2370 MPa for the CFRP rod with 8-mm diameter).

During the fatigue loading for 2 million cycles, no failure occurred either in the CFRP rod or in the anchor, and no slippage was observed between different components of the wedge-barrel. In addition, at the end of the fatigue test, a static test was carried out, which showed no reduction in the residual static strength of the anchor system, indicating that during the fatigue loading, no significant damage was accumulated in the anchors.

In addition, further verification of the anchor behavior with respect to slippage was carried out by increasing the loading frequency up to 23 Hz in the fatigue tests. All the tests confirmed that no slippage occurred in the anchorage system under fatigue loads. All subsequent tests described in the next sections confirmed this excellent behavior; i.e., the rods suffered neither slippage nor any significant damage in the wedge-barrel anchorage system.

2.3.4. Static pull-off tests

To experimentally investigate the static performance of the strengthening system, static pull-

off tests were performed in the test set-up shown in Fig. 5(a). In these tests, the goal was to obtain the failure load of the CFRP rod and the slippage load of the clamping system.

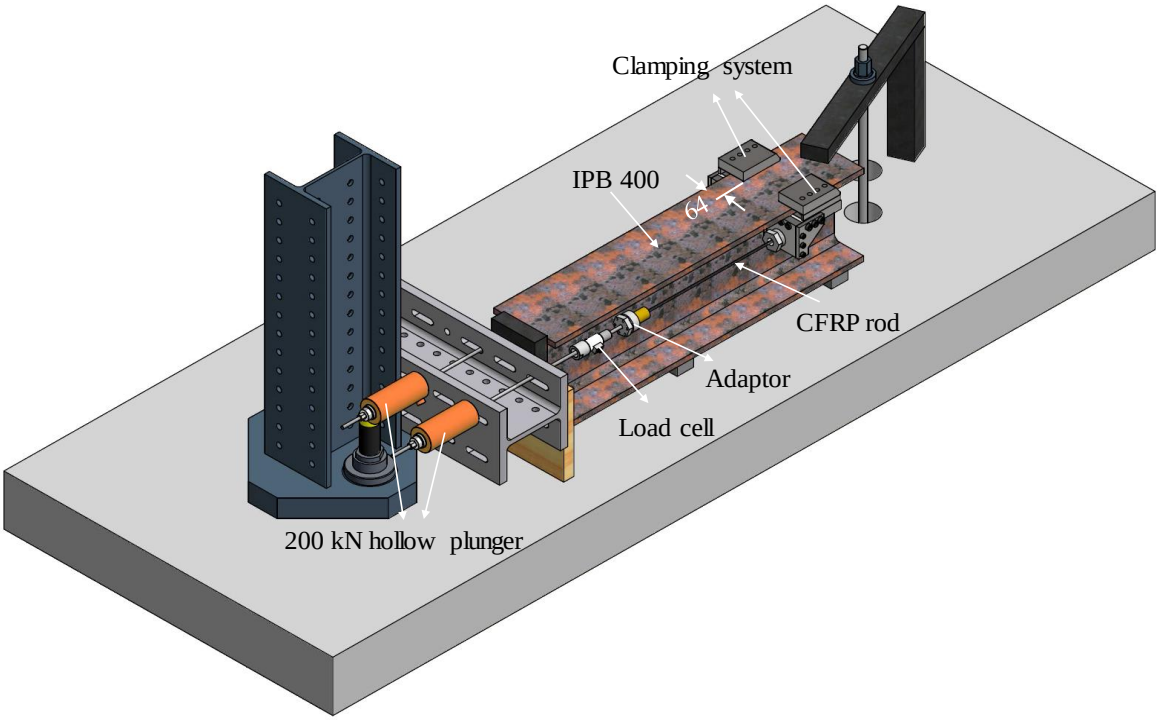

(a)

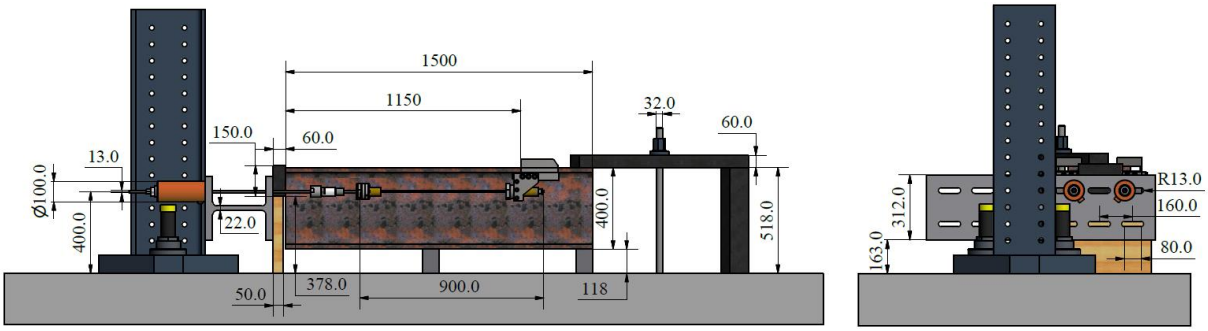

(b)

Fig. 5. Test set-up for the static pull-off tests: (a) main components of the set-up; and (b) details and dimensions of the components.

2.3.4.1. Test set-up and instrumentation

A clamping system was installed on either side of an IPB 400 beam. The geometrical dimensions (i.e., cross-section) of the beam used in the set-up were the same as those used in the Aabach Bridge, which is an old riveted railway bridge in Switzerland. The reason for this choice was that the retrofit system was designed for strengthening the connections of this bridge. The length of the beam was 1.5 m. The pulling force was applied using two 200-kN hydraulic cylinders, and the applied load was measured using a 150-kN load cell (HBM AG, Darmstadt,

Hesse, Germany) with an accuracy of 0.2 kN. The detailed dimensions of the set-up are provided in Fig. 5(b).

The unidirectional CFRP rod used in the pull-off tests was manufactured by S&P Clever Reinforcement Company AG, Switzerland, with a diameter of 8 mm. The nominal tensile strength (the guaranteed value) of the CFRP rod, F_u, was 102.9 kN (equivalent to 2047 MPa), with a fiber volume fraction of 65% and an elastic modulus of 160 GPa in the fiber direction.

The instrumentation used in the static pull-off test is shown in Fig. 6(a). When the CFRP rod was being pulled, a line laser model 2660-50 (MICRO-EPSILON, Dresden, Saxony, Germany) with a resolution of 4 μm was used to measure the displacement of different components of the wedge-barrel anchor, i.e., the CFRP rod, two of the wedges, and the barrel. In addition, the displacements of the top plates of the clamping system were measured using two linear variable differential transformers (LVDTs).

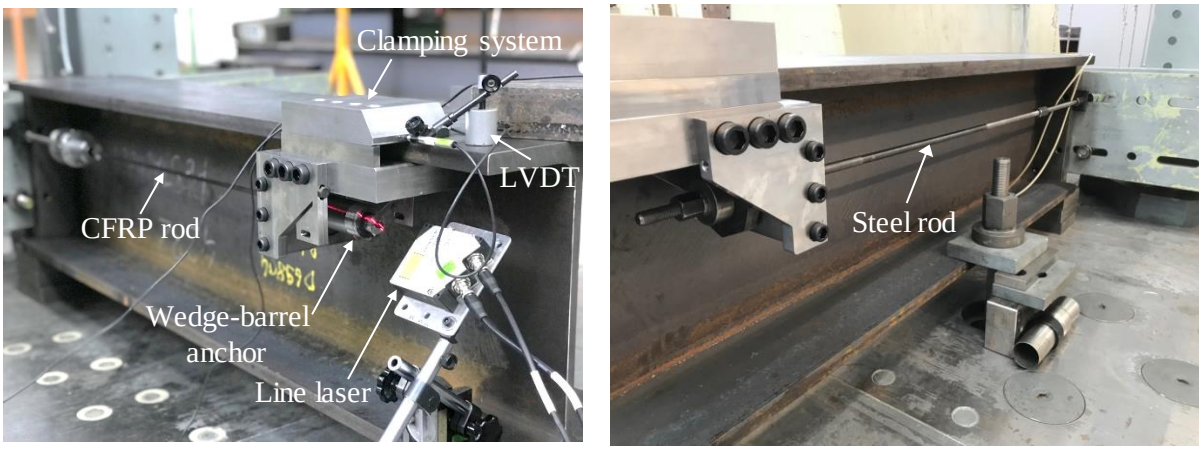

(a) (b)

Fig. 6. Details of the clamping system on each side of the beam: (a) clamping system on the left side; and (b) clamping system on the right side.

It should be noted that in these tests, the CFRP rod was used on only one side of the beam, while a high-strength steel rod (with a tensile strength of 150 kN) was used on the other side (see Fig. 6(b)). This would ensure that the beam would be symmetrically loaded, and, the failure would occur solely in the CFRP rod/anchorage. Thus, it would be possible to focus on the behavior of the anchor on the side with the CFRP rod, and to perform the measurements only on this side.

2.3.4.2. Results of the static pull-off tests

Based on the loading protocol proposed by the draft guidelines for the acceptance testing of

FRP post-tensioning tendons [51], the cylinder load was increased stepwise, as shown in Fig. 7(a). The applied cylinder load in the pull-off tests *P* is shown in Fig. 7(b), in which the oil pressure in the cylinder was kept constant for 5 min at steps A, B and C, and more than 1 h at step D. This loading protocol was proposed to ensure that the displacements in the wedge-barrel anchor were stabilized after 0.5 h at step D.

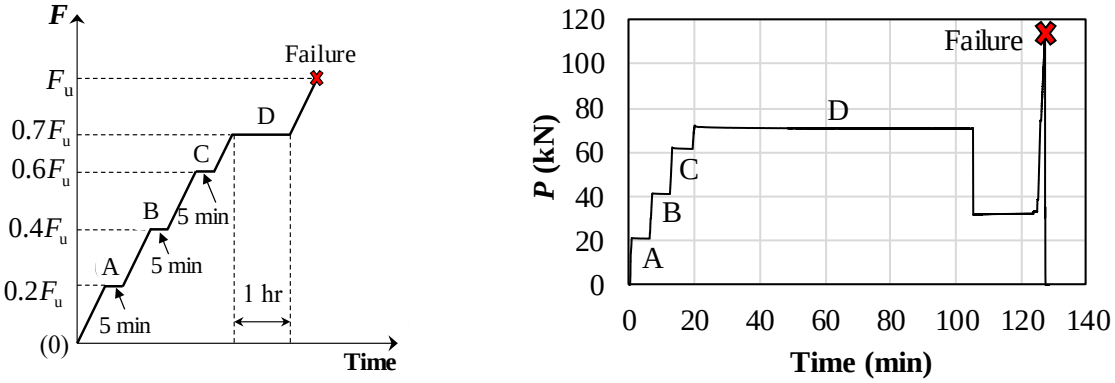

(a) (b)

Fig. 7. Loading protocol in the static pull-off tests: (a) protocol proposed in [51]; and (b) applied load in the pull-off tests.

The displacements of the wedge-barrel components were measured by the line laser during the load steps A to D, as illustrated in Fig. 8(a). As shown in the figure, for the duration of all the different steps, the displacements were quite stable indicating that there was no gradual slippage in the wedge-barrel anchors.

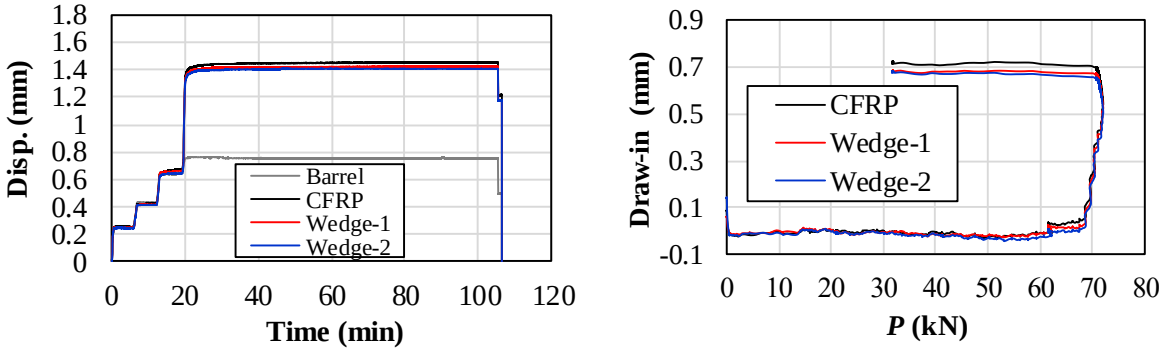

(a) (b)

Fig. 8. Measurements in the wedge-barrel anchor during the static pull-off tests: (a) displacement of the wedge-barrel components; and (b) draw-ins.

In addition, the relative displacement of the two wedges and the CFRP rod with respect to the barrel, called the draw-in, versus the applied load is plotted in Fig. 8(b). This figure shows that at the load levels slightly lower than 70 kN, the wedges and the CFRP started going into the

barrel simultaneously. It shows that there was no relative displacement between the CFRP rod and the wedges. This is the ideal behavior for the wedge-barrel anchors because when the wedges and the rod are inserted into the barrel simultaneously, the contact pressure around the rod increases, leading to an increase in the frictional resistance.

At the end of step D, the cylinder load was reduced (see Fig. 7(b)) to around 30 kN, and then, the line laser was removed to prevent the laser from being damaged at the failure load of the CFRP rod. Then, the CFRP was loaded up to failure. In total, four static pull-off tests were conducted. In one of the tests (Test no. 1), a strain gauge was applied on the CFRP rod. The measurement showed a linear stress–strain behavior, with an elastic modulus of 160 GPa, which was in good agreement with the value provided by the manufacturer.

The results of the four pull-off tests are summarized in Table 1, based on which it can be concluded that failure occurred in the CFRP rod. No slippage could be observed in the clamping system. The obtained failure load in all the tests was higher than the nominal failure load of the rods, which was equal to 102.9 kN (equivalent to 2047 MPa). The average failure load of the pull-off tests was equal to 110 kN (equivalent to 2188 MPa), which was only 9 kN lower than the average value obtained in the uniaxial tensile tests on the rods.

Table 1. Summary of the results of the static pull-off tests

Test no.	Ultimate CFRP force (kN)	Maximum CFRP stress (MPa)	Failure mode
1	104	2070	CFRP rupture
2	109	2168	CFRP rupture
3	112	2228	CFRP rupture
4	114	2268	CFRP rupture

It is worth mentioning that the force in the CFRP rod would tend to rotate the clamping system. The rotation of the clamping system and the consequent rotation of the barrel would apply bending stresses on the loading end of the wedge-barrel anchor, which could ultimately lead to a premature rupture in the CFRP rod. However, the high average failure load obtained in the pull-off tests shows that the clamping system was rigid enough to minimize the rotation. Therefore, it can be concluded that the failure load of the CFRP rods was only marginally affected. The displacement of the clamp, measured using the LVDTs, during the pulling of the CFRP rod and a failed sample (sample no. 4) are shown in in Fig. 9.

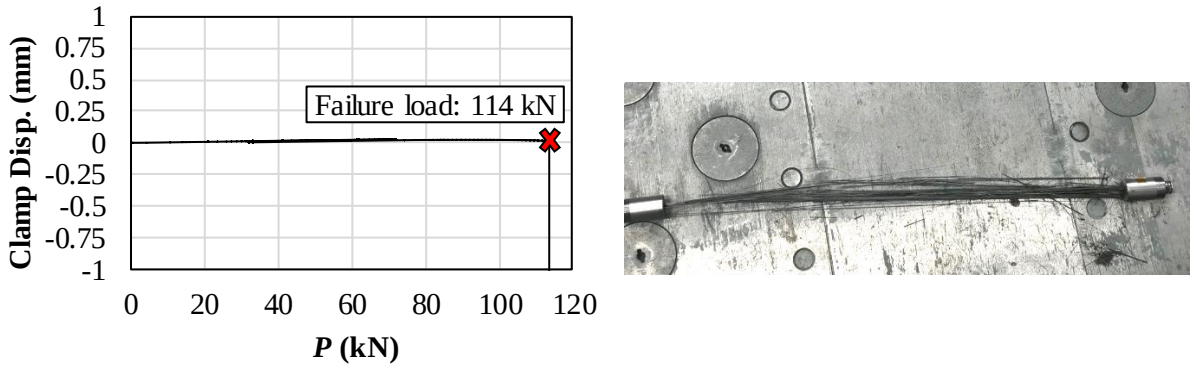

(a) (b)

Fig. 9. The experimental results from test no. 4: (a) load-displacement curve of the clamp; and (b) failed CFRP rod.

To obtain the slippage load of the clamping system, high-strength steel rods, as shown in Fig. 6(b), were used on both sides of the beam to ensure that slippage of the clamp would not occur before the failure of the rods. The slippage load is defined as the load at which the displacement of the entire clamping system in the load direction increases suddenly. The test result, as depicted in Fig. 10, shows that the slippage load of the clamping system was 128 kN, at which slippage occurred in one of the clamps. The slippage load was higher than the ultimate strength of the CFRP rods.

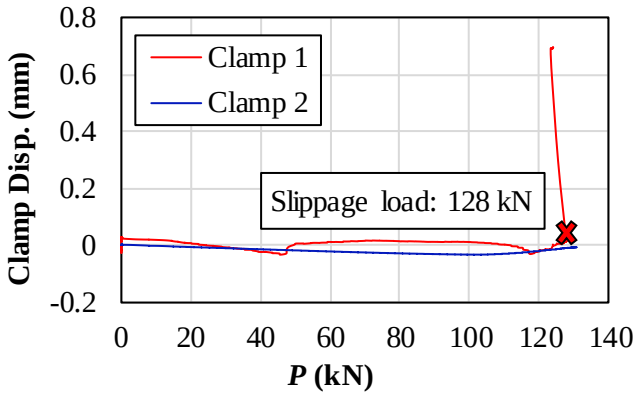

Fig. 10. Slippage load of the clamping system.

2.3.5. Finite Element (FE) model

2.3.5.1. Description of the model

An FE model was developed for different parts of the clamping system, as illustrated in Fig. 11, using the ABAQUS version R2019x HotFix 4 FEM software. In the FE analysis, the clamping system components were modeled as 3D solid parts. Due to the symmetry, only half of the beam IPB400, with a length of 1.5 m, was considered. The parts were modeled with an isotropic elastic material having an elastic modulus of 200 GPa and a Poisson's ratio of 0.3.

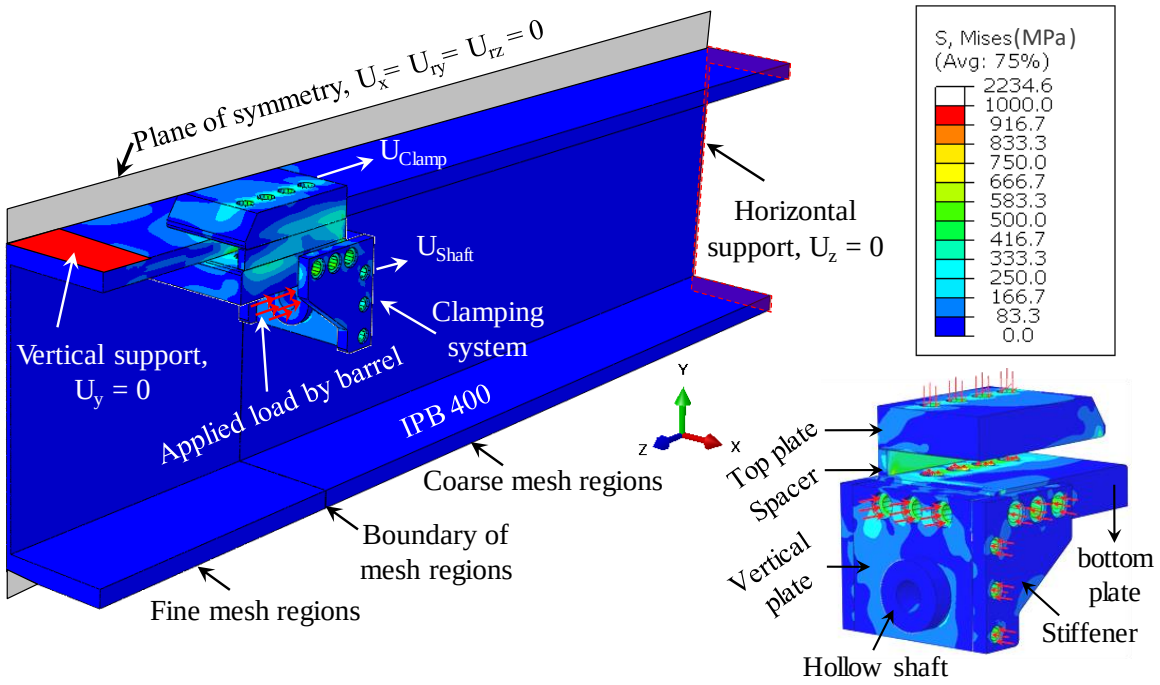

Fig. 11. FE model of the beam and the clamping system, with the von Mises stress distribution under a load of 125 kN (slippage load).

The boundary conditions used in the model are depicted in Fig. 11. In the plane of symmetry, which lies in the middle of the beam web, the displacement, U_x, and the rotations, U_{ry} and U_{rz}, were assumed to be zero. In the horizontal and vertical supports, the movements of the surfaces shown in Fig. 11 in the z- and y- directions, respectively, were constrained.

In addition, to consider the effect of the M20 bolts, which connected the top and bottom plates to each other, the surface of each hole in the top plate was tied to its corresponding hole surface in the bottom plate. A tie constraint makes the active degrees of freedom (i.e., translational and rotational motion) of the tied surfaces equal so that there is no relative motion between them. Therefore, using the tie constraint, it was ensured that the top and bottom plates would move simultaneously in the event of a slippage.

The analysis was performed through different steps, as outlined below:

(1) Bolt load: in the first step after the initial step (in which the boundary conditions were applied), the resultant force exerted by each bolt was applied; Each M20 12.9 bolt applied a total force of 212 kN on the top plate. In the FE model, this force was applied as a shear traction of 840.4 MPa to the surface of the holes in the top plate. These bolts would apply the same load to the bottom plate through the bolt head and it was applied as a pressure load. The bolts M16 12.9 and M12 12.9 also applied 135 and 72 kN, respectively, through both shear traction or pressure load as shown in Fig. 11.

(2) CFRP load: In the proposed system, the tensile load of the CFRP was applied to the clamping system from the barrel to threaded hollow shaft. In the FE model, the CFRP force was applied to the threaded shaft as a pressure load on an area where the barrel touched the shaft, as demonstrated in Fig. 11.

Different formulations and approaches have been conducted for modeling the contact behavior between different interfaces [42, 52]. In this study, similar to the approach conducted in [42], a surface-to-surface master/slave discretization was used for modelling the contact between different interfaces using finite sliding formulation, indicating that the separation and the arbitrary finite sliding and rotation of the surfaces were allowed. To have an identical sliding properties in all directions, isotropic directionality was selected [53]. The normal contact behavior was modeled as "Hard Contact," which would prevent the parts from penetrating each other. The tangential contact behavior was considered using the penalty friction formulation, which permits a small relative motion (i.e., a small fraction of the element size) of the surfaces before the surface traction reaches a critical shear stress [53]. The critical shear stress is obtained by multiplying the normal contact pressure by the surface friction coefficient. The small relative motion in the penalty friction formulation prevents from the convergence problems due to the discontinuity between the sticking and slipping states. Further in-depth information about different methodologies for modeling the contact for the interfaces as well as the required formulations are given in [54]. In this study, the friction coefficient between the top and bottom plate with the top flange of the beam was determined via verification with the experimental result, as described before.

The elements in the beam, and top, bottom, and vertical plates, in which the bending deformation was dominant, were discretized into quadratic reduced-integration elements, while the other parts were discretized into linear elements. It is noted that on one hand, the use of quadratic elements rather than linear elements increases the computational cost because for these elements, the strain and stress fields have to be computed for a larger number of integration points. On the other hand, the linear elements are not an appropriate choice in bending unless the mesh is made extremely fine, resulting in an increased computational cost. Therefore, in the FE model, the quadratic reduced-integration elements were used for the parts with the dominant bending deformations.

The free mesh type was adopted for the top and bottom plates; for the threaded hollow shaft, beam, and spacer a structured mesh was used; and for the stiffeners a sweeping mesh was used. Different meshing techniques, i.e., sweeping, structured, and free meshes, were chosen based

on the complexity of each part's geometry. To account for the mesh size effect, different mesh sizes were selected, as described before.

2.3.5.2. Correlation between the FE model and experimental results

To verify the FE model with the experiment, the obtained value of the slippage load in the FE model was compared with the experimental results. The slippage load depended on the friction coefficient of the surfaces between the top and bottom plates of the clamping system, and the top flange of the beam. After considering different friction coefficients for these surfaces, a value of 0.16 was found to lead to a slippage load of 125 kN for the clamping system, which is very close to the 128 kN obtained in the experiment, as shown in Fig. 12(a). In this figure, the displacement of the entire clamping system (a node on the top plate) in the loading direction, U_{Clamp}, is plotted against the applied load, P.

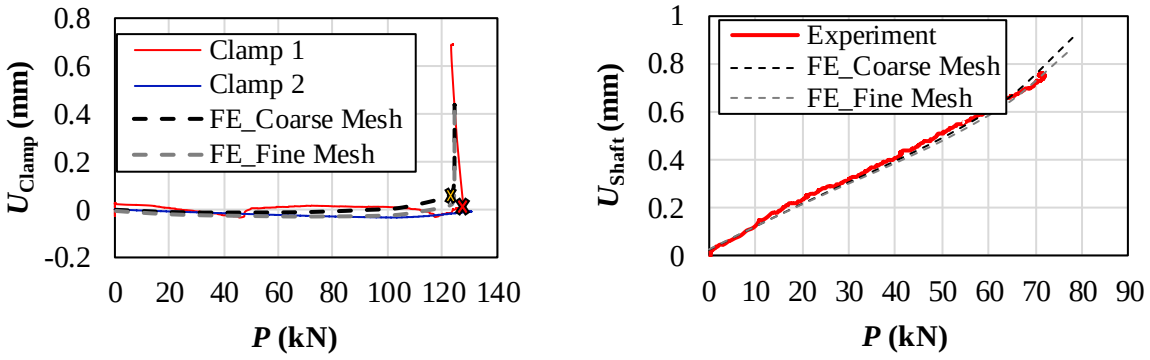

Fig. 12. Verification of the FE model with the experimental results: (a) slippage load of the whole clamping system; and (b) displacement of the threaded hollow shaft in the loading direction.

In addition, the parametric analysis on the friction coefficient showed that the slippage load and the stress distribution in the clamping system do not depend on the friction coefficient between the stiffeners, and between the vertical and bottom plates, as long as this coefficient was greater than 0.1. With a friction coefficient lower than 0.1, a slippage would occur between the vertical plate and the stiffeners before the slippage of the whole clamping system. However, as such a slippage was not observed in the experiment, the same value of 0.16 for the friction coefficient was considered throughout the model.

Two different types of meshes, a fine mesh and a course mesh, were considered to investigate the effect of mesh size, the details of which are summarized in Table 2. The mesh size in regions, where the bending deformation was dominant, and where slippage could occur was changed. Therefore, as given in the table, the mesh sizes for the top, bottom, and vertical plates,

as well as the fine mesh region of the beam were different for the fine and coarse mesh cases. The mesh size for the other parts was the same for the two cases. As shown in Fig. 12(a), a change in the mesh size in the two different mesh size cases did not influence the obtained slippage load.

Table 2. Mesh sizes in different parts in the FE model

Case	Mesh size (mm)							
	Hollow shaft	Spacer	Stiffeners	Top plate	Bottom plate	Vertical plate	Beam	
							Fine mesh region	Coarse mesh region
Fine mesh	5	3	5	5	5	5	5	30
Coarse mesh	5	3	5	10	10	10	8	30

In addition, in Fig. 12(b), the displacement of the barrel in the z-direction, measured by the line laser, was compared with that obtained from the FE model. As shown in the figure, the change in the mesh size did not have a significant effect on the obtained displacement.

Furthermore, the FE model showed that the displacement of the threaded hollow shaft, U_{Shaft}, was not dependent on the value of the friction coefficient between the stiffeners and the vertical and bottom plates at the load levels of 70–80 kN (which can be inferred from Fig. 12(b)), even for a friction coefficient less than 0.1. The reason for this behavior is that the bolts connecting these parts provided sufficient friction resistance, particularly at the aforementioned low load levels.

In the FE model, it was assumed that the displacement of the barrel was equal to the displacement of the hollow shaft. This assumption was valid because the axial displacement of the barrel could be ignored. The displacement of the barrel (or the threaded hollow shaft) was greater than that for the whole clamping system (shown in Fig. 12(a)), which was because of the rotation of the clamping system, as well as the bending deformations due to the applied load.

Notably, as shown in Fig. 11, the von Mises stress in different parts of the clamping system was lower than the yield stress of the material, i.e., 1000 MPa, at the slippage load. However, under the service loads, the applied load to the clamping system was further lower; For example, for the CFRP rod used in the experiments in this study, the maximum load in the acceptance tests (based on ETAG 013 [49] and [50]) in the CFRP rod was 66.9 kN (equivalent to 1331 MPa).

2.3.5.3. Tensile stress in the top flange of the beam

One of the most important considerations for designing the clamping system is the bending

stresses generated in the top flange of the beam due to the rotation of the clamping system. As shown in Fig. 13, when the CFRP load was applied to the clamping system, there were two regions in the beam top flange with high tensile bending stresses σ_b. As shown in Fig. 13, due to the application of a CFRP load of 125 kN, the tensile bending stresses in the bottom and top of the beam top flange were 293 and 297 MPa, respectively, which were smaller than the yield stress of the beam material (the beam was made of S235 steel with a yield strength of 380 MPa according to the coupon tests). In addition, the FE model showed that the tensile bending stresses in the top flange were smaller than 200 MPa when a CFRP load of 66.9 kN (as the maximum load in the acceptance tests) was applied. It is noted that in the proposed clamping system, the application of fillets at the end of the top and bottom plates played an important role in reducing the stress concentration in highly stressed regions.

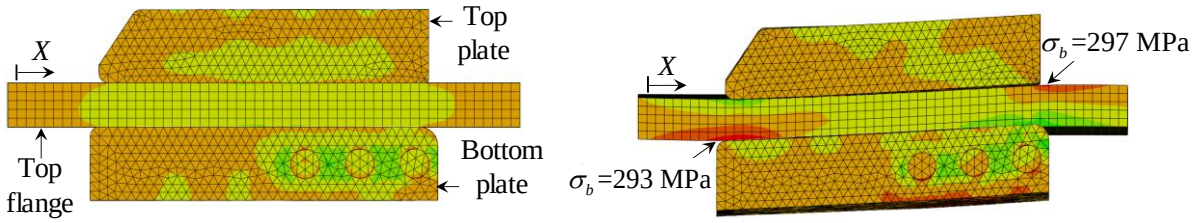

(a) (b)

Fig. 13. Tensile stresses in the top flange due to the rotation of the clamp: (a) undeformed shape (P=0); and (b) deformed shape (P=125 kN).

2.3.6. Performance of the clamping system under fatigue loading

2.3.6.1. Test set-up

The fatigue performance of the developed clamping system was investigated in the test set-up shown in Fig. 14(a) and (b). The set-up consisted of two IPB 400 stringers, each with a span of 2.66 m, connected to an IPB 550 floor-beam with a span of 1 m, using four L160×160×15 web-to-web bolted angles. The other ends of the stringers rested on rolling supports. All the parts were made of S235 steel. The vertical cyclic loads were applied on the stringers using two 500-kN Amsler hydraulic actuators located at the mid-span of each stringer. The strengthening system was installed in the set-up as shown in the figure. More detailed information about the dimensions of the set-up is available in the Appendix I. As the clamping system was later used

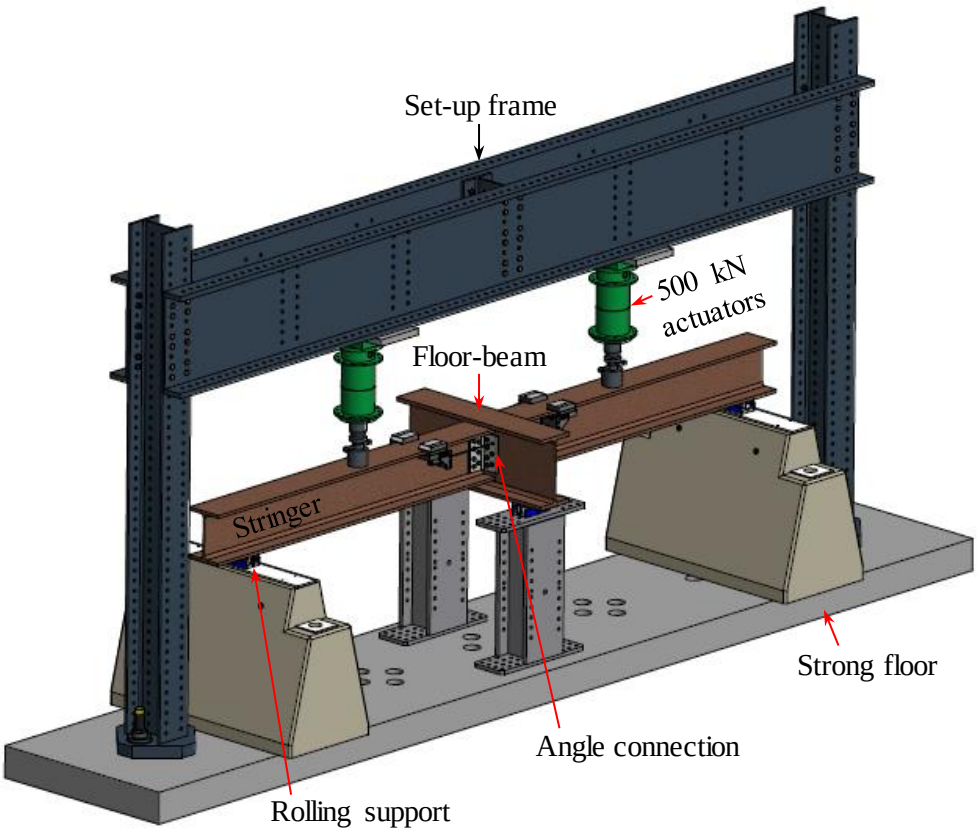

(a)

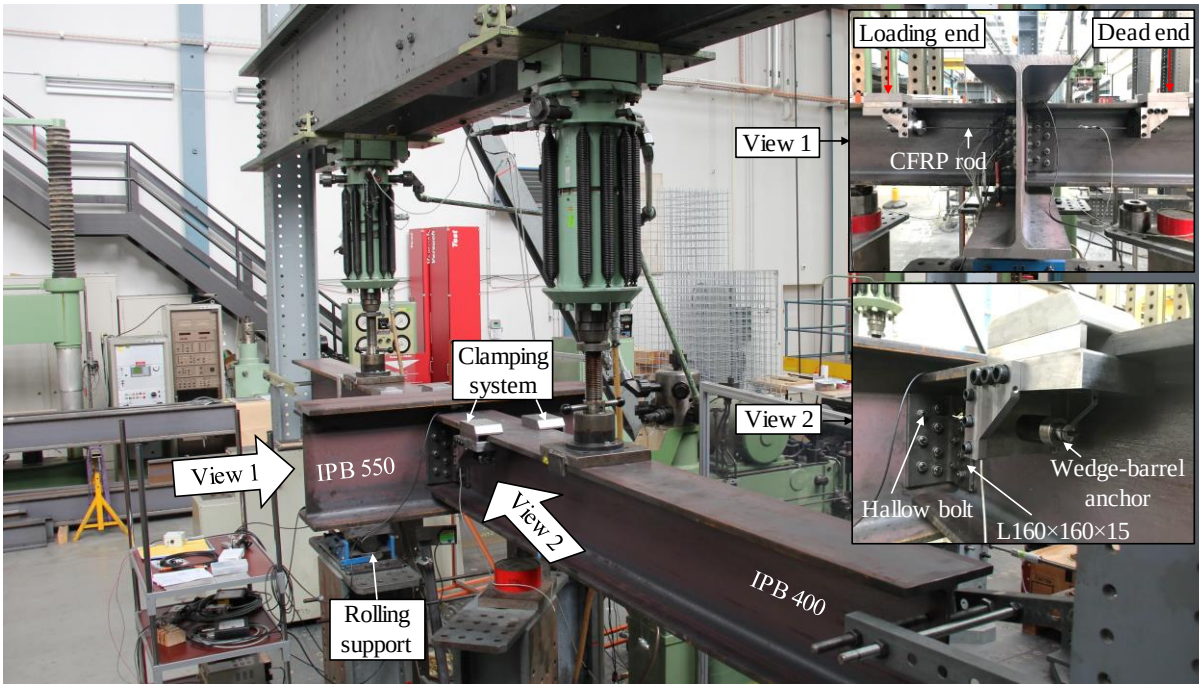

(b)

Fig. 14. Test set-up for the fatigue tests: (a) overview of the fatigue test set-up; and (b) details of the fatigue test set-up.

to strengthen the connections in the old riveted bridge in Switzerland, the stringer section and

the angle connections used in the set-up had the same dimensions as those of the bridge.

The fatigue tests were performed under load-control condition, with a load ratio R=0.1 and a maximum load of 240 kN per actuator. The loading frequency was 4.35 Hz, and the load levels were monitored using two pressure gauges. The prestressing force of each CFRP rod was 50 kN (equivalent to 995 MPa) in all the fatigue tests.

2.3.6.2. Stress in the CFRP rods

Before application of the fatigue loadings, each CFRP rod (i.e., rods A and B) was prestressed up to 50 kN. To apply the desired prestressing force, the strains in each CFRP rod were measured using the strain gauges (Type 1-LY66-6/120, HBMAG, Darmstadt, Hesse, Germany) during the pumping of the hydraulic cylinders. Fig. 15 shows the stresses in the CFRP rods during the fatigue tests. In total, 11.2 million cycles were applied by the actuators. The measurements from the strain gauges indicate that the stress range in the CFRP rod was approximately 20 MPa. During the fatigue test, no prestressing loss occurred. The fluctuations in the stresses, shown in Fig. 15(c), were caused by the daily temperature changes in the laboratory.

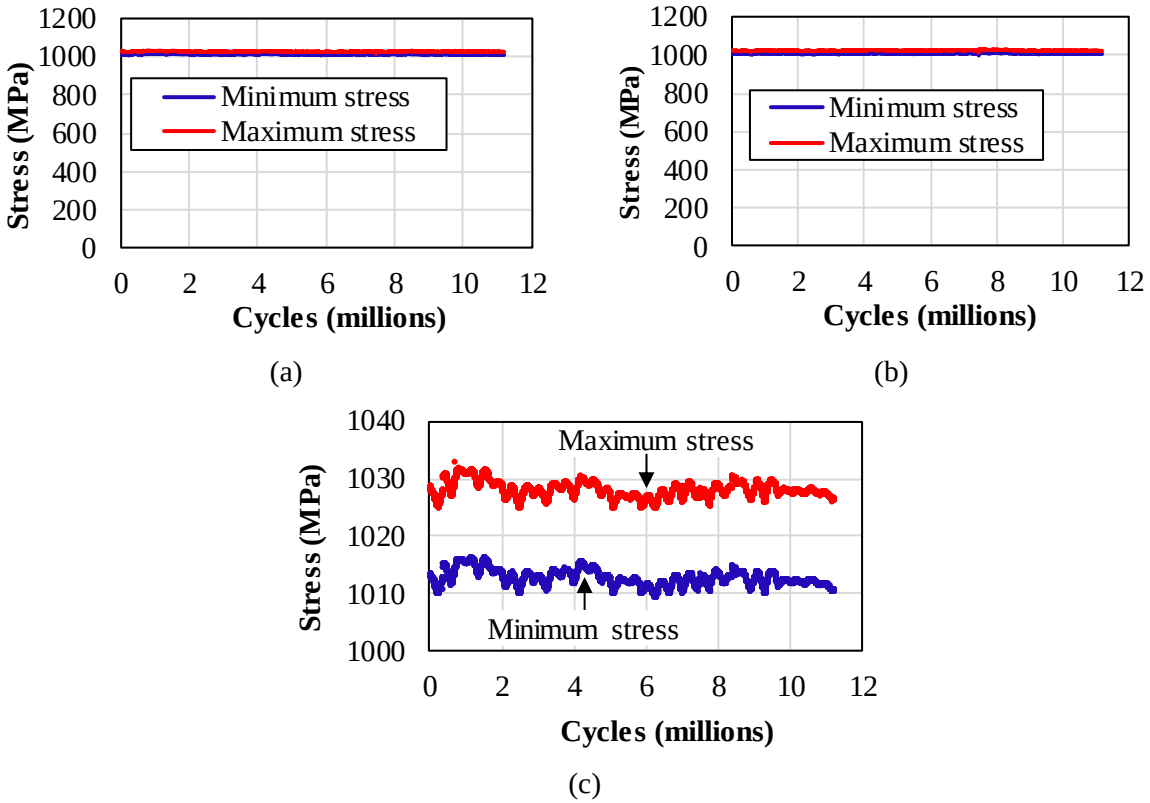

Fig. 15. Stress in the CFRP rods during the fatigue loading: (a) stress in CFRP_A; (b) stress in CFRP_B; and (c) *fluctuations in stresses of CFRP_A due to the daily variation of temperature*[*].

[*] The underlined sentence is a modification to the original published paper.

2.3.7. Effect of the strengthening system on the stresses in the connections

Prior to the fatigue tests, static tests were also conducted to evaluate the effect of the strengthening system on the connection behavior. In the static tests, the vertical load per actuator was increased from 0 to 240 kN (maximum force in the fatigue tests), with different prestressing levels, *P*, in the CFRP rods.

2.3.7.1. Description of the FE model developed for the connection tests

To investigate the stress state in the connections in the test set-up shown in Fig. 14, an FE model was developed, as illustrated in Fig. 16(a); this figure shows the planes of symmetry and the boundary conditions. As the model contained two symmetry planes, only a quarter of the set-up was modeled.

To model the rolling support, on which the floor-beam rested, a reference point RF_3 was defined, with a constraint in the y- (vertical) direction. Then, the end section surface of the floor-beam was tied to the reference point. For the rolling support of the stringer, first, the reference point RF_1 was defined, and the corresponding surface was tied to it. Next, RF_1 was connected to the fixed reference point, RF_2, using a nonlinear spring. The function of the nonlinear spring was to constrain the stringer in the vertical direction only when it moved downward (i.e. there would be no constraint on the stringer when an uplift from the support occurred). Therefore, in this model, the stiffness of the spring was extremely high (i.e., sufficient to be considered as infinity) in compression and was zero in tension.

In addition, through the nonlinear spring, it was possible to consider the effect of imperfections. In the set-up shown in Fig. 14, the elevations of the supports were not identical for all supports. In addition, the stringer was not completely straight. Therefore, it was possible that when the stringer was connected to the floor-beam by angles, the other side of the stringer did not perfectly rest on the rolling support. Appendix II provides more information about the manner in which the imperfections were considered in the FE model through the nonlinear spring, as well as the significance of the imperfections.

All parts in the model, i.e., the stringer, floor-beam, and angle, were modeled as isotropic elastic materials with an elastic modulus of 200 GPa and a Poisson's ratio of 0.3. The elements were 3D solid, quadratic reduced-integration type for angle and linear type for stringer and floor-beam.

The mesh sizes of the stringer and the floor-beam were 25 and 15 mm, respectively. For the

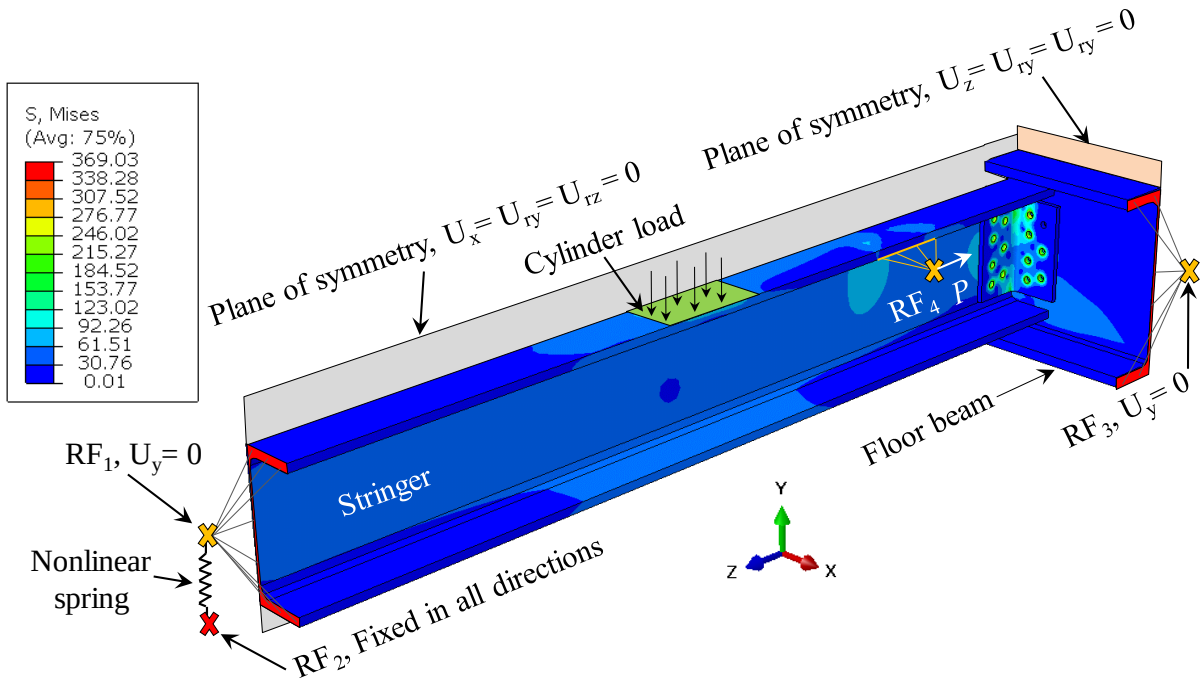

(a)

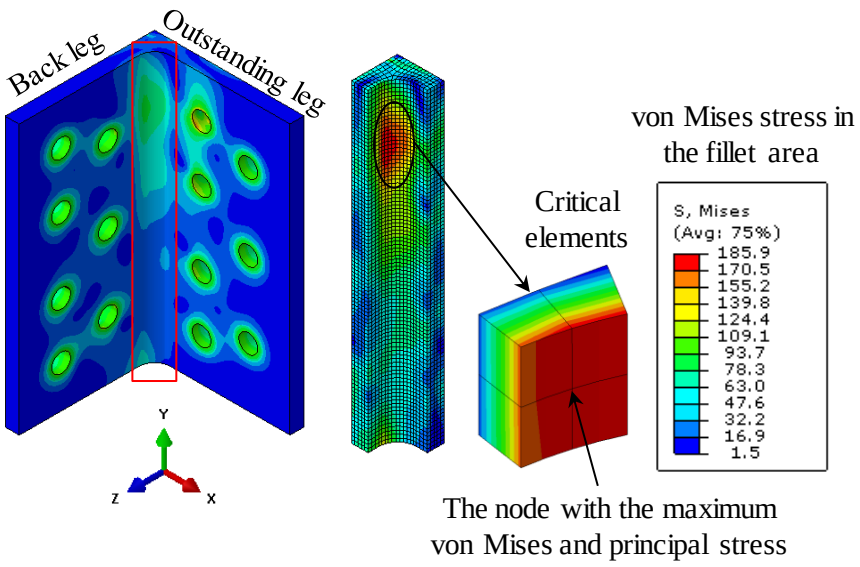

(b)

Fig. 16. FE model of the connection tests set-up: (a) details of the ¼ FE model and the von Mises stress distribution under a cylinder load of 120 kN (in model); and (b) critical location in the angle.

angle, an optimum value of 3 mm for the mesh size was finalized on the basis of a mesh sensitivity study. The contact condition between different parts was similar to that described in the FE model of the beam and the clamping system, i.e., a surface-to-surface discretization with finite sliding formulation, isotropic directionality, “Hard Contact” for normal behavior and the penalty friction formulation for tangential behavior, with a friction coefficient of 0.16.

The analysis was performed separately for two different conditions: unstrengthened and strengthened. The steps used for the analysis of the unstrengthened case were as follows:

(1) Bolt loads: After the initial step, a bolt force of 100 kN for each bolt (M18, 8.8) was applied as a pressure load around the bolt holes.

(2) External load: In the next step, the vertical cylinder load was applied at the mid-span of the stringer, as a pressure load on a surface, as shown in Fig. 16(a), resulting in a 120-kN force (only half of the cylinder load applied in the experiment was considered because of the symmetry).

For the analysis of the strengthened case, the following steps were used:

(1) Bolt loads: These were same as in the first step for the unstrengthened case; however, in this case, no bolt load was applied around the hole through which the CFRP rod passed.

(2) CFRP Load: In this step, the prestressing load *P* was applied, as shown in Fig. 16(a).

(3) Cylinder load: It was same as in the second step for unstrengthened case.

In the model, the surface of the stringer top flange, which was below the bottom plate of the clamping system, was tied to the reference point, RF_4, and the prestressing load, *P*, was applied to this reference point. RF_4 was located in the same position as the CFRP was in the set-up.

The FE results show that the critical location was in the angle, where the von Mises and maximum principal stresses were simultaneously maximum, exactly on the angle fillet, as shown in Fig. 16(b). The most stressed part was the back leg of the angle (i.e., the leg of the angle that was connected to the stringer). It is worth mentioning that a change in the arrangement of the bolts could alter the stress distribution and the critical location, shifting it to the fillet towards the outstanding leg (i.e., the leg of the angle connected to the floor-beam).

2.3.7.2. Experimental results

At the critical location, a multiaxial stress state existed; i.e., not only were the tensile stresses significant, but the shear stresses were also high. Therefore, in the set-up and in the critical locations, instead of normal strain gauges, rosette strain gauges (type 1-RY91-3/120, HBM AG, Germany) were used in the hot spots of the connections. Strain gauges (1) and (2) in Fig. 17(a), were rosette strain gauges, while the other two were normal strain gauges. The strain gauges were placed on the two angles connected to the stringer on the left side, with a layout similar to that shown in Fig. 17(b). No strain gauge was placed on the other two connections on the stringer on the right side.

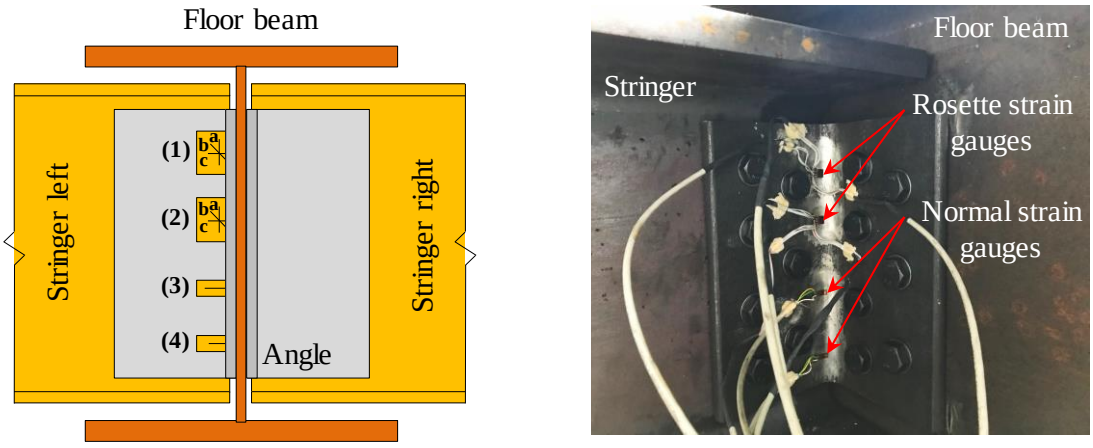

(a) (b)

Fig. 17. Strain gauges used for the measurement of strain state in the connections: (a) schematic of the arrangement of rosette and normal strain gauges; and (b) strain gauges applied on the connection.

The strains measured using the strain gauges were used to verify the FE model. The measured strains in the a-, b-, and c- directions were compared with the FE results for both the unstrengthened and strengthened cases.

In this paper, the results of only the measurements using rosette strain gauge (1) are presented, as depicted in Fig. 18. As shown in this figure, the FE model was capable of accurately predicting the strains in different directions. In addition, the results show that the strains in the a-direction were negligible, while the strains in the c-direction were the highest. The reason was that the out-of-plane deformation of the angles mainly applied tensile strains (or stresses) in the c-direction due to local bending in the angle connections.

Furthermore, the results show the effectiveness of the strengthening system in reducing the strains, especially in the c-direction. The application of 50 kN of prestressing to the CFRP rods reduced the strains in the c-direction from 813 to 468 microstrain (i.e., approximately 42% reduction), and from 555 to 354 microstrain in the b-direction. The reduction of the strains, and consequently the stresses, in the critical location of the connections was the result of the reduction in the out-of-plane deformation of the angles.

Using the verified FE model, for a cylinder load of 120 kN, the different components of the stress tensor at the critical node before and after strengthening (50 kN per rod) are summarized in Table 3. With this information, it was possible to distinguish the dominant stress components, and evaluate the effect of strengthening system on each stress component.

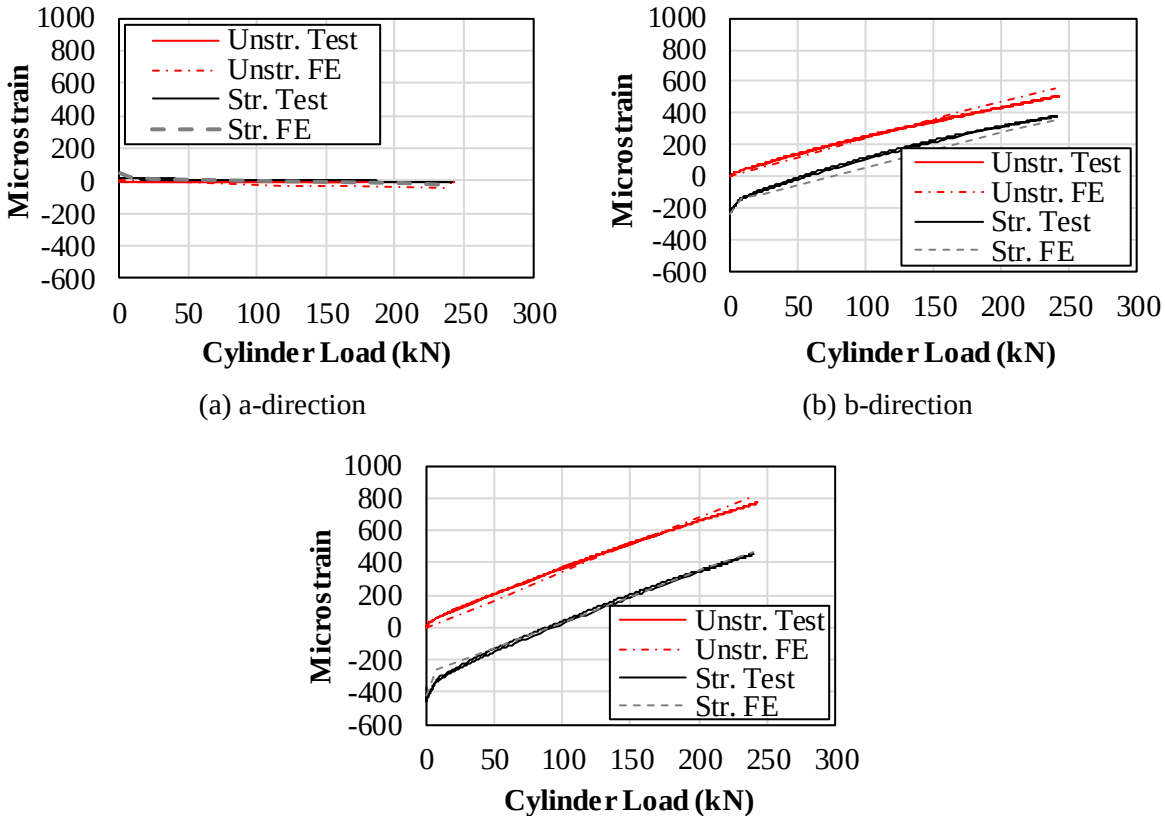

(a) a-direction

(b) b-direction

(c) c-direction

Fig. 18. Strain components in the angles based on the measurements from strain gauge (1): (a) a-direction; (b) b-direction; and (c) c-direction.

Table 3. Strengthening effect on different stress components

Stage	Stress level (MPa)					
	σ_x	σ_y	σ_z	τ_{xy}	τ_{xz}	τ_{yz}
Before Strengthening	33.6	44	146.4	11.3	–65.1	–24
After Strengthening	18.9	26.4	84.5	8.4	-37.7	–18.3
Reduction (%)	44	40	42	26	42	24

As given in Table 3, the strengthening system reduced the stress components significantly. The stress reduction for the components σ_z and τ_{xz}, which had the highest values among all, was 42% each. Therefore, it could be inferred that the proposed strengthening system was capable of effectively increasing the fatigue life of the connections. In addition, the results in Table 3 reveal the importance of considering the multiaxial state of stress in the critical location.

Notably, the determination of appropriate multiaxial fatigue criteria for the prevention of fatigue cracks in the critical locations of the angles, in which the strengthening effect was also

incorporated, is crucial. Discussing the multiaxial theoretical models together with experimental verifications is beyond the scope of this study and will be taken up as a follow-up study by the authors in the future.

2.3.8. Field application of the proposed strengthening system

After a demonstration of the reliable and effective performance of the strengthening system in a laboratory, the proposed clamping system was applied on the Aabach Bridge, which is an old riveted railway bridge in Lachen, Switzerland, as shown in Fig. 19.

The prestressing level in each of the CFRP rods (on both sides of the stringers) was 50 kN, which was 994.7 MPa and 49% of the CFRP nominal ultimate tensile strength. For long-term monitoring of the prestressing level in the CFRP rods, a wireless sensor network (WSN) system was applied on the bridge, as shown in the figure. Therefore, for at least one year, any prestressing loss in the CFRP rods due to the slippage of the clamping system or of the rods inside the barrels would be monitored. In addition, for protection against corrosion and galvanic corrosion between different materials inside the wedge-barrel system, a plastic cap was used on the wedge-barrel anchors, as shown in the figure. A comprehensive coverage of the field application is beyond the scope of this study and will be performed in a subsequent study.

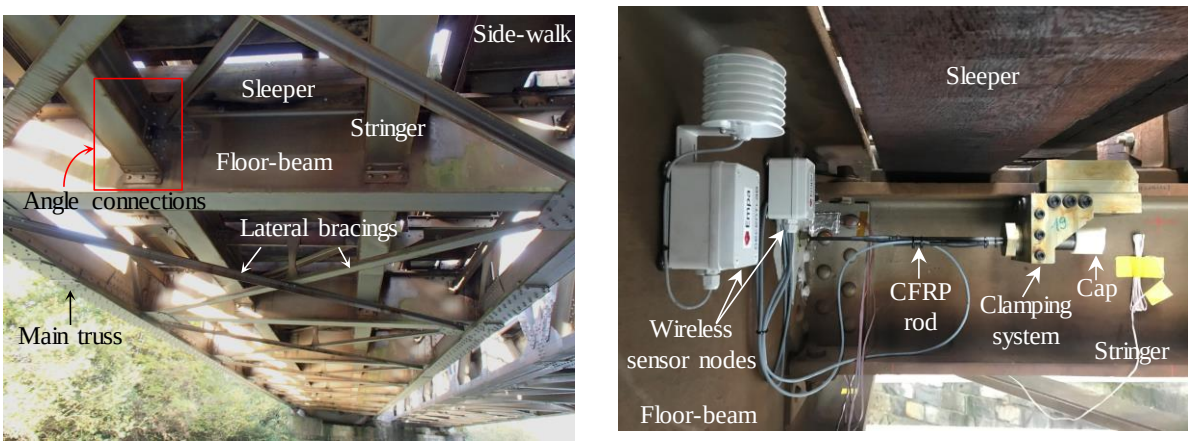

(a) (b)

Fig. 19. Application of the proposed strengthening system on Aabach Bridge, Lachen, Switzerland: (a) different elements of the bridge floor system; and (b) installed system on the bridge.

2.3.9. Summary and conclusions

This paper presents a retrofit solution that can be used for strengthening bridge connections with minimal damage and interventions (i.e., without closing the bridge or enforcing any traffic management). The strengthening system reduces the out-of-plane deformation and stresses in

the angle connections using prestressed CFRP rods. The retrofit system consists of a newly developed wedge-barrel anchor and a friction-based clamping system. Prestressed CFRP rods are used (rather than strips) as they can easily pass through the connection (in the openings made by removing bolts/rivets). A simple presetting system was also developed, enabling the application of high presetting forces on-site for the installation of the wedge-barrel system. The installation procedure requires a few temporary plates and housing, and includes assembling, presetting, and prestressing (of the CFRP rods using a hydraulic jack). Furthermore, it is possible to disassemble the system using the same temporary parts without any residual effect on the original structure. The clamping system consists of different plates, which are bolted together and grab the flange of the steel beam. The prestressing force of the CFRP rod is transmitted to the beam solely through friction, without the need for drilling holes and without damaging the parent steel structure. The key findings of this study are summarized as follows:

- The slippage load of the system was 128 kN, which was greater than 100% of the actual CFRP ultimate tensile strength of 2367 MPa (i.e., 119 kN).
- No slippage occurred between the components during pulling of the CFRP rods, either in the clamping system or in the wedge-barrel anchors.
- When the CFRP load exceeded a certain level, both the wedges and the CFRP rod moved simultaneously further into the barrel, which was the desired behavior for the anchors.
- A detailed FE model was developed to simulate the retrofit system and optimize its dimensions and performance. The stresses in different parts of the clamping system, as well as in the top flange of the clamped stringer, were observed to remain below the yield stress of the material in all the parts.
- A novel set-up for testing bridge connections was designed and used in this study. The test set-up included four supports, which could simulate the complexities of the boundary conditions of bridge connections.
- A series of fatigue tests was performed on the steel connections with dimensions identical to those in a riveted railway bridge in Switzerland. The proposed strengthening system was demonstrated to be capable of reducing the stresses at critical locations (hotspots) in the angle connections by more than 40%.
- The fatigue results showed that the designed retrofit system could survive more than 11 million load cycles, without any damage to the CFRP rods, connections, and clamping system. Furthermore, there was no indication of any loss in the CFRP prestress level during cyclic

loading.

- Using a detailed FE model, the effects of geometrical imperfections during the installation of different components of the connections were extensively discussed and verified by laboratory measurements. The steel connections were also modeled before and after strengthening, and the results of the FE model correlated well with experimental measurements obtained in the laboratory.
- After the successful design and completion of the laboratory static and fatigue tests, the maintenance system was finally used for strengthening the old steel bridge. The long-term performance of the system is currently being monitored using a wireless monitoring system.

2.3.10. Recommendations for future studies

The proposed strengthening system can be further optimized for different applications. Development of a strengthening system consisting of a clamping system and an anchor head with multiple prestressed CFRP rods (rather than a single rod) for applications in which a high prestressing force is required would be recommended.

In addition, to identify the appropriate multiaxial fatigue criteria for predicting the fatigue failure in the stringer-to-floor-beam angle connections, experimental and numerical investigations have to be conducted.

Appendix I. Detailed dimensions of the clamping system and different setups

The detailed dimensions of the parts used in the clamping system, housing, and set-up for the fatigue tests on the connections are shown in Figs. 20-22, respectively.

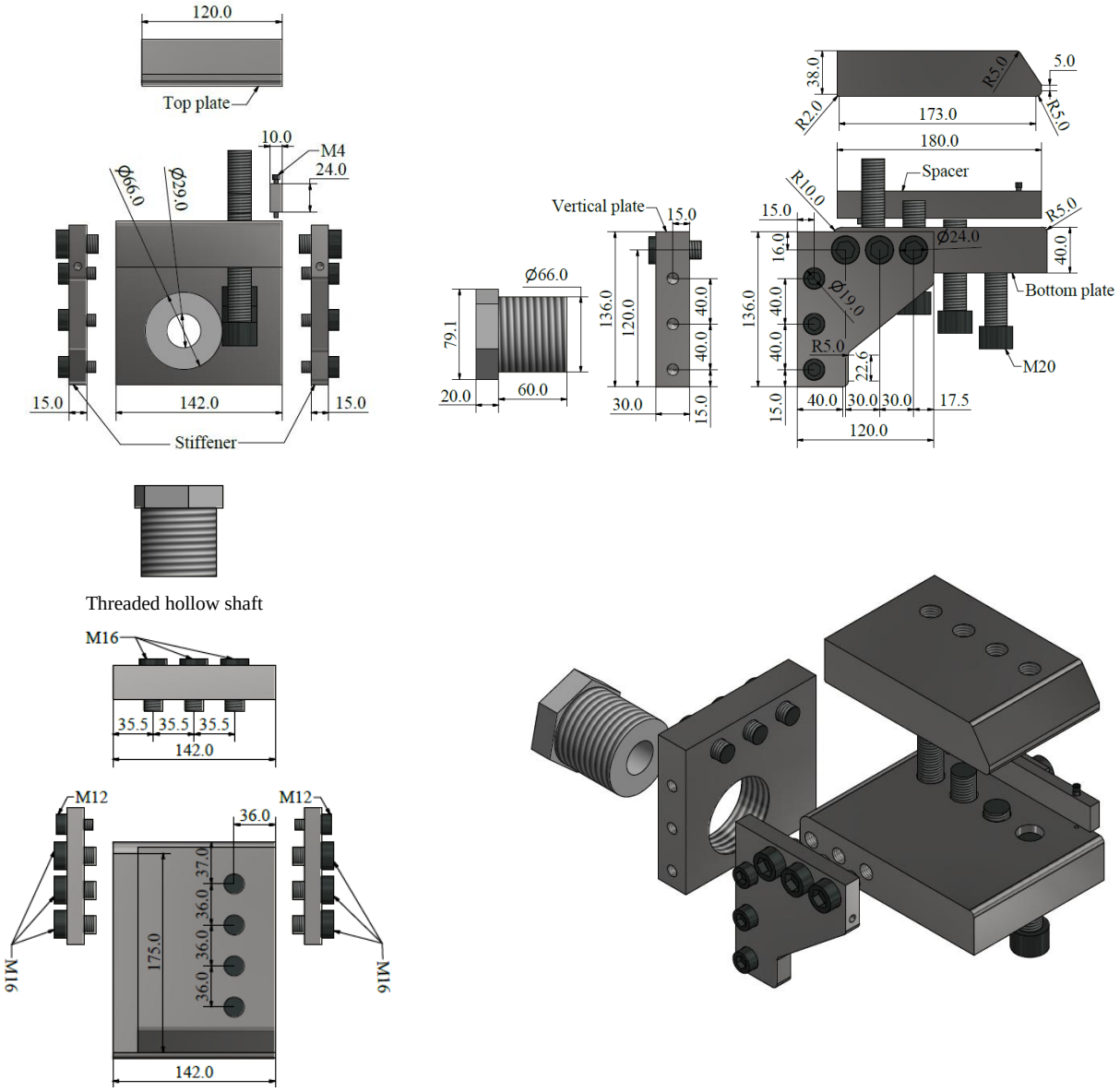

Fig. 20. Details and dimensions of different components of the clamping system.

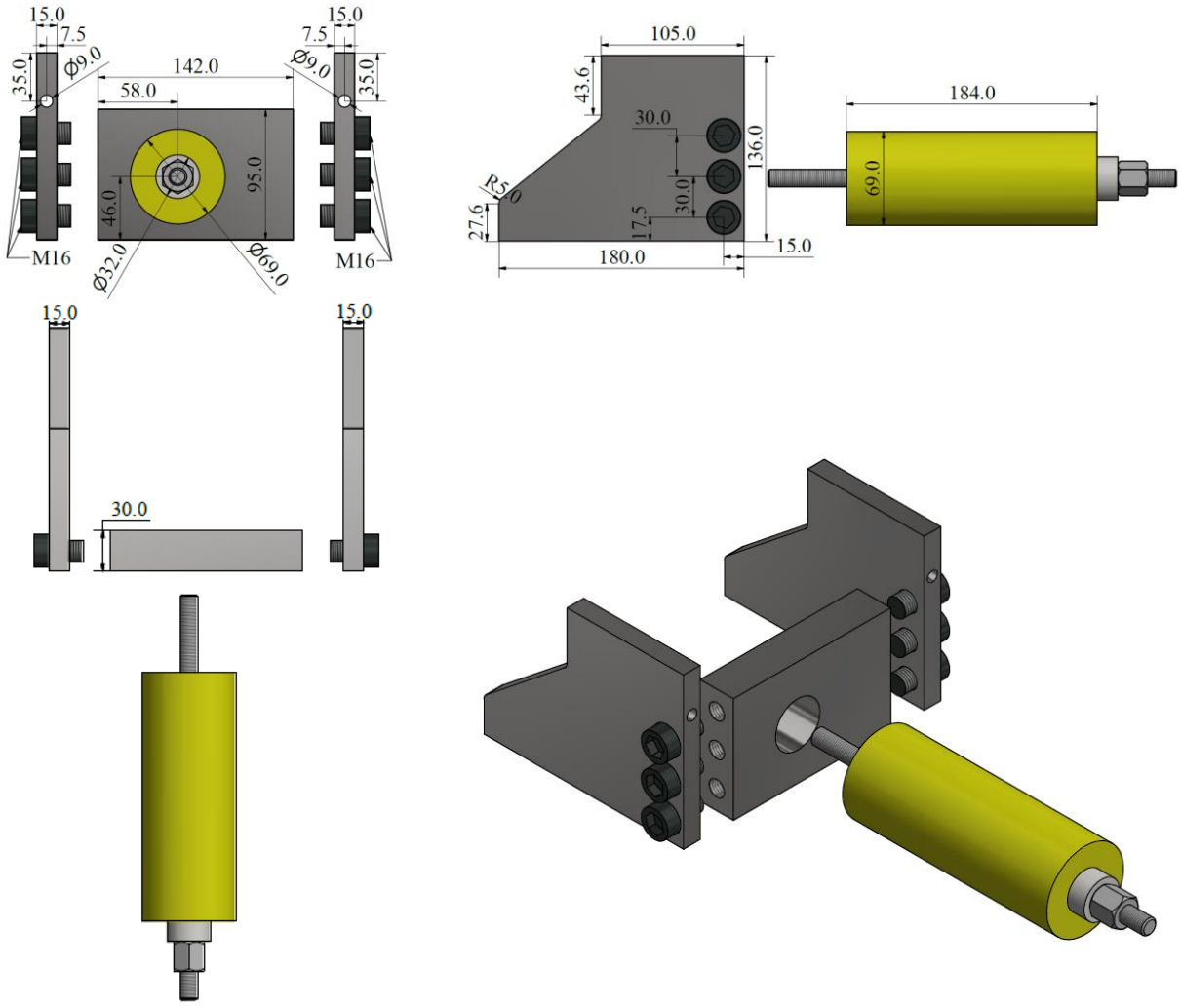

Fig. 21. Details and dimensions of the housing system.

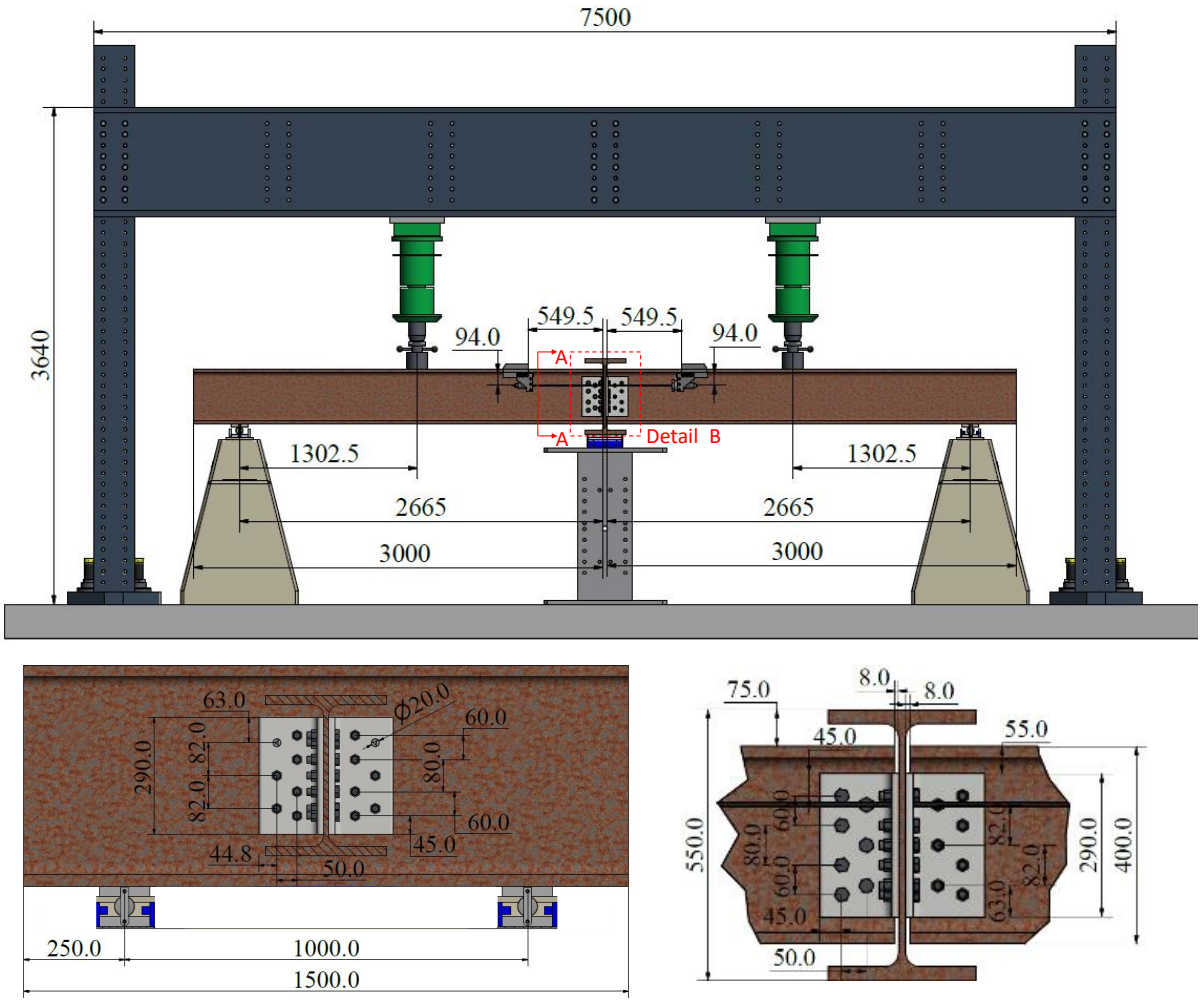

Section A Detail B

Fig. 22. Details and dimensions of different components of the set-up for the fatigue tests.

Appendix II. FE modeling of the imperfections in the connection tests

As mentioned in the section regarding the FE model developed for the connection tests, due to the presence of imperfections in the set-up shown in Fig. 14, there can be a gap distance Δ between the stringer and the rolling support, as shown in Fig. 23(a). In this case, stresses are formed in the connection when the stringer touches the support, because of the stringer self-weight during the installation process. In the laboratory tests, at this time, the values of the strain gauges were reset to zero.

When a prestressing force is applied in the CFRP rod, an uplift occurs in the support due to the sagging bending moment (see Fig. 23(b)). At this stage, the strain gauges display compressive strains in the top of the connections. Due to the application of the external (cylinder) loads, the stringer rests on the support, as demonstrated in Fig. 23(c).

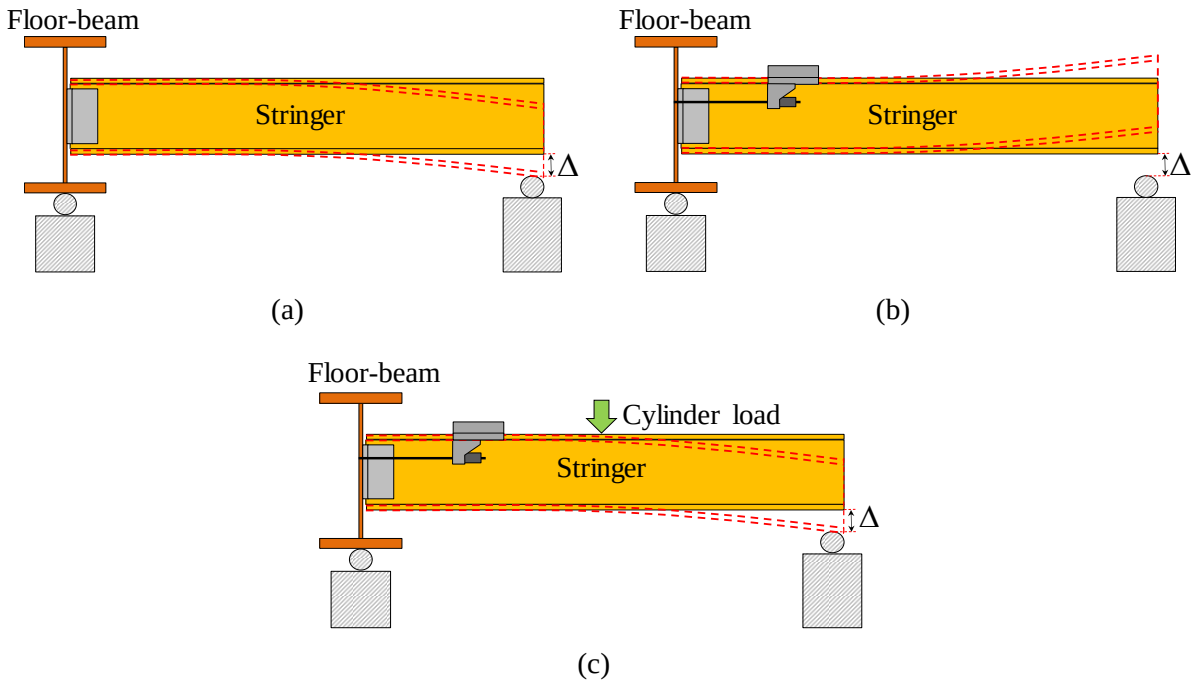

Fig. 23. Deflection of the stringer considering the imperfections: (a) deflection due to self-weight of the stringer; (b) deflection due to the prestressing force; and (c) deflection after the application of the cylinder load.

The effect of Δ in the FE model was simulated using a nonlinear spring in ABAQUS, as shown in Fig. 24, where the spring stiffness in tension was taken as zero because there was no constraint on the stringer for upward deflection on the support. When the spring was compressed up to $-\Delta$, no force was generated in the spring (i.e., the stiffness was zero). When the compressive deformation in the spring was greater than $-\Delta$, the stiffness of the spring would become extremely high (i.e., high enough to be considered to be infinity). The $\delta - F$ relationship considered in ABAQUS is given in Fig. 24.

The effect of Δ on the strain in the c-direction of the strain gauge (1) (see Fig. 17(a)) is depicted graphically in Fig. 25. When the external load was low, the stringer actually behaved similar to a cantilever beam (see Fig. 23(c)). Therefore, the strain in the connection increased rapidly. When the stringer touched the support, the rate of increase of the strain in the connections decreased because of the change in the static condition (boundary condition) of the stringer.

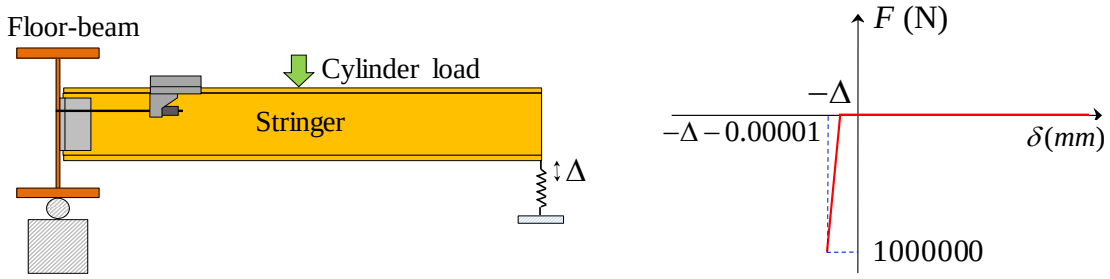

Fig. 24. Modeling the imperfection effect in FE simulation using a nonlinear spring.

As shown in Fig. 25, for low load levels (< 50 kN), when the effect of Δ was not considered (i.e., $\Delta = 0$), the experimental and the FE results differed significantly. However, taking $\Delta = 0.8$ mm provided a good agreement between the FE model and experimental results. In this study, $\Delta = 0.8$ mm was considered for the FE model. As evident, when the external load level was high (> 50 kN), this effect was negligible because the stringer had already rested on the support.

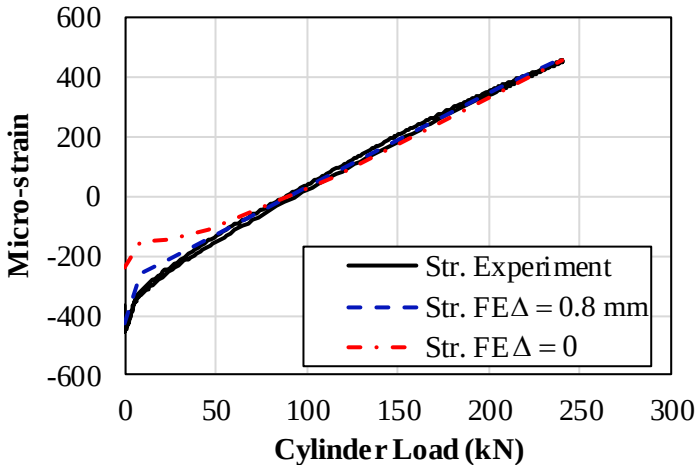

Fig. 25. Effect of gap distance Δ on the strain in the c-direction of the strain gauge (1).

Data Availability Statement

Some or all data, models, or code that support the findings of this study are available from the corresponding author upon reasonable request.

Acknowledgements

This work has been funded primarily by the Innosuisse Swiss Innovation Agency (Grant ID: 12993.1 PFIW-IW). The authors would also like to acknowledge the financial and technical support from S&P Clever Reinforcement Company AG, Switzerland; the Swiss Federal Railways (SBB) AG, Bern; and dsp Ingenieure + Planer AG Engineering Office, Uster, Switzerland,

for this project. They also thank the technicians from the Structural Engineering Research Laboratory of Empa for their outstanding collaborations during the experiments. Finally, the scientific and technical support from Dr. Ardalan Hosseini, postdoctoral scholar at the University of California, Davis, in different stages of the design of the strengthening system is highly appreciated.

References

1. Ghafoori E. Editorial for special issue on Sustainable Metallic Structures. Engineering Structures 2019;18383. https://doi.org/10.1016/j.engstruct.2018.12.086. http://www.sciencedirect.com/science/article/pii/S014102961834327X.
2. Haghani R, Al-Emrani M, Heshmati M. Fatigue-prone details in steel bridges. Buildings 2012;2(4)456-476. https://doi.org/10.3390/buildings2040456
3. Al-Emrani M, Kliger R. Fatigue prone details in steel bridges. in: Nordic Steel Construction Conference. 2009.
4. Fisher JW, Yen B, Wang D, Mann J. Fatigue and fracture evaluation for rating riveted bridges. 1987, Washington, DC United States: Transportation Research Board.
5. Fisher JW, Yen BT, Wang D. Fatigue strength of riveted bridge members. Journal of structural Engineering 1990;116(11)2968-2981.
6. Al-Emrani M. Fatigue in Riveted Railway Bridges-a study of the fatigue performance of riveted stringers and stringer-to-floor-beam connections. 2002: Chalmers University of Technology.
7. Baker K, Kulak G. Fatigue of riveted connections. Canadian Journal of Civil Engineering 1985;12(1)184-191. https://doi.org/10.1139/l85-017
8. Reemsnyder HS. Fatigue life extension of riveted connections. Journal of the Structural Division 1975;101(ASCE# 11795 Procceding).
9. Kuehn B, et al. Assessment of existing steel structures: recommendations for estimation of remaining fatigue life. 2008. http://publications.jrc.ec.europa.eu/repository/handle/JRC43401.
10. Bowman MD. Fatigue evaluation of steel bridges. Vol. 721. 2012: Transportation Research Board.
11. Roeder CW, MacRae G, Leland A, Rospo A. Extending the fatigue life of riveted coped stringer connections. Journal of Bridge Engineering 2005;10(1)69-76. https://doi.org/10.1061/(ASCE)1084-0702(2005)10:1(69)
12. Dawood M, Rizkalla S, Sumner E. Fatigue and overloading behavior of steel-concrete composite flexural members strengthened with high modulus CFRP materials. Journal of Composites for Construction 2007;11(6)659-669. http://www.scopus.com/inward/record.url?eid=2-s2.0-36249004257&partnerID=40&md5=84b4832fa44e403621bdb113e990e4e1.
13. Haghani R. Analysis of Adhesive Joints Between Fibre-Reinforced Polymer Laminates and Structural Steel Members. Australian Journal of Structural Engineering 2014;15(4)393-406. 10.7158/13287982.2014.11465173. https://www.tandfonline.com/doi/abs/10.7158/13287982.2014.11465173.
14. Haghani R, Al-Emrani M, Kliger R. Interfacial stress analysis of geometrically modified adhesive joints in steel beams strengthened with FRP laminates. Construction and Building Materials 2009;23(3)1413-1422.
15. Mertz DR, Gillespie JWJ. Rehabilitation of steel bridge girders through the application of advanced composite materials. Contract NCHRP-93-ID011. Transportation Research Board, Washington, D.C. 1996.
16. Schnerch D, Dawood M, Rizkalla S, Sumner E. Proposed design guidelines for strengthening of steel bridges with FRP materials. Construction and Building Materials 2007;21(5)1001-1010.
17. Zhao X-L. FRP-strengthened metallic structures. 2013: CRC Press.
18. Ghafoori E, Motavalli M, Botsis J, Herwig A, Galli M. Fatigue strengthening of damaged metallic beams using prestressed unbonded and bonded CFRP plates. International Journal of Fatigue 2012;44303-315.
19. Ghafoori E, Motavalli M. Innovative CFRP-Prestressing System for Strengthening Metallic Structures. Journal of Composites for Construction 2015;19(6)04015006. https://doi.org/10.1061/(ASCE)CC.1943-5614.0000559. http://www.scopus.com/inward/record.url?eid=2-s2.0-84939204537&partnerID=40&md5=3422ce7a81b87ad1b00e68ab9a965d3e.

20. Kianmofrad F, Ghafoori E, Elyasi MM, Motavalli M, Rahimian M. Strengthening of metallic beams with different types of pre-stressed un-bonded retrofit systems. Composite Structures 2017;15981-95. http://dx.doi.org/10.1016/j.compstruct.2016.09.020. http://www.sciencedirect.com/science/article/pii/S0263822316304081.
21. Hosseini A, Ghafoori E, Motavalli M, Nussbaumer A, Zhao XL, Al-Mahaidi R. Flat Prestressed Unbonded Retrofit System for Strengthening of Existing Metallic I-Girders. Composites Part B 2018;155156-172. https://doi.org/10.1016/j.compositesb.2018.08.026
22. Ghafoori E, Motavalli M. Lateral-torsional buckling of steel I-beams retrofitted by bonded and un-bonded CFRP laminates with different pre-stress levels: experimental and numerical study. Construction and Building Materials 2015;76194–206. https://doi.org/10.1016/j.conbuildmat.2014.11.070
23. Ghafoori E, Motavalli M, Nussbaumer A, Herwig A, Prinz G, Fontana M. Determination of minimum CFRP pre-stress levels for fatigue crack prevention in retrofitted metallic beams. Engineering Structures 2015;8429–41. https://doi.org/10.1016/j.engstruct.2014.11.017
24. Ghafoori E, Motavalli M, Nussbaumer A, Herwig A, Prinz G, Fontana M. Design criterion for fatigue strengthening of riveted beams in a 120-year-old railway metallic bridge using pre-stressed CFRP plates. Composites Part B: Engineering 2015;681-13. https://doi.org/10.1016/j.compositesb.2014.08.026
25. Ghafoori E, Hosseini A, Al-Mahaidi R, Zhao X-L, Motavalli M. Prestressed CFRP-strengthening and long-term wireless monitoring of an old roadway metallic bridge. Engineering Structures 2018;176585-605. https://doi.org/10.1016/j.engstruct.2018.09.042. http://www.sciencedirect.com/science/article/pii/S0141029618320224.
26. Hosseini A, Ghafoori E, Al-Mahaidi R, Zhao X-L, Motavalli M. Strengthening of a 19th-century roadway metallic bridge using nonprestressed bonded and prestressed unbonded CFRP plates. Construction and Building Materials 2019;209240-259. https://doi.org/10.1016/j.conbuildmat.2019.03.095
27. Hosseini A, Ghafoori E, Motavalli M, Nussbaumer A, Zhao X-L, Koller R. Prestressed Unbonded Reinforcement System with Multiple CFRP Plates for Fatigue Strengthening of Steel Members. Polymers 2018;10(3)264. http://www.mdpi.com/2073-4360/10/3/264.
28. Hosseini A, Ghafoori E, Motavalli M, Nussbaumer A, Zhao X-L, Al-Mahaidi R, Terrasi G. Development of prestressed unbonded and bonded CFRP strengthening solutions for tensile metallic members. Engineering Structures 2019;181550-561. https://doi.org/10.1016/j.engstruct.2018.12.020. http://www.sciencedirect.com/science/article/pii/S0141029618312926.
29. Hosseini A, Michels J, Izadi M, Ghafoori E. A comparative study between Fe-SMA and CFRP reinforcements for prestressed strengthening of metallic structures. Construction and Building Materials 2019;226976-992. https://doi.org/10.1016/j.conbuildmat.2019.07.169. http://www.sciencedirect.com/science/article/pii/S0950061819318434.
30. Izadi MR, Ghafoori E, Motavalli M, Maalek S. Iron-based shape memory alloy for the fatigue strengthening of cracked steel plates: Effects of re-activations and loading frequencies. Engineering Structures 2018;176953-967. https://doi.org/10.1016/j.engstruct.2018.09.021. http://www.sciencedirect.com/science/article/pii/S0141029618305042.
31. Izadi MR, Ghafoori E, Shahverdi M, Motavalli M, Maalek S. Development of an iron-based shape memory alloy (Fe-SMA) strengthening system for steel plates. Engineering Structures 2018;174433-446.
32. Fritsch E, Izadi M, Ghafoori E. Development of nail-anchor strengthening system with iron-based shape memory alloy (Fe-SMA) strips. Construction and Building Materials 2019;229117042. https://doi.org/10.1016/j.conbuildmat.2019.117042. http://www.sciencedirect.com/science/article/pii/S0950061819324845.
33. Izadi M, Hosseini A, Michels J, Motavalli M, Ghafoori E. Thermally activated iron-based shape memory alloy for strengthening metallic girders. Thin-Walled Structures 2019;141389-401. https://doi.org/10.1016/j.tws.2019.04.036. http://www.sciencedirect.com/science/article/pii/S0263823118314125.
34. Izadi M, Motavalli M, Ghafoori E. Iron-based shape memory alloy (Fe-SMA) for fatigue strengthening of cracked steel bridge connections. Construction and Building Materials 2019;227116800. https://doi.org/10.1016/j.conbuildmat.2019.116800. http://www.sciencedirect.com/science/article/pii/S0950061819322305.
35. Al-Mayah A, Soudki K, Plumtree A. Gripping Behavior of CFRP PrestressingRods for Novel Anchor Design. Special Publication 2005;230209-228.
36. Al-Mayah A, Soudki K, Plumtree A. Development and assessment of a new CFRP rod–anchor system for prestressed concrete. Applied Composite Materials 2006;13(5)321-334. https://doi.org/10.1007/s10443-006-9019-6

37. Al-Mayah A, Soudki K, Plumtree A. Novel anchor system for CFRP rod: Finite-element and mathematical models. Journal of Composites for Construction 2007;11(5)469-476.
38. Campbell T, Shrive NG, Soudki K, Al-Mayah A, Keatley J, Reda M. Design and evaluation of a wedge-type anchor for fibre reinforced polymer tendons. Canadian Journal of Civil Engineering 2000;27(5)985-992.
39. Sayed-Ahmed EY, Shrive NG. A new steel anchorage system for post-tensioning applications using carbon fibre reinforced plastic tendons. Canadian Journal of Civil Engineering 1998;25(1)113-127. https://doi.org/10.1139/l97-054
40. Schmidt JW, Bennitz A, Täljsten B, Goltermann P, Pedersen H. Mechanical anchorage of FRP tendons–A literature review. Construction and Building Materials 2012;32110-121. https://doi.org/10.1016/j.conbuildmat.2011.11.049
41. Schmidt JW, Bennitz A, Täljsten B, Pedersen H. Development of mechanical anchor for CFRP tendons using integrated sleeve. Journal of Composites for Construction 2010;14(4)397-405.
42. Schmidt JW, Smith ST, Täljsten B, Bennitz A, Goltermann P, Pedersen H. Numerical simulation and experimental validation of an integrated sleeve-wedge anchorage for CFRP rods. Journal of Composites for Construction 2011;15(3)284-292. https://doi.org/10.1061/(ASCE)CC.1943-5614.0000171
43. Bennitz A, Schmidt JW, Nilimaa J, Täljsten B, Goltermann P, Ravn DL. Reinforced concrete T-beams externally prestressed with unbonded carbon fiber-reinforced polymer tendons. ACI Structural Journal 2012;109(4)521.
44. Meier U. Extending the life of cables by the use of carbon fibers. in: Proc., International Association for Bridge and Structural Engineering Symp. 1995.
45. Ghafoori E Fatigue strengthening of metallic members using un-bonded and bonded CFRP laminates. 2015, ETH Zurich.
46. Hosseini A, Ghafoori E, Motavalli M, Nussbaumer A, Zhao X-L, Al-Mahaidi R. Flat prestressed unbonded retrofit system for strengthening of existing metallic I-Girders. Composites Part B: Engineering 2018;155156-172. https://doi.org/10.1016/j.compositesb.2018.08.026
47. Kulak GL, Fisher JW, Struik JH. Guide to Design Criteria for Bolted and Riveted Joints Second Edition. 2001.
48. Munse W, Petersen K. Strength of rivets and bolts in tension. Journal of the Structural Division 1959;85(3)7-28.
49. EOTA ETAG 013 Guideline for European Technical Approval of Post-Tensioning Kits for Prestressing of Structures. 2002, EOTA Brussels, Belgium.
50. fib IFfSC. Recommendations for the acceptance of post-tensioning systems 1993. Lausanne, Switzerland: fib.
51. Rostásy FS. Draft guidelines for the acceptance testing of FRP posttensioning tendons. Journal of Composites for Construction 1998;2(1)2-6. https://doi.org/10.1061/(ASCE)1090-0268(1998)2:1(2)
52. Al-Mayah A, Soudki K, Plumtree A. FEM and mathematical models of the interfacial contact behaviour of CFRP-metal couples. Composite Structures 2006;73(1)33-40.
53. DassaultSystèmes ABAQUS 6.14 analysis user's manual. 2014, Dassault Systems Inc Waltham, USA.
54. Wriggers P, Zavarise G. Computational contact mechanics. Encyclopedia of computational mechanics 2004.

3. Multiaxial fatigue criteria for steel connections

Motivation

Steel connections in civil structures are typically subjected to combined tension/compression, bending, and shear loading. The effect of this complex loading often complicates fatigue analysis. In this chapter, the multiaxial fatigue theory based on the critical plane approach is employed to identify the proper thresholds for the prediction of high-cycle fatigue crack initiation in angle connections considering the effect of the prestressed strengthening system. The introduced criteria enable the determination of the required prestressing force to prevent crack initiation in connections.

Summary

In Chapter 3, a literature review is presented on the experimental and numerical studies on the high-cycle fatigue behavior of angle connections subjected to distortion-induced stresses. After a brief introduction to the critical plane approach, a calculation procedure is introduced for the multiaxial fatigue analysis, and formulations of various multiaxial fatigue models are provided. The equations for the estimation of the fully reversed uniaxial and shear fatigue limits as a function of the material tensile strength are presented. The estimated fatigue limits are used in different multiaxial fatigue criteria to compare the obtained thresholds with the existing uniaxial and multiaxial fatigue test data on mild steel. To identify the appropriate thresholds for the prediction of crack initiation in angle connections, a series of fatigue tests are conducted on the steel connections, which are strengthened by the retrofitting system introduced in the previous chapter. By incorporating the effect of the prestressing force and residual stresses in the multiaxial fatigue models, proper thresholds are introduced, and the location of the crack initiation is identified. Finally, the effect of the prestressed strengthening system on increasing the fatigue strength of connections is evaluated.

Supplementary materials to this chapter is provided in Supplement B at the end of the thesis. This supplement gives: (i) MATLAB script for multiaxial fatigue analysis based on the critical plane approach, (ii) stresses in prestressed CFRP rods during fatigue tests, (iii) strain measurements in cut-compliance method, and (iv) probabilistic analysis of the fatigue test data.

Bibliographic details

Section 3.1 presents the paper with the following full bibliographic details:

- Hossein Heydarinouri, Alain Nussbaumer, Masoud Motavalli, Elyas Ghafoori. Multiaxial fatigue criteria for prestressed strengthening of steel connections. Submitted to International Journal of Fatigue and accepted on 4th of August 2021.

Author's contribution

Hossein Heydarinouri, as the first author of the above-mentioned paper, developed the theory and formulations, designed and performed the experiments, analyzed the results of the experiments, and wrote the manuscript. The co-authors provided support and supervision for the contents of this chapter.

3.1. Multiaxial fatigue criteria for prestressed strengthening of steel connections*

Abstract

In this study, the high-cycle fatigue behavior of bridge connections subjected to distortion-induced loadings (generating multiaxial stresses) and strengthened with prestressed elements were experimentally investigated. Thereafter, appropriate critical plane-based multiaxial fatigue thresholds based on the modified Wohler curve method (MWCM) and Fatemi-Socie's (FS) criteria were used to predict the initiation of cracks in the angles considering the estimated fully reversed uniaxial and shear fatigue limits as well as residual stresses. The prestressed strengthening system was effective in reducing the mean values as a result of the prestressing force, enabling a shift in the stress state to below the initiation threshold.

Keywords: multiaxial fatigue, critical plane approach, angle connections, crack initiation, distortion-induced loading, prestressed strengthening.

Nomenclature

a	Cut depth	ν	Poison's ratio
E	Elastic modulus	ρ	Critical plane stress ratio
F	vertical load due to the actuator	ρ_{lim}	Maximum critical plane stress ratio
FS	Fatemi-Socie model	σ_A	Fully reversed uniaxial fatigue limit
G	Shear modulus	σ'_A	Uniaxial fatigue limit for a rotating beam
$k_{a\text{-}f}$	Marin factors	$[\sigma_a]$	Cyclic stress matrix
$k_{x,\,y,\,z}$	Slope of stress increase in the x-, y- or z-direction	$\sigma_{a1,2,3}$	Principal stresses due to cyclic stresses
M_F	Bending moment due to the actuator load	$[\sigma_{eff}]$	Effective stress matrix
M_P	Bending moment due to the Prestressing force	$[\sigma_m]$	Static stress matrix
MWCM	Modified Wohler curve method	σ_{na}	Normal stress amplitude on critical plane
n_A	Ratio between σ_A and S_{ut}	σ_{nm}	Normal static stress on critical plane
n'_A	Ratio between σ'_A and S_{ut}	$\sigma_{n,max}$	maximum normal stress on critical plane
$n_{a1,2,3}$	Principal stress directions	$[\sigma_P]$	Stress matrix due to prestressing force
$n'_{a1,2,3}$	Directions for maximum shear stress amplitude planes	$[\sigma_{res}]$	Residual stress matrix
P	Prestressing force	$[\sigma_{res\text{-}b}]$	Residual stress due to imperfections
s	Distance of strain gauge from the cutting disk	$[\sigma_{res\text{-}m}]$	Residual stress due to manufacturing
S_{ut}	Material tensile strength	σ_x	Stress in the x-direction
S_y	Material yield strength	σ_y	Stress in the y-direction
$[\alpha]$	Transformation matrix	σ_z	Stress in the z-direction
β, k	Constants of FS model	$[\sigma_0]$	Initial stress state
γ_a	Shear strain amplitude on the critical plane	τ_A	Fully reversed shear fatigue limit
ε_a	Measured strain in the a-direction	τ_{xy}	Shear stress in the xy-plane
ε_b	Measured strain in the b-direction	τ_{xz}	Shear stress in the xz-plane
ε_c	Measured strain in the c-direction	τ_{yz}	Shear stress in the yz-plane
θ	The angle from the a-direction to n_{a1}	τ_α	Maximum shear stress amplitude on critical plane

* Hossein Heydarinouri, Alain Nussbaumer, Masoud Motavalli, Elyas Ghafoori. Submitted to International Journal of Fatigue, Accepted on 4th of August 2021.

3.1.1. Introduction

In many steel structures, the steel connections are subjected to a combined loading of tension/compression, bending, and shear. The effect of this complex loading often makes these details prone to fatigue. In bridges, the longitudinal beams are connected to the cross-girders using double-angle connections (see Fig. 1). These connections are one of the most fatigue-prone details in metallic bridges [1]. Distortion-induced loadings are the main cause of the fatigue problems in these connections [2-5]. Fatigue failures can occur in two forms: initiation of cracks near the fillet of the angles, or popping out of the rivet head [2, 6]. The cracks in the fillet areas of the angles occur due to the distortion-induced bending stresses [7]. The popping out of the rivet head originates from the prying effect as well as an insufficient clamping force in the rivets [8]. In this study, the initiation of fatigue cracks in the fillet area was investigated.

These connections are traditionally designed to carry only shear forces. Modern codes have provided specifications to improve the detailing of new connections. However, thousands of aging bridges are prone to fatigue cracks [3]. Therefore, to prolong the fatigue life, different strengthening solutions have been proposed, such as (i) applying stop holes [9], (ii) replacement of the rivets with high-strength bolts [10, 11], and (iii) softening the connections by removing the fasteners [12]. However, these retrofitting techniques do not permanently prevent the re-initiation of cracks [13].

In recent years, carbon fiber-reinforced polymers (CFRPs) have been used for retrofitting metallic structures, thanks to their superior properties in regards to high strength, light weight, and high corrosion resistance [14]. As bonded strengthening systems (see [15-17]) cannot be applied on the surface of riveted structures, prestressed unbonded systems have been proposed for strengthening the girders of metallic structures using mechanical clamping systems [18-24]. For bridge connections, both CFRP materials [25, 26], and shape memory alloy materials have been used [27, 28]. In this study, the prestressed strengthening system developed in [25] was employed for the fatigue strengthening of connections.

To consider the strengthening effect, a proper fatigue criterion is required for the prediction of fatigue cracks. In the following subsections, previous experimental and numerical studies on the high-cycle fatigue behaviors of these connections are reviewed.

3.1.1.1. High-cycle fatigue behavior of the connections

3.1.1.1.1. Experimental studies

A large number of tests have been conducted on several full-scale riveted members dismantled

from old bridges in recent decades, with the rivets essentially subjected to shear. A common conclusion from these studies is that the detail category C71 (71 MPa is the characteristic fatigue strength at 2 million cycles) in Eurocode 3 [29], corresponding to category D from the American Association of State Highway and Transportation (AASHTO) [30], provides a lower bound for the prediction of fatigue strength in new riveted members [9, 31-35]. However, these studies did not specifically focus on riveted connections subjected to secondary distortion-induced tensile loading.

Wilson and Coombe [7] conducted fatigue tests on three series of riveted connections subjected to tensile loading, as shown in Fig. 1(a). It was reported that fatigue failures occurred in the angle fillets and rivet heads. An analytical model was also provided but considerably overestimated the stresses in the angles, thus triggering the comment that one should always be careful regarding the ways stress range/number of cycles (S-N) data are presented, that is, how is the stress range is evaluated/plotted.

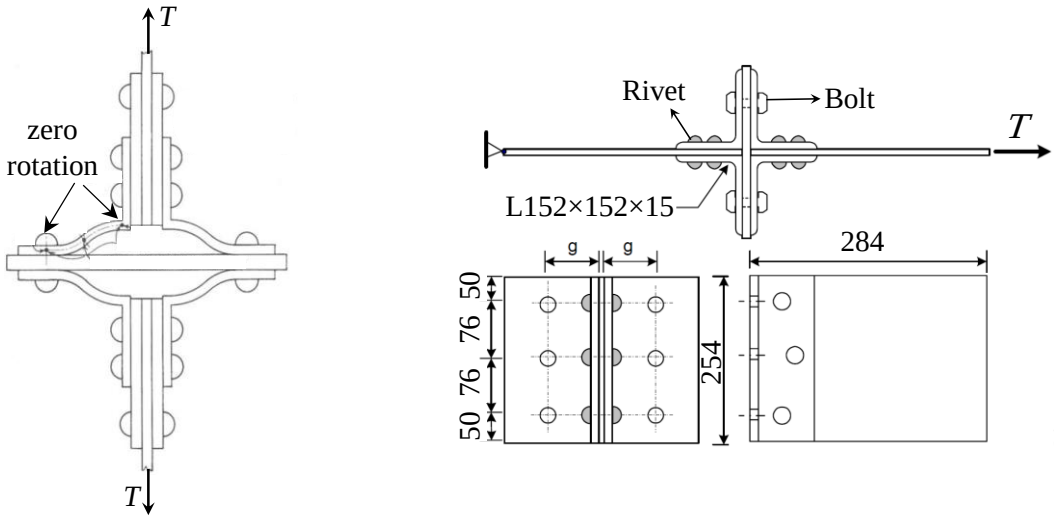

(a) Tests by Wilson and Coombe's [7] (b) Tests by Wang [36]

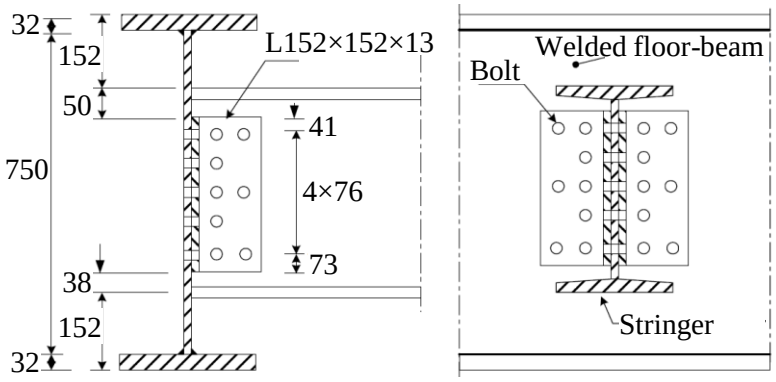

(c) Tests by Abouelmaaty [37]

Fig. 1. Fatigue tests on riveted/bolted connections from literature.

Wang [36] conducted fatigue tests on 16 double-angle connections cut from an old riveted

bridge girder and subjected to tensile loading, as shown in Fig. 1(b). The main findings of this study were as follows: (i) fatigue cracks initiated exclusively from the angle fillets, except for one case, in which after crack initiation in the fillets, another fatigue crack developed in the outstanding leg at the bolt line; (ii) the strain measurements showed that the flexural stresses at the angles were always lower than those the model proposed in [7]; and (iii) the stress distribution, both across and along the depth of the connection, was uneven. Higher stresses were registered near the angle fillet than near the bolt line.

Abouelmaaty [37] performed fatigue tests on bolted stringer-to-floor-beam connections. In the tests, high-strength bolts were used instead of rivets. Two newly manufactured full-scale specimens were tested under constant-amplitude loading. Each test specimen consisted of a 3-m-long hot-rolled stringer connected to a 1.2-m welded girder representing a floor-beam. A view of this connection is shown in Fig. 1(c). In all of the tests, the fatigue cracks initiated in the web of the floor-beam at the locations where the upper and lower flanges of the stringer came into contact with the floor-beam web. This was owing to the local out-of-plane bending in the web of the floor-beam. Therefore, the results of this study cannot be used for the fatigue behavior of connections, as the cracks initiated somewhere else.

3.1.1.1.2. Numerical studies

Al-Emrani and Kliger [38] developed finite element (FE) and analytical models for a double-angle web-to-web connection, and verified the models based on experimental results. The results of this study showed that the rivet clamping force does not have a significant effect on the stiffness of the connection. This was also observed by Imam et al. [39]. Nevertheless, it was shown that a higher rivet clamping force resulted in a lower stress range in the rivets. However, no fatigue model was proposed for predicting the fatigue life of the connections.

Imam et al. [39] developed global-local FE models for identifying the most fatigue-critical locations in stringer-to-floor-beam connections using plain S-N curve and Miner's rule for fatigue damage calculations; they used the rain flow technique for counting the stress cycles due to the passage of a train. The possible locations for initiation of the cracks in the angles and rivets were identified, based on the maximum principal hot-spot stresses. However, the accumulated damage in the angles and rivets was computed without considering the effect of the mean stress, which is more pronounced in rivets with high tensile residual stresses.

3.1.1.2. Gaps to be filled in this study

In the experimental and numerical studies mentioned above, no criteria were proposed for the

prediction of crack initiation under high-cycle fatigue in connections. In addition, no one has considered the multiaxial state of stress in the critical location of the angle connections, except in [39], where only the equivalent maximum principal stress was considered, and without any experimental evidence of its accuracy.

In this study, for the first time to the authors' knowledge, the multiaxial stress state in the critical location of the connections was measured using rosette strain gauges, and a multiaxial criterion was validated. The residual stresses due to the manufacturing process and fastening of the bolts were considered in the prediction models. The critical location of the connections was identified. Finally, using a critical plane-based multiaxial fatigue theory, an appropriate threshold for the prediction of crack initiation in the angles was proposed, enabling the consideration of the positive effects of a strengthening system.

The fatigue tests were performed on two angles subjected to distortion-induced loadings using the setup shown in Fig. 2. In the setup, the actuator applied a vertical load of F near the cantilever tip, thereby applying a shear force of F and bending moment of M_F to the connections. In addition, the mechanical clamping system held a prestressed element. The prestressing element applied a compressive force of P and a bending moment of M_P, which counteracted M_F.

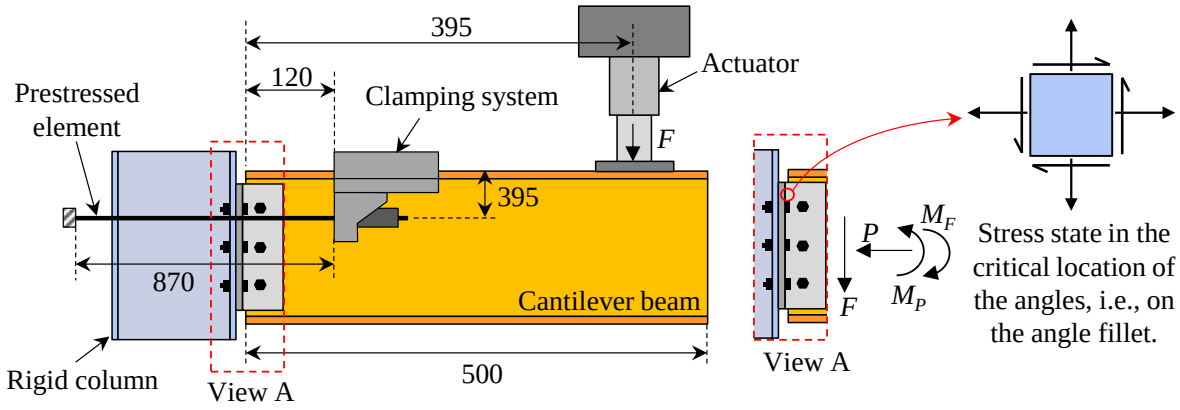

Fig. 2. Fatigue test setup (the dimensions are in mm).

As shown in Fig. 2, in addition to the normal stresses in different directions due to the out-of-plane deformation, shear stress is present at the critical location of the angles (in the fillet area). Therefore, using this setup, the multiaxial stress and strengthening effects are simultaneously considered.

3.1.1.3. Outline of this study

In this paper, first, the critical plane approach is briefly described, and the fatigue models used

in the analyses are introduced. Second, the calculation procedure for the multiaxial fatigue analysis is explained. Third, the formulations for the multiaxial fatigue models and estimations of the fatigue limits are presented, and then are compared with the existing test data. Fourth, different parts of the fatigue test setup and instrumentation are described. Fifth, the results of the fatigue tests are presented, considering the different sources of residual stresses prior to fatigue loading. Sixth, the appropriate threshold for the prediction of crack initiation in the angle is determined. Finally, the effect of the prestressed strengthening system on increasing the fatigue strength of the angles is highlighted.

3.1.2. Critical plane approach

The fatigue cracks in ductile materials such as mild steel nucleate on the plane with the maximum shear stress amplitude τ_a known as the critical plane [40, 41]. In addition to the maximum shear stress amplitude, the maximum normal stress acting on the critical plane, $\sigma_{n,max}$, affects the fatigue strength. $\sigma_{n,max}$ helps to open the microcracks and reduce the interlocking and friction between the surfaces of the crack [42], as shown in Fig. 3.

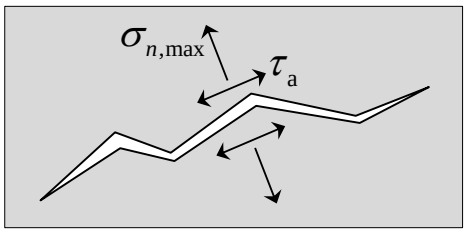

Fig. 3. Required parameters in the stress-based critical plane approach.

Various stress- or strain-based critical plane models have been proposed by different researchers [41]. The difference between the models lies in how the maximum shear stress/strain amplitude is combined with the maximum normal stress/strain on the critical plane. In this study, two different critical plane-based models were employed for the multiaxial fatigue analysis, that is, the modified Wohler curve method (MWCM) [42, 43] and Fatemi-Socie (FS) model [40]. The detailed formulations for each model are briefly presented in later sections.

3.1.3. Calculation procedure for multiaxial fatigue analysis

In this section, the step-by-step calculation procedure implemented in a MATLAB code (version R2018a) for the stress-based multiaxial fatigue analysis is described. The proposed procedure is valid only for proportional loadings.

(i) Determination of the stress state in the critical location

Fig. 4 shows an arbitrary state of stress for all six stress components at the critical location. As shown in the figure, the stress cycle corresponding to each stress component is identified by the stress amplitude (the amplitude, and not the stress range, is used) and mean stress.

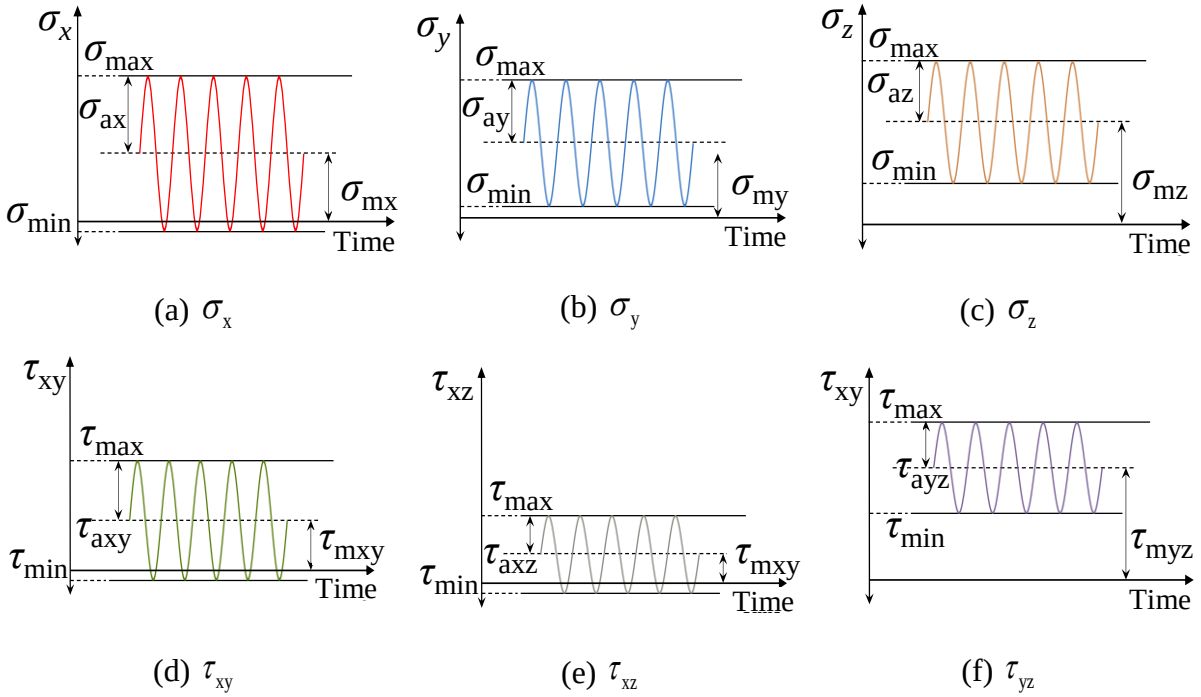

Fig. 4. Arbitrary stress state in the critical location.

(ii) Cyclic and static stress matrices

As the critical plane is defined according to the cyclic portion of the stress cycles, it is necessary to divide the stress cycle corresponding to each stress component into a cyclic $[\sigma_a]$ and static $[\sigma_m]$ portion, as given in Eq. (1).

$$[\sigma_a]=\begin{bmatrix}\sigma_{ax} & \tau_{axy} & \tau_{axz}\\ \tau_{axy} & \sigma_{ay} & \tau_{ayz}\\ \tau_{axz} & \tau_{ayz} & \sigma_{az}\end{bmatrix} \text{ and } [\sigma_m]=\begin{bmatrix}\sigma_{mx} & \tau_{mxy} & \tau_{mxz}\\ \tau_{mxy} & \sigma_{my} & \tau_{myz}\\ \tau_{mxz} & \tau_{myz} & \sigma_{mz}\end{bmatrix} \quad (1)$$

(iii) Determination of the cyclic stress components on the critical plane

The critical plane is defined as the plane with the maximum shear stress amplitude τ_α. To calculate τ_α, the eigenvalues of matrix $[\sigma_a]$ are calculated to obtain the principal stresses σ_{a1}, σ_{a2}, and σ_{a3}. The expression for τ_a is obtained using Eq. (2).

$$\tau_a=\frac{\sigma_{a1}-\sigma_{a3}}{2} \quad (2)$$

The normal stress on the plane with the maximum shear stress amplitude due to the cyclic portion of the stress cycles is calculated using Eq. (3).

$$\sigma_{na} = \frac{\sigma_{a1} + \sigma_{a3}}{2} \tag{3}$$

(iv) Determination of the critical plane directions

The principal stress directions, i.e., n_{a1}, n_{a2}, and n_{a3}, as shown in Fig. 5, are the eigenvectors of the matrix $[\sigma_a]$. The directions of the planes with the maximum shear stress amplitude n'_{a1} and n'_{a3}, i.e., the critical plane directions, are obtained by rotating the principal coordinate system by 45° around the second principal direction n_{a2}.

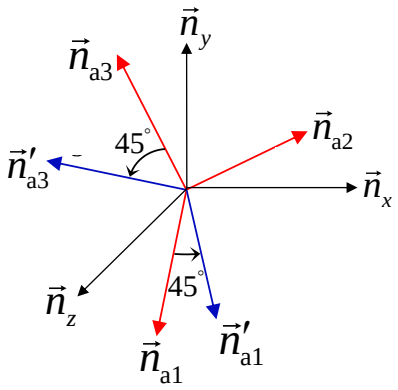

Fig. 5. Principal directions and directions of the critical plane.

The transformation matrix [α] is defined as follows:

$$[a] = [\vec{n}_{a1}\ \vec{n}_{a2}\ \vec{n}_{a3}]^T \tag{4}$$

The normal directions of the critical planes are defined as follows:

$$\vec{n}'_{a1} = [a]^T \times \begin{bmatrix} \cos 45 \\ 0 \\ -\sin 45 \end{bmatrix},\ \vec{n}'_{a2} = [a]^T \times \begin{bmatrix} 0 \\ 1 \\ 0 \end{bmatrix}, \text{ and } \vec{n}'_{a3} = [a]^T \times \begin{bmatrix} \sin 45 \\ 0 \\ \cos 45 \end{bmatrix} \tag{5}$$

The transformation matrix constructed with the critical plane directions is calculated using Eq. (6).

$$[a'] = [\vec{n}'_{a1}\ \vec{n}'_{a2}\ \vec{n}'_{a3}]^T \tag{6}$$

This matrix is used to obtain the mean stress components in the critical plane directions.

(v) Determination of static stresses in the critical plane directions

The stress components on the critical plane due to the static portion of the stress cycles must be calculated to obtain $\sigma_{n,max}$. The static stress matrix in the critical plane directions $[\sigma'_m]$ is computed using Eq. (7).

$$[\sigma'_m] = [a'] \times [\sigma_m] \times [a']^T \quad (7)$$

Considering that only the normal static stress affects the fatigue strength, i.e., the static shear stress does not have an influence on the fatigue strength [41], only the normal stress components in the n'_{a1} and n'_{a3} directions, i.e., σ'_{m11} and σ'_{m33} are considered. The plane with the maximums (σ'_{m11}, σ'_{m33}) is considered as the critical plane. The normal stress due to the static portion of the stress cycles σ_{nm} is obtained as follows:

$$\sigma_{nm} = \max.(\sigma'_{m11} \text{ and } \sigma'_{m33}) \quad (8)$$

(vi) Determination of the maximum normal stress on the critical plane

The maximum normal stress $\sigma_{n,max}$ is the sum of the normal stresses due to the cyclic and static portion of the stress cycles, and is obtained using Eq. (9).

$$\sigma_{n,\,max} = \sigma_{na} + \sigma_{nm} \quad (9)$$

(vii) Predicting the fatigue failure using a critical plane-based criterion

In the final step, the maximum shear stress amplitude, τ_a, and maximum normal stress acting on the critical plane, $\sigma_{n,max}$, are used in a stress-based critical plane model for fatigue failure prediction.

3.1.4. Stress-based critical plane models

In this section, the MWCM [44] and FS [40] critical plane-based fatigue models are considered, and the required formulations are presented and derived.

3.1.4.1. Modified Wohler curve method (MWCM)

The equation proposed in the MWCM is as follows [44]:

$$\tau_a + (\tau_A - \frac{\sigma_A}{2})\rho = \tau_A \quad (10)$$

In this equation, τ_A and σ_A are the fully reversed shear and uniaxial fatigue limits, respectively. The parameter ρ is the critical plane stress ratio; it is defined as the ratio between τ_a and $\sigma_{n,max}$, as follows:

$$\rho = \frac{\sigma_{n,max}}{\tau_a} \tag{11}$$

The MWCM diagram is shown in Fig. 6. Based on Eq. (10), a fatigue crack initiates when the combination of the shear and normal stresses on the critical plane on the left side of the equation exceeds τ_A. The MWCM threshold is plotted using two sets of experimental data. For the cases of fully reversed shear and uniaxial cyclic loading, the ρ values equal 0 and unity, respectively.

The mean stress effect is accounted for by the parameter ρ; an increase in the mean stress, and consequently the ρ value, results in a smaller permissible τ_a. Considering Eq. (10) and (11), the MWCM mathematically leads to a maximum limit ρ_{lim}, as follows:

$$\rho_{lim} = \frac{\tau_A}{2\tau_A - \sigma_A} \tag{12}$$

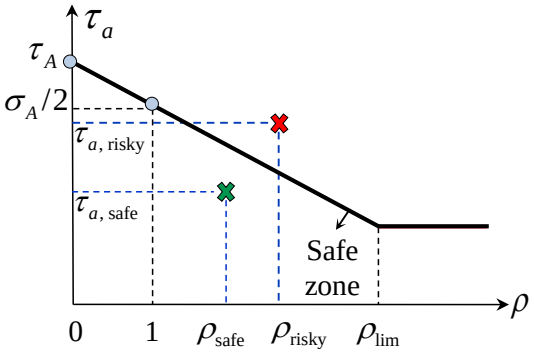

Fig. 6. Modified Wohler curve method (MWCM) diagram.

In the diagram shown in Fig. 6, the fatigue limit remains constant for ρ values greater than ρ_{lim} because for large ρ values, it is assumed that the microcracks are always fully open. Thus, a further increase in the normal mean stress, and consequently the ρ value, does not result in a reduction in the friction and interlocking between the crack surfaces. Therefore, for $\rho > \rho_{lim}$, the fatigue limit τ_a does not decrease with an increase in ρ [44].

3.1.4.2. Fatemi-Socie's (FS) model

The FS model is originally considered as a strain-based model, as follows:

$$\gamma_a (1 + k \frac{\sigma_{n,max}}{S_y}) = \beta \tag{13}$$

In the above, k and β are constants, and γ_a and S_y are the shear strain on the critical plane and material yield strength, respectively. The value of the constant β can be obtained based on

calibrating the model with the results of the fully reversed shear tests, where $\sigma_{n,max}$=0. The value of k can be determined based on calibration with experimental data. When the test data are not available, the first approximation is k=l [45]. As the stresses are elastic in this study, $\gamma_a=\tau_a/G$, where G is the shear modulus. Thus, the FS model can be rewritten as follows:

$$\tau_a(1+k\frac{\sigma_{n,\max}}{S_y})=\tau_A \tag{14}$$

For consistency, the FS model is expressed with the ρ value defined in Eq. (11), and reformulated as follows:

$$\tau_a=\sqrt{(\frac{S_y}{2k\rho})^2+\frac{S_y}{k\rho}\tau_A}-\frac{S_y}{2k\rho} \tag{15}$$

3.1.4.3. Estimation of the fully reversed fatigue limits

3.1.4.3.1. Fully reversed uniaxial fatigue limit σ_A

The fully reversed uniaxial fatigue limit for a rotating beam, σ'_A, has a correlation with the material tensile strength S_{ut} [46, 47]. The ratio between σ'_A and S_{ut} is considered using the ratio n'_A, as follows:

$$n'_A=\frac{\sigma'_A}{S_{ut}} \tag{16}$$

As σ'_A is obtained under controlled laboratory conditions, the fully reversed uniaxial fatigue limit σ_A, is smaller than σ'_A in service conditions, and is estimated as follows:

$$\sigma_A=k_a k_b k_c k_d k_e k_f \times n'_A S_{ut} \tag{17}$$

The Marin factors k_a, k_b, k_c, k_d, k_e, and k_f serve as reduction factors for considering the detrimental effects of the surface condition, size, loading, temperature, and miscellaneous effects, respectively [47, 48]. The ratio n_A is defined as follows:

$$n_A=k_a k_b k_c k_d k_e k_f \times n'_A \tag{18}$$

Therefore, Eq. (17) can be reformulated as follows:

$$n_A=\frac{\sigma_A}{S_{ut}} \tag{19}$$

Considering that for carbon steel, the value of n'_A is between 0.4 and 0.6, and that the upper limit of each Marin factor is unity [20, 47], the upper limit for n_A is equal to 0.6. In general, the

smaller the value of n_A, the more conservative the obtained threshold. A more conservative estimation of σ_A, which can be used for design purposes, is obtained using Johnson's formulation [49], as follows:

$$\sigma_A = \frac{S_{ut}}{3} \tag{20}$$

Estimation of σ_A using Johnson's formulation leads to n_A =0.33.

3.1.4.3.2. Fully reversed shear fatigue limit τ_A

The fully reversed shear fatigue limit τ_A can be estimated based on the von Mises hypothesis, as follows:

$$\tau_A = \sigma_A / \sqrt{3} \tag{21}$$

This hypothesis has been verified based on a large amount of experimental data, and has been found to lead to a relatively accurate estimations for the prediction of multiaxial fatigue for different stress ratios [42].

3.1.4.4. Comparison with experimental data

In this subsection, the thresholds based on the MWCM and FS models are compared with existing experimental data on the mild steel from uniaxial and multiaxial fatigue tests. For the fatigue limits, the estimated values presented in Subsection 4.3 are applied.

Fig. 7(a) shows the experimental results for mild steel, with S_{ut} =410 MPa, under uniaxial cyclic stresses with the non-zero mean stress taken from [50]. In this figure, the MWCM threshold was calibrated using two experimental datasets: one with zero mean stress and the other with non-zero mean stress, resulting in a threshold with n_A=0.46. The MWCM thresholds with n_A=0.4 and 0.45 are also plotted. Furthermore, the threshold based on the FS model is plotted using Eq. (15), considering τ_A= 106.5 MPa, k=1, and S_y=300 MPa (which was not provided in [50]).

Fig. 7(b) depicts the experimental results for mild steel, with $S_{ut=}$382 MPa subjected to in-plane, in-phase, and out-of-phase fully reversed shear and normal stresses [51, 52]. The calibrated MWCM threshold using two experimental datasets, with n_A=0.62, as well as those with n_A=0.45 and 0.55 are plotted in this figure. For the FS threshold, τ_A=135.7 MPa, k=1 and S_y=300 MPa are used.

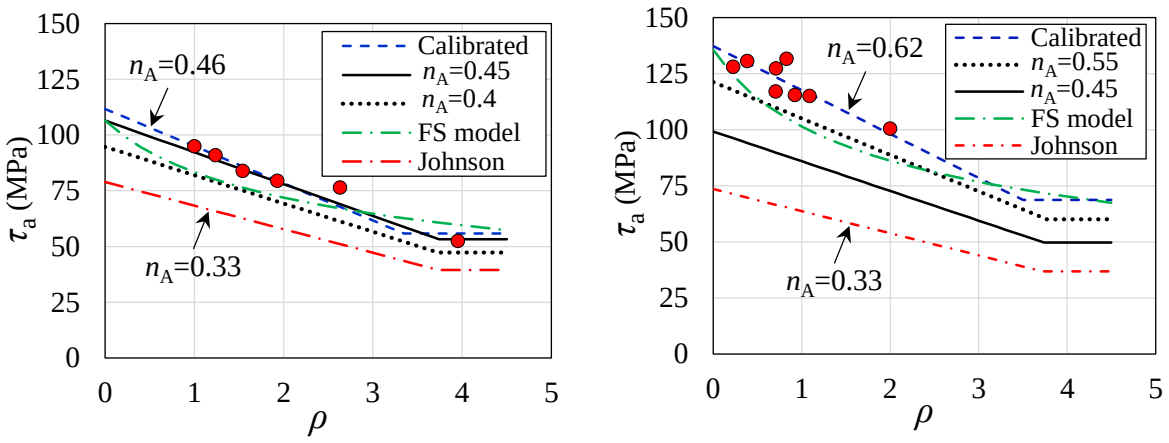

(a) Uniaxial loading with zero and non-zero mean stresses (experimental data was taken from [50])

(b) Multiaxial fully reversed in-phase and out-of-phase bending and torsion (experimental data was taken from [42, 51, 52])

Fig. 7. Comparison of the MWCM, FS, and design thresholds with the existing experimental results.

The two plots in Fig. 7 show that the ratio n_A can be adjusted to fit the MWCM threshold to the experimental data; a reduction in the ratio n_A results in a more conservative threshold. For the uniaxial and multiaxial fatigue results, different n_A ratios, i.e., n_A=0.4, and n_A=0.55, respectively, lead to MWCM thresholds below the experimental data points. For the FS model, except for a single data point with a high mean stress from the uniaxial test results, all of the other data points are above the model threshold. For all the experimental data, the most conservative criterion is the threshold based on Johnson's formulation in Eq. (20), with n_A=0.33.

3.1.5. Description of the test setup

3.1.5.1. Different parts of the setup

The setup used for the fatigue tests is illustrated in Fig. 8. In this setup, a cantilever IPB 240 beam, made of S235 steel with a length of 0.5 m, was connected to a stiff shear wall using two L70×70×7 angles, each with a length of 160 mm. The angles were hot-rolled S235 steel, with S_{ut}=440 MPa, S_y=325 MPa, and an elasticity modulus of E=192 GPa, according to the coupon test results based on DIN EN ISO 6892-1 [53].

An attaching plate was placed between the angles and shear wall, with a thickness of 40 mm. Each angle was connected to the front surface of the attaching plate using three M16, 10.9 bolts. The back surface of the attaching plate was connected to the shear wall by eight M20, 8.8 bolts to provide sufficient stiffness against out-of-plane deformations. Vertical cyclic loads were applied to the cantilever beam using a 125-kN Amsler hydraulic actuator located at a distance of

395 mm from the fixed end of the cantilever (see Fig. 2).

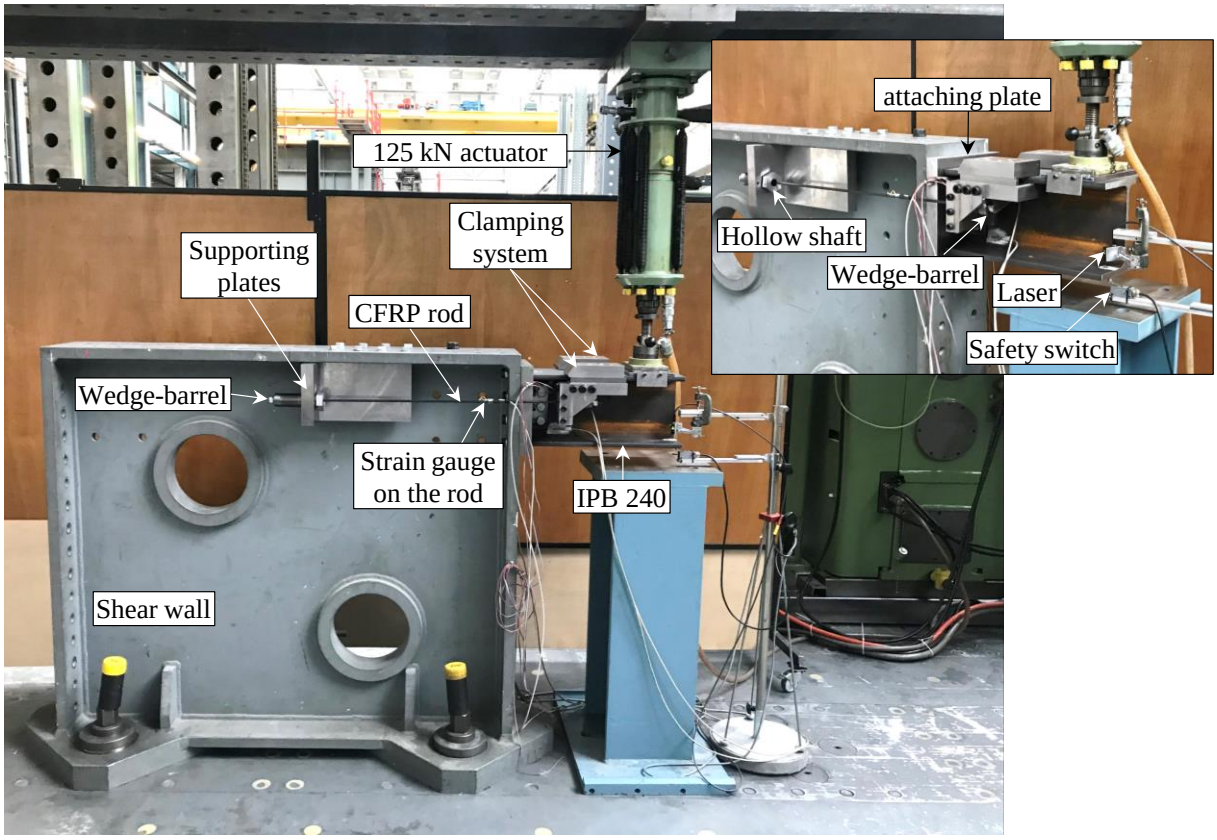

Fig. 8. Different parts of the test setup.

The connections were strengthened with two prestressed elements positioned symmetrically on both sides of the beam. CFRP rods and steel rods were used as the prestressed elements. The diameter of the unidirectional CFRP rods was 8 mm, and they were manufactured by S&P Clever Reinforcement Company AG, Switzerland, with a nominal tensile strength of 102.9 kN (equivalent to 2047 MPa), a fiber volume fraction of 65%, and an elastic modulus of 160 GPa in the fiber direction. The steel rods were high-strength M13 threaded elements with a tensile strength of 150 kN. Each CFRP rod was held by two wedge-barrel anchors on both sides. The reliable static and fatigue performances of wedge-barrel anchors are presented in [54]. The steel elements were anchored using nuts in the threaded area.

The prestressed elements applied a compressive force of P to the connections, resulting in a reduction of the distortion-induced stresses in the angles. The prestressing force was transmitted to the beam purely through friction, using the clamping system shown in Fig. 8. The clamping system consisted of different plates bolted to each other, and was attached to the top flange of the beam. The static and fatigue behavior of the clamping system are reported in [25]. On the other end, the prestressed elements rested on the supporting plates. Each supporting plate was

fixed to the shear wall through four M20, 8.8 bolts.

A hydraulic pump was used to pull the rods, as shown in Fig. 9. Nuts and threads were used for the steel rods. For the CFRP rods, the prestressing force was applied to the wedge-barrel anchors using the connector shown in Fig. 9. This connector was also used to preset the wedges. Detailed information regarding the prestressing and presetting procedures of the CFRP rods can be found in [25]. The dimensions of the setup are shown in Fig. 2.

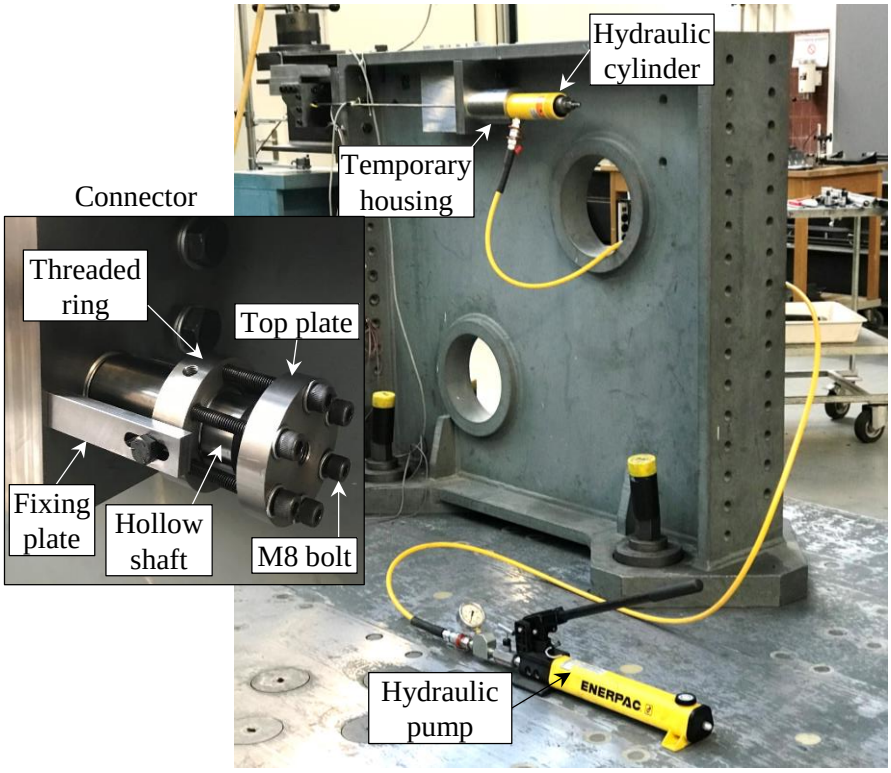

Fig. 9. Presetting and prestressing the CFRP rods.

3.1.5.2. Instrumentation

Fig. 10(a) shows a rosette strain gauge type RY8x-3/120 (HBM, AG, Darmstadt, Hesse, Germany), which was applied on each angle in the fillet area considered as the critical location. The rosette strain gauge measured the strains in three different directions: the b-direction was horizontal, and the a- and c-directions had a 45° deviation from the b-direction. The grid length was 3 mm. The critical location of the angle is shown in Fig. 10(b), and was determined using an FE model before being verified based on test results. The descriptions of the developed FE model are beyond the scope of this study, and will be presented in a separate study. The rosette strain gauges were partly applied on the fillets of the angles in the back leg, i.e., the leg that was bolted to the beam.

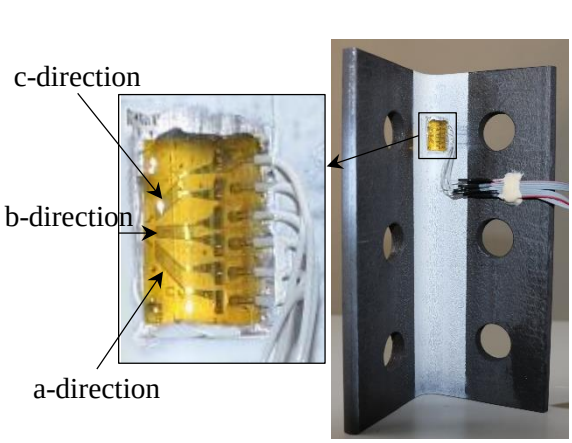

(a) Direction of the grids

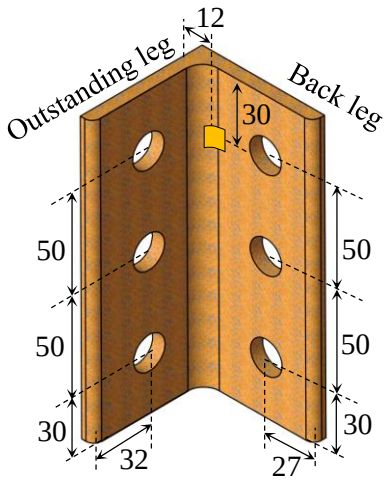

(b) Location of the rosette strain gauge on the angle

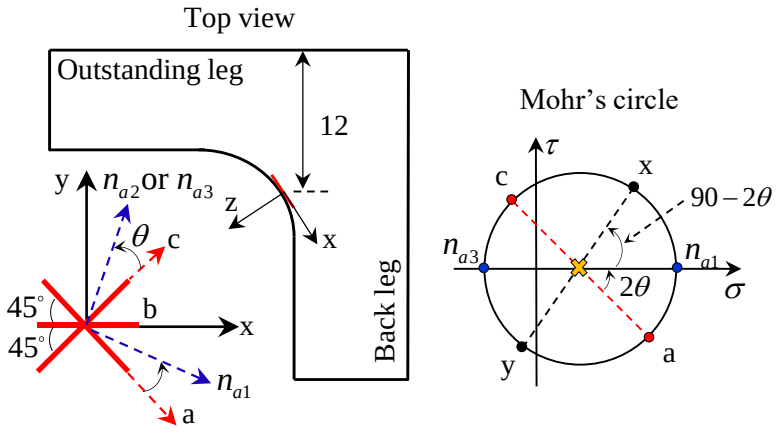

(c) Coordinate system and Mohr's circle

Fig. 10. Measurement of the strain in the critical location of the angles using rosette strain gauges.

The strains were measured on the xy-plane, as shown in Fig. 10(c). Using the measured strains in the a-, b-, and c-directions as well as Mohr's circle, as schematically shown in Fig. 10(c), the stresses were calculated in the xy-plane. As there was a plane-stress condition at the surface, $\sigma_z=\tau_{xz}=\tau_{yz}=0$. The calculations were implemented in a MATLAB code using the equations given in Appendix A.

3.1.6. Initial stress state

The stress state in the critical location of the angle before the application of the actuator loads $[\sigma_0]$ was considered as the initial stress state. The initial state depended on the residual stresses $[\sigma_{res}]$, as well as on the compressive stresses due to the prestressing force $[\sigma_P]$, which is expressed as follows:

$$[\sigma_0]= [\sigma_{res}]+[\sigma_P] \quad (22)$$

3.1.6.1. Residual stresses

The residual stresses originate from the manufacturing process [$\sigma_{res,\ m}$] and fastening of the bolts [$\sigma_{res,\ b}$] owing to the existence of geometric imperfections in the angles. Therefore, the total residual stress at the critical location was obtained using the following formulation:

$$[\sigma_{res}]= [\sigma_{res,\ m}]+[\sigma_{res,\ b}] \quad (23)$$

3.1.6.1.1. Residual stress due to manufacturing process

Generally, the residual stress distribution due to the manufacturing process in hot-rolled steel profiles is attributed to the cooling process, as well as the cold work for straightening the profiles [55]. In the corresponding codes, there are recommendations to consider these residual stresses [56, 57]. For steel angle (L-shape) profiles, the residual stresses in the longitudinal direction are considered to reach 20–30% of the steel yield strength [56-58]. In these recommendations, only longitudinal residual stresses are addressed, as they play an important role in the buckling of the profiles. For the angles used in this study, the residual stresses in different directions were of interest, and were unavailable from the above-mentioned recommendations. In addition, the effects of the bolt holes as well as cutting the long profiles into 160-mm-long pieces could change the residual stress state in the critical location of the angle. For this reason, it was not possible to predict the state of the residual stresses; therefore, a series of destructive tests were conducted to obtain a rough estimation of the values at the locations of interest, as explained below.

The sectioning method has been commonly used to measure the residual stresses in angle profiles [59]. This method was previously used for measuring the residual stresses in I-shaped profiles [60], but again, only in the longitudinal direction. In this study, a crack-compliance (or cut-compliance) method [61] was used to measure [$\sigma_{res,\ m}$] in the critical location of the angles in both the longitudinal and transverse directions. In this method, a cut was introduced into the surface, and the strain in the vicinity of the cut was measured as a function of the cut depth a. The setup is shown in Fig. 11(a). The cuts were introduced by a diamond cutting disk with a diameter of 20 mm and thickness of 0.5 mm. A strain gauge was applied at a distance of s=2.61 mm from the cut edge.

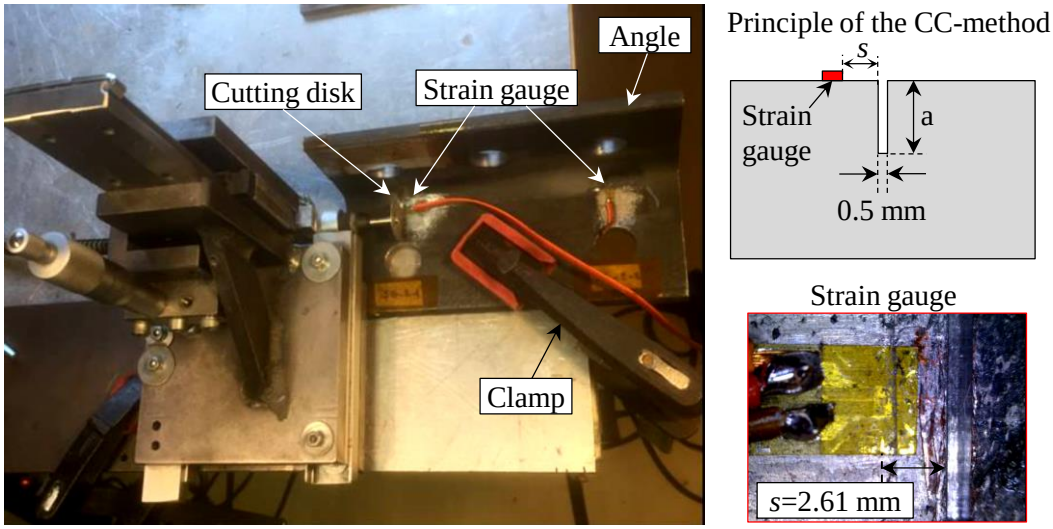

(a) Setup for destructive measurement of the residual stresses (CC: cut-compliance)

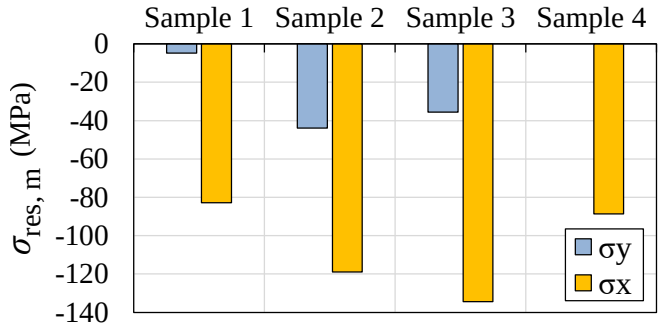

(b) Residual stresses at a=0.3 mm (measurement for σ_y in sample 4 was invalid)

Fig. 11. Residual stresses due to manufacturing process.

The residual stresses were derived based on the unique mathematical relations between the measured strains and residual stresses acting prior to the introduction of the cut perpendicular to the cut plane. In this study, the residual stress was considered as the equivalent average stress acting on a surface layer of thickness a, which would produce the same stress intensity factor at the tip of a hypothetical crack. For detailed information regarding this method, see [61-64].

The measurements were performed on four samples (angles). The residual stresses depended on the cut depth. The equivalent residual stresses as a function of the cut depth a are presented in Appendix B. To consider [$\sigma_{res,\,m}$] for the analyses, a cut depth of 0.3 mm was chosen. The results of the measured equivalent stresses in the x- and y-directions corresponding to a cut depth of 0.3 mm are shown in Fig. 11(b). The results show that the residual stresses in the x-direction (transverse direction) are significantly greater than those in the y-direction.

All of the residual stresses [$\sigma_{res,\,m}$] in the different directions, as shown in Fig. 11(b), were compressive, which would increase the fatigue strength. As the most conservative approach,

the maximum values were assumed for [$\sigma_{res,\ m}$] in the angles. Therefore, $\sigma_{res,\ m\text{-}x}$=-135 MPa and $\sigma_{res,\ m\text{-}y}$=-44 MPa were chosen in the x- and y-directions from samples 3 and 2, respectively. It should be noted that for the sample 4, the measurement in the y-direction was not correctly performed.

3.1.6.1.2. Effect of fastening the bolts

The residual stresses due to fastening of the bolts, [$\sigma_{res,\ b}$], depended mainly on the geometrical imperfections of the angles and clamping force of the fasteners. In all of the tests, the bolts were fastened to a standard torque, and the clamping force in all bolts were identical. However, it was observed that the geometrical imperfections led to a different stress state at each angle.

For all of the tested angles, the stress components during fastening the bolts were measured using the rosette strain gauges (see Fig. 10) and the results of the measurements are shown in Fig. 12. In Fig. 12, the angle A1-L indicates the angle in specimen 1 located on the left-hand side of the cantilever beam. As shown in the figure, a consistent pattern was not observed for [$\sigma_{res,\ b}$]. For example, the stress in the x-direction for the angle A2-L is approximately 200 MPa, whereas for angles A1-L and -R, it is 20 and 102 MPa, respectively. This demonstrates a significant scatter in the results. For the angle A3-A5-L, the residual stresses have a lower scatter, that is, the stress in the x-direction was in the order of 150–170 MPa.

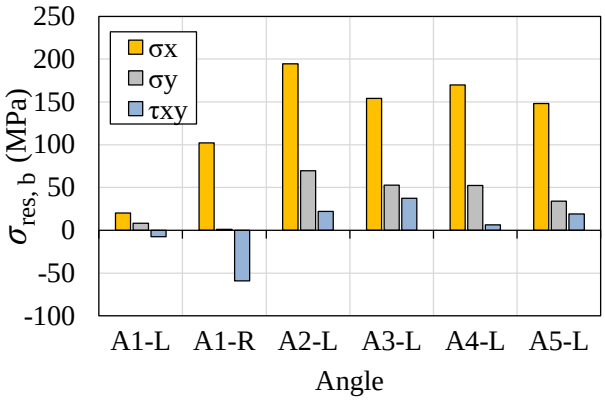

Fig. 12. Residual stress components in different angles due to fastening the bolts.

3.1.6.2. Effect of the prestressing force

In addition to the residual stresses, the application of the prestressing force changed the stress state in the angle before the application of the actuator loads. Due to the application of the prestressing force, the stresses in different directions, which were measured by the rosette strain gauges, were simultaneously reduced for all angles. As an example, Fig. 13 shows that for the

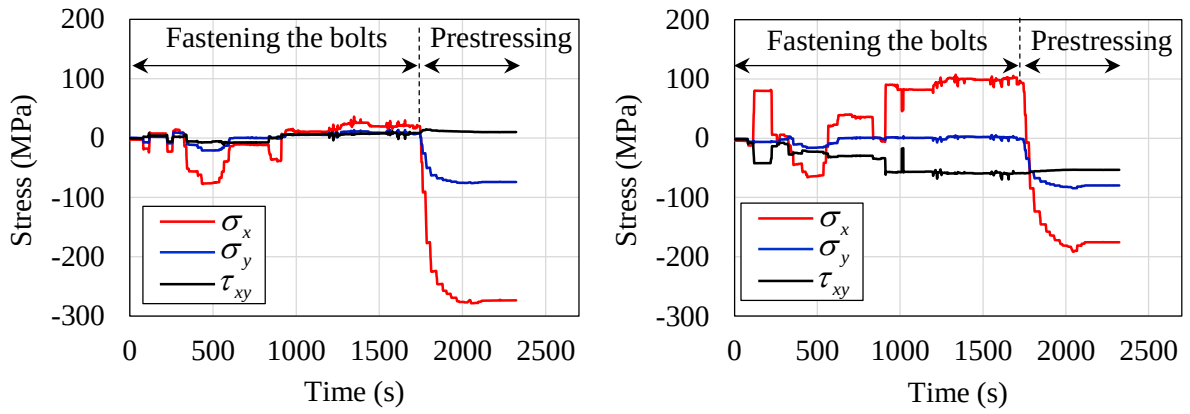

(a) A1-L (b) A1-R

Fig. 13. Stress components for the angles A1-L and A1-R during fastening the bolts and prestressing up to P=39.2 kN.

angles A1-L and A1-R, the application of a prestressing force of P=39.2 kN resulted in a reduction of approximately 280 and 80 MPa in the stresses in the x- and y-directions, respectively, without a significant effect on the shear stresses. The same trend was observed for the other angles.

It is noted that Fig. 13 shows also the development of stress components during the fastening of the bolts (i.e., installation of the angle connections) prior to the application of prestressing force to the angles A1-L and A1-R. The measurements indicated a significant difference for the stresses components in these two angles (as also shown in Fig. 12).

3.1.7. Fatigue test results

3.1.7.1. Effective stresses in the fatigue tests

The goal of the fatigue tests was to find a multiaxial fatigue threshold based on the critical plane approach to predict the fatigue crack initiation at different angles. As mentioned previously, conservative values were chosen for $[\sigma_{res,\,m}]$. Therefore, using the strain gauge measurements for $[\sigma_{res,\,b}]$ and $[\sigma_P]$, the initial stress state $[\sigma_0]$ was obtained using Eq. (22) and (23), respectively. With the stress components due to the actuator loads, $[\sigma_F]$, the effective stresses $[\sigma_{eff}]$ during the fatigue tests were obtained using Eq. (24), as follows:

$$[\sigma_{eff}]=[\sigma_0]+[\sigma_F] \tag{24}$$

The minimum and maximum effective stresses for the tested angles are presented in Table 1. In this table, the angle A1-L-1 indicates the angle A1-L in the first fatigue test. The fatigue tests were conducted on five specimens, i.e., S1–S5. Each specimen consisted of two angles on the

left and right sides of the cantilever beam. Each specimen was subjected to a presetting force of P and the minimum and maximum actuator loads (F_{min} and F_{max}).

Table 1. Effective stress components in the fatigue tests.

Specimen No.	P (kN)	F (kN)		Angle	Effective stress components (MPa)						Test observation
		Min.	Max.		$\sigma_{x\text{-}eff}$		$\sigma_{y\text{-}eff}$		$\tau_{xy\text{-}eff}$		
					Min.	Max.	Min.	Max.	Min.	Max.	
S1	39.2	3.3	21.6	A1-L-1	-300.6	105.9	-88.5	34.4	9.3	17.3	Run-out
				A1-R-1	-233.1	163.8	-105.5	34.9	-55.5	-75.1	Cracked
		3.3	22.6	A1-L-2	-302.3	135.4	-86.5	47.3	8.4	25.9	Cracked
				A1-R-2	-	-	-	-	-	-	-
S2	41	3.1	18.6	A2-L-1	-122.5	98.5	-21.5	39.3	10.4	21.6	Run-out
		4.6	21.4	A2-L-2	-106.2	148.9	-18.3	55.6	11.6	22.0	Run-out
S3	34.5	2.1	19.2	A3-L-1	-154.8	169.9	-38.7	67.5	37.5	40.8	Run-out
		2.1	20.8	A3-L-2	-153.3	193.8	-38.5	71.3	37.5	41.2	Run-out
		2.05	21.95	A3-L-3	-156.8	216.5	-38.6	69.9	23.2	35.7	Run-out
S4	30.7	4.2	12.6	A4-L-1	-71.8	153.7	-17.0	47.2	4.1	8.1	Run-out
		3	14.4	A4-L-2	-106.9	195.1	-26.5	57.1	-0.15	8.7	Run-out
S5	38.4	3.6	20.6	A5-L-1	-80.6	303.9	-41.9	84.0	-3.9	11.1	Cracked

The fatigue tests on the specimens were conducted based on the following scheme:

(i) For S1, in the first fatigue test, the angle A1-L-1 did not crack after two million cycles, but the angle A1-R-1 was cracked. In the next fatigue test, the maximum load of the actuator was increased to F_{max}=2 2.6 kN, resulting in a crack at the angle A1-R-2.

(ii) For the other specimens S2–S5, it was decided to focus only on the left angles, and to control the measurements at these angles.

To compute the critical plane parameters σ_{nm}, σ_{na}, and τ_a, the values in Table 1 were used as inputs in the calculation procedure presented in Section 3. The corresponding ρ values were obtained using Eq. (11). The critical plane parameters calculated for each angle are listed in Table 2.

Table 2. Critical plane parameters for the tested angles.

Angle	σ_{nm} (MPa)	σ_{na} (MPa)	τ_a (MPa)	ρ	Test observation
A1-L-1	-48.3	101.7	101.7	0.53	Run-out
A1-R-1	-12.4	99.6	99.6	0.88	Cracked
A1-L-2	-40.6	109.7	109.7	0.63	Cracked
A1-R-2	-	-	-	-	-
A2-L-1	-4.8	55.5	55.5	0.91	Run-out
A2-L-2	11.6	63.9	63.9	1.18	Run-out
A3-L-1	4.4	81.2	81.2	1.05	Run-out
A3-L-2	10.7	86.8	86.8	1.12	Run-out
A3-L-3	16.3	93.5	93.5	1.17	Run-out
A4-L-1	20.6	56.4	56.4	1.37	Run-out
A4-L-2	22.2	75.6	75.6	1.29	Run-out
A5-L-1	55.9	96.3	96.3	1.58	Cracked

3.1.7.2. Comparison of the test results with the MWCM and FS thresholds

Using the obtained values for the parameters τ_a and ρ in Table 2, the experimental results are plotted in Fig. 14. In the plots, the green and red data points represent the run-out cases after two million cycles and cracked cases, respectively. The MWCM and FS thresholds are plotted in Fig. 14(a) and (b) based on Eq. (10) and (15), respectively.

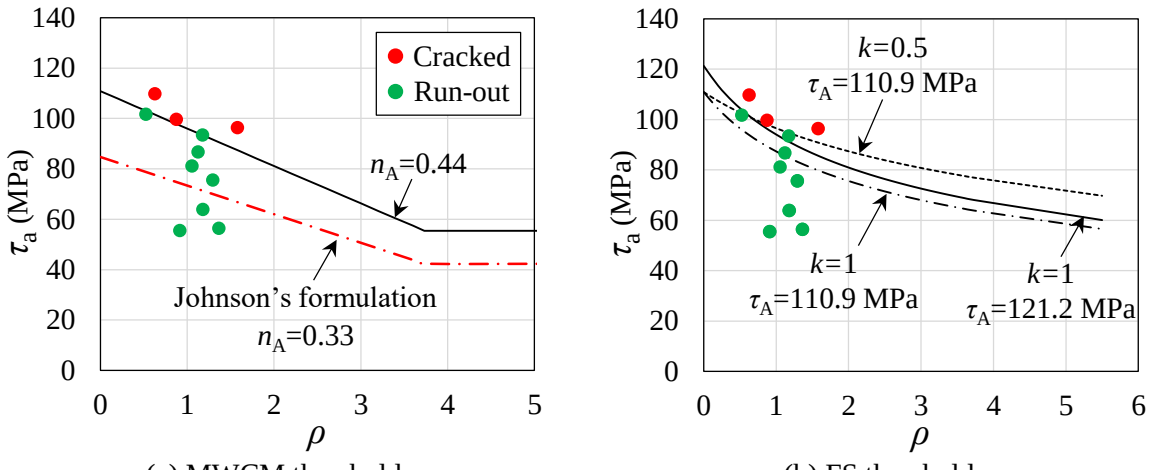

(a) MWCM threshold (b) FS threshold

Fig. 14. Comparison of the fatigue test results with the multiaxial fatigue thresholds.

For the MWCM threshold that lies below the cracked data points, the estimated value for the fully reversed uniaxial fatigue limit is σ_A=192 MPa. Using Eq. (21), the fully reversed shear fatigue limit is found to be equal to τ_A=110.9 MPa. This threshold corresponds to n_A=0.44

according to Eq. (19), as shown in Fig. 14(a). In addition, the threshold according to Johnson's formulation, with σ_A=146.7 MPa, is plotted in Fig. 14(a). For this threshold, n_A=0.33, which is 25% smaller than that considered for the MWCM threshold (i.e., n_A=0.44). Therefore, the use of this criterion for design purposes will lead to a conservative prediction.

The FS threshold is plotted in Fig. 14(b) for different values of k and τ_A. It indicates that when using k=1 and τ_A=121.2 MPa or k=0.5 and τ_A=110.9 MPa, the thresholds lie below the crack test data. The use of k=1 and τ_A=110.9 MPa leads to a conservative prediction. The conservatism arises from two reasons: it has a greater k value (compared to 0.5), which amplifies the influence of the mean stresses (see Eq. (14)), and has a smaller τ_A value relative to 121.2 MPa.

3.1.7.3. Effect of $[\sigma_{res,\,m}]$ on the threshold

Considering $\sigma_{res,\,m\text{-}x}$=-135 MPa and $\sigma_{res,\,m\text{-}y}$=-44 MPa, the circular data points shown in Fig. 15 are obtained. If no residual stresses due to the manufacturing process are considered, i.e., $[\sigma_{res,\,m}]$=0, the triangular data points in Fig. 15 are obtained using Eq. (24). As shown, the consideration of $[\sigma_{res,\,m}]$ corresponds to a reduction in the ρ value, i.e., the compressive $[\sigma_{res,\,m}]$ reduces the mean values of the stress components.

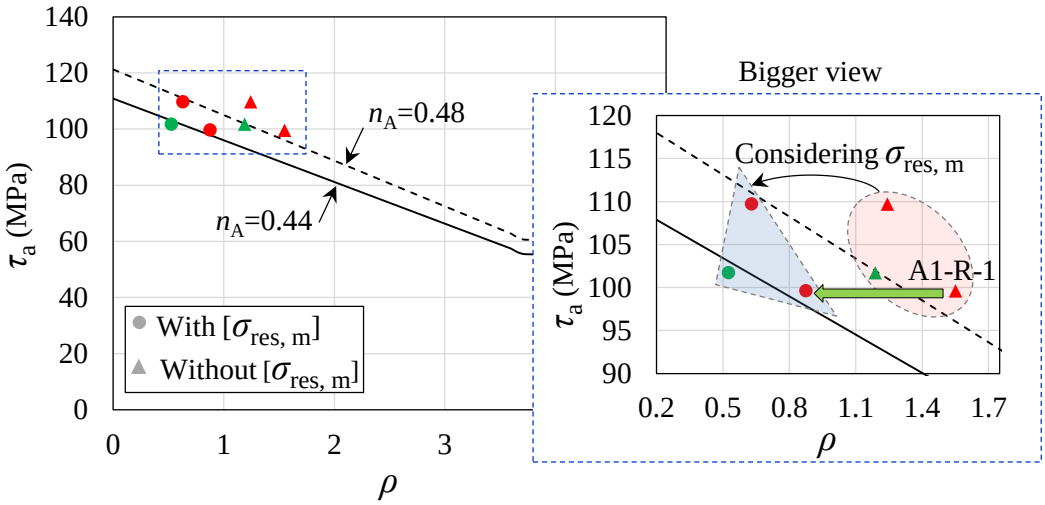

Fig. 15. Effect of $[\sigma_{res,\,m}]$ on the MWCM threshold.

As shown in Fig. 15, consideration of the compressive stress $[\sigma_{res,\,m}]$ results in an MWCM threshold with n_A=0.44, while ignoring it leads to a threshold with n_A=0.48. This shows that consideration of the compressive stress $[\sigma_{res,\,m}]$ leads to a more conservative threshold. As an example, the angle A1-R, which is predicted as a cracked angle using the threshold with

n_A=0.44, is not predicted to crack using the threshold with n_A=0.48, as it lies below this threshold.

3.1.7.4. Initiation and propagation of the fatigue cracks

At all of the cracked angles, the crack initiated under the strain gauge area. Fig. 16 shows the strains in different directions during the fatigue tests at the angles A1-L and A1-R. As shown in Fig. 16(a), the fatigue test resulted in no crack in the angle A1-L-1 after two million cycles, while the angle A1-R-1 cracked after more than 1 million cycles, as shown in Fig. 16(b). For the angle A1-R-2, the crack initiated after approximately 0.4 million cycles, as depicted in Fig. 16(c). It was observed that the initiation of the crack at one angle did not affect the stress state at other angle.

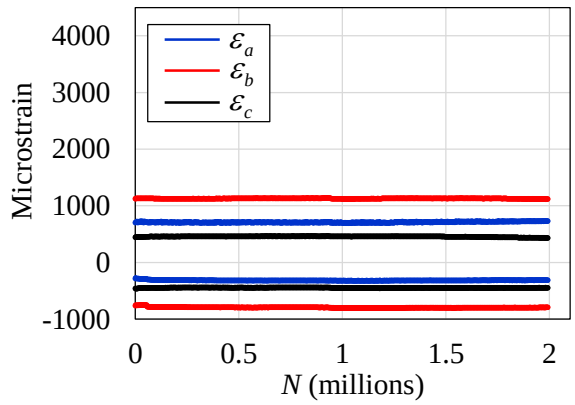

(a) Measured strains in the angle A1-L-1

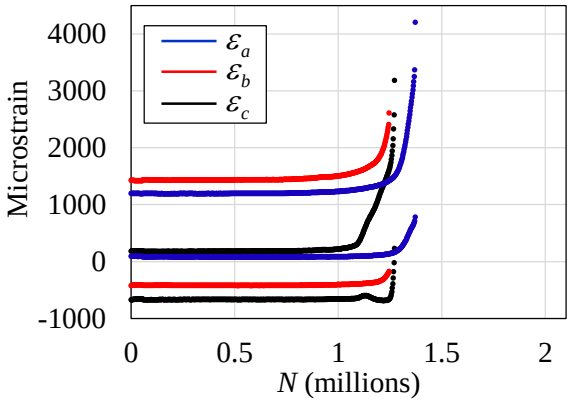

(b) Measured strains in the angle A1-R-1

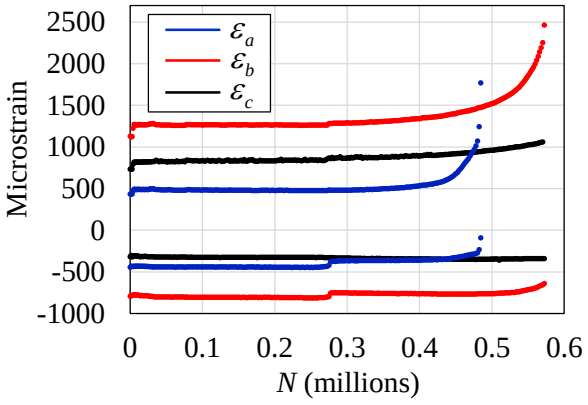

(c) Measured strains in the angle A1-L-2

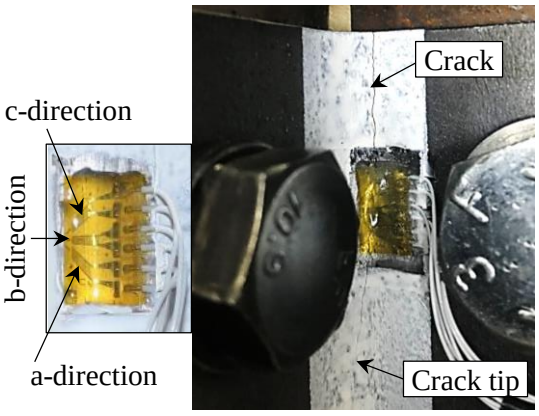

(d) Crack in the fillet area of the angle A1-R-1

Fig. 16. Strains in the angles A1-L and A1-R during fatigue test and the fatigue crack.

For the angle A1-R-1, first, the strain gauge grids in the c-direction were broken by the fatigue crack, and then, the grids in the b- and a-directions were broken, respectively. For this angle, the grids along the c-direction are located above the horizontal grids in the b-direction, as shown in Fig. 10(a). For the angle A1-L-2, the grids in the a-direction were broken first, followed by

the breaking of the grids in the b- and c-directions, respectively. For this angle, the grids along the a-direction are located above the horizontal grids in the b-direction.

This observation shows that for both angles A1-R-1 and A1-L-2, the crack initiated under the upper area of the strain gauges and propagated downward and upward. Fig. 16(d) shows the long crack at angle A1-R-1 after propagation. This observation was repeated in the other cracked angles. Notably, for a number of cycles (approximately 50,000 cycles) after the breaking of the first grids, no crack was detected beyond the strain gauge area, indicating that the crack initiated under the strain gauge area.

3.1.8. Strengthening effect

The strengthening system used in the setup would improve the fatigue strength of the connections in two ways: (i) adding flexural stiffness to the connections, and (ii) applying a compressive force to the connections due to prestressing. The additional flexural stiffness depends on the longitudinal stiffness of the prestressing element and its eccentricity from the center of rotation of the connection. In the following subsections, each effect is discussed.

3.1.8.1. Additional flexural stiffness

For the angle A3-L, the increase in the stress components under the application of static actuator loads is shown in Fig. 17. In this figure, three different cases are considered, i.e., the connections without strengthening, and those strengthened with CFRP and steel rods, respectively. As shown, the stresses in the x-direction are dominant; however, the stresses in the y-direction cannot be neglected. The shear stress is negligible compared to the normal stresses, as shown in Fig. 17(c).

The slopes of the increase for σ_x and σ_y as estimated by lines are 18.3 and 4.9, respectively. These slopes are not affected by the strengthening system, showing that the flexural stiffness added to the connections by the strengthening system was negligible. It is clear that using a great eccentricity for the prestressing element would result in a greater flexural stiffness; however, this is not the case for the current test setup.

3.1.8.2. Prestressing effect

The reduction in the stress components as a result of the prestressing force for the angle A3-L is shown in Fig. 18. In this figure, the plot corresponding to each stress component is approximated with a line as a function of the prestressing force *P*. The figure shows that prestressing

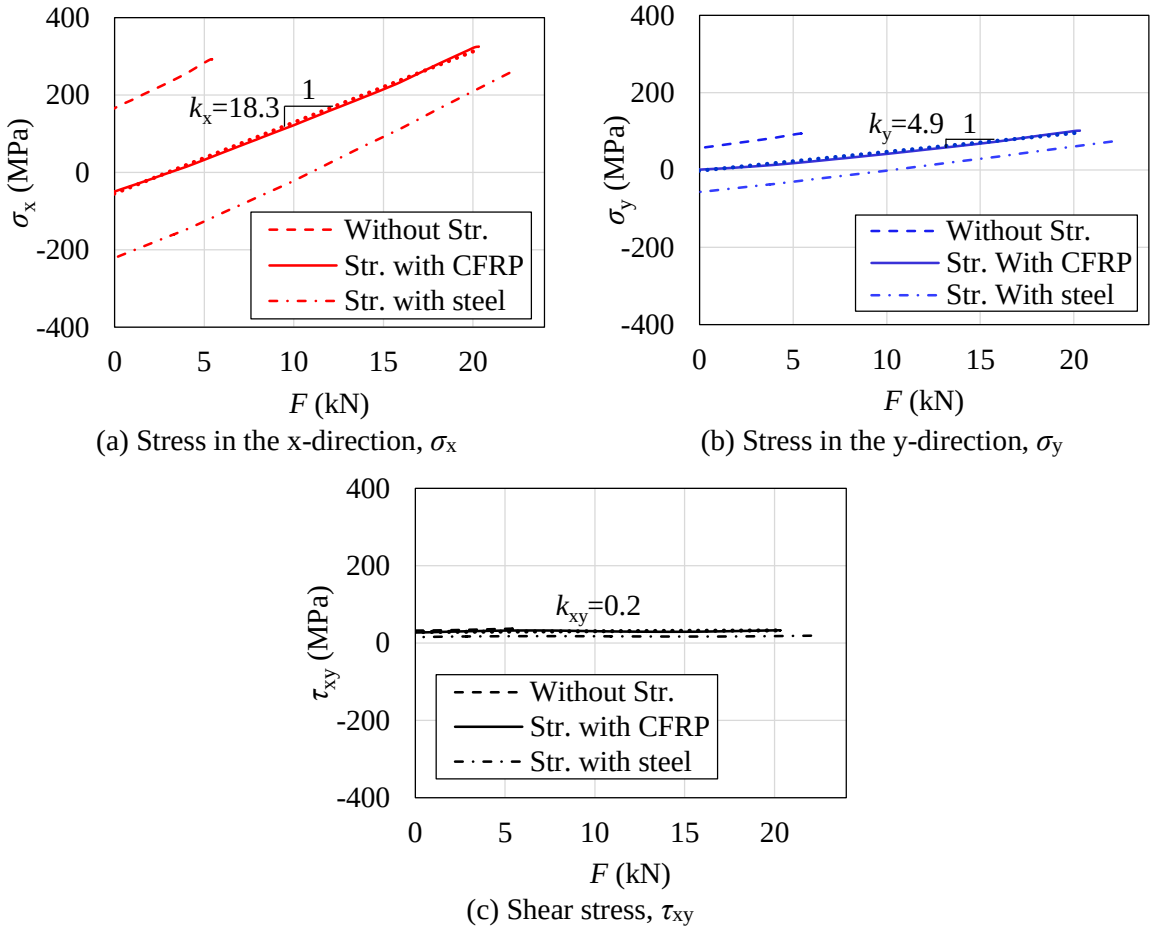

(a) Stress in the x-direction, σ_x

(b) Stress in the y-direction, σ_y

(c) Shear stress, τ_{xy}

Fig. 17. Effect of the strengthening on the measured stress components and flexural stiffness of the angle A3-L.

significantly reduced the stress in the x-direction (as the dominant stress component). The slope of the reduction for the stress in the y-direction is -1.6, which is less than one-third of that in the x-direction. The effect of the prestressing force on the shear stress is negligible.

The stress components during the application of the prestressing force are considered as $\sigma_{x\text{-}P}$, $\sigma_{y\text{-}P}$, and $\tau_{xy\text{-}P}$ in Fig. 18. As the prestressing force is applied after fastening the bolts, the residual stresses due to fastening the bolts, $[\sigma_{res,\,b}]$, serve as the values corresponding to P=0 in Fig. 18. After the prestressing, due to the actuator loads, the stress components increase with the slopes of k_x, k_y, and k_{xy}, respectively, as shown in Fig. 17. Considering the residual stresses due to the manufacturing process, $[\sigma_{res,\,m}]$, under the application of a prestressing force of P and an actuator load of F, the effective stress components are estimated as follows:

$$\begin{aligned}\sigma_{x-\text{eff}} &= \sigma_{res,\,m-x} + \sigma_{x-P}(P) + k_x \times F \\ \sigma_{y-\text{eff}} &= \sigma_{res,\,m-y} + \sigma_{y-P}(P) + k_y \times F \\ \tau_{xy-\text{eff}} &= \tau_{res,\,m-xy} + \tau_{xy-P}(P) + k_{xy} \times F\end{aligned} \tag{25}$$

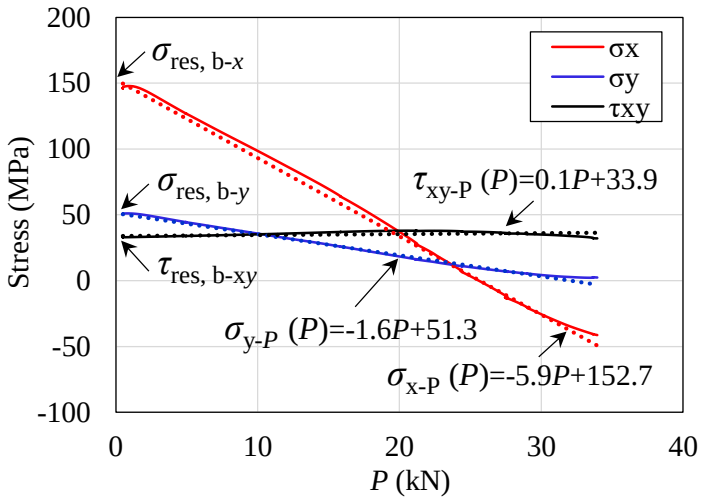

Fig. 18. Reduction in the measured stress components due to prestressing force P for the angle A3-L.

The first two expressions on the right-hand side of Eq. (25) represent the initial stress state (Eq. (22)). Thus, the residual stresses caused by fastening the bolts, i.e., $\sigma_{res,\,b\text{-}x}$, $\sigma_{res,\,b\text{-}y}$, and $\tau_{res,\,b\text{-}xy}$, are already included in $\sigma_{x\text{-}P}$ (P), $\sigma_{y\text{-}P}$ (P), and $\tau_{xy\text{-}P}$ (P), as shown in Fig. 18. Therefore, to compute the effective stresses, only the residual stresses due to the manufacturing process, i.e., $\sigma_{res,\,m\text{-}x}$, $\sigma_{res,\,m\text{-}y}$, and $\tau_{res,\,m\text{-}xy}$, were added in Eq. (25).

From the above, it can be concluded that the strengthening system improves the fatigue performance of the angles only by reducing the mean values of the stress components owing to the prestressing force. The stress range, however, is not reduced, as the slope of the increase in the stress components due to the actuator loads is not affected by the strengthening system.

3.1.8.3. Example of the strengthening effect

To clarify the effect of the prestressing force in improving the fatigue behavior of the connections, consider the example angles A1-, A2-, and A3-Ex in Table 3. Angle A1-Ex is subjected to a prestressing force of P=35 kN and actuator loads of F_{min}=1 kN and F_{max}=20 kN. Assuming $[\sigma_{res,\,m}]$=0 and considering k_x, k_y, and k_{xy} in Fig. 17, the effective stress components are computed using Eq. (25). Table 3 lists the effective stress components and multiaxial fatigue parameters ρ and τ_a. The point corresponding to angle A1-Ex is shown in Fig. 19, and is beyond the MWCM threshold. Thus, it is predicted that a crack is initiated in the fillet of the angle.

Table 3. Exemplary stress conditions to consider the prestressing effect.

Angle	P (kN)	F (kN)		$\sigma_{x\text{-eff}}$ (MPa)		$\sigma_{y\text{-eff}}$ (MPa)		$\tau_{xy\text{-eff}}$ (MPa)		ρ	τ_a (MPa)
		min.	max.	min.	max.	min.	max.	min.	max.		
A1-Ex	35	1	20	-35.5	312.2	0.2	93.3	37.6	41.4	1.8	86.9
A2-Ex	50	1	20	-124	223.7	-23.8	69.3	39.1	42.9	1.29	86.9
A3-Ex	50	1	21.5	-124	251.15	-23.8	76.65	39.1	43.2	1.35	93.8

Under the same actuator loads, the application of a prestressing force of 50 kN for the angle A2-Ex brings the point below the threshold, as shown in the figure. The transition from A1-Ex to A2-Ex follows a horizontal path (1) because only the mean stress is reduced by the prestressing force. If under the prestressing force of 50 kN, the maximum actuator load increases to 21.5 kN, the point moves up just beyond the threshold, as shown for the angle A3-Ex in Fig. 19. This shows that under greater prestressing forces, the applied superimposed loads can be increased.

Notably, in this example, a small increase in F_{max}, i.e., from 20 to 21.5 kN, can result in a crack in the angle. This is because in the setup used in this study, the actuator load is applied to a cantilever beam. Therefore, the bending moment applied to the connections changes considerably as a result of a change in the actuator load. In real applications, however, where the two ends of the beam are supported, greater superimposed loads are required to change the distortion-induced stresses in the angles, as the connections on both ends contribute to carrying the bending. This example is given here only to show the prestressing effect in improving the multiaxial fatigue behavior of the angle connections. This effect can be considered to determine the prestressing force in real applications.

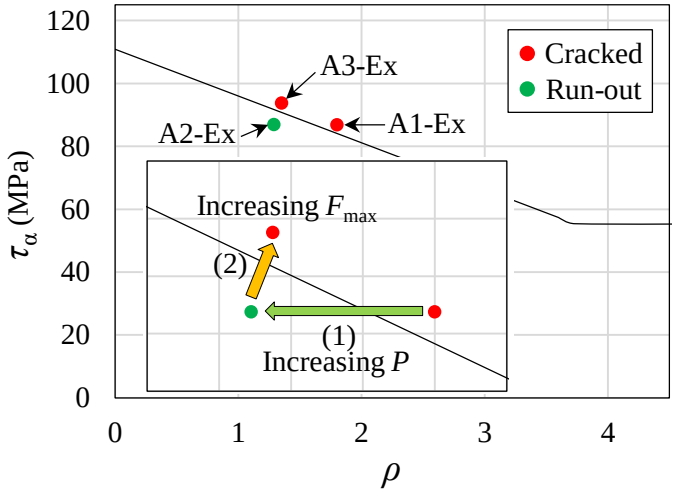

Fig. 19. Effect of prestressing force on the multiaxial stress state.

3.1.9. Conclusions

In this study, a multiaxial fatigue theory based on the critical plane approach was employed to find an initiation threshold criterion for steel connections, as strengthened with prestressed elements and subjected to distortion-induced fatigue loadings. The main conclusions are as follows.

- The fully reversed uniaxial and shear fatigue limits were estimated as a function of the material tensile strength using the ratio n_A. Using this ratio, the MWCM threshold was plotted, with a smaller n_A leading to a more conservative threshold.
- Using n_A=0.4 and 0.55 for the uniaxial and multiaxial test data, respectively, all data points corresponding to fatigue failure lied beyond the MWCM threshold. For the FS model, except for a single data point with a high mean stress from uniaxial test results, all other data points were above the model threshold considering k=1, S_y=300 MPa, and τ_A=106.5 and 135.7 MPa for the uniaxial and multiaxial test data, respectively. The threshold based on John-son's formulation was the most conservative criterion.
- Rosette strain gauges were applied at the critical location of the angles to measure the multiaxial stress state at this area. The fatigue cracks initiated under the rosette strain gauges, and then propagated downward and upward.
- The residual stresses in the critical location due to the manufacturing process, $[\sigma_{res,\,m}]$ were measured using cut-compliance method. The results showed that the residual stresses in the x- and y-directions were compressive. At a cut depth of a=0.3 mm, the maximum measured equivalent compressive stresses in the x- and y-directions were -135 and -44 MPa, respectively. The measurement of the residual stresses due to fastening the bolts showed that the geometric imperfections of the angles resulted in a scatter in the results, ranging from approximately 20 to 200 MPa in the x-direction.
- The effects of the residual stresses, prestressing force of the strengthening system, and actuator load were incorporated in the multiaxial fatigue models based on the critical plane approach.
- The results from the fatigue tests showed that the MWCM threshold with n_A=0.44 lied below the crack test data. For the FS criterion, the threshold could predict the crack initiation at the angles using k=1 and τ_A=121.2 MPa or k=0.5 and τ_A=110.9 MPa. Using Johnson's formulation with n_A=0.33 being 25% smaller than 0.44 used for the MWCM threshold, a more conservative threshold (relative to the other thresholds) was obtained.
- The strengthening system could increase the fatigue resistance only through the prestressing

force, without a considerable effect on the flexural stiffness of the angles. The prestressing force could reduce the mean stress of σ_x as the dominant stress component, with a slope of -5.9, whereas for σ_y, the reduction slope was -1.6. In this way, it could bring the data points from the risky zone into the safe zone. This shows that a prestressed retrofitting system can be used for the fatigue strengthening of steel connections.

Appendix A. Equations for the calculation of stresses from the measured strains

To calculate the stress components from the measured strain values in the a-, b-, and c-directions, the equations proposed in [65] were reformulated for an easier implementation in the MATLAB code. First, the value θ' was calculated as follows:

$$\theta' = \frac{1}{2}\tan^{-1}\left(\frac{\varepsilon_a - 2\varepsilon_b + \varepsilon_c}{\varepsilon_a - \varepsilon_c}\right) \quad \text{A1}$$

As $\tan 2\theta' \equiv \tan 2(\theta' + 90°)$, the calculated angle θ' is not necessarily the angle from the a-direction to the first principal direction, i.e., it can refer to either principal axes. To address this ambiguity, the data-reduction algorithms proposed in [65] were implemented in the MATLAB code as follows:

$$\theta = \theta' - \text{sign}(\theta') \times \frac{\pi}{4} + \text{sign}(2\varepsilon_b - \varepsilon_a - \varepsilon_c) \times \frac{\pi}{4} \quad \text{A2}$$

In the above, the function sign determines the sign of the expressions. Using this θ value, the stresses in the x-y plane were calculated as follows:

$$\sigma_x = \frac{E}{2(1-\nu)}(\varepsilon_a + \varepsilon_c) + \frac{E}{\sqrt{2}(1+\nu)}\sqrt{(\varepsilon_a - \varepsilon_b)^2 + (\varepsilon_b - \varepsilon_c)^2}\sin 2\theta$$

$$\sigma_y = \frac{E}{2(1-\nu)}(\varepsilon_a + \varepsilon_c) - \frac{E}{\sqrt{2}(1+\nu)}\sqrt{(\varepsilon_a - \varepsilon_b)^2 + (\varepsilon_b - \varepsilon_c)^2}\sin 2\theta \quad \text{A3}$$

$$\tau_{xy} = \frac{E}{\sqrt{2}(1+\nu)}\sqrt{(\varepsilon_a - \varepsilon_b)^2 + (\varepsilon_b - \varepsilon_c)^2}\cos 2\theta$$

Here, E is the elastic modulus and ν is Poisson's ratio (equal to 0.3).

Appendix B. Measurement results for $\sigma_{res,\,m\text{-}x}$ and $\sigma_{res,\,m\text{-}y}$ as a function of the cut depth

The equivalent residual stresses due to the manufacturing process as a function of the cut depth a in the x- and y-directions are shown in Fig. B1. Physically, the equivalent residual stress represents the stress in the surface layer of $0 < z < a$ that produces the same stress intensity

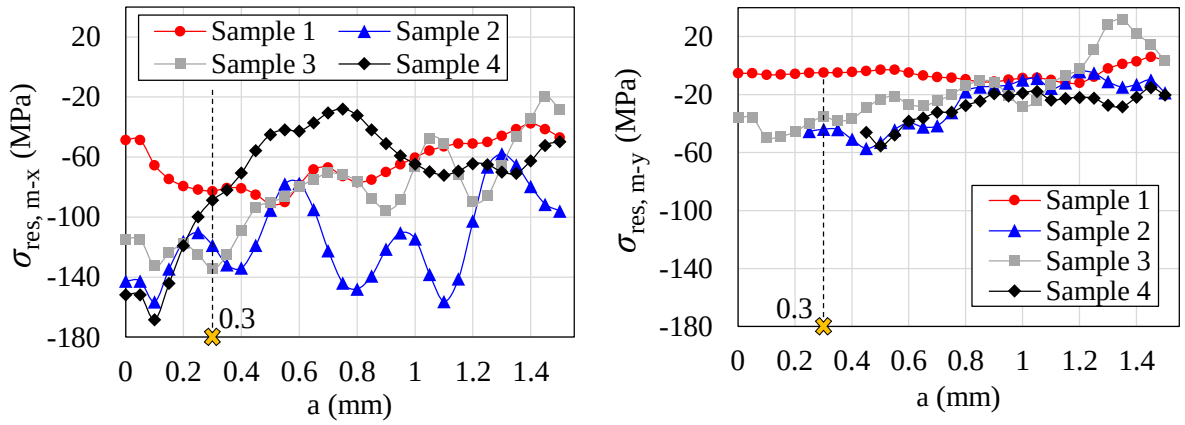

(a) x-direction (b) y-direction

Fig. B1. Equivalent residual stresses due to manufacturing process as a function of the cut depth a.

factor in mode I at the tip of a hypothetical crack as the original residual stresses. Quantitatively, it is close to the mean value of the residual stresses within $0 < z < a$.

Declaration of Competing Interest

The authors declare that they have no known competing financial interests or personal relationships that could have appeared to influence the work reported in this paper.

Acknowledgement

The authors acknowledge the Innosuisse Swiss Innovation Agency (Grant ID: 19240.1 PFIW-IW) for funding this research project. The financial and technical support from the project partners, namely S&P Clever Reinforcement Company AG, Switzerland; the Swiss Federal Railways (SBB) AG, Bern; and dsp Ingenieure + Planer AG Engineering Office, Uster, Switzerland are highly appreciated. Special thanks go to the teams of the Structural Engineering Research Laboratory of Empa (Dübendorf, Switzerland). The authors also appreciate Dr. Hans-Jakob Schindler at Mat-Tec AG, Switzerland, for his support in measuring the residual stresses.

References

1. Haghani R, Al-Emrani M, Heshmati M. Fatigue-prone details in steel bridges. Buildings 2012;2(4)456-476. https://doi.org/10.3390/buildings2040456
2. Al-Emrani M Fatigue in Riveted Railway Bridges. 2002, PhD Thesis, Chalmers University of Technology, Gothenburg, Sweden.
3. Connor RJ, Fisher JW. Identifying effective and ineffective retrofits for distortion fatigue cracking in steel bridges using field instrumentation. Journal of Bridge Engineering 2006;11(6)745-752. https://doi.org/10.1061/(ASCE)1084-0702(2006)11:6(745)
4. Fisher JW, Yen B, Wang D, Mann J. Fatigue and fracture evaluation for rating riveted bridges. 1987, Washington, DC United States: Transportation Research Board.
5. Fisher JW, Yen BT, Wang D. Fatigue strength of riveted bridge members. Journal of structural Engineering

1990;116(11)2968-2981.

6. Al-Emrani M, Åkesson B, Kliger R. Overlooked secondary effects in open-deck truss bridges. Struct. Eng. Int. 2004;14307-312. https://doi.org/10.2749/101686604777963612
7. Wilson WM, Coombe VV fatigue tests of connection angles, N. Series 317, Editor. 1939: Bulletin of University of Illinois Urbana.
8. Leonetti D, Maljaars J, Pasquarelli G, Brando G. Rivet clamping force of as-built hot-riveted connections in steel bridges. Journal of Constructional Steel Research 2020;167105955. https://doi.org/10.1016/j.jcsr.2020.105955
9. Kühn B, et al. Assessment of Existing Steel Structures: Recommendations for Estimation of Remaining Fatigue Life. Joint Research Centre of Eurocodes 2008. http://publications.jrc.ec.europa.eu/repository/handle/JRC43401.
10. Baker K, Kulak G. Fatigue of riveted connections. Canadian Journal of Civil Engineering 1985;12(1)184-191. https://doi.org/10.1139/l85-017
11. Reemsnyder H. Fatigue life extension of riveted connections. J. Struct. Div., ASCE 1975;2591-2607.
12. Bowman MD. Fatigue evaluation of steel bridges. Vol. 721. 2012: Transportation Research Board.
13. Roeder CW, MacRae G, Leland A, Rospo A. Extending the fatigue life of riveted coped stringer connections. Journal of Bridge Engineering 2005;10(1)69-76. https://doi.org/10.1061/(ASCE)1084-0702(2005)10:1(69)
14. Zhao X-L. FRP-strengthened metallic structures. 2013: CRC Press.
15. Dawood M, Rizkalla S, Sumner E. Fatigue and overloading behavior of steel-concrete composite flexural members strengthened with high modulus CFRP materials. Journal of Composites for Construction 2007;11(6)659-669. http://www.scopus.com/inward/record.url?eid=2-s2.0-36249004257&partnerID=40&md5=84b4832fa44e403621bdb113e990e4e1.
16. Mertz DR, Gillespie JWJ. Rehabilitation of steel bridge girders through the application of advanced composite materials. Contract NCHRP-93-ID011. Transportation Research Board, Washington, D.C. 1996.
17. Schnerch D, Dawood M, Rizkalla S, Sumner E. Proposed design guidelines for strengthening of steel bridges with FRP materials. Construction and Building Materials 2007;21(5)1001-1010.
18. Ghafoori E, Hosseini A, Al-Mahaidi R, Zhao X-L, Motavalli M. Prestressed CFRP-strengthening and long-term wireless monitoring of an old roadway metallic bridge. Engineering Structures 2018;176585-605. https://doi.org/10.1016/j.engstruct.2018.09.042
19. Ghafoori E, Motavalli M. Innovative CFRP-Prestressing System for Strengthening Metallic Structures. Journal of Composites for Construction 2015;19(6)04015006. https://doi.org/10.1061/(ASCE)CC.1943-5614.0000559. http://www.scopus.com/inward/record.url?eid=2-s2.0-84939204537&partnerID=40&md5=3422ce7a81b87ad1b00e68ab9a965d3e.
20. Ghafoori E, Motavalli M, Nussbaumer A, Herwig A, Prinz G, Fontana M. Design criterion for fatigue strengthening of riveted beams in a 120-year-old railway metallic bridge using pre-stressed CFRP plates. Composites Part B: Engineering 2015;681-13. https://doi.org/10.1016/j.compositesb.2014.08.026
21. Ghafoori E, Schumacher A, Motavalli M. Fatigue behavior of notched steel beams reinforced with bonded CFRP plates: Determination of prestressing level for crack arrest. Engineering Structures 2012;45270-283.
22. Heydarinouri H, Nussbaumer A, Maljaars J, Ghafoori E. Proposed criterion for fatigue strengthening of riveted bridge girders. Procedia Structural Integrity 2019;19482-493. https://doi.org/10.1016/j.prostr.2019.12.052
23. Hosseini A, Ghafoori E, Al-Mahaidi R, Zhao X-L, Motavalli M. Strengthening of a 19th-century roadway metallic bridge using nonprestressed bonded and prestressed unbonded CFRP plates. Construction and Building Materials 2019;209240-259. https://doi.org/10.1016/j.conbuildmat.2019.03.095
24. Hosseini A, Ghafoori E, Motavalli M, Nussbaumer A, Zhao XL, Al-Mahaidi R. Flat Prestressed Unbonded Retrofit System for Strengthening of Existing Metallic I-Girders. Composites Part B 2018;155156-172. https://doi.org/10.1016/j.compositesb.2018.08.026
25. Heydarinouri H, Motavalli M, Nussbaumer A, Ghafoori E. Development of Mechanical Strengthening System for Bridge Connections Using Prestressed CFRP Rods. Journal of Structural Engineering 2021;147(3)04020351.
26. Heydarinouri H, Nussbaumer A, Motavalli M, Ghafoori E. Strengthening of Steel Connections in a 92-Year-Old Railway Bridge Using Prestressed CFRP Rods: Multiaxial Fatigue Design Criterion. Journal of Bridge Engineering 2021;26(6)04021023.
27. Hosseini A, Michels J, Izadi M, Ghafoori E. A comparative study between Fe-SMA and CFRP reinforcements for prestressed strengthening of metallic structures. Construction and Building Materials

2019;226976-992. https://doi.org/10.1016/j.conbuildmat.2019.07.169. http://www.sciencedirect.com/science/article/pii/S0950061819318434.

28. Izadi M, Motavalli M, Ghafoori E. Iron-based shape memory alloy (Fe-SMA) for fatigue strengthening of cracked steel bridge connections. Construction and Building Materials 2019;227116800. https://doi.org/10.1016/j.conbuildmat.2019.116800. http://www.sciencedirect.com/science/article/pii/S0950061819322305.
29. -1-9 E. Eurocode 3: Design of steel structures-Part 1-9: Fatigue. European Committee for Standardization: Brussels, Belgium 2005.
30. Officials T. Standard specifications for highway bridges. 2002: AASHTO.
31. Adamson DEJ. Fatigue tests of riveted bridge girders. 1995.
32. Al-Emrani M, Akesson B. Experimental study on the fatigue performance of riveted girders. Stahlbau 2002;71(2)145-150.
33. Baker K, GL K. Fatigue of riveted connections. Can. J. Civ. Eng. 1985;12184-191. https://doi.org/10.1139/l85-017
34. Brühwiler E, Smith I, Hirt M. fatigue and fracture of riveted bridge members. Journal of Structural Engineering 1990;116(1).
35. Reemsnyder HS. Fatigue life extension of riveted connections. Journal of the Structural Division 1975;101(ASCE# 11795 Procceding).
36. Wang D. Fatigue behavior of mechanically fastened double angle shear connections in steel bridges. Dissertation Abstracts International 1990.
37. Abouelmaaty WM. Experimental fatigue evaluation of steel double-angle connections in railway bridges. 1998.
38. Al-Emrani M, Kliger R. FE analysis of stringer-to-floor-beam connections in riveted railway bridges. Journal of Constructional Steel Research 2003;59(7)803-818. http://dx.doi.org/10.1016/S0143-974X(02)00114-1. http://www.sciencedirect.com/science/article/pii/S0143974X02001141.
39. Imam BM, Righiniotis TD, Chryssanthopoulos MK. Numerical modelling of riveted railway bridge connections for fatigue evaluation. Engineering Structures 2007;29(11)3071-3081.
40. Fatemi A, Socie DF. A critical plane approach to multiaxial fatigue damage including out-of-phase loading. Fatigue & Fracture of Engineering Materials & Structures 1988;11(3)149-165.
41. Socie DF, Marquis GB. Multiaxial fatigue. 2000: Society of Automotive Engineers Warrendale, PA.
42. Susmel L, Tovo R, Lazzarin P. The mean stress effect on the high-cycle fatigue strength from a multiaxial fatigue point of view. International Journal of Fatigue 2005;27(8)928-943. https://doi.org/10.1016/j.ijfatigue.2004.11.012
43. Susmel L. Multiaxial fatigue limits and material sensitivity to non-zero mean stresses normal to the critical planes. Fatigue & Fracture of Engineering Materials & Structures 2008;31(3-4)295-309.
44. Susmel L, Lazzarin P. A bi-parametric Wöhler curve for high cycle multiaxial fatigue assessment. Fatigue & Fracture of Engineering Materials & Structures 2002;25(1)63-78. https://doi.org/10.1046/j.1460-2695.2002.00462.x
45. Stephens RI, Fatemi A, Stephens RR, Fuchs HO. Metal fatigue in engineering. 2000: John Wiley & Sons.
46. Ghafoori E, Motavalli M, Nussbaumer A, Herwig A, Prinz G, Fontana M. Determination of minimum CFRP pre-stress levels for fatigue crack prevention in retrofitted metallic beams. Engineering Structures 2015;8429–41. https://doi.org/10.1016/j.engstruct.2014.11.017
47. Shigley JE. Shigley's mechanical engineering design. 2011: Tata McGraw-Hill Education.
48. Ghafoori E, Motavalli M. A Retrofit Theory to Prevent Fatigue Crack Initiation in Aging Riveted Bridges Using Carbon Fiber-Reinforced Polymer Materials. Polymers 2016;8308.
49. Johnson JB. The materials of construction. 1897: (1st ed.) John Wiley and Sons, New York, pp. 537–47.
50. Frost N, Marsh K, Pook L Metal fatigue. Clarendon. 1974, Oxford.
51. McDiarmid D. Fatigue under out-of-phase bending and torsion. Fatigue & Fracture of Engineering Materials & Structures 1987;9(6)457-475. https://doi.org/10.1111/j.1460-2695.1987.tb00471.x
52. Nishihara T, Kawamoto M. The strength of metals under combined alternating bending and torsion with phase difference. Memoirs of the College of Engineering, Kyoto Imperial University 1945;11(5)85-112.
53. DIN E 6892-1: 2017-02: Metallic materials-Tensile testing-Part 1: Method of test at room temperature (ISO 6892-1: 2016). 2017, Beuth Verlag GmbH.
54. Heydarinouri H, Motavalli M, Nussbaumer A, Ghafoori E. Development of a Mechanical Wedge-Barrel

Anchor for CFRP Rods: Static and Fatigue Behaviors. Journal of Composites for Construction 2021;25(3)04021015. doi:10.1061/(ASCE)CC.1943-5614.0001124. https://ascelibrary.org/doi/abs/10.1061/%28ASCE%29CC.1943-5614.0001124

55. Cruise RB. The influence of production routes on the behaviour of stainless steel structural members. 2007.
56. Galambos TV. Guide to stability design criteria for metal structures. 1998: John Wiley & Sons.
57. Stability ECfCSCo. Manual on stability of steel structures. 1976. European Convention for Constructional Steelwork.
58. Kitipornchai S, Lee H. Inelastic buckling of single-angle, tee and double-angle struts. Journal of Constructional Steel Research 1986;6(1)3-20.
59. Ban H, Shi G, Shi Y, Wang Y. Residual stress tests of high-strength steel equal angles. Journal of Structural Engineering 2012;138(12)1446-1454. https://doi.org/10.1061/(ASCE)ST.1943-541X.0000585
60. Tebedge N, Alpsten G, Tall L. Residual-stress measurement by the sectioning method. Experimental Mechanics 1973;13(2)88-96. http://worldcat.org/issn/00144851.
61. Prime MB. Residual stress measurement by successive extension of a slot: the crack compliance method. 1999.
62. Schindler H-J, Cheng W, Finnie I. Experimental determination of stress intensity factors due to residual stresses. Experimental mechanics 1997;37(3)272-277.
63. Schindler H-J. Residual stress effects on crack growth mechanisms and structural integrity. in: 9th Conf. on Mechanical Behaviour of Materials, Geneva, Switzerland. 2003.
64. Schindler H-J, Bertschinger P. Some steps towards automation of the crack compliance method to measure residual stress distributions. in: 5th International Conference on Residual Stresses, Sweden. 1997.
65. Perry C. Data-reduction algorithms for strain-gage rosette measurements. Experimental Techniques 1989;13(5)13-18.

4. Multiaxial fatigue strengthening of connections of an old railway bridge

Motivation

The development of an applicable strengthening system for bridge connections is a challenge because of the geometric complexity of such details; that is, the presence of floor-beams, sleepers, and rails, as well as the applied multiaxial stresses. In this chapter, using the scientific results and technical experiences gained in the studies presented in the previous chapters, the developed strengthening system is used for the fatigue strengthening of the connections in a 92-year-old riveted railway bridge in Switzerland, named Aabach Bridge. In addition to demonstrating the applicability of the developed system, the improvement in the multiaxial fatigue behavior of the connections is investigated.

Summary

This chapter focuses on the strengthening of the stringer-to-floor-beam double-angle connections of the Aabach Bridge using a mechanical retrofitting system for prestressed CFRP rods. The installation procedure of the strengthening system is described, and the results of the short-term on-site measurements are provided. Furthermore, the results of the long-term measurements, including the monitoring of the prestressing loss in the CFRP rods using a wireless sensor network (WSN) system are presented. Finally, using the modified Wohler curve method (MWCM) as a critical-plane-based multiaxial fatigue criterion, the effectiveness of the strengthening system in reducing the distortion-induced stresses in the connections due to the passage of different trains over the bridge is evaluated.

Supplementary materials to this chapter is provided in Supplement C at the end of the thesis. This supplement gives: (i) effect of bolt removal, (ii) removal of rivets, (iii) MATLAB script for strain and stress calculations from measurements on the Aabach Bridge, (iv) stresses in web of stringer before and after strengthening, and (v) air temperature and humidity history in long-term measurements.

Bibliographic details

Section 4.1 presents the post-print version of the paper with the following full bibliographic details:

- Hossein Heydarinouri, Alain Nussbaumer, Masoud Motavalli, Elyas Ghafoori. Strengthening of Steel Connections in a 92-Year-Old Railway Bridge Using Prestressed CFRP Rods: Multiaxial Fatigue Design Criterion. Journal of Bridge Engineering 2021; 26(6)04021023. https://doi.org/10.1061/(ASCE)BE.1943-5592.0001714

Author's contribution

Hossein Heydarinouri, as the first author of the above-mentioned paper, designed the strengthening system, performed the experiments and measurements, analyzed the results of the measurements, developed theory and formulations, wrote the manuscript, and revised the final version of the paper. The co-authors provided support and supervision for the contents of this chapter.

4.1. Strengthening of Steel Connections in a 92-Year Old Railway Bridge using Prestressed CFRP Rods: a Multiaxial Fatigue Design Criterion*

Abstract

This paper presents a new retrofit system for strengthening the stringer-to-floor-beam double-angle connections in a 92-year old riveted railway bridge in Switzerland, using prestressed carbon fibre-reinforced polymer (CFRP) rods. The strengthening system transmits the forces purely through friction, with minimum interference with bridge traffic. The system consists of two components: a newly developed mechanical wedge-barrel anchor to hold the prestressed CFRP rod, and a clamping system attaching the stringer flange. The strengthening system reduces the out-of-plane deformation of the connections, resulting in a reduction in the distortion-induced stresses in the connections. The short-term bridge measurements showed that the application of a total prestressing force of 100 kN reduced the dominant mean stress in the connection hotspot by 47% (from 22.9 to 10.9 MPa) under the passage of passenger trains, while the stress range remained unchanged. Using the modified Wöhler curve method (MWCM) as a critical-plane-based multiaxial fatigue model, the strengthening system was observed to reduce the multiaxial mean-stress parameter by 30% under the passenger train loads. The long-term monitoring of the strengthening system, using a wireless sensor network (WSN) system, indicates no prestress loss in the CFRP rods during the seven-month period since its installation.

Keywords: Carbon fibre-reinforced polymer (CFRP) rod; Multiaxial fatigue; Post-tensioning; Strengthening bridge connections; Wedge-barrel anchor.

4.1.1. Introduction

In Europe, nearly 70% of all steel bridges are more than 50 years old, and 30% are over 100 years old [1]. In the US, more than 29,000 roadway steel bridges are classified as structurally deficient [2]. The Engineers Australia Report Card 2000 [3] has provided bridges with a rating of D (poor) and stated that an increase in the mass limit will exacerbate the situation. A similar situation exists in Japan [4]. Therefore, the problem of bridge aging is worldwide. Bridge replacement is costly; the US Federal Highway Administration has estimated that in 2016, the

* Hossein Heydarinouri, Alain Nussbaumer, Masoud Motavalli, Elyas Ghafoori. Journal of Bridge Engineering 2021; 26(6)04021023. https://doi.org/10.1061/(ASCE)BE.1943-5592.0001714

total cost for the replacement of all structurally deficient highway bridges is more than 47 billion dollars. It is estimated that the cost for bridge rehabilitation is 68% of the cost for their complete replacement [2]. Therefore, development of reliable rehabilitation techniques has a significant economic impact.

Aging steel bridges suffer globally from fatigue problems. Fatigue cracks can initiate in different details of steel bridges. In general, bridge members are subjected to two different types of fatigue loadings: load-induced and distortion-induced fatigue loading. For the first type, design codes and standards normally provide formulations to determine the allowable fatigue load limit and to prevent the fatigue cracking. However, although the modern specifications provide some prescriptive rules to address the distortion-induced fatigue in new bridges through improved detailing, thousands of older bridges are susceptible to such cracking [5]. Previous works have reported that around 90% of fatigue damage in steel bridges was caused by distortion-induced loading [5, 6].

According to different studies [6, 7], one of the most common types of distortion-induced damage occurs in the stringer-to-floor-beam angle connections, i.e., more than 16% of all the fatigue damage cases collected in [6] and the most frequent case. This type of connections is a common detail in many existing steel bridges. A number of fatigue-crack cases have been reported for this type of connection [8, 9]. In most cases, fatigue cracks appeared in the angle fillet. In other cases, rivet failure was observed, where the fatigue crack began in the junction between the shank and the head of the rivets. In this case, the insufficient clamping force [10] causes bending as well as a prying effect, leading to the rivet head popping out [8]. These two fatigue failure types in connections are shown in Fig. 1.

As shown in Figs. 1(a) to (d), the two mechanisms causing distortion-induced fatigue cracks in these connections [6, 11] are:

- Rotation of the stringer ends associated with bending:

Although double-angle connections are normally designed as simple shear connections, they have a certain amount of rotational stiffness; thus, they partially restrain the end rotation of the stringer, inducing tensile stresses in the connections (see Figs. 1(b) and (c)). Depending on the relative stiffness between the stringer and the floor beam, either top or bottom of the connections could be in tension. The latter occurs because of the relatively low stiffness (i.e., large deformation) of the floor beam compared to that of the stringers, as shown in Fig. 1(c). Conversely, when the floor beam is stiff, the negative bending in the connection results in tension in the top of the connections, as demonstrated in Fig. 1(b). These tensile stresses have

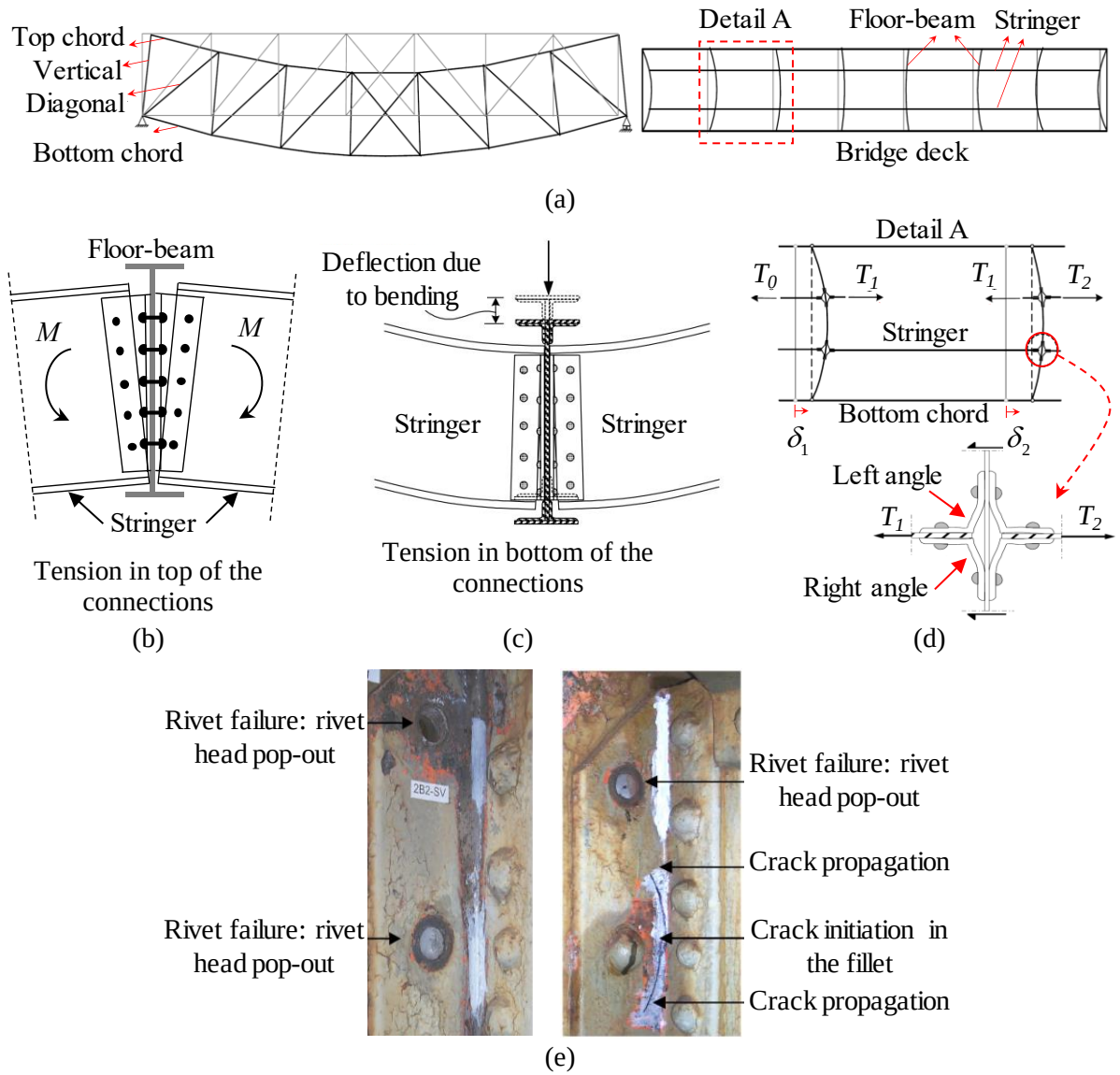

Fig. 1. (a) Global deflection of the bridge; Secondary tensile stress due to semi-rigidity of the connections with the tensile stress in the: (b) top of the connections; (c) bottom of the connections; (d) Secondary tensile forces in the connections due to the interaction between stringers and bottom chords; (e) Fatigue cracks observed in the double-angle web-to-web connections [6].

a relatively short influence line, and therefore, a significant number of cycles (e.g., in the order of axle load numbers) are applied by the trains passing over the bridge.

- Overall interaction between the floor system and the main trusses:

  In through-truss bridges, the vertical load of axles is transmitted to the stringers through sleepers. The floor beams carry the vertical reactions of the stringers and transmit them to the main truss. The global flexural deformation of the main truss bridge involves the longitudinal displacement of the truss joints, δ, to which the floor beams are connected (see Fig. 1(a)). However, the floor beams are partially restrained from following this deformation because of

the axial stiffness of the stringers and their connections to the floor beams. As a result, the additional axial forces, *T*, develop in the stringers and their connections to the floor beams. In this case, the floor beams are subjected to additional bending around the weak axis, as depicted in Fig. 1(d). This type of interaction has an influence line that is equal to the bridge span, and, in the case of railway bridges, there is essentially one loading cycle owing to the passage of each train. This phenomenon was first explained by [11], and later, was verified through onsite bridge testing by [8, 9].

In order to prevent fatigue cracks in the angles, the design formulations have been proposed by the American Railway Engineering and Maintenance-of-way Association (AREMA) [12] as well as [13, 14], to ensure that the angles have enough flexibility. However, many existing bridges do not satisfy the recommended formulations [15]. Therefore, the repairing techniques have been proposed by different researchers to solve the fatigue problem with existing bridges.

Traditional retrofitting techniques for retrofitting riveted metallic structures include the use of high-strength pre-tensioned bolts [8, 16, 17], welding additional elements, stop holes, repair of support conditions, etc. [15, 18, 19]. Additionally, in some cases, the connections were softened by removing some rivets [20]. The stiffness reduction in the connection, however, resulted in larger deformations, and led to some damage in other elements. These strengthening solutions could not permanently solve the fatigue problem in the connections and led to re-initiation of the fatigue cracks either from the same location or from another location [21]. For example, in the case of stringer-to-floor-beam angle connections, replacing the rivets with pre-tensioned bolts reduces the risk of fatigue failure in the fasteners but it does not solve the fatigue problem in the angle fillet, as it does not reduce the out-of-plane deformations.

Recently, carbon fibre-reinforced polymer (CFRP) materials have been used for strengthening metallic structures owing to their superior properties such as the higher fatigue and corrosion resistance, and their light weight compared to steel [22]. Both trapezoidal [23] and flat [24] prestressed unbonded reinforcement (PUR) systems were developed, in which prestressed CFRP plates were held using mechanical clamps working purely through friction under a symmetric loading condition. The systems were used for strengthening steel girders against flexural [25], buckling [26], and fatigue [27] loads. In addition, they were applied to strengthen the girders of an old steel bridge in Switzerland ([28]) and Australia [29, 30]. Furthermore, prestressed shape memory alloy (SMA) plates were used in a PUR system for strengthening stringer-to-floor-beam double angle connections [31]; however, this was only performed in the laboratory and not in any actual applications.

Development of a strengthening system being applicable to the real bridge connections is a greater challenge. Fig. 2(a) shows the details of a stringer-to-floor-beam double angle connection including sleepers and rails in a typical riveted steel bridge. Owing to the complex geometry of such details (i.e., the presence of floor beams, sleepers, and rails), it is nearly impossible to use prestressed plates (CFRP or SMA) for strengthening connections. Therefore, existing retrofitting solutions are not applicable to such details.

4.1.2. Outline of the study

In this study, for the first time, an applicable retrofitting solution for bridge connections with such complex geometric details is introduced. In the proposed system, prestressed CFRP rods (rather than plates) are used and the results of static and fatigue tests on the proposed system are briefly described. Next, the installation of the system for strengthening connections in an old riveted railway bridge in Switzerland is presented. Then, to demonstrate the effectiveness of the system to reduce the stresses in the connection hotspot, the results of short-term on-site measurements are presented. Next, the long-term monitoring of the strengthening system performance using a wireless sensor network (WSN) system is described, and the results are discussed. Finally, a multiaxial design criterion based on the critical plane approach is presented to evaluate the effect of strengthening on the fatigue state of the connections.

4.1.3. Development of the strengthening system

The concept of the proposed system for strengthening the top of stringer-to-floor-beam double angle connections is depicted in Fig. 2. As shown in Fig. 2(b), the system consists of two key components: a wedge-barrel anchor and a clamping system. The wedge-barrel anchor consists of a steel shaft with a conical hole inside, and three split aluminium wedges being in direct contact with the prestressed CFRP rod. The wedge-barrel anchor holds the prestressed CFRP rod through friction. The clamping system consists of high-strength steel plates that are connected together using high-strength bolts, as shown in Fig. 2(b).

By fastening the bolts in the bottom plates, the top and bottom plates grip the stringer flange, providing frictional resistance. The CFRP prestressing force is transmitted to the clamping system though the wedge-barrel anchor, and the clamping system transmits all the load to the stringer through friction. Additional details regarding the dimensions and the design of the strengthening system can be found in [32] .

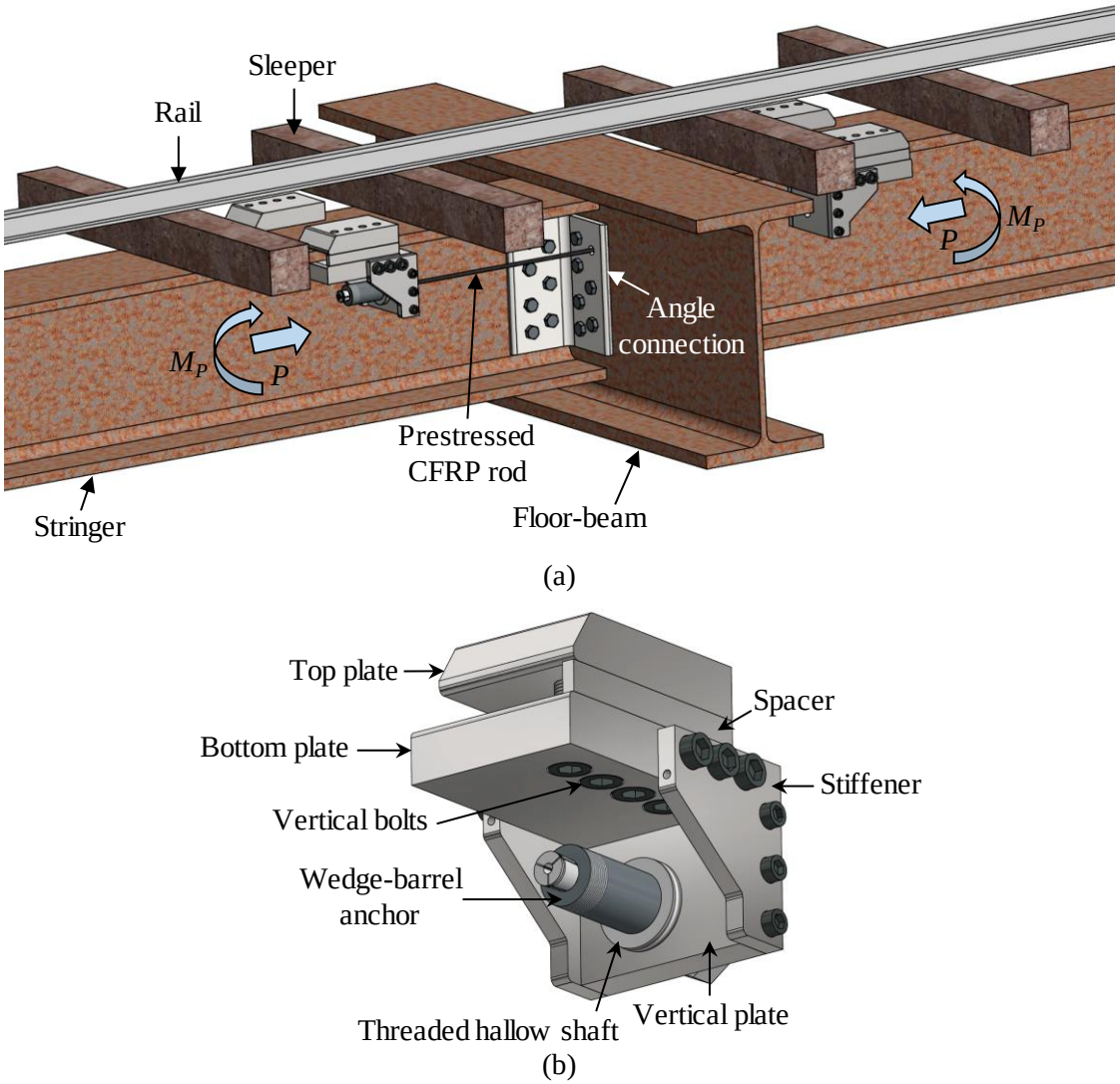

Fig. 2. Stringer-to-floor-beam double angle connection: (a) Geometric complexity; (b) Different components of the strengthening system.

The prestressing force in the CFRP rod applies a compressive force, *P*, and a positive bending moment, M_P, which counteracts with the negative bending moment in the connections (see Fig. 2(a)). Thus, the out-of-plane deformation, and consequently, the distortion-induced stresses in the connections are reduced. In the following sub-sections, a brief description of the experimental results of the wedge-barrel anchors and the clamping is provided.

4.1.3.1. Laboratory tests on the retrofitting system

To hold the prestressed CFRP rods, with a diameter of 8 mm, a new mechanical wedge-barrel anchor was developed at the Structural Engineering Research Laboratory Empa, Switzerland. The reliable performance of the wedge-barrel anchor was investigated through static and fatigue tests according to the standard procedures [33-35]. The test results showed that the anchor

fulfils the requirements of the codes and standards. The key results are summarised as follows:

In all static tests, the failure mode was the fracture of the CFRP rods, with an average tensile strength of 2370 MPa, which was higher than the guaranteed tensile strength of the CFRP rods (i.e., 2047 MPa). In addition, during the fatigue loading for 2 million cycles, neither slippage nor the CFRP rod failure occurred.

The fatigue performance of the clamping system was also experimentally investigated. The fatigue tests were conducted in a set-up shown in Fig. 3, in which two IPB 400 stringers, each with a span of 2.66 m, were connected to an IPB 550 floor beam, with a span of 1 m, using four L160×160×15 web-to-web angle connections. In this set-up, the stringers on one side and the floor beams on both sides rested on rolling supports. The dimensions of the parts in the set-up were initially similar to those in the bridge, which was to be later strengthened. Fatigue loadings were applied on the stringers with two 500 kN vertical actuators. The load ratio in the fatigue tests was 0.1 with the maximum load of 240 kN per actuator. The prestressing of each CFRP rod in the fatigue tests was 995 MPa (equivalent to 50 kN).

The fatigue tests showed that after 11 million loading cycles, no failure occurred in the CFRP rods. Moreover, no prestressing loss was observed in the CFRP rods, implying that during the fatigue tests, no slippage occurred in either the clamping systems or in the wedge-barrel anchors. The strengthening system reduced the stresses in the connection hotspots by more than 40%. It is noted that the connection hotspot, which is located on the angle fillet, were determined based on the finite element (FE) model, as described in [36].

4.1.3.2. Effect of removing the bolts

To install the strengthening system, two bolts/rivets (from the second row of the fasteners) have to be removed from the angles to let the CFRP rods pass the floor beam (see Fig. 2(a)). As shown in Fig. 3, the removed bolts were replaced with two hollow bolts. The strains in the angle hotspot were measured during bolt removal. In the connection hotspot, a rosette strain gauge with directions a, b, and c (a and c were perpendicular to each other) was applied to measure the state of stress in the connections. During bolt removal, the strain change in different directions was negligible, i.e., less than 10 microstrains.

Furthermore, before the installation of the strengthening system, the external loads on the stringers were statically increased up to 240 kN (as the maximum load in the fatigue tests) for the connections with and without bolts. The removal of the bolts did not change the strain in different directions during the application of the external loads. This observation is consistent

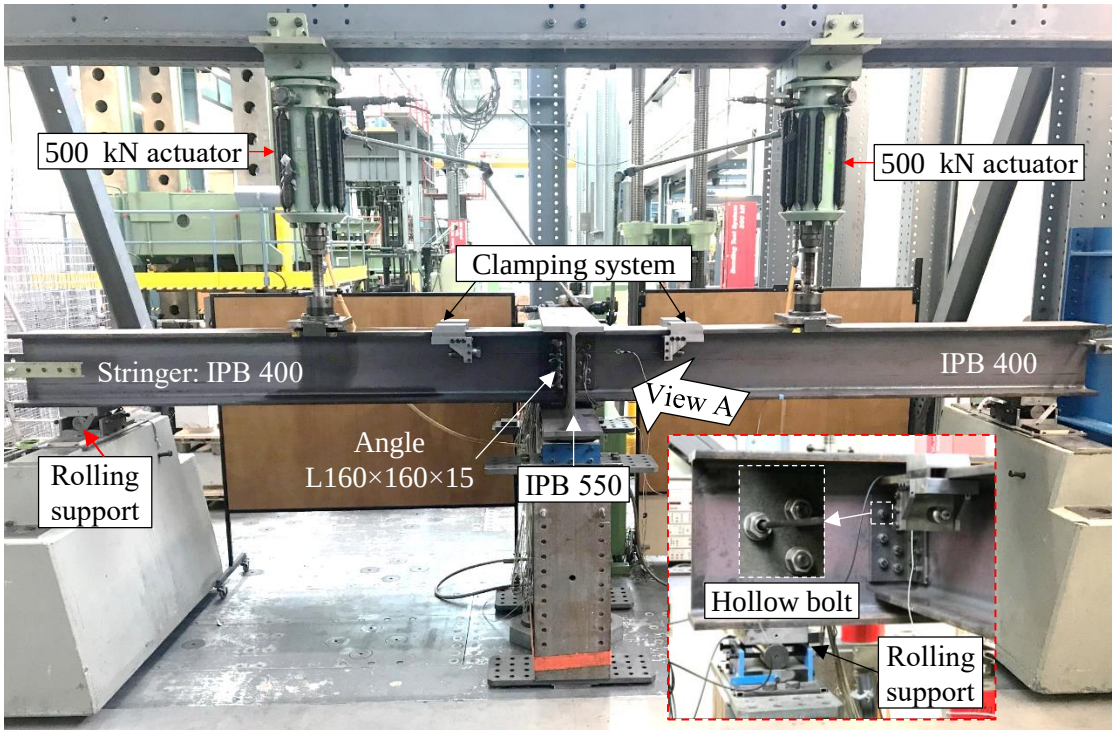

Fig. 3. Set-up for the laboratory tests.

with existing experimental results [37, 38], indicating that the removal of the bolts/rivets from the second row of bolts does not affect the out-of-plane deformation of the connections.

4.1.3.3. Advantages of the proposed strengthening system

Considering the above-mentioned results and descriptions, the proposed strengthening has the following advantages:

- The proposed system is capable of lowering the fatigue failure risk in the angle fillet and rivets simultaneously by reducing the out-of-plane deformations. Particularly, considering the fact that there is a considerable variation in the rivet clamping forces [10], the proposed prestressed system is a reliable alternative to previous retrofitting methods such as replacing every single rivet with pre-tensioned bolts.
- Unlike the previous PUR systems, the proposed clamping system is reliably performing under asymmetric loading conditions, increasing the versatility for different structural details and applications.
- The use of the CFRP rods rather than plates makes it possible to pass the rod through the hole. Therefore, it can be used for complex geometries such as stringer-to-floor-beam connections.

- As for the installation of the strengthening system the space under the bridge deck is used, it has minimum interference with bridge traffic. In addition, the proposed system minimises the structural damage, i.e., it works solely through friction, without the need to drill a hole in the parent structure.
- The applications of the developed wedge-barrel anchor in the civil engineering domain are not limited to the strengthening of metallic connections. The system can be used as an alternative to conventional prestressed steel strands, e.g., in cable-stayed bridges, prestressed concrete decks and box girders, and post-tensioned walls [39]. It is in particular suitable when there are concerns related to the long-term durability of prestressed steel strands in terms of corrosion, fatigue and relaxation.

4.1.4. Geometrical details of Aabach Bridge

The Aabach Bridge (see Fig. 4) is an old steel railway bridge, which was built in 1928 on the main line between Zürich and Chur in Switzerland. It was originally designed as a riveted single-track bridge that contains 10 panels. The bridge was constructed over a river with a total length of 38.7 m, a width of 5 m, and a height of 4.6 m, as shown in Figs. 5(a) and (b). The Aabach Bridge was constructed on a skew such that it spans the river at a 35° angle. The bridge is subjected to both passenger and freight trains on a daily basis.

All elements of the Aabach Bridge are made of structural steel. The bridge girders are either rolled or riveted built-up. The top and bottom chords, diagonals, and vertical members are shown in Fig. 4. The two rails are mounted on wooden sleepers, and the wooden sleepers are bolted to the longitudinal stringers using steel angles. The double angle stringer-to-floor-beam connections are shown in Fig. 5(c). The stringers and floor beams have rolled IPB 400 and

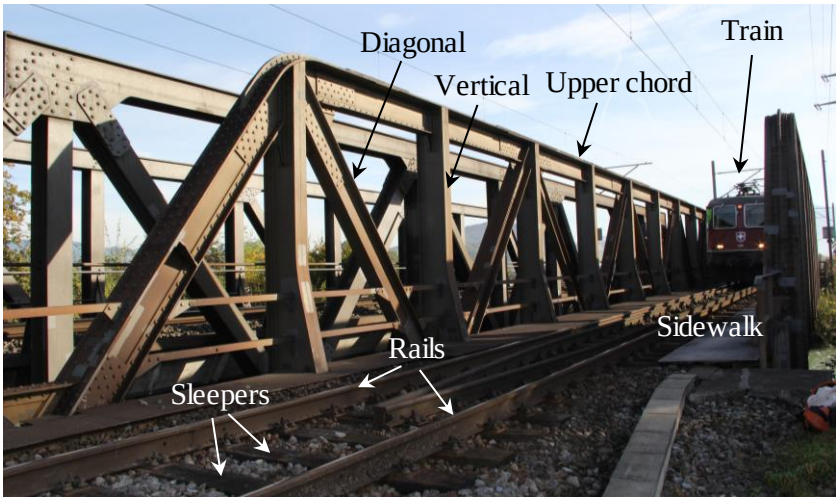

Fig. 4. Aabach Railway Bridge, Lachen, Switzerland.

IPB 800 sections, respectively. The connection that was selected for the strengthening is shown inside the circle in Fig. 5(a). The stresses in the left and right angles at this connection (see Fig. 5(c)) are investigated later in this study.

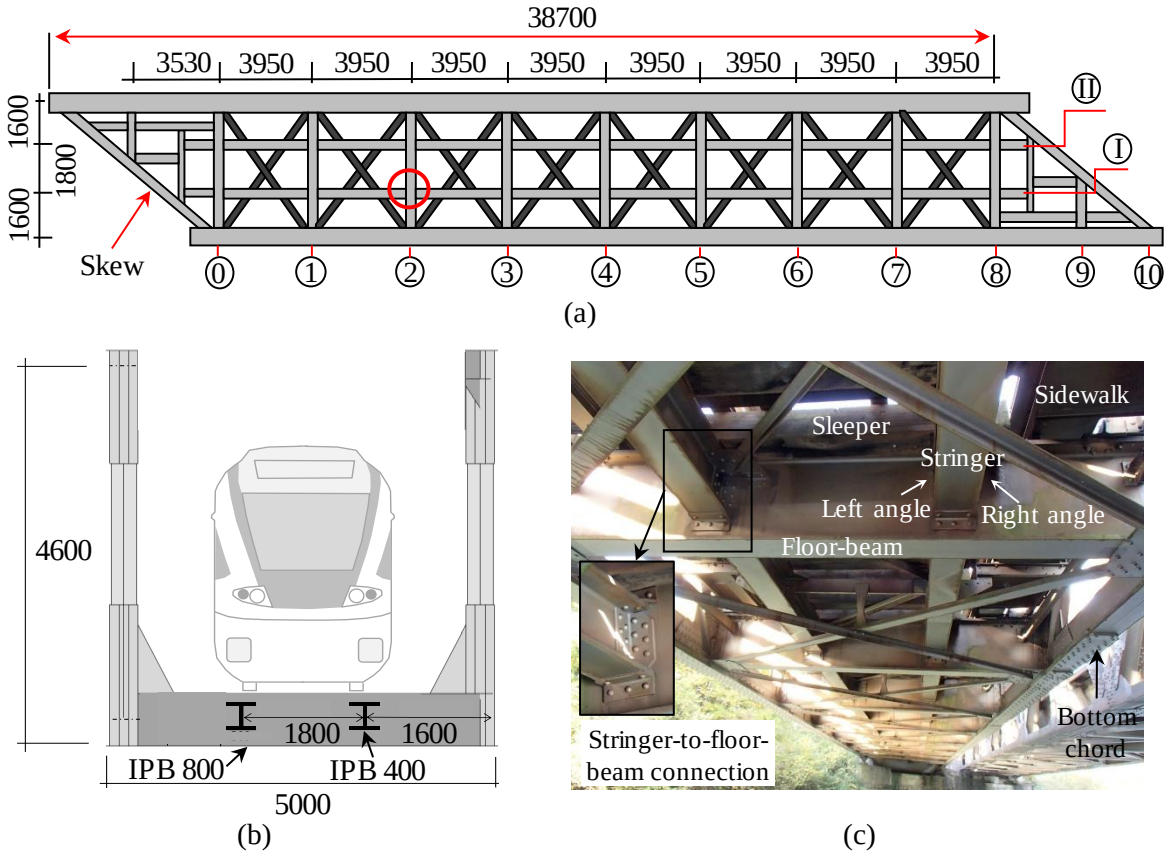

Fig. 5. Details of Aabach Bridge: (a) Layout of the bridge deck; (b) Dimensions of the bridge frame; (c) Elements of the bridge (bottom view).

It is noted that the stiffness ratio (i.e., the ratio of the flexural stiffness of the stringer to that of the floor beam), γ, introduced by [8] is equal to 0.01 for the Aabach Bridge. The reason for such a small relative stiffness is that the floor beam, with a depth of two times greater than that of the stringer, has a greater flexural stiffness than the stringers. The latter indicates that the tensile stresses develop at the top of the connections, as shown in Fig. 1(b), and, therefore, the strengthening system has to be installed on the top flange of the stringer.

4.1.5. Installation of the strengthening system on the Aabach Bridge

In this section, the stepwise installation procedure of the proposed strengthening system on the Aabach Bridge is described. Before the installation, two rivets were removed from the second row of the rivets in the angles located in either side of the stringer.

4.1.5.1. Presetting procedure

Once the two rivets were removed, the hollow bolts substituted the rivets, and the CFRP rods passed through the hole, as shown in Fig. 6(a). The diameter of the rivet hole was 22 mm and the hollow bolt was an M20, 8.8 with a hole diameter of 14 mm. The torque applied to fasten the hollow bolt was 100 Nm resulting in a pre-tensioning of 32 kN.

It is noted that the diameter of the hole has to be relatively larger than that of the rod in order to ensure that the rod does not touch the edge of the hole to prevent any transverse stresses on the rod and possible damaging the fibres. The CFRP rod did not touch the edge of the hole either in the laboratory tests or in the field application at the Aabach Bridge because the relative deflection of the CFRP rod inside the hole was very small. However, for the cases where there is a risk that the rod touches the edges of the hole, either the diameter of the hole should be slightly increased or a soft material could be placed around the rod inside the hole to prevent any damage to the carbon fibers.

Next, the clamping system was installed. On one side of the CFRP rods, the wedge-barrel anchors were already installed and preset, and on the other side, the wedge-barrel anchors were installed after the CFRP rods passed through the hollow bolt, as shown in Fig. 6(b).

To apply the presetting force to the wedges that were installed on-site, a presetting system shown in Fig. 6(c) was used. This system includes a ring with a threaded hole inside, which is connected to the threaded area around the barrel. A presetting hollow shaft with a certain length is then placed around the wedges and on the top surface of the barrel. Then, a presetting top plate is placed on the wedges. The length of the presetting hollow shaft was determined based on the laboratory tests to provide an adequate presetting force. Six M8 bolts are passed through the holes in the presetting top plate, and then, the threaded holes in the ring. By fastening the bolts (see Fig. 6(c)), the presetting top plate pushed the wedges into the barrel. The fastening of the bolts continued until the top plate touched the presetting hollow shaft. To prevent the wedge-barrel anchor from rotating during the fastening of the six M8 bolts, two temporary presetting walls. Once the presetting procedure for both anchors was completed, the required parts for presetting, i.e., the presetting ring, the hollow shaft, and the top plate, were removed.

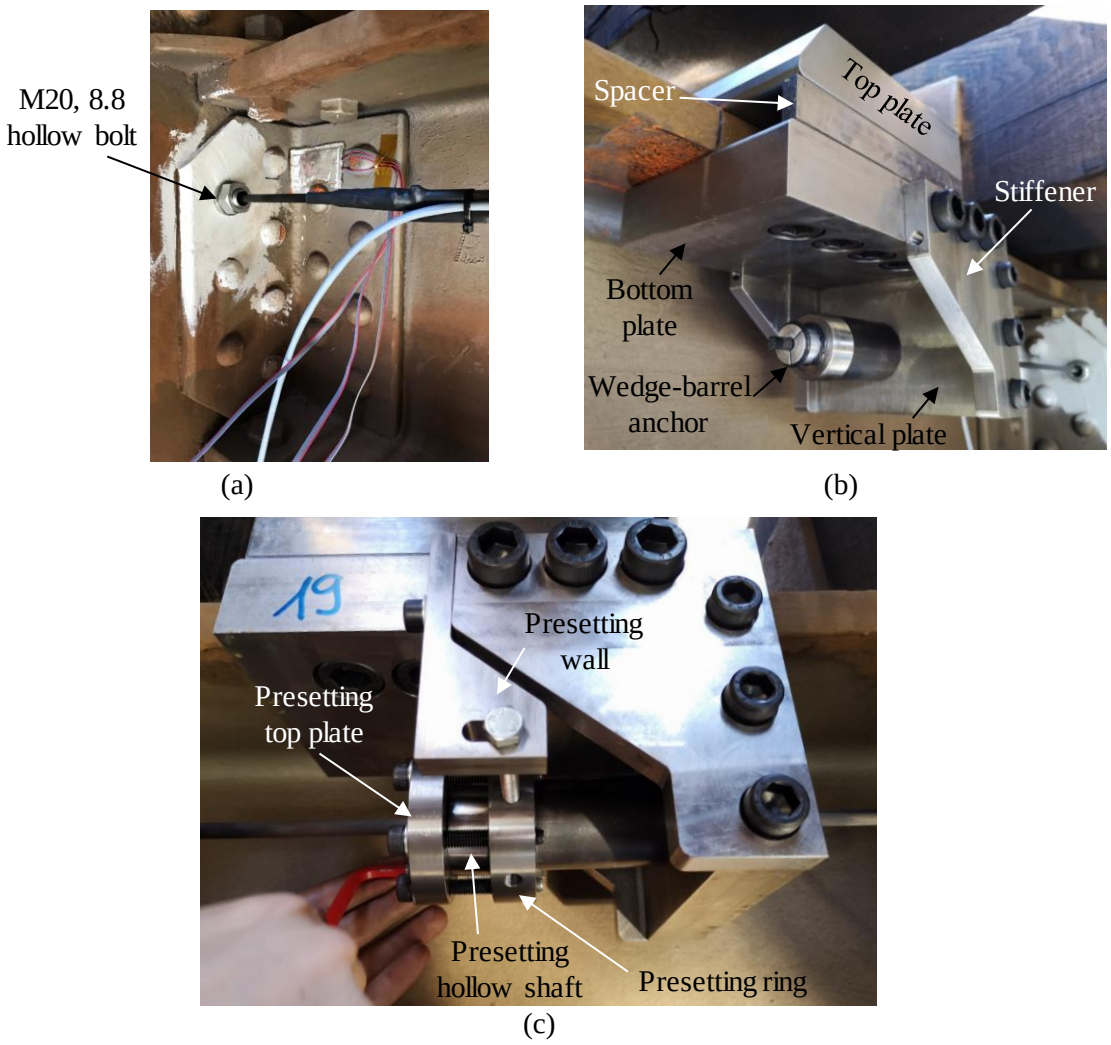

Fig. 6. Presetting procedure: (a) Passing the CFRP rod through the hollow bolt; (b) Installing the clamping system before presetting; (c) Pushing the wedges into the barrel.

4.1.5.2. Procedure of CFRP prestressing

After presetting, each CFRP rod, with a diameter of 8 mm, was pulled with a prestressing force of up to 50 kN (equivalent to 995 MPa and 49% of the CFRP guaranteed tensile strength of 2047 MPa). The CFRP rods were manufactured by the S&P Clever Reinforcement Company AG, Switzerland. The fibre volume fraction of the CFRP rods and the elastic modulus in the fibre direction were 65% and 160 GPa, respectively.

The prestressing force was applied to the CFRP rods by pumping two hydraulic cylinders, as shown in Fig. 7. As given in the figure, a temporary housing was connected to the clamping system acting as a support for the hydraulic cylinders. The parts that were previously used for presetting were used here as a connector between the wedge-barrel anchor and the hydraulic cylinder using a high strength M13 threaded rod, with a tensile capacity of 150 kN.

Fig. 7. Prestressing procedure: Pumping the hydraulic cylinders to pull the CFRP rods using a temporary housing.

During the pulling, the prestressing level was monitored by two strain gauges applied on each rod. Once the desired value of the prestressing force was achieved, the oil pressure behind the cylinders was fixed, and then, the threaded hollow shaft (see Fig. 2(b)), was fastened until it touched the back of the barrel. At this stage, the system became fixed, and, the oil pressure in the hydraulic cylinders was released.

The applied prestressing to the CFRP rods on the right and left sides of the stringer is illustrated in Fig. 8. As shown in Fig. 8, the prestressing level in both CFRP rods was approximately the same. In Fig. 8, a fluctuation in the prestressing level of approximately 1000 MPa is observed. The first reduction in Fig. 8 occurred after the fixation of the system using the threaded hollow shaft, resulting in a prestressing level lower than the target value. To compensate this prestress reduction, the CFRP rods were again pulled up to a force a bit greater than the target prestressing level. In this manner, after the second prestressing reduction, the required prestressing force in the CFRP rods was achieved.

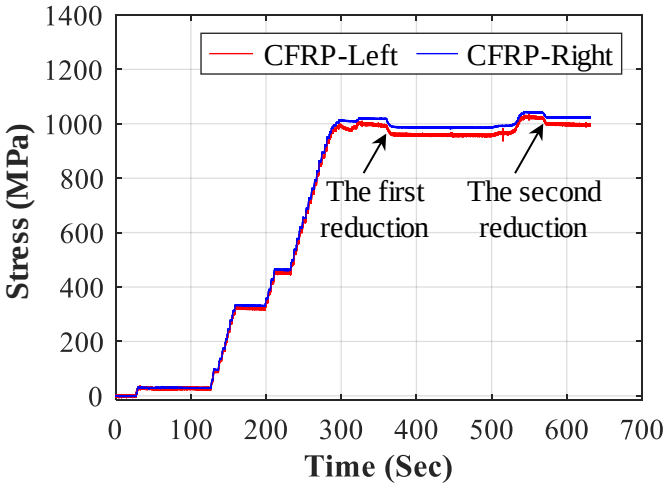

Fig. 8. Applied prestressing to the CFRP rods during the oil pumping.

4.1.6. Short-term measurements

To evaluate the strengthening effect, short-term measurements were conducted using a data acquisition system (HBM, AG, Darmstadt, Hesse, Germany), during the passage of different trains, as shown in Fig. 7. The strain gauges used for the short-term measurements are shown in Fig. 9. As shown in Fig. 9(a), two rosette strain gauges of type RY8x-3/120 (HBM, AG, Darmstadt, Hesse, Germany), with the grids in three different directions, were applied on the left and right angle fillets to obtain the multiaxial state of stress in the connection hotspots.

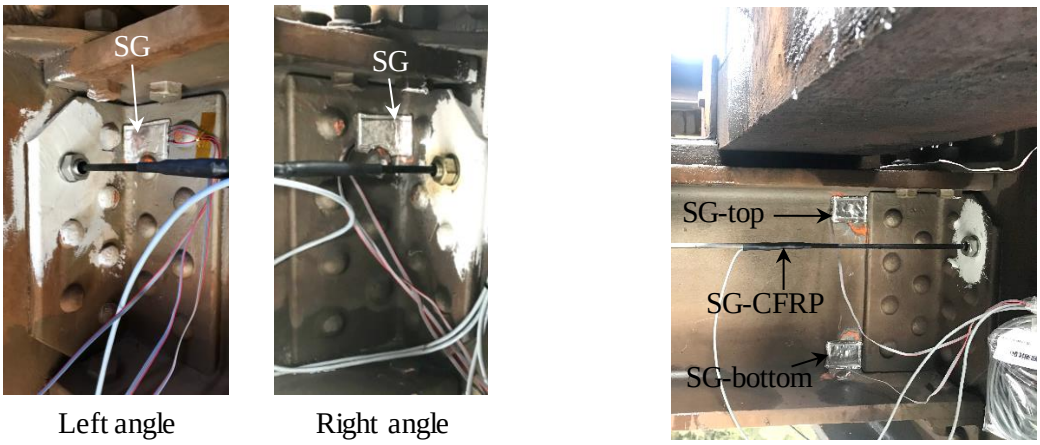

Fig. 9. Strain gauges used for short-term measurements: (a) Rosette strain gauges on the angles; (b) Strain gauges on the web and the CFRP rod.

Furthermore, the strain in each CFRP rod was measured using strain gauges of type 1-LY66-6/120 (HBM, AG, Darmstadt, Hesse, Germany), shown in Fig. 9(b). these strain gauges were also used during the prestressing process. In addition, two unidirectional strain gauges of type 1-LV41-3/120 (HBM, AG, Darmstadt, Hesse, Germany), were used in the outermost top and

bottom of the stringer web immediately after the stringer fillet ends. The total duration of the short-term measurements was four hours, i.e., two hours before and two hours after strengthening. The frequency of the measurement was 2400 Hz. The results of short-term measurements in the angles and the web are presented in the following sections.

4.1.6.1. Left angle

The location and the grid directions of the rosette strain gauge on the left angle are schematically illustrated in Fig. 10(a). The strain gauge was positioned 52 mm away from the top surface of the angle. The strain history in different directions measured by the rosette strain gauge on the left angle (see Fig. 5(c)) before the installation of the strengthening system is shown in Fig. 11(a). As shown in the figure, during the two-hour measurements, 17 trains passed over the bridge. The majority of the fluctuations were due to the passenger trains, resulting in nearly the same stress range. It is noted that to distinguish between the different curves, the high-frequency measurement noise was suppressed by means of a digital 50th-order lowpass filter with a cut-off frequency of 70 Hz in the MATLAB software (Version R2018a).

The strain cycles for a passenger train, i.e., Train (6), is shown in Fig. 11(b). As shown in the figure, the strains in the a- and c-directions are approximately the same, while the strain in the

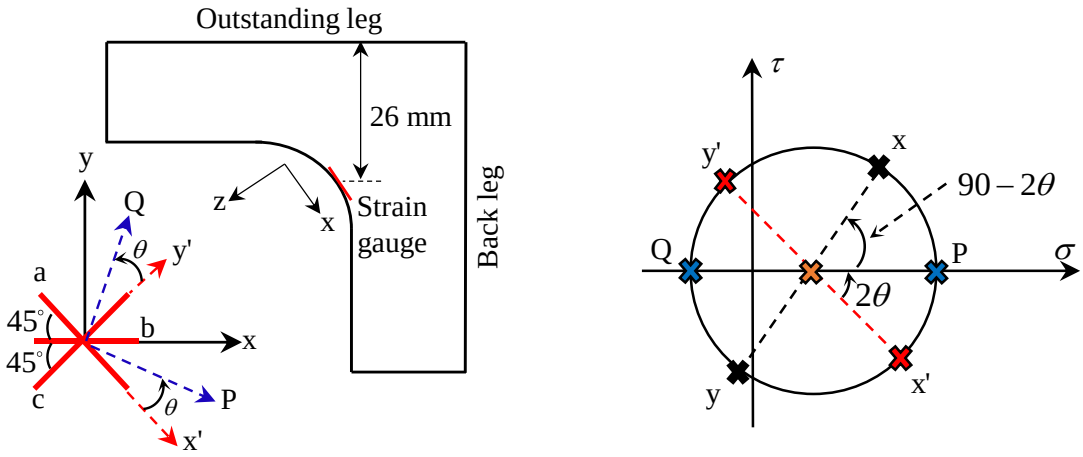

(a) (b)

Fig. 10. Directions of the rosette strain gauge on the left angle: (a) Top view of the angle and coordinate system; (b) Corresponding Mohr's circle.

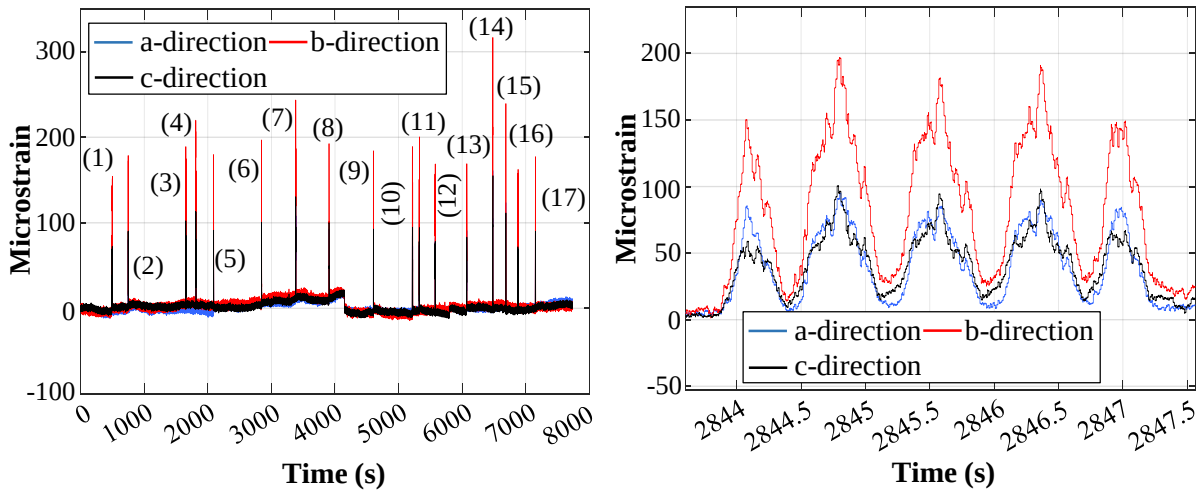

(a) (b)

Fig. 11. Strain history in the hotspot of the left angle before strengthening: (a) Due to the passage of different trains; (b) Due to the passage of Train (6).

b-direction has the greatest magnitude. From the measured values of the strains in the a-, b-, and c-directions, the principal strains in the x'-y' plane, i.e., ε_P and ε_Q, as well as its angle with the x' and y' axes, θ, were calculated with Eq. 1,

$$\varepsilon_P = \frac{\varepsilon_a + \varepsilon_c}{2} + \frac{1}{\sqrt{2}}\sqrt{(\varepsilon_a - \varepsilon_b)^2 + (\varepsilon_b - \varepsilon_c)^2} \tag{1.1}$$

$$\varepsilon_Q = \frac{\varepsilon_a + \varepsilon_c}{2} - \frac{1}{\sqrt{2}}\sqrt{(\varepsilon_a - \varepsilon_b)^2 + (\varepsilon_b - \varepsilon_c)^2} \tag{1.2}$$

$$\theta = \frac{1}{2}\tan^{-1}\left(\frac{\varepsilon_a - 2\varepsilon_b + \varepsilon_c}{\varepsilon_a - \varepsilon_c}\right) \tag{1.3}$$

Both the principal strains and stresses are in the P- and Q-directions. The principal stresses are calculated using the following equations:

$$\sigma_P = \frac{E}{1-\nu^2}(\varepsilon_P + \nu\varepsilon_Q) \tag{2.1}$$

$$\sigma_Q = \frac{E}{1-\nu^2}(\nu\varepsilon_P + \varepsilon_Q) \tag{2.2}$$

Where E and ν are elastic modulus and the poison's ratio of the steel, respectively. According to the Mohr's circle shown in Fig. 10-b, to obtain the stresses in the x-y plane, they have to be calculated on the plane with an angle of $90-2\theta$ with respect to the principal directions P-Q in the Mohr's circle (i.e. angle of $45-\theta$ in the element). Therefore, considering plane stress

conditions, the stresses in the x-y coordinate system are calculated as follows:

$$\sigma_x = \frac{\sigma_P + \sigma_Q}{2} + \frac{\sigma_P - \sigma_Q}{2}\sin 2\theta \tag{3.1}$$

$$\sigma_y = \frac{\sigma_P + \sigma_Q}{2} - \frac{\sigma_P - \sigma_Q}{2}\sin 2\theta \tag{3.2}$$

$$\tau_{xy} = \frac{\sigma_P - \sigma_Q}{2}\cos 2\theta \tag{3.3}$$

As the stress state on the surface is considered, the other stress matrix components in the x-y-z coordinate system are zero, i.e., $\sigma_z = \tau_{xz} = \tau_{yz} = 0$. Using E = 200 GPa and ν = 0.3, the above equations were solved in the MATLAB to obtain the stress history in the rosette strain gauge located on the left angle before and after strengthening, and the results are depicted in Fig. 12. Before strengthening, as shown in Fig. 12(a), the stresses in the y-direction, σ_y, are generally less than one-third of those in the x-direction, σ_x. The shear stress, τ_{xy}, is negligible. This shows that the x and y directions are very close to the principal directions in the element. Additionally, in most fluctuations, the maximum stress in the x-direction is in the order of 40 MPa. These fluctuations were due to the passage of the passenger trains.

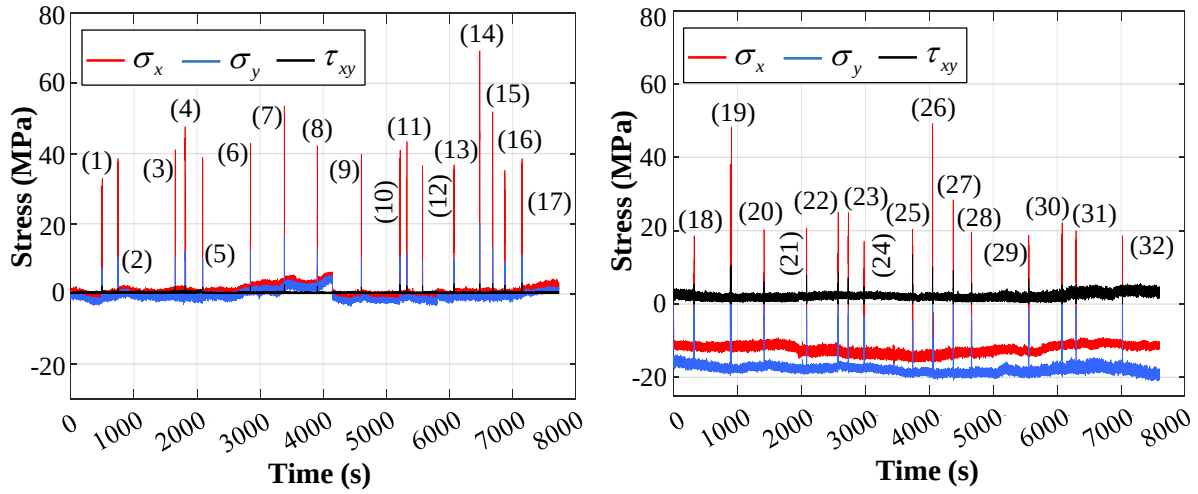

(a) (b)

Fig. 12. Stress history in the hotspot of the left angle: (a) Before strengthening; (b) After strengthening.

After strengthening, short-term measurements, with the same 2400 Hz frequency were conducted. During this period, 15 trains passed over the bridge. As shown in Fig. 12(b), due to the prestressing, a compressive stress of 12 MPa and 16 MPa was measured in the x- and y-

directions, respectively, with the shear stress being approximately zero. Due to the passage of the passenger trains, most fluctuations have a nearly identical maximum stress in the x-direction, i.e., approximately 20 MPa.

It is noted that the short-term measurements were conducted as follows: at the end of the first 2-hour short-term measurements (before strengthening), the measurement was stopped. Then, it was resumed during the prestressing, as shown in Fig. 8. When the prestressing process was completed, the measurement was stopped again, and immediately, the next 2-hour short-term measurements (after strengthening) were conducted. Therefore, the time 0s in Fig. 12(b) corresponds to the start of the data recording when the prestressing process was completed.

The stress cycles before and after strengthening due to the passage of passenger trains (6) and (23) are depicted in Fig. 13. Note that the cycles in the figure did not occur simultaneously, i.e., they are depicted here together for the sake of comparison. Due to the passage of Train (6), a stress range of 36.2 MPa, with a minimum stress of 6.5 MPa is observed in the x-direction. After strengthening, the $\Delta\sigma_x$ stress range due to the passage of Train (23) is approximately 36.5 MPa, with a minimum stress of -12 MPa. It shows that the strengthening system reduced the mean stress by 18.35 MPa (i.e., from 24.6 to 6.25 MPa). However, the stress range magnitude before and after the strengthening is approximately the same. The stress range values in the y-direction before and after strengthening were 10.4 and 12 MPa, with the corresponding minimum stress being approximately 1.6 and -16 MPa, respectively (see Fig. 13(b)). Neglecting shear stress τ_{xy}, the stress cycles for σ_x and σ_y show that the strengthening system reduces only the mean stress, and not the stress range. The reason is that the proposed strengthening system does not add a considerable flexural stiffness to the connections.

In addition to the passenger trains, there were other types of trains such as Trains (14), (19), and (23), which generated completely different cyclic patterns compared to the passenger trains. The stress cycles due to these three trains are depicted in Fig. 14. It is noted that Train (14) passed over the unstrengthened connections and Trains (19) and (23) passed over the strengthened connections. For Train (19), first, a large cycle was applied, and then, after a number of smaller cycles, the bridge was subjected to a series of larger load cycles. Conversely, for Train (26), after a large cycle, with the largest measured amplitude among all the trains, the subsequent cycles are negligible.

To investigate the strengthening effect under the load of Train (14), consider the cycles in Fig. 14(a). As shown in the figure, for some cycles, the mean stress value in the x-direction, σ_{mx}, is

equal to 53.25 MPa. Considering the fact that the strengthening system does not change the

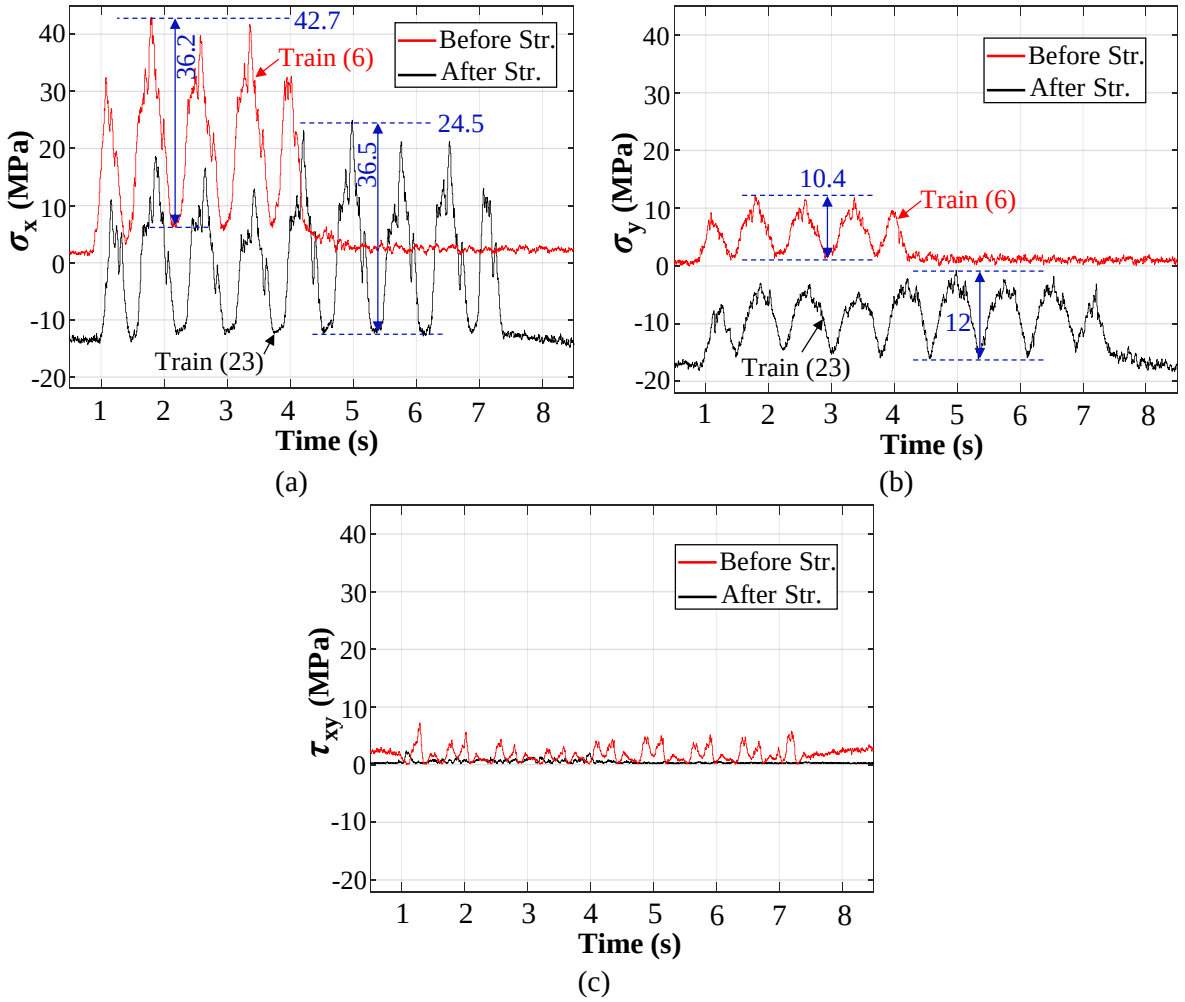

Fig. 13. Stress history due to (6) and (23) in left angle: (a) x-direction; (b) y-direction; (c) Shear stress.

stress range, and it reduces only the mean stress by 12 MPa in the x-direction, it is inferred that if exactly the same train passed over the bridge after strengthening, the mean stress would be equal to 41.25 MPa, which is equivalent to a 23% reduction in the mean stress. In the same manner, for the first cycle of Train (26), the reduction of the mean stress value would be from 31.85 to 19.85 MPa, resulting in 38% reduction in the mean stress.

The above descriptions indicate that the effectiveness of the strengthening system in reducing the stresses due to the passage of each train depends on the type of the train. To evaluate the strengthening effect, all the stress cycles applied to the left angle were collected; the stress cycles due to the passage of each train in the x- and y-directions were identified by the stress range $\Delta\sigma$, the mean stress σ_m, and the corresponding number of cycles *n*. A total of 229 cycles were applied to the connection by 32 trains (including the trains before and after the

strengthening), ignoring the small cycles with stress ranges below 10 MPa in the x-direction. As most of the trains were passenger trains (i.e., same type of trains), the stress components

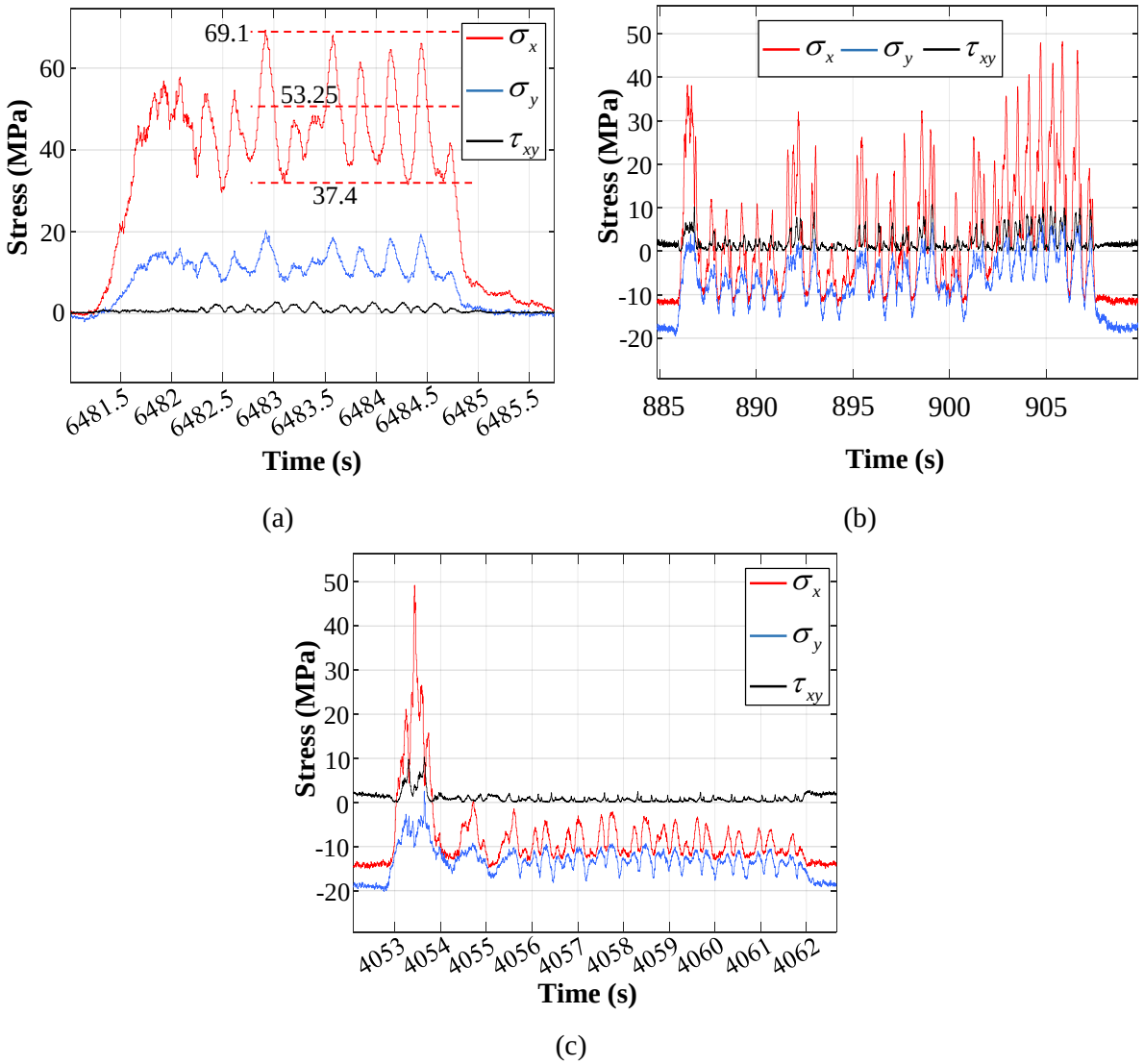

Fig. 14. Stress history in the left angle due to: (a) Train (14); (b) Train (19); (c) Train (26).

that represent all the passenger trains were obtained. Therefore, the stress cycles due to Trains (14), (19), and (26) were removed from the pool of passenger trains. The effect of strengthening on the stress components due to non-passenger trains were considered as separate cases.

The information related to the stress cycles due to the passenger trains are summarised in Table 1. In this table, the cycles due to Trains (18)–(32), which were obtained after the strengthening, were accounted as the cycles that would be generated if the strengthening system were not installed. It means that the mean stress values in the table due to Trains (18)–(32) were obtained by ignoring the compressive stress due to the strengthening. For the stress range, however, the measured values were directly used as the stress range was unaffected by the strengthening system.

The average values for the stress range and the mean stress in the x- and y-directions, as well as the standard deviations (SD) are presented in Table 1. Previous studies [19] showed that the stress range fractile from 50 to 75% makes the largest contribution to the fatigue

Table. 1. Cyclic stresses in the left angle hotspot due to the passenger trains

Parameter	$\Delta\sigma_x$ (MPa)	σ_{mx} (MPa)	$\Delta\sigma_y$ (MPa)	σ_{my} (MPa)
Average	29	17	10.6	6.6
SD	4.8	3	2.3	2
$S_{95\%}$	36.7	22.9	14	9.8

damage sum in metallic bridges because the number of cycles with greater stress ranges (i.e., the fractile from 90 to 95%) is very limited. However, to the best of the authors' knowledge, such a recommendation has not been proposed for the mean stress.

In this study, the values for the stress range and the mean stress are given for the percentile of 95^{th}, $S_{95\%}$, (i.e., those that are greater than 95% of all values) as a more conservative value compared to 50 to 75%. These values can be used to evaluate the strengthening effect. For example, the compressive stress of 12 MPa in the x-direction reduces the mean stress value of the 95^{th} percentile by 47% from 22.9 to 10.9 MPa. The compressive stress of -16 in the y-direction would reduce the 95^{th} percentile mean stress from 9.8 MPa to -6.2 MPa. Later in this study, a multiaxial fatigue analysis is performed to investigate the fatigue state in the angles before and after strengthening.

4.1.6.2. Right angle

The stress history in the right angle hotspot (see Fig. 5-c) before strengthening showed that the stress levels were lower than those in the left side, i.e., in the order of 20 MPa in the x-direction for the passenger trains. The reason is that due to the overall interaction between the floor system and the main trusses, a flexural deformation occurs in the floor beam around the weak axis, as depicted in Figs. 1(a) and d. As a result, a greater tensile stress is imposed to the angle that is located closer to the floor beam mid-span (here, it is the left angle). Therefore, the fatigue state in the left angle is more critical than that of the right angle.

4.1.6.3. Stresses in the web

In the short-term measurement, the stress history in the stringer web, before and after the strengthening, was measured. The measurement results showed that the stress levels due to the passage of the trains are generally low even before the strengthening, i.e., lower than 16 MPa.

The strengthening system caused a compressive stress of approximately 8 MPa in both the top and bottom of the web. The stress history due to the passage of Trains (6) and (14), provided in Appendix I, showed that the tensile stress in the stringer, due to the global deformation of the bridge is 4 and 7.5 MPa, respectively. The global distortion-induced tensile stresses in the stringer due to the passage of all trains (including non-passenger trains) were collected. The 95th percentile value of this stress was 6.75 MPa, which was lower than the compressive stress applied by the strengthening system.

4.1.7. Long-term measurements over a 7-month period

Since the installation of the retrofitting system on the bridge, the long-term performance of the system is being monitored using a WSN system (Decentlab GmbH, Switzerland). The measurements will continue for at least one year. The WSN system consists of two nodes for measuring the strain in each CFRP rod, and one node for the air humidity and temperature measurement, as depicted in Fig. 15. The WSN system collects the sensors' output values, and sends the data to a platform based in Switzerland every 10 min. The data is accessible for authorised users via the internet.

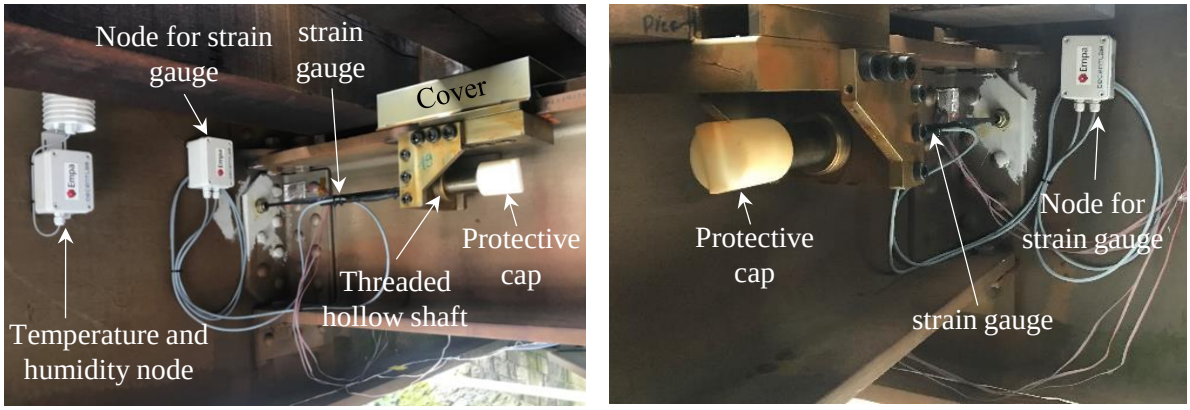

(a) (b)

Fig. 15. WSN system for the long-term monitoring and protective measures against corrosion: (a) Left side; (b) Right side.

To measure the strain in each CFRP rod, two strain gauges of type 1-LY66-6/120 (HBM, AG, Darmstadt, Hesse, Germany) were connected to each node using a wired connection: a strain gauge that was applied on the CFRP rod, and a dummy strain gauge to compensate the temperature effect. The strain gauges for the long-term measurements were prepared in advance at Empa, Switzerland, and they were protected against moisture for long-term outdoor application. For detailed information about the WSN system see [29].

The prestressing loss in the CFRP rods due to the slippage of the clamping system or CFRP rods inside the wedge-barrel anchors is monitored using the WSN system. The CFRP rods stress evolution during nearly a 7-month period after installation of the strengthening system is shown in Fig. 16(a). The results showed that after an initial drop, the prestressing level in the CFRP rods have stabilised, indicating no strengthening system slippage. The initial drop in the prestressing level is attributed to the fact that the wedge-barrel anchor functions solely through friction, and immediately after the prestressing application, the CFRP rods and wedges move slightly in the barrel. This was also observed in the uniaxial tensile tests on the wedge-barrel

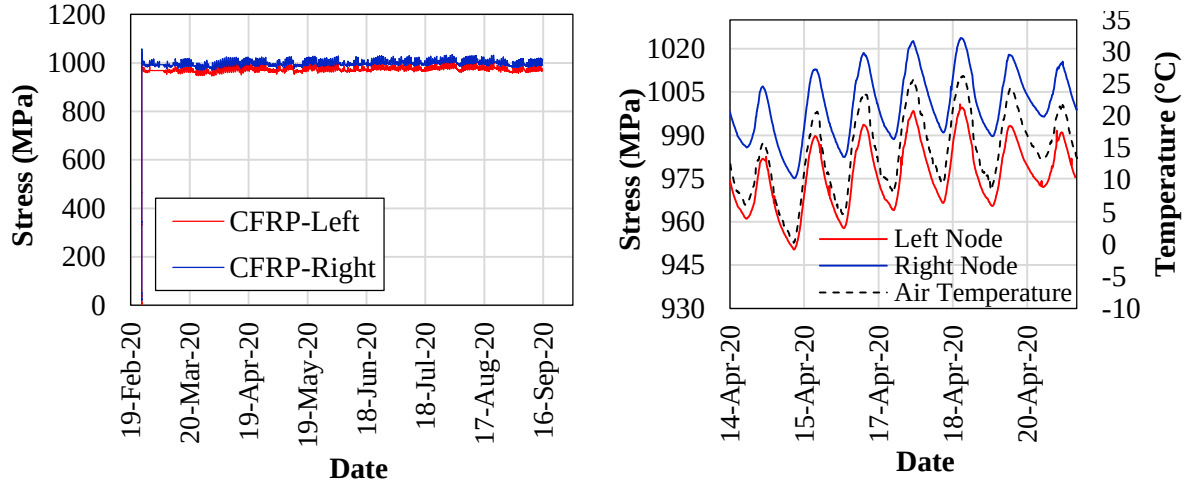

Fig. 16. Long-term measurements over a 7-month period after the installation: (a) Stress history in the CFRP rods measured by the WSN system; (b) Stress variation in the CFRP rods with the air temperature change.

anchors. However, after a short time period, the CFRP rod stress level stabilised. Here, a target prestressing level of 995 MPa was selected. The CFRP rods were initially prestressed up to approximately 1050 MPa, and after the initial prestressing loss, the prestressing of approximately 1000 MPa was achieved, showing less than a 5% loss compared to the initial value.

It is noted that the results of the long-term monitoring are valid only for the above-mentioned specific period and not beyond that. During this period, the minimum and maximum air temperature were -3.5 and 36 °C, respectively, and the minimum and maximum relative humidity were 18.7 and 99.2%, respectively. The fluctuations in the CFRP prestressing level in Fig. 16(a) originate from the air temperature change. As shown in Fig. 16(b), the prestressing change in both CFRP rods are synchronised with the air temperature change. When the temperature increases, the steel elements between the clamping systems expand, and thus, the

CFRP prestressing increases. Therefore, in general, an increase in the air temperature leads to an increase in the CFRP prestressing level.

4.1.8. Protection of the strengthening system

Although the CFRP materials have excellent long-term durability in terms of corrosion, fatigue, and show minimum stress relaxation, the mechanical anchors, which were made of steel, need to be protected against corrosion. For protection against corrosion, a layer of Tectyl multi-purpose anti-corrosion coating (Petro-Lubricants-Mineraloel AG, Switzerland) was sprayed on all metallic components of the strengthening system, i.e., the clamping system plates and the wedge-barrel anchors. In addition, in the wedge-barrel anchors, CFRP rods, aluminium wedges, and steel barrels are in direct contact; thus, there is a galvanic corrosion risk. To isolate the wedges, the barrel, and the CFRP rod from the air, a protective cap made of Polyoxymethylene (POM) material (see Fig. 15) was fastened on the free end of the barrel using the threads. The hole in the loading end of the barrel was also filled with a flexible covering agent of type Abdeckkitt AK22 (HBM, AG, Darmstadt, Hesse, Germany) to prevent air and humidity penetration into the anchor. Thus, the wedge-barrel anchors were completely isolated from the surrounding air. Furthermore, to prevent direct rainfall on the clamping system, a galvanised steel cover (i.e., shelter) was installed on top of the clamping system, as shown in Fig. 15(a).

4.1.9. Multiaxial fatigue criterion

The mean stress effect is not clearly considered in the calculation procedure suggested in European and the US standards. Thus, the positive effect of the reduction of the mean stress by the retrofitting systems cannot be considered in such calculations [40]. In addition, the presence of multiaxial stress state in the stringer-to-floor-beam angle connections increases the complexity of the problem. The reasons for overlooking the mean stress effect in codes could be the complexity of the calculations, and also the fact that prestressed retrofitting systems for the riveted structures have been mainly introduced in recent years and are not among the well-established repairing methods [15].

In this study, a critical plane-based multiaxial fatigue criterion was proposed to consider the mean stress and multiaxiality at the same time. In this section, first, the multiaxial fatigue theory based on the critical plane approach is briefly discussed. Then, the theory is used to obtain the fatigue state in the angle connections before and after the strengthening.

4.1.9.1. Critical plane approach

Experimental observations indicate that the cracks nucleate and grow on specific planes called critical planes [41]. Depending on the material and loading conditions, these planes are those with the maximum shear or tensile stress amplitude [42]. Multiaxial fatigue models that relate fatigue damage to stresses and/or strains on these planes are called critical-plane-based models.

In this study, the modified Wohler curve method (MWCM) proposed in [43] is employed for multiaxial fatigue analysis. In this model, similar to most stress-based multiaxial models, two parameters are required: the shear stress amplitude and the maximum normal stress on the critical plane. In ductile steels, the driving force for the crack nucleation at the micro level is shear movement. Therefore, the critical plane is the plane with the maximum shear stress amplitude τ_a, as shown in Fig. 17. In addition to the shear stress amplitude, the maximum normal stress acting on the critical plane, $\sigma_{\text{n, max}}$, helps the crack open and propagate at the micro level by reducing the interlocking and friction between the crack surfaces. The MWCM proposes the following equation ([43]):

$$\tau_a + (\tau_A - \frac{\sigma_A}{2})\rho = \tau_A \tag{4}$$

where, τ_A is the fully reversed shear fatigue limit, σ_A is fully reversed uniaxial fatigue limit, and ρ is the critical plane stress ratio defined with the following formulation:

$$\rho = \frac{\sigma_{\text{n,max}}}{\tau_a} \tag{5}$$

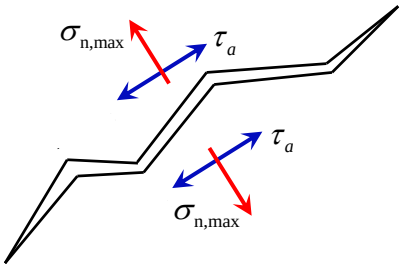

Fig. 17. Effective parameters in fatigue crack nucleation in the MWCM.

The mean stress effect in MWCM is taken into account with the ρ value. The MWCM diagram is shown in Fig. 18, where τ_α, is plotted as a function of ρ.

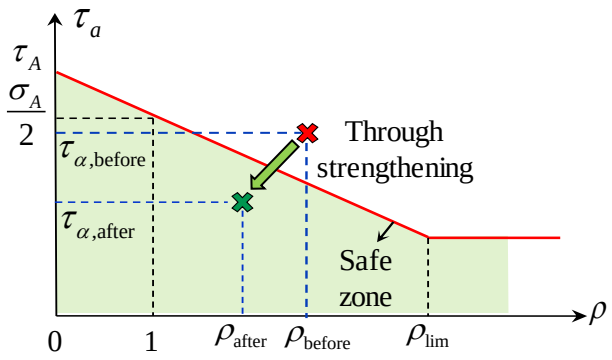

Fig. 18. Modified Wöhler curve method diagram.

As shown in the figure, the τ_α value decreases when ρ increases. However, when ρ is greater than a certain limit, namely ρ_{lim}, a further increase in the ρ value no longer affects the τ_α value. The reason is that when micro cracks are fully open in large ρ values, a further increase in the normal mean stress (accounted for by the ρ value) does not result in an increase in the fatigue damage ([43]). The value of ρ_{lim} is mathematically obtained using Eqs. (4) and (5) with the following formulation:

$$\rho_{\text{lim}} = \frac{\tau_A}{2\tau_A - \sigma_A} \tag{6}$$

Note that for the case of a fully reversed uniaxial cyclic loading, $\tau_\alpha = \sigma_A / 2$ and $\rho = 1$. For design purposes, the value of fully reversed uniaxial fatigue limit is calculated by Johnson's formulation ([44, 45]) as follows:

$$\sigma_A = \frac{S_{ut}}{3} \tag{7}$$

where S_{ut} is the material tensile strength. Moreover, through comparison with the experimental data ([46]), it has been shown that the fully reversed shear fatigue limit τ_A, where $\rho = 0$, can be estimated by the following equation:

$$\tau_A = \frac{\sigma_A}{\sqrt{3}} \tag{8}$$

Eq. (8) is proposed based on the von Mises hypothesis. To plot the MWCM threshold using Eqs. (6) to (8), only the steel tensile strength is required, which is easily used in design. In Appendix II, the existing experimental data obtained from the uniaxial and multiaxial

proportional and non-proportional fatigue tests on mild steel are compared with the proposed design threshold.

Considering Eqs. (6) to (8), independent of the material tensile strength, the value of $\rho_{\lim} = 3.73$ is obtained. Assuming $S_{ut} = 400\ \text{MPa}$ for structural steel S235, the MWCM formulation for design can be formulated as follows:

$$\tau_a^* = 77 - 10.3\rho \tag{9}$$

where τ_a^* is the allowable shear stress amplitude on the critical plane for a specific value of ρ. As shown in Fig. 18, the highlighted area below the MWCM diagram is estimated as a safe zone, where a crack is not expected to initiate. Therefore, the point beyond the threshold has to be shifted into the safe zone as a result of the strengthening. The effect of the proposed strengthening system on the stresses is described in the following section.

4.1.9.2. Multiaxial calculations for the measured cycles

To evaluate the effect of the strengthening system on the fatigue performance of the angle connections in the Aabach Bridge, the MWCM parameters τ_a and ρ, were calculated using the measured stress cycles in the left angle hotspot, as presented in Table 2.

Table 2. MWCM parameters before and after strengthening in the left angle hotspot

Strengthening	Angle	Train	Stress (MPa)				MWCM parameters			
			$\Delta\sigma_x$	σ_{mx}	$\Delta\sigma_y$	σ_{my}	ρ	τ_α (MPa)	τ_α^* (MPa)	$\tau_\alpha / \tau_\alpha^*$ (%)
Without	Left	(6)	36.2	26.4	10.4	6.8	2.36	9.05	52.6	17.2
	Right	(6)	5	22	-5	5	2.59	4.25	50.3	8.4
	Left	(26)*	63.7	31.9	18	12.5	2	16.25	50.7	28.8
	Left	$S_{0.95}$	36.7	22.9	14	9.8	2.25	9.2	53.8	17
With	Left	(23)	36.5	8.25	12	-8.5	1.45	9.13	62	14.7
	Left	(26)	63.7	19.9	18	-3.5	1.62	15.9	60.3	26.4
	Left	$S_{0.95}$*	36.7	10.9	14	-6.2	1.59	9.2	60.6	15.1

*The values were obtained not from the measurements but based on the assumption that the strengthening system would reduce only the mean stress by 12 and 16 MPa in the x- and y- directions, respectively.

In all of the stress cycles given in Table 2, the stress component τ_{xy} was neglected, and only the stress cycles σ_x and σ_y were considered. In general, the maximum shear stress amplitude

was obtained by the calculation of the stress matrix eigenvalues corresponding to the cyclic portion of the stress cycles. As seen in Table 2, the maximum stress amplitude due to different trains are considerably lower than the threshold value of τ_{α}^{*} obtained by Eq. (9). Particularly, for the right angle, the ratio of $\tau_{\alpha}/\tau_{\alpha}^{*}$ is lower than that for the left angle due to the passage of Train (6), showing that the left angle is more critical compared to the right angle.

The stress cycles due to Trains (6) and (23) were considered. The application of 50 kN prestressing force to each of the CFRP rods in the strengthening system reduced the ρ value from 2.36 (due to Train (6)) to 1.45 (due to Train (23)), resulting in approximately a 39% reduction, without a change in the applied shear stress amplitude. Considering the 95th percentile stress values for passenger trains (see Table 1), the ρ value decreased from 2.25 to 1.59 (approximately 30% reduction).

For Train (26), with the stress cycles shown in Fig. 14(c), only the first large cycle was considered. In Table 2, it was assumed that passage of this train over the unstrengthened connections would generate the stress cycles with the same stress range as that after strengthening, without an initial compressive stress due to the prestressing. As presented in Table 2, the strengthening system would reduce the ρ value from 2 to 1.62, (19% reduction). The above-mentioned figures show that the effectiveness of the strengthening system in moving the points in the MWCM diagram, shown in Fig. 19, depends on the type of train passing over the bridge.

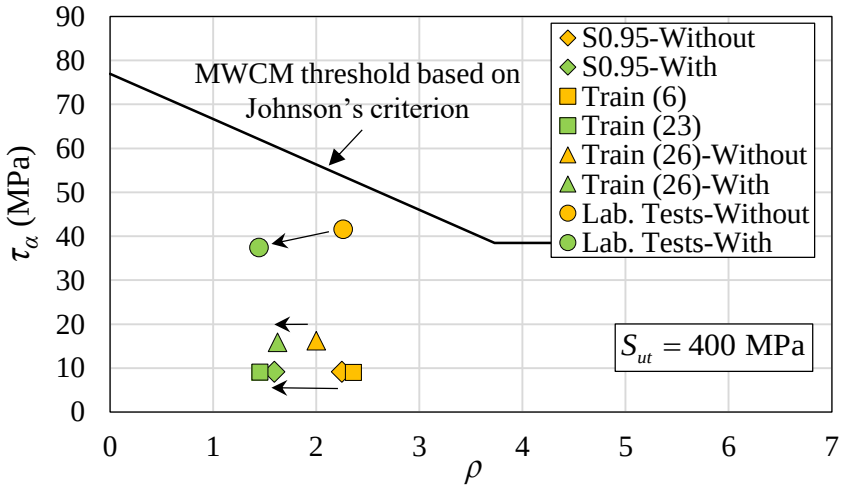

Fig. 19. MWCM diagram to evaluate the fatigue state before and after strengthening in the left angle*.

The fatigue state in the left angle due to the passage of the trains given in Table 2, are plotted

* The figure contains modifications to Fig. 19 of the original published paper.

in the MWCM diagram in Fig. 19. As the strengthening system reduces only the mean stresses, the points primarily follow a horizontal path as a result of the strengthening, i.e., the applied maximum shear stress amplitude remains unchanged and the ρ value decreases.

It is noted that in Fig. 19, the existing residual stresses in the critical location of the angle due to the manufacturing process and installation were not considered, and only the stresses due to the superimposed loads were included in the calculations. To estimate the existing residual stresses, non-destructive onsite measurements, e.g., using ultrasonic method, could be conducted.[*]

4.1.9.3. Determination of the prestressing level in the strengthening system

The prestressing level in the strengthening system was determined in the laboratory tests, as shown in Fig. 3. The set-up was designed so that the fatigue state in the connections are more severe than that in the bridge, as shown in Fig. 19. The stress state in the connection hotspot in the laboratory tests is given in ([36]). In the laboratory tests, it was observed that through 50 kN prestressing force applied to each of the CFRP rods (100 kN in total), the ρ value decreased from 2.26 to 1.46 (i.e. 35% reduction), with a slight decrease in the τ_α value from 41.6 MPa to 37.5 MPa.

The results of the short-term measurements, shown in Fig. 19, indicate that under a certain prestressing force, the reduction in ρ value for the Train (26), which induced a higher mean stress in the angle, was smaller. Therefore, it is more conservative to consider such trains for design of the strengthening system and determination of the required prestressing force.

4.1.10. Summary and conclusions

In this study, a new retrofitting system for strengthening the stringer-to-floor-beam angle connections in a 92-year old riveted bridge in Switzerland is introduced. In the proposed system, prestressed CFRP rods are used to enable the application in complex details. The mechanical strengthening system consists of a newly developed wedge-barrel anchor to hold the prestressed CFRP rod and a clamping system attached to the stringer flange, transmitting the loads solely through friction. The key conclusions of the current study are as follows:

- The strengthening system was installed using the space under the bridge floor system, with

[*] Underlined sentences are additional to the original published paper.

no interruption of traffic on the bridge. For the on-site presetting of the wedges, a new system was introduced, where there was no need for the hydraulic jack to apply the presetting force.

- For prestressing, two 8 mm-CFRP rods were simultaneously pulled using a hydraulic pump, and a temporary housing. The prestressing force at each CFRP rod was 50 kN (equivalent to 995 MPa), which is 49% of the guaranteed tensile strength of the rods. After installation, all parts of the strengthening system were protected against corrosion using the anti-corrosion coatings and isolation from the surrounding environment.
- Short-term measurements indicated that the strengthening system reduced only the mean stress, without changing the stress range magnitude.
- For at least one-year after installation, the long-term performance of the strengthening system is being monitored using the WSN system. The measurements show that during a 7-month measurement period since installation, no prestress loss has been observed.
- A critical-plane-based multiaxial fatigue criterion (i.e., the MWCM) was used to evaluate the fatigue state in the connections before and after strengthening. The MWCM threshold can be plotted using only the material tensile strength, making it easy to use in design. The results of the short-term measurements show that the applied stresses due to the passage of different trains are smaller than 30% of the fatigue threshold, i.e., $\tau_\alpha / \tau_\alpha^* < 0.3$.
- The mean stress reduction by the strengthening system is considered using the ρ value in the MWCM, which depends on the type of trains; for 95th percentile stress values for the passenger trains, the ρ value decreased from 2.25 to 1.59 (approximately 30% reduction), while for Train (26), as a non-passenger train, the ρ value was reduced from 2 to 1.62 (19% reduction).

Appendix I. Stress history in the web for Trains (6) and (14)

The stress history due to the passage of Trains (6) and (14) in the stringer web is depicted in Fig. 20.

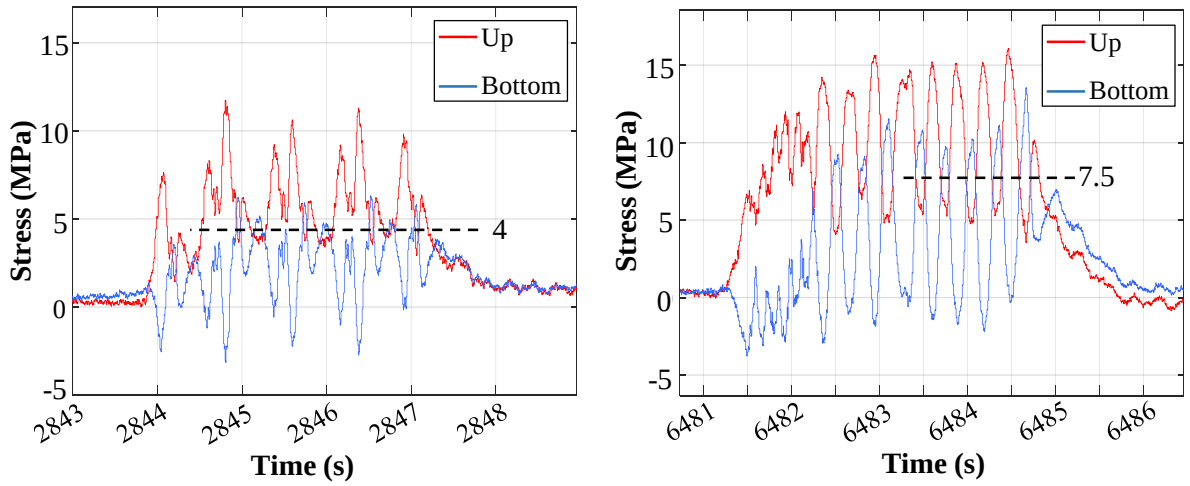

(a) (b)

Fig. 20. Stress history in the web of the stringer: (a) Train (6); (b) Train (14).

Appendix II. Multiaxial fatigue tests

In this section, the design threshold according to the MWCM criterion is compared with the experimental results from the fatigue tests on mild steel, under uniaxial and multiaxial loading conditions. A series of multiaxial tests on mild steel performed by [47] were reanalysed by [48] using the critical plane theory. These data were later used by [46] to check the accuracy of the proposed MWCM diagram to predict the fatigue failure, as shown in Fig. 21(a). In the experimental results shown in this figure, the specimens were subjected to the in-phase and out-of-phase fully reversed σ_x and τ_{xy} stresses.

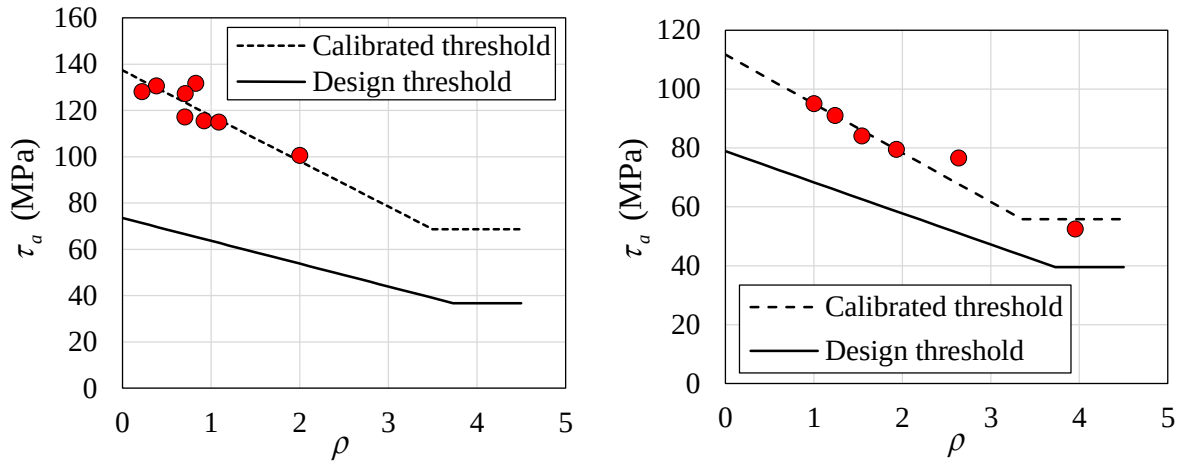

(a) Left side (b) Right side

Fig. 21. Comparison of the MWCM diagram with the experimental results generated: (a) from plane specimens under multiaxial fully reversed in-phase and out-of-phase bending and torsion; (b) under uniaxial loading with zero and non-zero mean stresses.

In general, to be plotted, the MWCM diagram needs to be calibrated with two series of experimental data. For the experimental data shown in Fig. 21(a), $\sigma_A = 235.4\ \text{MPa}$ and $\tau_A = 137.3\ \text{MPa}$. Therefore, the MWCM diagram can be plotted using Eqs. (4) and (6), considering the fact that the tensile strength of the steel used in the tests was $S_{\text{ut}} = 382\ \text{MPa}$. As shown in the figure, the experimental data are well above the design threshold. *The probabilistic analysis on the design thresholds is provided in Supplement B4 at the end of the thesis.*[*]

The MWCM diagram is also compared with the experimental results under uniaxial cyclic stresses with non-zero mean stress taken from [49], as given in Fig. 21(b). The MWCM threshold has been calibrated with two experimental datasets, i.e., one with zero mean stress and the other with non-zero mean stress. Using the tensile strength value of $S_{\text{ut}} = 410\ \text{MPa}$ for the steel used in the tests, the design threshold illustrated in Fig. 21(b) shows the state of the design threshold compared to the experimental data.

Data Availability Statement

Some or all data, models, or code that support the findings of this study are available from the corresponding author upon reasonable request. The items are listed as follows: the data of the short- and long-term measurements, as well as the MATLAB code used for calculation of the stress history.

Acknowledgements

The authors acknowledge the Innosuisse Swiss Innovation Agency (Grant ID: 19240.1 PFIW-IW) for funding this research project. The authors would also like to acknowledge the financial and technical support from the project partners, namely: S&P Clever Reinforcement Company AG, Switzerland; the Swiss Federal Railways (SBB) AG, Bern; and dsp Ingenieure + Planer AG Engineering Office, Uster, Switzerland.

Special thanks go to Slavko Tudor, Giovanni Saragoni, Dimitri Ott, and Robert Widmann from the Structural Engineering Research Laboratory of Empa (Dübendorf, Switzerland), Martin Hüppi from S&P AG, Herbert Friedl, André von Aarburg, and Lukas Bodenmann from SBB, Ann Schumacher from dsp AG, and finally, Reinhard Bischoff, Jonas Meyer, and Khash-Erdene Jalsan from Decentlab GmbH (Dübendorf, Switzerland) for their support and help in

[*] Underlined sentence is additional to the original published paper.

this project.

References

1. Bien J, Elfgren L, Olofsson J. Sustainable bridges, assessment for future traffic demands and longer lives. Wroclaw: Dolnoslaskie Wydawnictwo Edukacyjne 2007. urn:nbn:se:ltu:diva-21622
2. FHWA. FHWA, Federal Highway Administration. U.S. Dempartment of Transportation 2016. https://www.fhwa.dot.gov/bridge/.
3. IEAust. Report Card on the Nation's Infrastructure, The Institution of Engineers. The Institution of Engineers, Australia 1999.
4. Yamada K, Ojio T, Inden T. Bridge monitoring and weigh-in-motion systems in Japan. Post-IABSE Workshop on Structural Monitoring of Bridges, Monash University, Melbourne, Australia 2002.
5. Connor RJ, Fisher JW. Identifying effective and ineffective retrofits for distortion fatigue cracking in steel bridges using field instrumentation. Journal of Bridge Engineering 2006;11(6)745-752. https://doi.org/10.1061/(ASCE)1084-0702(2006)11:6(745)
6. Haghani R, Al-Emrani M, Heshmati M. Fatigue-prone details in steel bridges. Buildings 2012;2(4)456-476. https://doi.org/10.3390/buildings2040456
7. Al-Emrani M Fatigue-Critical Details in Steel Bridges. 2006.
8. Al-Emrani M Fatigue in Riveted Railway Bridges. 2002, PhD Thesis, Chalmers University of Technology, Gothenburg, Sweden.
9. Al-Emrani M, Åkesson B, Kliger R. Overlooked secondary effects in open-deck truss bridges. Struct. Eng. Int. 2004;14307-312. https://doi.org/10.2749/101686604777963612
10. Leonetti D, Maljaars J, Pasquarelli G, Brando G. Rivet clamping force of as-built hot-riveted connections in steel bridges. Journal of Constructional Steel Research 2020;167105955. https://doi.org/10.1016/j.jcsr.2020.105955
11. Wilson WM, Coombe VV fatigue tests of connection angles, N. Series 317, Editor. 1939: Bulletin of University of Illinois Urbana.
12. AREMA. American railway engineering and maintenance-of-way association. Manual for railway engineering 2016;Lanham, MD: American Railway Engineering and Maintenance-of-way Association.
13. Fisher JW. Distortion-induced fatigue cracking in steel bridges. Vol. 336. 1990: Transportation Research Board.
14. Fisher JW, Yen B, Wang D, Mann J. Fatigue and fracture evaluation for rating riveted bridges. 1987, Washington, DC United States: Transportation Research Board.
15. Connor RJ, Lloyd JB Maintenance Actions to Address Fatigue Cracking in Steel Bridge Structures. 2017, NCHRP Project.
16. Baker K, Kulak G. Fatigue of riveted connections. Canadian Journal of Civil Engineering 1985;12(1)184-191. https://doi.org/10.1139/l85-017
17. Reemsnyder HS. Fatigue life extension of riveted connections. Journal of the Structural Division 1975;101(ASCE# 11795 Procceding).
18. Dexter RJ, Ocel JM Manual for repair and retrofit of fatigue cracks in steel bridges. 2013, United States. Federal Highway Administration.
19. Kuehn B, et al. Assessment of existing steel structures: recommendations for estimation of remaining fatigue life. 2008. http://publications.jrc.ec.europa.eu/repository/handle/JRC43401.
20. Bowman MD. Fatigue evaluation of steel bridges. Vol. 721. 2012: Transportation Research Board.
21. Roeder CW, MacRae G, Leland A, Rospo A. Extending the fatigue life of riveted coped stringer connections. Journal of Bridge Engineering 2005;10(1)69-76. https://doi.org/10.1061/(ASCE)1084-0702(2005)10:1(69)
22. Zhao X-L. FRP-strengthened metallic structures. 2013: CRC Press.
23. Ghafoori E, Motavalli M. Lateral-torsional buckling of steel I-beams retrofitted by bonded and un-bonded CFRP laminates with different pre-stress levels: Experimental and numerical study. Construction and Building Materials 2015;76194-206. https://doi.org/10.1016/j.conbuildmat.2014.11.070
24. Hosseini A, Ghafoori E, Motavalli M, Nussbaumer A, Zhao XL, Al-Mahaidi R. Flat Prestressed Unbonded Retrofit System for Strengthening of Existing Metallic I-Girders. Composites Part B 2018;155156-172. https://doi.org/10.1016/j.compositesb.2018.08.026

25. Hosseini A, Ghafoori E, Motavalli M, Nussbaumer A, Zhao X-L, Al-Mahaidi R. Flat prestressed unbonded retrofit system for strengthening of existing metallic I-Girders. Composites Part B: Engineering 2018;155156-172. https://doi.org/10.1016/j.compositesb.2018.08.026
26. Ghafoori E, Motavalli M. Lateral-torsional buckling of steel I-beams retrofitted by bonded and un-bonded CFRP laminates with different pre-stress levels: experimental and numerical study. Construction and Building Materials 2015;76194–206. https://doi.org/10.1016/j.conbuildmat.2014.11.070
27. Ghafoori E, Motavalli M, Nussbaumer A, Herwig A, Prinz G, Fontana M. Determination of minimum CFRP pre-stress levels for fatigue crack prevention in retrofitted metallic beams. Engineering Structures 2015;8429–41. https://doi.org/10.1016/j.engstruct.2014.11.017
28. Ghafoori E, Motavalli M, Nussbaumer A, Herwig A, Prinz G, Fontana M. Design criterion for fatigue strengthening of riveted beams in a 120-year-old railway metallic bridge using pre-stressed CFRP plates. Composites Part B: Engineering 2015;681-13. https://doi.org/10.1016/j.compositesb.2014.08.026
29. Ghafoori E, Hosseini A, Al-Mahaidi R, Zhao X-L, Motavalli M. Prestressed CFRP-strengthening and long-term wireless monitoring of an old roadway metallic bridge. Engineering Structures 2018;176585-605. https://doi.org/10.1016/j.engstruct.2018.09.042
30. Hosseini A, Ghafoori E, Al-Mahaidi R, Zhao X-L, Motavalli M. Strengthening of a 19th-century roadway metallic bridge using nonprestressed bonded and prestressed unbonded CFRP plates. Construction and Building Materials 2019;209240-259. https://doi.org/10.1016/j.conbuildmat.2019.03.095
31. Izadi M, Motavalli M, Ghafoori E. Iron-based shape memory alloy (Fe-SMA) for fatigue strengthening of cracked steel bridge connections. Construction and Building Materials 2019;227116800. https://doi.org/10.1016/j.conbuildmat.2019.116800. http://www.sciencedirect.com/science/article/pii/S0950061819322305.
32. Heydarinouri H, Motavalli M, Nussbaumer A, Ghafoori E. Development of Mechanical Strengthening System for Bridge Connections Using Prestressed CFRP Rods. Journal of Structural Engineering 2021;147(3)04020351. https://doi.org/10.1061/(ASCE)ST.1943-541X.0002923
33. EOTA ETAG 013 Guideline for European Technical Approval of Post-Tensioning Kits for Prestressing of Structures. 2002, EOTA Brussels, Belgium.
34. fib IFfSC. Recommendations for the acceptance of post-tensioning systems 1993. Lausanne, Switzerland: fib.
35. Rostásy FS. Draft guidelines for the acceptance testing of FRP posttensioning tendons. Journal of Composites for Construction 1998;2(1)2-6. https://doi.org/10.1061/(ASCE)1090-0268(1998)2:1(2)
36. Heydarinouri H, Motavalli M, Nussbaumer A, Ghafoori E. Development of mechanical strengthening systems for bridge connections using prestressed CFRP rods. Journal of Structural Engineering, accepted 2020. DOI: 10.1061/(ASCE)ST.1943-541X.0002923
37. Kulak GL, Fisher JW, Struik JH. Guide to Design Criteria for Bolted and Riveted Joints Second Edition. 2001.
38. Munse W, Petersen K. Strength of rivets and bolts in tension. Journal of the Structural Division 1959;85(3)7-28.
39. Sayed-Ahmed EY, Lissel SL, Tadros G, Shrive NG. Carbon fibre reinforced polymer (CFRP) post-tensioned masonry diaphragm walls: prestressing, behaviour, and design recommendations. Canadian Journal of Civil Engineering 1999;26(3)324-344. https://doi.org/10.1139/l98-073
40. Heydarinouri H, Nussbaumer A, Maljaars J, Ghafoori E. Proposed criterion for fatigue strengthening of riveted bridge girders. Procedia Structural Integrity 2019;19482-493. https://doi.org/10.1016/j.prostr.2019.12.052
41. Socie DF, Marquis GB. Multiaxial fatigue. 2000: Society of Automotive Engineers Warrendale, PA.
42. Fatemi A, Socie DF. A critical plane approach to multiaxial fatigue damage including out-of-phase loading. Fatigue & Fracture of Engineering Materials & Structures 1988;11(3)149-165.
43. Susmel L, Lazzarin P. A bi-parametric Wöhler curve for high cycle multiaxial fatigue assessment. Fatigue & Fracture of Engineering Materials & Structures 2002;25(1)63-78. https://doi.org/10.1046/j.1460-2695.2002.00462.x
44. Johnson JB. The materials of construction. 1897: (1st ed.) John Wiley and Sons, New York, pp. 537–47.
45. Johnson JB. Correspondence on `The Launhardt Formula, and Railroad Bridge Specifications'. Trans. Am. Soc. Civil Eng. 1899;41187–188.
46. Susmel L, Tovo R, Lazzarin P. The mean stress effect on the high-cycle fatigue strength from a multiaxial fatigue point of view. International Journal of Fatigue 2005;27(8)928-943. https://doi.org/10.1016/j.ijfatigue.2004.11.012
47. Nishihara T, Kawamoto M. The strength of metals under combined alternating bending and torsion with phase difference. Memories of the College of Engineering, Kyoto Imperial University 1945;11(85)112.

48. McDiarmid D. Fatigue under out-of-phase bending and torsion. Fatigue & Fracture of Engineering Materials & Structures 1987;9(6)457-475. https://doi.org/10.1111/j.1460-2695.1987.tb00471.x
49. Frost N, Marsh K, Pook L Metal fatigue. Clarendon. 1974, Oxford.

5. Conclusions and recommendations for future studies

In this chapter, the main findings of the previous chapters (papers) are summarized and a series of recommendations for future studies are proposed.

5.1. Conclusions

5.1.1. FE analysis and experimental validation of mechanical wedge–barrel anchors for CFRP rods

- The computed contact pressure distributions on the CFRP rod and wedge (at the wedge–barrel interface) were compared for various anchor configurations. The results showed that for anchors with constant differential angles, an increase in the differential angle from 0.1° to 0.23° reduced the peak contact pressure on the wedge and, consequently, on the rod at the loading end. It was also observed that geometric modifications using a fillet or cut at the loading end of the wedge for anchors A-fr-4° and A-cut-40°, respectively, reduced the peak contact pressure on the CFRP rod.
- The Tsai–Wu failure criterion was selected to identify the optimal geometry because of its simplicity and high prediction accuracy under a multiaxial stress state, which is the case for the stress state on the surface of the CFRP rod. Using the failure index *F*s in this criterion, the anchor with the smallest *F*s values for the nodes on the surface of the CFRP rod was selected as the optimal design.
- The greatest *F*s value was obtained for the anchor with a constant differential angle of 0.1°; that is, the A-cd-0.1° anchor with an *F*s of 2.25. By modifying the A-fr-4° and A-cut-40° anchors, the *F*s values were reduced to 1.62 and 1.37, respectively. The smallest *F*s value was achieved for the A-curved anchor with a curved conical profile with an *F*s of 1.22. This was attributed to the smooth increase in the differential angle from the loading end toward the free end. Therefore, this anchor was selected as the optimal design and was used for further experimental studies.

5.1.2. Development of a mechanical wedge–barrel anchor for CFRP rods: static and fatigue behaviours

- A mechanical wedge–barrel anchor for prestressed CFRP rods with a diameter of 8 mm was developed. The anchor consisted of a steel barrel and three split aluminum wedges with curved conical profiles. Aluminum, as a soft material, was used for the wedge to eliminate

the need for a sleeve around the rods and to improve the gripping of the rod through the yielding inside the barrel. The static and fatigue tests were performed according to the European standard test procedures for mechanical post-tensioned (PT) anchorages, such as ETAG 013.

- The results of the uniaxial tensile tests showed that the average tensile strength of the PT system was 2371.4 MPa, which was nearly 16% greater than the nominal tensile strength of the rods. In addition, the failure mode in the static tests was always the rupture of CFRP rods, and not the slippage of the rods inside the anchors. The residual tensile capacity after fatigue testing was still greater than the nominal tensile strength of the CFRP rods with a maximum residual strength of 2566 MPa, indicating no accumulated damage in the wedge–barrel anchors.
- The fatigue tests showed that no rupture occurred in the CFRP rods after 2 million cycles, and no loading frequency sensitivity was observed (range 5–23 Hz). The effect of the wedge seating distance before the application of the cyclic loadings on the slippage between the wedges and rod was also investigated in the fatigue tests. This revealed that the wedges must be adequately pushed into the barrel to provide a high contact pressure on the rods, and consequently, to prevent rod slippage. Therefore, a new presetting system was developed that eliminated the need for hydraulic jacks for the application of the presetting force.

5.1.3. Development of mechanical strengthening system for bridge connections using prestressed CFRP rods

- The main advantages of the developed friction-based retrofitting system consisting of a mechanical wedge–barrel anchor and clamping system are as follows:
  (i) The clamping system is able to transmit asymmetric forces and thereby increase the versatility of the system for various structural applications (requiring only one edge to be attached to the structure, without drilling holes). This is an advantage compared to previous versions of PUR systems that transmit forces only in symmetrical conditions.
  (ii) It is applicable in complex structural geometries such as stringer-to-floor-beam double-angle connections.
  (iii) It minimizes the intervention of traffic over the bridge; that is, there is no need for bridge closure during installation and dismantling.
  (iv) The installation and dismantling procedures have no residual effect and cause no damage to the parent structure thanks to a presetting system, which eliminates the need for a hydraulic jack, and a temporary housing for prestressing.

- The results of the static pull-off tests on the strengthening system are summarized as follows:
  (i) The failure mode was always the CFRP rupture with an average failure load of 110 kN (equivalent to 2188 MPa), which is greater than 2047 MPa, as the nominal tensile strength of the CFRP rods but smaller than 2367MPa obtained in the uniaxial tensile tests on the wedge–barrel anchors. The smaller value was attributed to the rotation of the wedge–barrel anchor and the consequent bending stresses at the loading end of the anchor.
  (ii) The slippage load of the clamping system was 128 kN, which was greater than the obtained uniaxial tensile strength of the CFRP rods being 119 kN (equivalent to 2367MPa). This indicates that the clamping system provided an adequate friction resistance to prevent slippage.
  (iii) At a tensile load level of approximately 70 kN in the CFRP rods, the wedges and rod were inserted simultaneously into the barrel, without any slippage, which is a desired behavior for wedge–barrel anchors.

- Using a large-scale test setup to simulate the dimensions and complexity of the connections of the Aabach Bridge, fatigue tests were conducted on the strengthened connections. The fatigue test results were as follows:
  (i) The application of a 50-kN CFRP prestressing force reduced the dominant stress components in the critical location of the connections near the angle fillet by more than 40%.
  (ii) After 11 million loading cycles, no rupture or prestressing loss in the CFRP rods and no slippage in the strengthening system components were observed.

- Geometric imperfections in the setup, originating from the difference in the elevations of the supports and stringers not being completely straight, resulted in significant strains/stresses in the connections. However, they did not affect the static nor the fatigue performances of the retrofitting system.

5.1.4. Multiaxial fatigue criteria for prestressed strengthening of steel connections

- Appropriate critical plane-based multiaxial fatigue thresholds were identified for predicting crack initiation in angle connections. Stress-based multiaxial models based on the MWCM and Fatemi-Socie (FS) models were employed, which allowed to consider the effect of the strengthening system as well as the residual stresses in the critical location of the connections.

- Residual stress measurements using the cut-compliance method showed compressive values at the critical locations of the connecting angles due to the manufacturing process. At a cut depth of 0.3 mm, the maximum measured equivalent compressive stresses in the x- and y-directions were -135 and -44 MPa, respectively. The stresses due to the fastening of the bolts originated from the geometric imperfections in the angles and showed a large scatter, ranging from approximately 20 to 200 MPa in the x-direction.
- The fatigue test results showed that using n_A=0.44, the crack test data was beyond the threshold based on the MWCM criterion. For the FS criterion, the threshold could predict the crack initiation considering k=1 and τ_A=121.2 MPa or k=0.5 and τ_A=110.9 MPa. Using Johnson's formulation (with n_A=0.33), a more conservative threshold was obtained. The identified thresholds for the prediction of crack initiation and the methodology used for consideration of prestressed strengthening can be used for the design of the retrofitting system.
- For the connection and configuration tested, it was shown that the prestressing force had the highest influence on the fatigue resistance threshold by reducing the mean stress of σ_x, as the dominant stress component. In contrast, the strengthening system had a negligible effect on the range of the stress components.

5.1.5. Strengthening of Steel Connections in a 92-Year Old Railway Bridge using Prestressed CFRP Rods: a Multiaxial Fatigue Design Criterion

- The installation of the strengthening system on the Aabach Bridge was conducted using the space under the bridge floor system with no interruption to traffic over the bridge. As a result of the prestressing force, which was 49% of the nominal tensile strength of the rods (equivalent to 995 MPa), compressive stresses of 12 MPa and 16 MPa were applied in the x- and y-directions, respectively, without changing the magnitude of the stress range.
- The mean stress reduction depended on the type of train passing over the bridge. The majority of trains were passenger trains. The value for the mean stress for the 95th percentile (those greater than 95% of all values) in the x-direction (as the dominant stress component) was equal to 22.9 MPa. Considering the compressive stresses due to prestressing, the 95th percentile stress in the x-direction was reduced by 47% from 22.9 to 10.9 MPa. This shows the effectiveness of the strengthening system in reducing the mean stress values.
- The MWCM threshold based on Johnson's formulation was employed as a conservative criterion to evaluate the stress state at the critical location of the connections before and

after strengthening. The results of the short-term measurements showed that the applied stresses due to the passage of different trains were less than 30% of the fatigue threshold. The mean stress reduction was considered using the parameter ρ. It was found that for the 95th percentile stress values of the passenger trains, the ρ value decreased from 2.25 to 1.59 (approximately 30% reduction), whereas for a non-passenger train (26), the ρ value decreased from 2 to 1.62 (19% reduction).

- Finally, long-term measurements were conducted using a wireless sensor network (WSN) system to monitor the long-term performance of the strengthening system. The post-installation measurements show that no prestress loss was observed in the CFRP rods, indicating that no slippage occurred in the components of the strengthening system.

5.2. Recommendations for future studies

The following research topics are recommended for future studies based on the knowledge and experience collected in the present thesis. The recommendations are categorized into two subsections: development of wedge-type anchors for CFRP tendons, and prediction of crack initiation in angle connections. For each section, the recommended studies are sorted according to their priority to fulfill the prerequisites of the subsequent studies.

5.2.1. Development of wedge-type anchors for CFRP tendons

1. A limited number of anchor configurations were considered in this study (paper I). In future studies, it is recommended that further configurations be considered in FE simulations to further optimize the design, that is, consideration of various constant differential angles and radii of the conical curved profiles.
2. In the current study, the Tsai-Wu failure criterion was used only for the sake of comparison between different anchor configurations; that is, the anchor with the smallest failure index *F*s was selected as the optimal design. However, the ability of the Tsai-Wu failure criterion or any other failure criteria for composite materials to predict the failure of the CFRP rod was not investigated in the laboratory tests. An interesting topic for future studies would be the determination of the proper criteria for the prediction of the failure load of PT systems by conducting further experiments on mechanical wedge–barrel anchors.
3. The development of reliable mechanical wedge–barrel anchors for a single prestressed CFRP rod paves the way for the development of (corrosion-free) anchor heads with multiple CFRP tendons. The development of such products has great potential in various structural

applications and can be considered as an alternative to the existing PT anchors for steel strands. The anchor heads for CFRP tendons can be applied in prestressed concrete box girders, bridge hangers in suspension bridges, and prestressed concrete slabs. Susceptibility of the anchorage to small deviations is an important aspect to be investigated.

5.2.2. Prediction of crack initiation and propagation in angle connections

1. In the current study, only stress-based multiaxial fatigue criteria were used for the prediction of crack initiation in the angle connection subjected to distortion-induced fatigue loadings because the stresses were always elastic. In reality, however, plastic deformations are likely to occur in connections for different reasons, such as the existence of high tensile residual stresses, the fastening of bolts/rivets, or overloading due to the passage of heavy trains. In future research, the effect of yielding in the first cycle followed by subsequent elastic cycles due to overload, or a large number of cycles with plastic deformations on the crack initiation threshold and the location of crack initiation can be investigated. For this purpose, the performance of the strain-based multiaxial fatigue criteria based on the critical plane approach can be compared to the stress-based criteria.
2. In this study, the crack initiation thresholds were determined for S235 steel under proportional and constant amplitude fatigue loadings. The estimated fatigue limits as a function of the steel tensile strength is valid for the steels with higher strengths. In addition, the multiaxial models used in the current study are capable of considering the non-proportional and variable amplitude loadings. The validity of the proposed thresholds for other steel grades, such as S355, as well as the effect of non-proportionality and variable amplitude loadings, are topics for future research.
3. Prediction of multiaxial fatigue crack initiation in the angle connections requires a calculation procedure that is more complicated than the codified calculations. To achieve a simplified calculation procedure, further experimental evidence is required with respect to the fatigue resistance and residual stresses in the connections in service. More fatigue test results in future studies might enable the use of an equivalent nominal stress and enhance the accuracy of the reliability analysis to determine the characteristic and design values.
4. Fatigue failure in angle connections subjected to distortion-induced cyclic loadings can occur either in the angle or in the rivets or bolts due to an inadequate clamping force combined with the prying action. In the current study, fatigue failure in only the angles was studied. In future studies, the prediction of fatigue failure in fasteners (rivets/bolts) can be investigated.

5. The current study focused on the initiation of a fatigue crack and not on the propagation behavior of an existing crack. In future works, the fatigue crack propagation for the connections with an existing crack under such a complex multiaxial stress condition can be numerically and experimentally investigated, and the ability of the proposed prestressed strengthening system to arrest the crack can be studied using fracture mechanics.

Supplement A: Supplementary materials for Paper III

A.1. Stress distribution in top flange of the beam in the clamped area

Fig. A1 shows the bending stress distribution in the *x*-direction on the top and bottom surfaces of the beam top flange under the clamped area due to the rotation of the clamping system. The stresses are depicted under the application of different tensile CFRP loads, *P*, considering coarse and fine meshes (see Table 2 in Paper III).

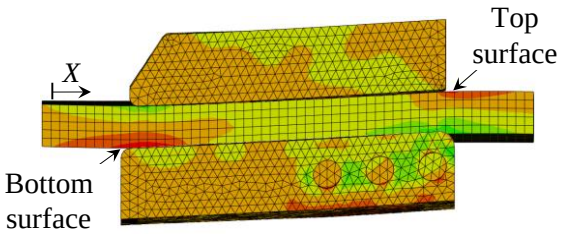

(a) Clamped area of beam top flange

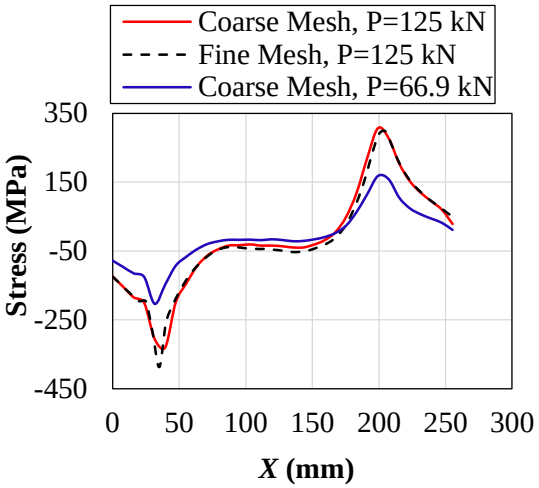

(b) Stress distribution on top surface

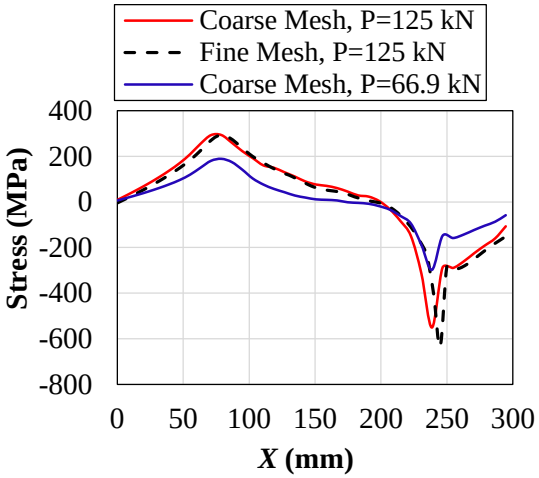

(c) Stress distribution on bottom surface

Fig. A1. Bending stress distribution on top flange of beam in the clamped area due to rotation of the clamping system.

Although the obtained stresses are smaller than the steel yield stress of the top flange for this case, the effect of the flange thickness on the bending stress distribution has to be investigated for the beams with other geometries.

A.2. Strain in angle connections during fatigue test

Figs. A2 and A3 show the strains measured in the a-, b-, and c-directions using rosette strain gauges in the angle connections under cyclic loadings before and after strengthening, respectively. In the fatigue tests, the cyclic loads were applied to the stringers by the actuators and fluctuated between 24 and 240 kN.

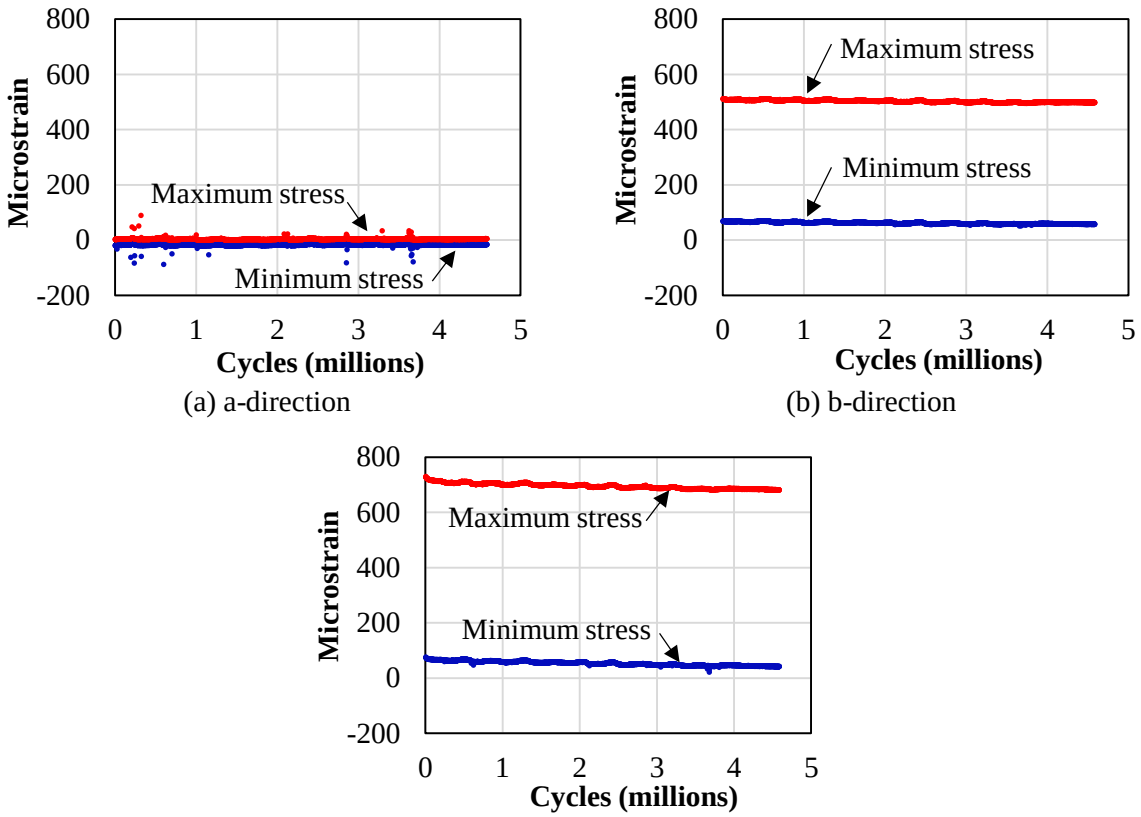

(a) a-direction (b) b-direction

(c) c-direction

Fig. A2. Strains in unstrengthened angle connections in fatigue tests.

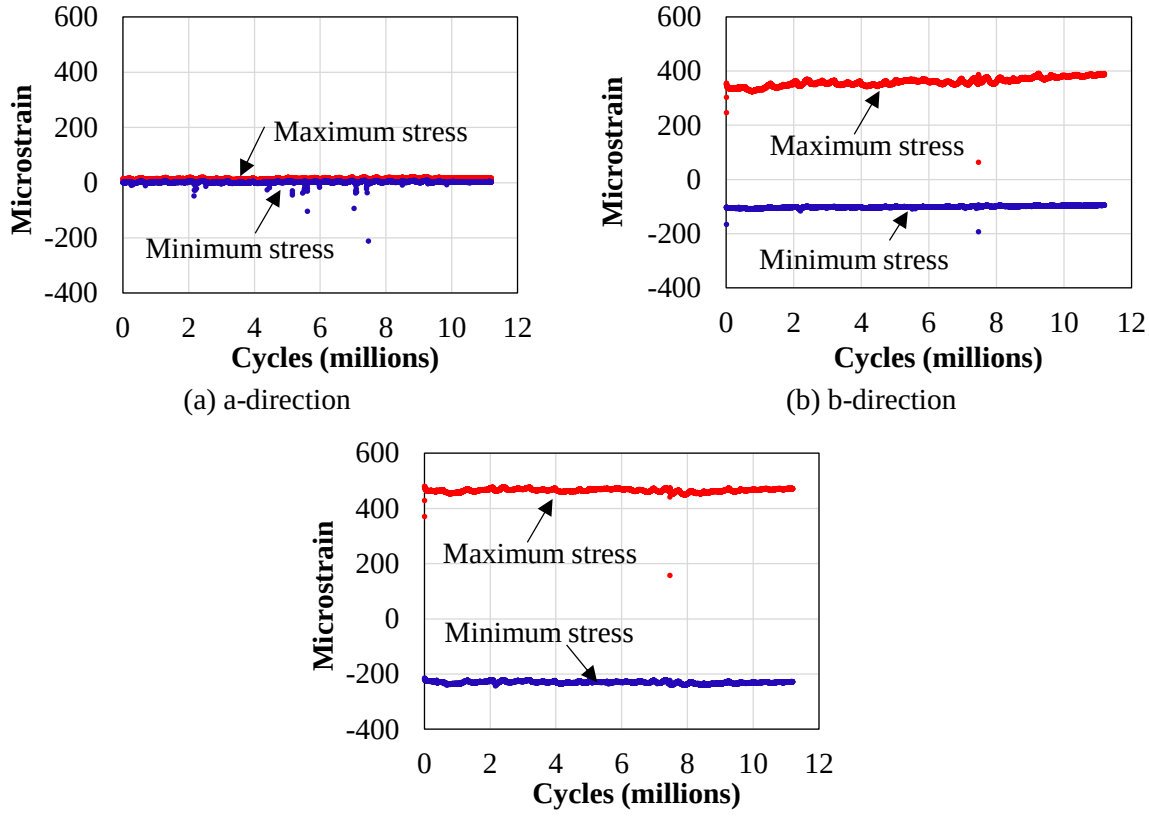

(a) a-direction (b) b-direction

(c) c-direction

Fig. A3. Strains in strengthened angle connections in fatigue tests.

Supplement B: Supplementary materials for Paper IV

B.1. MATLAB script for multiaxial fatigue analysis based on the critical plane approach

In the following script, the multiaxial stress state is calculated using the strains in the a-, b-, and c-directions measured by a rosette strain gauge. Then, the required parameters for the modified Wohler curve method (MWCM) and Fatemi-Socie (FS) criteria, as critical plane-based multi-axial fatigue criteria, are obtained.

```
% 1. Input of measured strains in the a-, b-, and c-directions under minimum and maximum fatigue loadings:
Strain_a_min=28;  Strain_a_max=1060;
Strain_b_min=280;  Strain_b_max=2086;
Strain_c_min=178;  Strain_c_max=1007;

% 2. Calculation of principal strains under minimum and maximum fatigue loadings:
Epsilon_P_min=0.5*(Strain_a_min+Strain_c_min)+sqrt((Strain_a_min-Strain_b_min)^2+(Strain_b_min-
Strain_c_min)^2)/sqrt(2);
Epsilon_Q_min=0.5*(Strain_a_min+Strain_c_min)-sqrt((Strain_a_min-Strain_b_min)^2+(Strain_b_min-
Strain_c_min)^2)/sqrt(2);
Teta_min_intial=0.5*atan((Strain_a_min-2*Strain_b_min+Strain_c_min)/(Strain_a_min-Strain_c_min));
Teta_min=Teta_min_intial-sign(Teta_min_intial)*pi/4+sign(2*Strain_b_min-Strain_a_min-Strain_c_min)*pi/4;

Epsilon_P_max=0.5*(Strain_a_max+Strain_c_max)+sqrt((Strain_a_max-Strain_b_max)^2+(Strain_b_max-
Strain_c_max)^2)/sqrt(2);
Epsilon_Q_max=0.5*(Strain_a_max+Strain_c_max)-sqrt((Strain_a_max-Strain_b_max)^2+(Strain_b_max-
Strain_c_max)^2)/sqrt(2);
Teta_max_intial=0.5*atan((Strain_a_max-2*Strain_b_max+Strain_c_max)/(Strain_a_max-Strain_c_max));
Teta_max=Teta_max_intial-sign(Teta_max_intial)*pi/4+sign(2*Strain_b_max-Strain_a_max-
Strain_c_max)*pi/4;

% 3. Calculation of principal stresses corresponding to minimum and maximum loadings:
Sigma_P_min=.192*(Epsilon_P_min+0.3*Epsilon_Q_min)/0.91;
Sigma_Q_min=.192*(0.3*Epsilon_P_min+Epsilon_Q_min)/0.91;

Sigma_P_max=.192*(Epsilon_P_max+0.3*Epsilon_Q_max)/0.91;
Sigma_Q_max=.192*(0.3*Epsilon_P_max+Epsilon_Q_max)/0.91;

% 5. Stress calculation in the x-y plane corresponding to minimum and maximum loadings:
Sigma_X_min=0.5*(Sigma_P_min+Sigma_Q_min)+.5*(Sigma_P_min-Sigma_Q_min)*(sin(2*Teta_min));
Sigma_Y_min=0.5*(Sigma_P_min+Sigma_Q_min)-.5*(Sigma_P_min-Sigma_Q_min)*(sin(2*Teta_min));
```

```
Tau_XY_min=.5*(Sigma_P_min-Sigma_Q_min)*cos(2*Teta_min);

Sigma_X_max=0.5*(Sigma_P_max+Sigma_Q_max)+.5*(Sigma_P_max-Sigma_Q_max)*(sin(2*Teta_max));
Sigma_Y_max=0.5*(Sigma_P_max+Sigma_Q_max)-.5*(Sigma_P_max-Sigma_Q_max)*(sin(2*Teta_max));
Tau_XY_max=.5*(Sigma_P_max-Sigma_Q_max)*cos(2*Teta_max);

Sigma_Z_min=0; Sigma_Z_max=0;
Tau_XZ_min=0; Tau_XZ_max=0;
Tau_YZ_min=0; Tau_YZ_max=0;

% 5. Calculation of cyclic and static portions of stress cycles:
Sigma_X_a=(Sigma_X_max-Sigma_X_min)/2; Sigma_X_m=(Sigma_X_max+Sigma_X_min)/2;
Sigma_Y_a=(Sigma_Y_max-Sigma_Y_min)/2; Sigma_Y_m=(Sigma_Y_max+Sigma_Y_min)/2;
Sigma_Z_a=(Sigma_Z_max-Sigma_Z_min)/2; Sigma_Z_m=(Sigma_Z_max+Sigma_Z_min)/2;

Tau_XY_a=(Tau_XY_max-Tau_XY_min)/2; Tau_XY_m=(Tau_XY_max+Tau_XY_min)/2;
Tau_XZ_a=(Tau_XZ_max-Tau_XZ_min)/2; Tau_XZ_m=(Tau_XZ_max+Tau_XZ_min)/2;
Tau_YZ_a=(Tau_YZ_max-Tau_YZ_min)/2; Tau_YZ_m=(Tau_YZ_max+Tau_YZ_min)/2;

Sigma_a=[Sigma_X_a Tau_XY_a Tau_XZ_a;Tau_XY_a Sigma_Y_a Tau_YZ_a;Tau_XZ_a Tau_YZ_a
Sigma_Z_a];
Sigma_m=[Sigma_X_m Tau_XY_m Tau_XZ_m;Tau_XY_m Sigma_Y_m Tau_YZ_m;Tau_XZ_m Tau_YZ_m
Sigma_Z_m];

% 6. Determination of principal stresses for te cyclic stresses and transformation matrix [α]:
[V,D]=eig(Sigma_a);
[d,ind] = sort(diag(D),'descend');
Sigma_a_Principal=D(ind,ind);
Eigenvectors=V(:,ind);

Sigma_1=Sigma_a_Principal(1,1);
Sigma_2=Sigma_a_Principal(2,2);
Sigma_3=Sigma_a_Principal(3,3);

Tau_a=(Sigma_1-Sigma_3)/2;
Sigma_na=(Sigma_1+Sigma_3)/2;

a=Eigenvectors';
clear d ind

% 7. Determination of directions of maximum shear stresses:
n1_Max_Shear=a'*[1/sqrt(2);0;-1/sqrt(2)];
```

```
n2_Max_Shear=a'*[0;1;0];
n3_Max_Shear=a'*[1/sqrt(2);0;1/sqrt(2)];
a_Max_Shear=[n1_Max_Shear n2_Max_Shear n3_Max_Shear]';

% 8. Determination of critical plane direction and static and alternating normal stresses acting on that:
Sigma_m_Max_Shear=a_Max_Shear*Sigma_m*a_Max_Shear';
Sigma_a_Max_Shear=a_Max_Shear*Sigma_a*a_Max_Shear';

if  Sigma_m_Max_Shear(1,1 )> Sigma_m_Max_Shear(3,3)
    n_Critical=n1_Max_Shear;
else
     n_Critical=n3_Max_Shear;
end
Sigma_nm=max(Sigma_m_Max_Shear(1,1),Sigma_m_Max_Shear(3,3));

% 9. Calculation of Rho value:
Rho=(Sigma_na+Sigma_nm)/Tau_a
```

B.2. Stresses in prestressed CFRP rods during fatigue tests

Fig. B1 shows the stresses in the CFRP rods used for the strengthening of specimen no. 3 during the fatigue test (see Table 1 in Paper IV). The stresses were obtained by measuring the strains of CFRP rods 8 mm in diameter and an elastic modulus of 160 GPa in the direction of the fibers. The stresses in both CFRP rods on the right and left sides were approximately the same. In addition, no prestressing loss was observed in the rods after 2 million cycles.

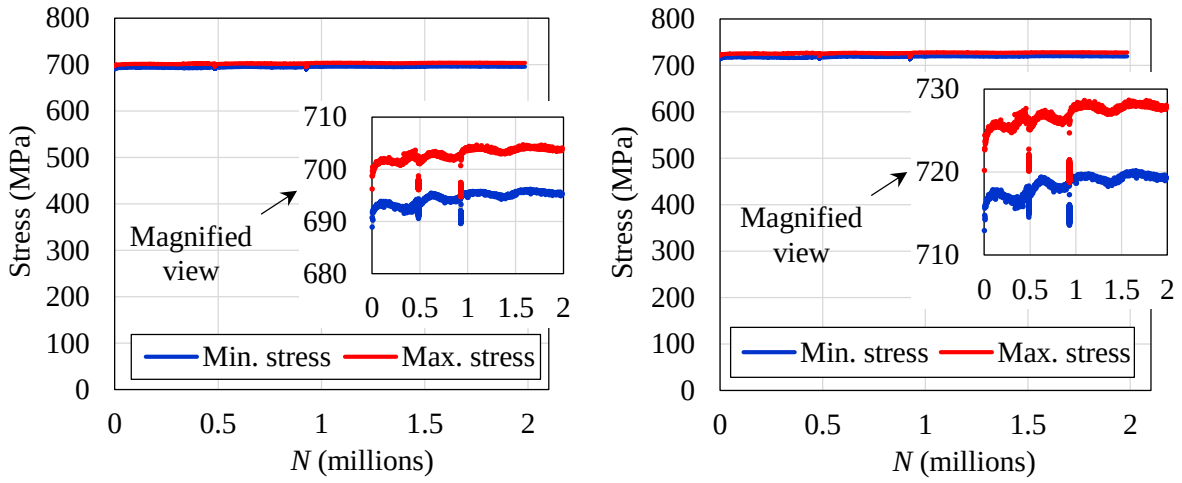

Fig. B1. Stress in the CFRP rods of specimen no. 3 during fatigue test.

B.3. Strain measurements in cut-compliance method

Fig. B2 shows the strain measurements as a function of the cut depth, a, in the cut-compliance (CC) method used to calculate the residual stresses. The measured strains in both the x- and y-directions were tensile, indicating that the residual stresses were compressive. In addition, the strains in the x-direction were greater. For more information regarding the CC method and samples, see section 3.1.6.1 of Paper IV.

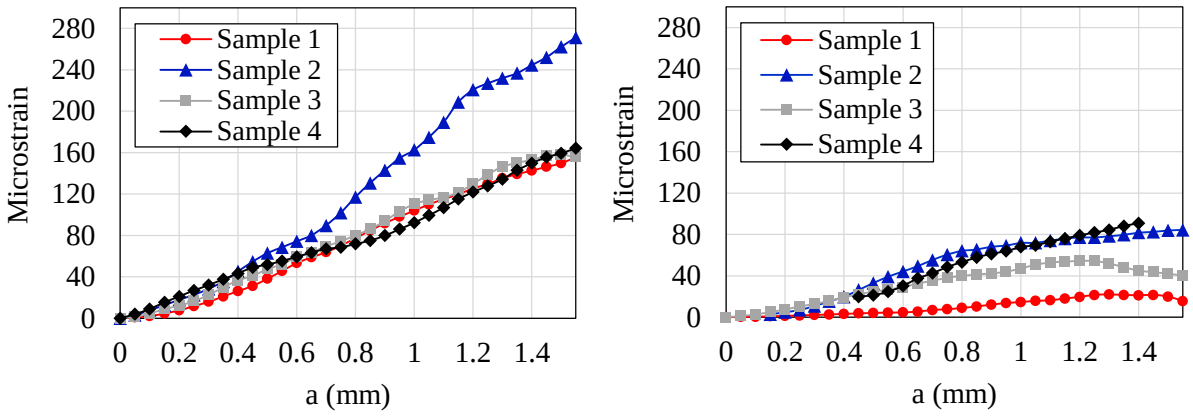

(a) In the x-direction (b) In the y-direction

Fig. B2. Strains as a function of cut depth in CC method.

B.4. Probabilistic analysis of the fatigue test data

In this section, a probabilistic analysis is performed on the uniaxial and multiaxial fatigue test results to determine the design thresholds and corresponding partial resistance factors. The partial resistance factor corresponding to the Johnson's criterion, γ_{Mf}, is calculated according to the lower tolerance bound method [1] and compared with the resistance factor γ^*_{Mf} obtained by the proposed method in annex D of the Eurocode — Basis of structural and geotechnical design.

B4.1. Calculation procedure based on the lower tolerance bound method

In this section, the calculations are based on the procedure introduced in [1]. Fig. B3 shows a series of fatigue test data, which are plotted in a τ_a–ρ diagram.

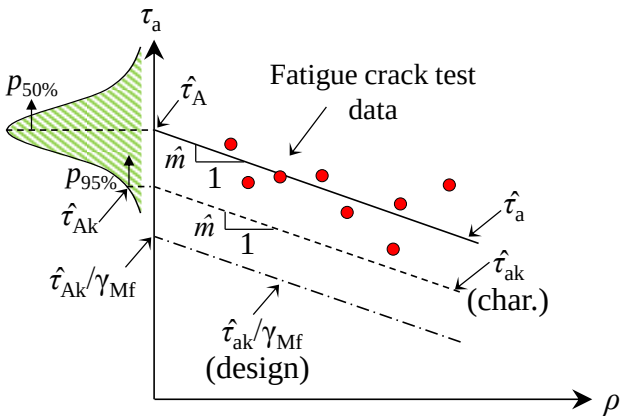

Fig. B3. Mean, characteristic, and design thresholds for a series of fatigue test data.

The mean threshold $\hat{\tau}_a$ is obtained using the linear regression and least square method, as below:

$$\hat{\tau}_a = \hat{\tau}_A - \hat{m}\rho \tag{B1}$$

In this equation, $\hat{\tau}_A$ and $\hat{m}$ are intercept and the slope of the line shown in Fig. B3, and are calculated using the following equations:

$$\hat{\tau}_A = \frac{\sum \tau_a \times \sum \rho^2 - \sum \rho \times \sum \rho \times \tau_a}{n \times \sum \rho^2 - (\sum \rho)^2}$$
$$\hat{m} = \frac{\sum \tau_a \times \sum \rho - n \times \sum \rho \times \tau_a}{n \times \sum \rho^2 - (\sum \rho)^2} \tag{B2}$$

The threshold $\hat{\tau}_a$ obtained by the linear regression represents the mean fatigue strength, with a survival probability of 50%, assuming a Normal distribution. For the design purpose, a characteristic threshold with a survival probability of 95% is used, as shown by $\hat{\tau}_{ak}$ in Fig. B3. The characteristic threshold is determined using a lower tolerance bound, which is defined as the bound that is expected to be smaller than 95% of the intercept of the whole population, shown by $\hat{\tau}_{Ak}$ in Fig. B3. The slope of the characteristic threshold is assumed equal to $\hat{m}$. The lower tolerance bound intercept is calculated as follows [2]:

$$\hat{\tau}_{Ak} = \hat{\tau}_A - k_{(1-\alpha),p,n} \times s \tag{B3}$$

where $k_{(1-\alpha),p,n}$ is a factor for an one-sided tolerance bound accounting for the covered proportion of the population, p, confidence level $(1-\alpha)$, and sample size, n. For $(1-\alpha)=0.75$ and $p=0.95$, $k_{(1-\alpha),p,n}$ is obtained for various values of n using Table A in [1]. The standard deviation s in Eq. B3 is calculated as follows:

$$s = \sqrt{\frac{\sum(\tau_a - \hat{\tau}_a)^2}{n-1}} \tag{B4}$$

The design threshold in Fig. B3 is obtained by dividing the characteristic threshold $\hat{\tau_{ak}}$ by the partial resistance factor γ_{Mf}, i.e., $\hat{\tau_{ak}}/\gamma_{Mf}$. Considering the Johnson's criterion as the design threshold, the intercept $\hat{\tau_{Ak}}/\gamma_{Mf}$ equals to $\hat{\tau_{A\text{-}Johnson}}$. Therefore, γ_{Mf} is obtained using the following equation:

$$\gamma_{Mf} = \frac{\hat{\tau}_{Ak}}{\hat{\tau}_{A\text{-}Johnson}} \tag{B5}$$

It is noted that Johnson's criterion has been proposed for design purposes [3] and it corresponded to the most conservative threshold for the test results presented in Paper IV, with n_A=0.33. Therefore, it is considered here as the design threshold.

B4.2. Calculation procedure based on annex D of Eurocode

The scientific background of the probabilistic model of the resistance proposed in the annex D of Eurocode — Basis of structural and geotechnical design is presented in [2]. In this appendix, only the calculation procedure and required formulations are presented.

The least squares coefficient *b* is obtained as follows:

$$b = \sum(\tau_a \times \hat{\tau}_a) / \sum \hat{\tau}_a^2 \tag{B6}$$

The error term for each experimental value (the data *i*) is calculated as:

$$\delta_i = \tau_{ai} / \hat{\tau}_{ai} \tag{B7}$$

The coefficient of variation V_δ is calculated using the following formulation:

$$V_\delta^2 = e^{s_\Delta^2} - 1 \tag{B8}$$

In Eq. B8, the parameter $e^{s_\Delta^2}$ is obtained using the following equations:

$$\Delta_i = \ln \delta_i \tag{B9-a}$$

$$\bar{\Delta} = \sum \Delta_i / n \tag{B9-b}$$

$$s_\Delta^2 = \frac{\sum(\Delta_i - \bar{\Delta})^2}{n-1} \tag{B9-c}$$

The coefficient of variation V_r of the probabilistic model depends on the coefficients V_δ as well

as V_{rt} of the estimated resistance, which are calculated using Eqs. B10 and B11.

$$V_{rt}^2 = \frac{s}{\hat{\tau}_{\mathrm{A}}} \tag{B10}$$

$$V_r^2 = V_\delta^2 + V_{rt}^2 \tag{B11}$$

The characteristic resistance τ_{Ak}^* is obtained by the following equation:

$$\tau_{Ak}^* = \hat{\tau}_A \exp(-k_\infty \times \alpha_{rt} \times Q_{rt} - k_n \times \alpha_\delta \times Q_\delta - 0.5Q^2) \tag{B12}$$

In Eq. B12, $k_\infty = 1.64$, and k_{n} is given in Table D.1 in the annex D of Eurocode. The other parameters in Eq. B12 are calculated using the following formulations:

$$\begin{aligned} Q_{rt} &= \sqrt{\ln(1+V_{rt}^2)} \\ Q_\delta &= \sqrt{\ln(1+V_\delta^2)} \\ Q &= \sqrt{\ln(1+V_r^2)} \\ \alpha_{rt} &= Q_{rt} / Q \\ \alpha_\delta &= Q_\delta / Q \end{aligned} \tag{B13}$$

The intercept of the design threshold, τ_D^*, is computed as follows:

$$\tau_D^* = \hat{\tau}_A \exp(-k_{d,\infty} \times \alpha_{rt} \times Q_{rt} - k_{d,n} \times \alpha_\delta \times Q_\delta - 0.5Q^2) \tag{B14}$$

where $k_{d,\infty} = 3.04$ and $k_{\mathrm{d,n}}$ is given in Table D.1 in the annex D of Eurocode. Note that the design fractile factor $k_{d,\infty}$ corresponds to a target reliability index of β=3.8 (for the 50-year reliability index according to the reliability requirement in prEN 1990:2020 section C.3.4) and a sensitivity factor for resistance of α_{R}=0.8, resulting in $k_{d,\infty} = \alpha_{\mathrm{R}} \times \beta = 0.8 \times 3.8 = 3.04$. These values are commonly used to obtain the design resistance value, as proposed in annex D of the Eurocode — Basis of structural and geotechnical design. The partial resistance factor is calculated as follows:

$$\gamma_{\mathrm{MF}}^* = \tau_{Ak}^* / \tau_D^* \tag{B15}$$

The design threshold can be obtained using the following equation:

$$\tau_d^* = \tau_{ak}^* / \gamma_{\mathrm{MF}}^* \tag{B16}$$

where characteristic threshold τ^*_{ak} is assumed to have the same slope as in Eq. B2, with the following formulation:

$$\tau^*_{ak} = \tau^*_{Ak} - \hat{m}\rho \tag{B17}$$

B4.3. Results of the probabilistic analysis

B4.3.1. Uniaxial test results

B4.3.1.1. Lower tolerance bound method

The uniaxial test results (see in Fig. 7 of Paper IV) are presented in Table B4.1, which contains the intermediate calculations required for probabilistic analysis. Using Eq. B2, the intercept and slope of the mean threshold, $\hat{\tau}_a$, (see Fig. B3) are obtained as: $\hat{\tau}_A$=107.4 MPa and $\hat{m}$=13.51.

Table B4.1. Intermediate calculations based on lower tolerance bound method for the uniaxial fatigue tests.

Test no.	ρ	τ_a	$\rho\times\tau_a$	ρ^2	τ^2_a	$\hat{\tau}_a$	$(\tau_a-\hat{\tau}_a)^2$
1	1.00	95	95	1.00	9025.0	93.9	1.2
2	1.24	91	112.5	1.53	8281.0	90.7	0.1
3	1.54	84	129.5	2.38	7056.0	86.6	6.8
4	1.93	79.5	153.5	3.73	6320.3	81.3	3.4
5	2.63	76.5	201.5	6.94	5852.3	71.8	21.6
6	3.95	52.5	207.5	15.62	2756.3	54.0	2.4
∑	12.30	478.5	899.50	31.19	39290.8		35.4

Considering $k_{(1-\alpha),p,n}$=2.336 and using Eqs. B3 and B4, the lower tolerance bound intercept is obtained as $\hat{\tau}_{Ak}$=101.2 MPa. Considering Johnson's criterion as the design threshold, with $\hat{\tau}_{A\text{-}Johnson}$=78.9 MPa (corresponding to n_A=0.33), the partial resistance factor is obtained using Eq. B5 as γ_{Mf}=1.28.The mean, characteristic, and design thresholds are plotted in Fig. B4.

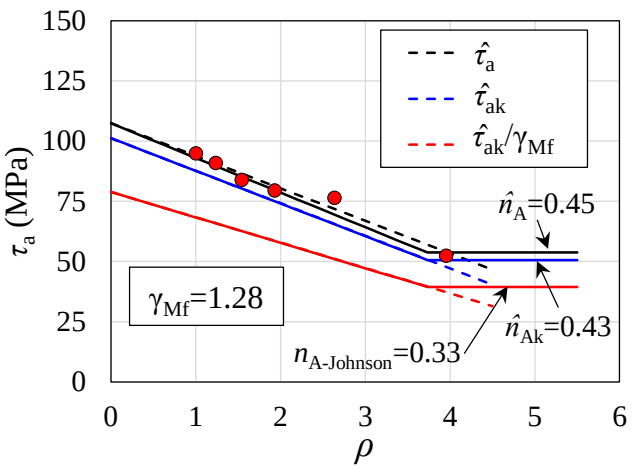

Fig. B4. Mean, characteristic, and design thresholds and the corresponding MWCM thresholds for the uniaxial fatigue tests.

In this figure, in addition to the thresholds obtained by the probabilistic analysis, the thresholds based on the MWCM criterion are plotted. Each MWCM threshold corresponds to a n_A value obtained as follows (see also Eqs. 19-21 in Paper IV):

$$\hat{n}_A = \frac{\sqrt{3}\hat{\tau}_A}{S_{ut}},\ \hat{n}_{Ak} = \frac{\sqrt{3}\hat{\tau}_{Ak}}{S_{ut}},\ \text{and}\ n_{A\text{-Johnson}} = 0.33 \tag{B18}$$

The tensile strength of the steel is S_{ut}=410 MPa. As shown in Fig. B4, the thresholds obtained by the probabilistic analysis and the corresponding MWCM thresholds are a close to each other.

B4.3.1.2. annex D of Eurocode

The intermediate calculation results required for the procedure proposed in the annex D of Eurocode are presented in Table B4.2.

Table B4.2. Intermediate calculations based on annex D of Eurocode for the uniaxial fatigue tests.

Test no.	ρ	τ_a	$\hat{\tau}_a$	$\tau_a \times \hat{\tau}_a$	$\hat{\tau}_a^2$	$\delta_i=\tau_a/\hat{\tau}_a$	$\Delta_i=\ln \delta_i$	$(\Delta_i-\bar{\Delta})^2$
1	1.00	95	93.9	8923.0	8822.2	1.01	0.0114	0.0002
2	1.24	91	90.7	8256.8	8232.7	1.00	0.0029	0.0000
3	1.54	84	86.6	7275.0	7500.9	0.97	-0.0306	0.0009
4	1.93	79.5	81.3	6467.3	6617.7	0.98	-0.0230	0.0005
5	2.63	76.5	71.8	5496.4	5162.2	1.06	0.0627	0.0040
6	3.95	52.5	54.0	2836.8	2919.7	0.97	-0.0288	0.0008
∑		478.5	478.5	39255.3	39255.3		-0.0053	0.0064

Using the Eqs. B6–B11, the required parameters are calculated as presented in Table B4.3.

Table B4.3. Required parameters for the calculations based on annex D of Eurocode for uniaxial fatigue tests.

b	$\bar{\Delta}$	s^2_Δ	V^2_δ	V^2_{rt}	V^2_r	Q_{rt}	Q_δ	Q	α_{rt}	α_δ	k_n
1	-0.001	0.001	0.001	0.001	0.002	0.025	0.036	0.043	0.571	0.821	2.177

The characteristic intercept is obtained using Eq. B12 as τ^*_{Ak} = 98.4 MPa, which is close to $\hat{\tau}_{Ak}$=101.2 MPa from the lower tolerance bound method. Considering, $k_{d,n}$=6.36, and using Eq. B14, the design threshold intercept is obtained as τ^*_D =85.3 MPa, which is close to $\hat{\tau}_{A\text{-Johnson}}$=78.9 MPa. Using the Eq. B15, the partial resistance factor is $\gamma^*_{MF} = 1.15.$, which is smaller than $\gamma_{MF} = 1.28.$

The characteristic and design thresholds according to the lower tolerance bound method and annex D of Eurocode are plotted in Fig. B5. As shown, both characteristic and design thresholds based on the two different methods are close to each other. In addition, the threshold based on the Johnson's criterion is plotted.

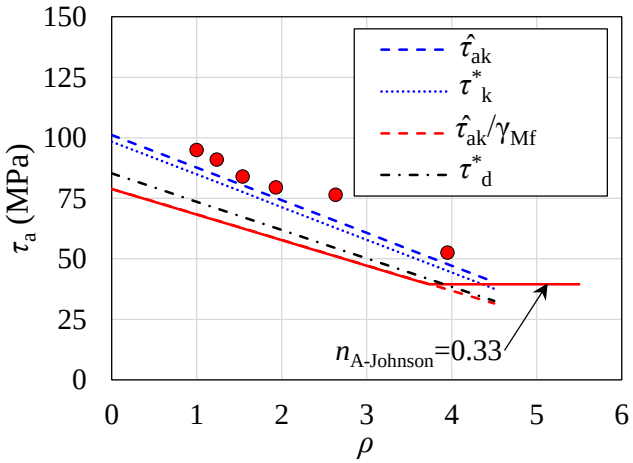

Fig. B5. Characteristic and design thresholds according to the lower tolerance bound method and annex D of Eurocode for the uniaxial fatigue tests.

B4.3.2. Multiaxial test results

In this section, the multiaxial fatigue test results (see Fig. 7 of Paper IV) are considered excluding the results obtained in the experiments in the present study. The crack data points obtained in the current study are not sufficient for probabilistic analysis, and, they cannot be plotted together with the existing fatigue test results due to the different tensile strengths of the steels. As the calculation procedure is the same as section B4.3.1, only the final results are presented in Table B4.4.

Table B4.4. Summary of the probabilistic analysis.

Test series	Characteristic values (MPa)		Design values (MPa)		Partial resistance factor	
	$\hat{\tau}_{Ak}$	$\hat{\tau}^*_{Ak}$	$\tau_{A\text{-}Johnson}$	$\hat{\tau}_D$	γ_{Mf}	γ^*_{Mf}
Uniaxial	107.4	101.2	78.9	85.3	1.28	1.15
Multiaxial excl. the obtained results	123.8	122.09	72.8	107.65	1.70	1.13

The mean, characteristic, design, and MWCM thresholds for the multiaxial fatigue test results excluding the current experimental results are plotted in Fig. B6. As shown in Fig. B6(a), the MWCM thresholds corresponding to different n_A values are close to the other thresholds. The consideration of the threshold based on Johnson's criterion results in a partial resistance factor of γ_{Mf}=1.70, which is larger than that from the uniaxial tests being γ_{Mf}=1.28.

As given in Table 4.4, the design intercept is $\hat{\tau}_D$=107.65 MPa, which is larger than $\hat{\tau}_{A\text{-}Johnson}$=72.8 MPa (considering S_{ut}=382 MPa), while the characteristic intercepts $\hat{\tau}_{Ak}$ and $\hat{\tau}^*_{Ak}$ are very close. Therefore, the partial resistance factor obtained using Eurocode method is smaller than that for the Johnson's criterion, being 1.13 and 1.70, respectively (see Table B4.4). Fig. B6(b) shows that the threshold based on the Johnson's criterion is more conservative than that obtained according to the annex D of Eurocode.

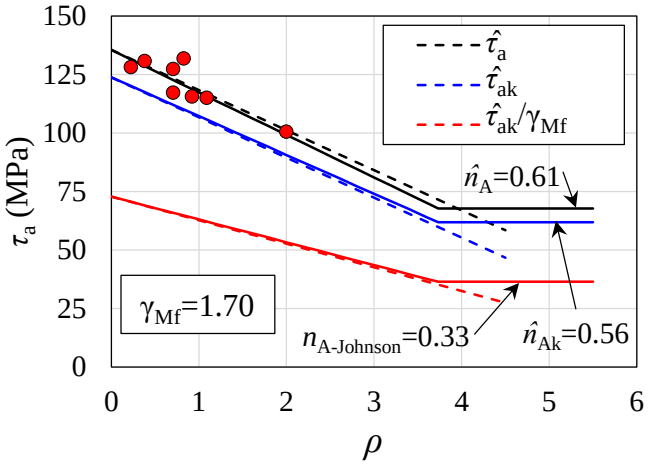

(a) Mean, characteristic, design, and MWCM thresholds

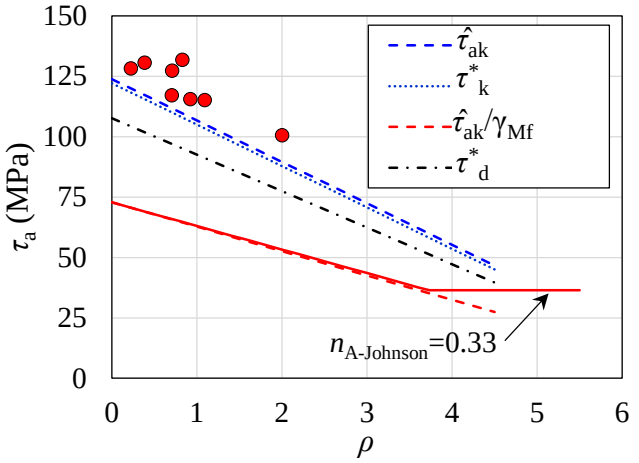

(b) Comparison of the thresholds according to the lower tolerance bound method and annex D of Eurocode

Fig. B6. Thresholds for the multiaxial fatigue tests excluding the current fatigue test results.

The problem with the existing multiaxial fatigue test results is that all test data are on the left side (see Fig. B6), i.e., there are a very limited number of data points for ρ > 1, leading to a weaker validation of the design curves compared to the uniaxial fatigue test results (see Figs. B4 and B5).

References

1. Drebenstedt K, Euler M Statistical analysis of fatigue test data according to Eurocode 3, in Maintenance, Safety, Risk, Management and Life-Cycle Performance of Bridges. 2018, CRC Press. p. 2244-2251.
2. Holický M. Basic statistical concepts and technique–Implementation of Eurocodes Handbook 2 Reliability Backgrounds. 2005.
3. Johnson JB. The materials of construction. 1897: (1st ed.) John Wiley and Sons, New York, pp. 537–47.

Supplement C: Supplementary materials for Paper V

C.1. Effect of bolt removal

As explained in Paper V, to install the strengthening system, two bolts/rivets (from the second row of the fasteners) were removed from the angles to allow the CFRP rods to pass through the floor-beam. The removed rivets were replaced with two hollow bolts. In the laboratory tests (see Fig. 3 of Paper V), the strains in the angle hotspot were measured during bolt removal using rosette strain gauges with directions a, b, and c (a and c were perpendicular to each other). As shown in Fig. C1(a), during bolt removal, the strain change in different directions was negligible, i.e., less than 10 microstrains. This shows that removing the bolts from the second row of fasteners did not change the strain/stress state in the connection hotspot.

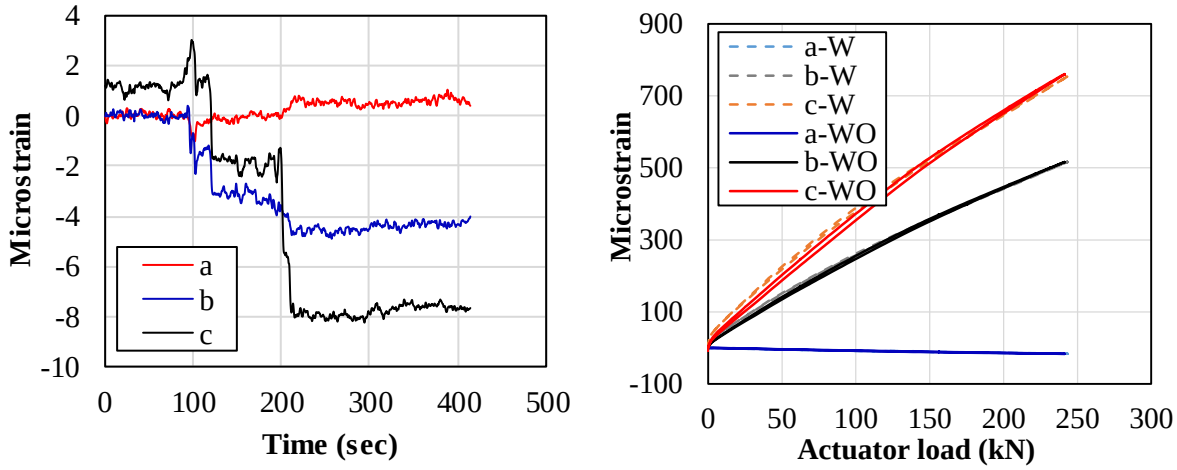

(a) (b)

Fig. C1. Effect of bolt removal on the strains in different directions at the angle hotspot: (a) strains during removal of bolts and (b) strains during loading of stringers by the actuators.

In addition, Fig. C1(b) shows that the removal of the bolts did not change the strains in different directions due to the application of the actuator loads. This is attributed to the fact that the removal of the bolts/rivets from the second row of bolts did not affect the out-of-plane deformation of the connections.

C.2. Removal of rivets

Before the installation of the strengthening system on the Aabach Bridge, two rivets from the second row in the angles located on either side of the stringer were removed to pass the CFRP rods through the rivet holes. The rivet head was removed using an angle grinder, then, a hole was drilled through the rivet head and shank, and finally, using a hammer, the rivet was pushed

out of the hole, as shown in Fig. C2(b). The drilled hole facilitated the removal of the rivets.

(a) Removal of rivet head

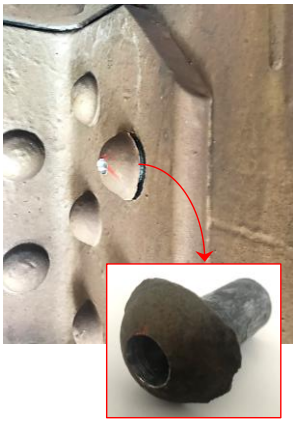

(b) Pushing rivet out with hammer

Fig. C2. Removal of rivets from the Aabach Bridge connections.

C.3. MATLAB script for strain and stress calculations from measurements on the Aabach Bridge

In this appendix, the MATLAB scripts for the calculation of the strains and stresses in the x-y plane using the strains measured on the Aabach Bridge are presented.

C.3.1. Before strengthening the connections

C.3.1.1. Strains and stresses in angle connection measured by rosette trains gauges

```
% 1. Input of measured data into MATLAB script:
First_hour_Before=table2array(Vorversuch1);
Second_hour_Before=table2array(Vorversuch2);
Third_hour_Before=table2array(Vorversuch3);
Fourth_hour_Before=table2array(Vorversuch4);

Time1_Before(:,1)=First_hour_Before(:,1);
Time2_Before(:,1)=Second_hour_Before(:,1)+Time1_Before(end,1);
Time3_Before(:,1)=Third_hour_Before(:,1)+Time2_Before(end,1);
Time4_Before(:,1)=Fourth_hour_Before(:,1)+Time3_Before(end,1);

Second_hour_Before(:,1)=Time2_Before(:,1);
Third_hour_Before(:,1)=Time3_Before(:,1);
Fourth_hour_Before(:,1)=Time4_Before(:,1);

Strain_Before=vertcat(First_hour_Before,Second_hour_Before,Third_hour_Before,Fourth_hour_Before);
Stress_Before(:,1)=Strain_Before(:,1);
```

```
% 2. Calculation of principal strains and stresses as well as the stresses in the x-y plane:
for i=1:18563123
   Epsilon_P(i,1)=0.5*(Strain_Before(i,4)+Strain_Before(i,6))+sqrt((Strain_Before(i,4)-Strain_Be-
   fore(i,5))^2+(Strain_Before(i,5)-Strain_Before(i,6))^2)/sqrt(2);
   Epsilon_Q(i,1)=0.5*(Strain_Before(i,4)+Strain_Before(i,6))-sqrt((Strain_Before(i,4)-Strain_Be-
   fore(i,5))^2+(Strain_Before(i,5)-Strain_Before(i,6))^2)/sqrt(2);
   Teta(i,1)=0.5*atan((Strain_Before(i,4)-2*Strain_Before(i,5)+Strain_Before(i,6))/(Strain_Before(i,4)-
   Strain_Before(i,6)));
   Sigma_P(i,1)=.2*(Epsilon_P(i,1)+0.3*Epsilon_Q(i,1))/0.91;
   Sigma_Q(i,1)=.2*(0.3*Epsilon_P(i,1)+Epsilon_Q(i,1))/0.91;
   Stress_Before(i,2)=0.5*(Sigma_P(i,1)+Sigma_Q(i,1))+.5*(Sigma_P(i,1)-Sigma_Q(i,1))*abs(sin(2*Teta(i,1)));
   Stress_Before(i,3)=0.5*(Sigma_P(i,1)+Sigma_Q(i,1))-.5*(Sigma_P(i,1)-Sigma_Q(i,1))*abs(sin(2*Teta(i,1)));
   Stress_Before(i,4)=.5*(Sigma_P(i,1)-Sigma_Q(i,1))*cos(2*Teta(i,1));
end

% 3. Lowpass filter to visually distinguish between the measured data
fs = 2400;
fLP = 70;
d = fdesign.lowpass('N,Fc',50,fLP,fs);
LP = design(d); % fvtool(LP)
```

C.1.1.1. Stresses in the web of the angles

```
Stress_Before_Web(:,1)=Strain_Before(:,1);
Stress_Before_Web(:,2)=Strain_Before(:,2)*.2;
Stress_Before_Web(:,3)=Strain_Before(:,3)*.2;
```

C.3.2. During prestressing

```
% Input of the measured data into the MATLAB script:
Stress_Prestressing(:,1)=Strain_Prestressing(:,1);
Stress_Prestressing(:,2:3)=Strain_Prestressing(:,2:3)*0.16; % Stress in CFRP rods
Stress_Prestressing(:,4:11)=Strain_Prestressing(:,4:11)*0.2; % Stress in connections and web
```

C.3.3. After strengthening the connections

C.3.3.1. Strains and stresses in angle connection and CFRP rods

```
% 1. Input of the measured data into the MATLAB script:
First_hour_After=table2array(prestressed1);
Second_hour_After=table2array(prestressed2);
Third_hour_After=table2array(prestressed3);
Fourth_hour_After=table2array(prestressed4);

Time1_After(:,1)=First_hour_After(:,1);
```

```
Time2_After(:,1)=Second_hour_After(:,1)+Time1_After(end,1);
Time3_After(:,1)=Third_hour_After(:,1)+Time2_After(end,1);
Time4_After(:,1)=Fourth_hour_After(:,1)+Time3_After(end,1);

Second_hour_After(:,1)=Time2_After(:,1);
Third_hour_After(:,1)=Time3_After(:,1);
Fourth_hour_After(:,1)=Time4_After(:,1);

Strain_After=vertcat(First_hour_After,Second_hour_After,Third_hour_After,Fourth_hour_After);
Stress_After(:,1)=Strain_After(:,1);
Stress_After(:,2:3)=Strain_After(:,2:3)*0.16;

% 2. Calculation of principal strains and stresses as well as stresses in the x-y plane:
for i=1:18242386
   Epsilon_P_After(i,1)=0.5*(Strain_After(i,6)+Strain_After(i,8))+sqrt((Strain_After(i,6)-Strain_Af-
   ter(i,7))^2+(Strain_After(i,7)-Strain_After(i,8))^2)/sqrt(2);
   Epsilon_Q_After(i,1)=0.5*(Strain_After(i,6)+Strain_After(i,8))-sqrt((Strain_After(i,6)-Strain_Af-
   ter(i,7))^2+(Strain_After(i,7)-Strain_After(i,8))^2)/sqrt(2);
   Teta_After(i,1)=0.5*atan((Strain_After(i,4)-2*Strain_After(i,5)+Strain_After(i,6))/(Strain_After(i,4)-
   Strain_After(i,6)));
   Sigma_P_After(i,1)=.2*(Epsilon_P_After(i,1)+0.3*Epsilon_Q_After(i,1))/0.91;
   Sigma_Q_After(i,1)=.2*(0.3*Epsilon_P_After(i,1)+Epsilon_Q_After(i,1))/0.91;
   Stress_After(i,4)=0.5*(Sigma_P_After(i,1)+Sigma_Q_After(i,1))+.5*(Sigma_P_After(i,1)-Sigma_Q_Af-
   ter(i,1))*abs(sin(2*Teta_After(i,1)));
   Stress_After(i,5)=0.5*(Sigma_P_After(i,1)+Sigma_Q_After(i,1))-.5*(Sigma_P_After(i,1)-Sigma_Q_Af-
   ter(i,1))*abs(sin(2*Teta_After(i,1)));
   Stress_After(i,6)=.5*(Sigma_P_After(i,1)-Sigma_Q_After(i,1))*cos(2*Teta_After(i,1));
end

% 3. Lowpass filter to visually distinguish between the measured data:
fs=2400;
fLP=70;
d=fdesign.lowpass('N,Fc',50,fLP,fs);
LP=design(d); % fvtool(LP)
```

C.3.3.1. Stresses in the web of the angles

```
Stress_After_Web(:,1)=Strain_After(:,1);
Stress_After_Web(:,2)=Strain_After(:,4)*.2;
Stress_After_Web(:,3)=Strain_After(:,5)*.2
```

C.4. Stresses in web of stringer before and after strengthening

In the short-term measurement, the stress history at the top and bottom of the stringer web (see Fig. 9 of Paper V) was measured before and after strengthening, as shown in Fig. C3. The results show that the stress levels due to the passage of trains were generally small, even before strengthening. The strengthening system caused a compressive stress of approximately 8 MPa at both the top and bottom of the web, as shown in Fig. C3(b).

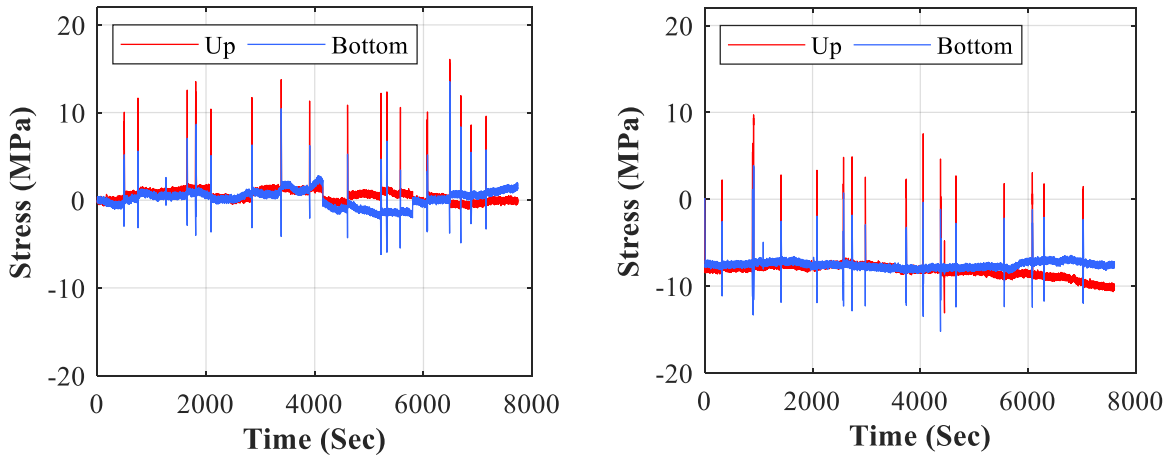

(a) Before strengthening (b) After strengthening

Fig. C3. Stress history the web of stringer.

C.5. Air temperature and humidity history in long-term measurements

Fig. C4 shows the updated results from the long-term measurements after the installation in February 2020 using a WSN system. Fig C4(a) shows that no prestressing loss occurred in the CFRP rods during this period. The changes in the humidity and air temperature during this period are shown in Fig. C4(b). The minimum and maximum air temperatures were -11.3 and 36 °C, respectively, and the minimum and maximum relative humidity were 18.7% and 99.2%, respectively. As shown in the plots, during the winter, the prestressing level slightly decreased, and during the spring of 2021, the prestressing level increased. For more information about the long-term measurements, see section 4.1.7 of Paper V.

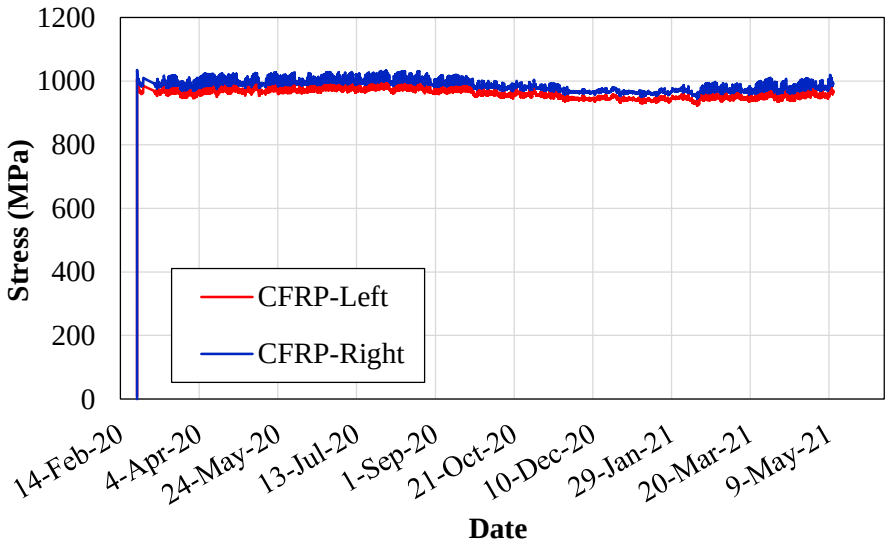

(a) Stress history of CFRP rods

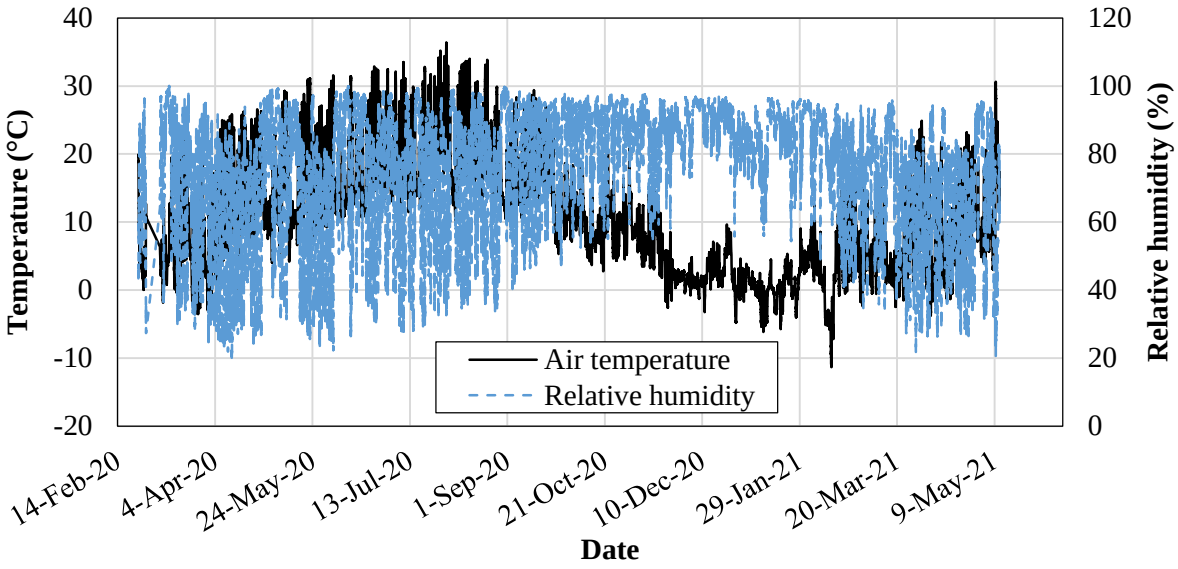

(b) Air temperature and humidity history

Fig. C4. Long-term measurements after installation of the strengthening system.

Curriculum Vitae

Personal information

Name: Hossein Heydarinouri

Date of birth: 22.06.1992

Nationality: Iran

Tel.: +41 58 765 4509

E-Mails: hossein.heydarinouri@empa.ch, hossein.heydarinouri@alumni.epfl.ch

Education

- **PhD** **Swiss Federal Institute of Technology, EPFL, Lausanne** **May. 2017- Aug. 2021**
  PhD in Civil & Environmental Engineering
- **MSc** **The university of Tehran, Tehran, Iran** **Sep. 2014 - Jan. 2017**
  MSc. in Structural Engineering
  Thesis: Optimized computer program for nonlinear analysis of unbonded prestressed concrete beams.
- **BSc** **The university of Tehran, Tehran, Iran** **Sep. 2010 - Sep. 2014**
  BSc. in civil Engineering

Research interests

- Fatigue in steel structures
- Strengthening and rehabilitation of structures
- Application of FRP materials in structures
- Vibration control of structures
- Numerical methods, in particular, FE analysis

Teaching Experiences

- Multiaxial fatigue, lecturer, ETH Zürich **since Oct. /2019**
- Mechanics of continuous media, Teaching Assistant, University of Tehran **Sep./ 2016 - Jan. / 2017**
- Steel Structures I and II, Teaching Assistant, University of Tehran **Jan 2015 - Feb. / 2016**

Computer Skills

- Structural softwares: ABAQUS, SAP2000, ETABS, Autodesk Inventor
- Office Software: Microsoft Office (Excel, Word, Power Point)
- Programming Languages: MATLAB , Fortran

Languages

- Persian: Native
- English: Fluent
- German: Fluent

Extracurricular Activities

- **Music**: Traditional Persian music
- **Sports**: Football, volleyball ,and swimming

Publications

ISI Journal Papers

1. Heydarinouri, H., Motavalli, M., Nussbaumer, A., & Ghafoori, E. (2021). Development of a Mechanical Wedge–Barrel Anchor for CFRP Rods: Static and Fatigue Behaviors. *Journal of Composites for Construction*, *25*(3), 04021015.
2. Heydarinouri, H., Motavalli, M., Nussbaumer, A., & Ghafoori, E. (2021). Development of Mechanical Strengthening System for Bridge Connections Using Prestressed CFRP Rods. *Journal of Structural Engineering*, *147*(3), 04020351.
3. Heydarinouri, H., Nussbaumer, A., Motavalli, M., & Ghafoori, E. (2021). Strengthening of Steel Connections in a 92-Year-Old Railway Bridge Using Prestressed CFRP Rods: Multiaxial Fatigue Design Criterion. *Journal of Bridge Engineering*, *26*(6), 04021023.
4. Heydarinouri, H., Nussbaumer, A., Motavalli, M., & Ghafoori, E. (2021). Multiaxial fatigue criteria for prestressed strengthening of steel connections. Submitted to *International Journal of Fatigue*, Accepted on 4th of August 2021.
5. Heydarinouri, H., Vidovic, A., Nussbaumer, A., & Ghafoori, E. (2021). FE analysis and experimental validation of mechanical wedge–barrel anchors for CFRP rods. Submitted to *Composite Structures*, Accepted on 1st of August 2021.
6. Heydarinouri, H., & Zahrai, S.M. 2017. Iterative Step-by-Step Procedure for Optimal Placement and Design of Viscoelastic Dampers to Improve Damping Ratio. *The Structural Design of Tall and Special Buildings*. 26(9), e1361.

Conference Papers

1. Heydarinouri, H., Motavalli, M., Nussbaumer, A., & Ghafoori, E. 2020. Development of a Strengthening System for Riveted/Bolted Steel Connections using Prestressed CFRP Rods. Accepted in *10th International Conference on FRP composites in Civil Engineering CICE*.
2. Heydarinouri, H., Motavalli, M., Nussbaumer, A., & Ghafoori, E. 2020. Experimental Study on the Static and Fatigue Behavior of a New Mechanical Wedge–barrel anchor. Accepted in *10th International Conference on FRP composites in Civil Engineering CICE*.
3. Heydarinouri, H., Motavalli, M., Nussbaumer, A., & Ghafoori, E. (2019). Proposed criterion for fatigue strengthening of riveted bridge girders. *Procedia Structural Integrity*, *19*, 482–493.